INAUGURAL-DISSERTATION

ZUR

ERLANGUNG DER DOKTORWÜRDE

DER

NATURWISSENSCHAFTLICH-MATHEMATISCHEN GESAMTFAKULTÄT

DER

RUPRECHT-KARLS-UNIVERSITÄT HEIDELBERG

VORGELEGT VON

PHILIPP DOMINIK ENGEL

AUS

WIESBADEN

TAG DER MÜNDLICHEN PRÜFUNG: 30. JANUAR 2026

Quantum-Chemical Investigations In Homogeneous Catalysis

Quantenchemische Untersuchungen zur homogenen Katalyse

Vorgelegt von

Philipp Dominik Engel

Erster Gutachter: Prof. Dr. Peter Comba
Zweiter Gutachter: Prof. Dr. Lutz Greb

"*If you think you understand quantum mechanics, then you don't understand quantum mechanics.*"

Richard P. Feynman

Acknowledgements

My PhD was performed in a rather complex setting involving three parties: the group of Peter Comba at the University of Heidelberg, the Catalysis Research Laboratory (CaRLa), formerly managed by Thomas Schaub and currently led by Jean-Pierre Lindner and Jaroslaw Mormul, and the BASF quantum chemistry group, led by Peter Deglmann (team lead) and Ansgar Schäfer (group lead). While this may sound complicated, it offered me a privilege that few PhD students enjoy: the opportunity to experience the different worlds of academic research at universities, industrial research at BASF SE, and research at CaRLa as the interface between both worlds.

Peter Comba, thank you for your supervision and constant support over the past three years. Even though I was technically an external PhD student, your door was (literally) always open for any question. Beyond the joy of working with such a wholehearted scientist, I particularly want to highlight the ski seminars we shared. I am grateful for the opportunity to have been among your final PhD students.

Thomas, thank you for your support and mentorship. I learned a lot from you about experimental organometallic chemistry, catalysis, and their applications in industry. As a computational chemist, our weekly discussions were always a valuable "reality check," giving me an experimental perspective on my simulations. I am especially grateful for the opportunities you gave me to attend many conferences and spend three months abroad.

Peter Deglmann, your ability to combine synthetic knowledge with computational chemistry was truly inspiring. I greatly enjoyed being trained by you. Ansgar Schäfer, you have been a mentor to me since my internship at BASF and throughout my PhD. Despite your time-consuming management duties, you always made time to discuss my science with me. Thank you both also for introducing me to the TURBOMOLE world.

Jaro, thank you for supervising me on our project and for all the input on how large language models can facilitate daily research tasks. Stephen and Jean-Pierre, I also greatly appreciate your valuable contributions and comments during group seminars and throughout the publication process.

One might think that such a multi-party supervision concept could be a nightmare; yet, I am deeply grateful to all of you for working together so harmoniously and never pressuring me between differing opinions.

I would like to thank Lutz Greb for preparing the second review of this thesis. I am also grateful to the University of Heidelberg and BASF for establishing and funding CaRLa, giving me and many other young scientists a unique opportunity to research application-oriented homogeneous catalysis.

I want to thank everyone who proofread parts of this thesis; your feedback was invaluable! I also thank all members of the Comba group, CaRLa, and the BASF quantum chemistry group for their valuable comments during group seminars.

I was the only PhD student directly at CaRLa, working in a team with eight postdocs. I never felt like an outsider; instead, it felt like a natural opportunity to learn from more experienced researchers. I would like to particularly acknowledge my project partners at CaRLa: Chang, Lucas, and Leo. I learned a lot from you, and it was a pleasure to work with people who truly value input from simulations.

Max (Menche), thank you for your close supervision; having someone who had been in the same position was always extremely helpful. Lucas, it was amazing working with you, especially integrating my simulations with your experiments. Beyond science, I enjoyed our Switch sessions and cooking evenings! Chang, thank you for your great work on our project and all the stick fights. Tobi, while we never fully mastered the local accent, our tram rides and time at work were always fun. Yannick, thank you for the enjoyable cooking evenings. Adrian, it was a pleasure to work with such a motivated scientist, and I wish we had started the project earlier. Max, although our project did not make it into this thesis, I learned a lot from you about organometallic chemistry. Vel, thank you for all the helpful discussions and especially for the time we shared as office mates. Frank, thank you for the lessons in Pfälzisch and your travel tips. I acknowledge the support provided by my colleagues at BASF, with particular mention of Max, Maike, Oliver (Welz), as well as my office partners Tiago and Max (Springer).

I also conducted a research stay in the Sigman group in Salt Lake City. Matt, thank you for your supervision and for teaching me. Jamie, it was a pleasure working with such an expert in data science. My stay abroad was an incredible experience in a large but welcoming group. Thank you to David, Jamie, James, Julia, Cristian, and all other members of the Sigman group for making it so memorable. Thank you, Pep and Lucas (Mele), for the collaboration on our project.

Finally, I want to thank my family, my partner, and my friends for their unwavering support throughout my PhD. A special mention also goes to the AK Simbel. Without all of you, I would not have made it this far.

QUANTENCHEMISCHE UNTERSUCHUNGEN ZUR HOMOGENEN KATALYSE

Zusammenfassung

Die vorliegende Arbeit beschreibt Beispiele der Nutzung quantenchemischer Methoden zur Aufklärung von Reaktionsmechanismen im Bereich der homogenen Katalyse. Vier Projekte werden beschrieben, wobei es sich bei zwei Projekten um Hauptgruppen- und bei zwei Projekten um Übergangsmetallkatalysatoren handelt.

Im ersten Projekt wurde der Mechanismus einer organokatalytisierten Isomerisierung von *exo*- zu *endo*-Vinylencarbonaten untersucht. Das Katalysatorsystem ist eine Mischung aus einer organischen Base und einem Phenol. Dichtefunktionaltheorie (DFT)-Rechnungen klärten auf, dass für alle untersuchten Substrate ein ringöffnender Mechanismus der plausibelste ist, der über ein ringoffenes, experimentell isolierbares Keton verläuft. Für Substrate mit Arylsubstituenten ist außerdem ein ringerhaltender Mechanismus zugänglich, der ohne Phenol ablaufen kann. Das erlangte Wissen aus den DFT-Untersuchungen ermöglichte das Design eines Kontrollexperiments, das weitere Hinweise auf den ringöffnenden Mechanismus lieferte.

Das zweite Projekt behandelt die Aufklärung des Mechanismus einer Cu^{II}-katalysierten Synthese von substituierten Anilin-Bausteinen ausgehend von zugänglichen Arylchloriden unter der Verwendung von wässrigem Ammoniak als Stickstoffquelle. DFT-Rechnungen zeigten, dass durch Deprotonierung des initialen Cu^{II}-Amminkomplexes als aktive Spezies ein Cu^{II}-Amido-Katalysator gebildet wird. Das Arylchlorid reagiert in einer nukleophilen, aromatischen Substitution mit dem Komplex. Nachfolgende Ligandenaustausche ermöglichen die Produktfreisetzung des Anilins. Auf Basis dieser Erkenntnisse konnten spektroskopische Kontrollexperimente entwickelt werden, um die aktive Katalysatorform zu untersuchen.

Im dritten Projekt wird die Reaktion von Acetylen mit Formaldehyd behandelt, um selektiv Propargylalkohol herzustellen, während die Weiterreaktion zum Butindiol unterbunden wird. Experimentelle Studien etablierten einen Cu^{I}-Katalysator mit kostengünstigem und luftstabilem Phenanthrolin-Liganden. In dieser Arbeit wurden quantenchemische Untersuchungen anhand von Phenylacetylen durchgeführt, welche darauf hindeuten, dass der Reaktionsmechanismus vorzugsweise über eine mononukleare aktive Spezies verläuft. Der Mechanismus konnte auf Acetylen übertragen werden. Kinetische Modellierung zeigte, dass die Selektivität zum Propargylalkohol maßgeblich konzentrationsgetrieben ist.

Das vierte Projekt beschreibt mechanistische Studien einer Bismuth-katalysierten C–N-Kupplung. Experimentell wird eine Mischung aus einem C–N- und einem C–O-Kupplungsprodukt erhalten. Die Selektivität ist abhängig vom eingesetzten Katalysator. Detaillierte DFT-Studien identifizierten die reduktive Eliminierung als selektivitätsbestimmenden Schritt. Mehrere Pfade sind für diesen Schritt zugänglich, die Bevorzugung variiert je nach Katalysator. Statistische Modellierung wurde angewendet, um ein interpretierbares multivariates lineares Regressionsmodell zu optimieren. Das Modell ermöglicht, die wechselnden Mechanismen auf die Fähigkeit des Liganden, eine kationische Substruktur zu stabilisieren, zurückzuführen.

Quantum-Chemical Investigations in Homogeneous Catalysis

Abstract

This thesis describes examples of the use of quantum-chemical calculations to investigate reaction mechanisms in homogeneous catalysis. Four projects are examined: two illustrate catalysis by main group elements and two focus on transition metal catalysis.

In the first project, an organocatalytic isomerization of *exo*- to *endo*-vinylene carbonates was investigated. The catalyst system is a mixture of an organic base and phenol. Density functional theory (DFT) calculations revealed a ring-opening mechanism with a ring-opened ketone intermediate, which is experimentally isolable. For substrates bearing an aryl substituent, a ring-retaining pathway is accessible as well, which proceeds without the involvement of phenol. Based on this knowledge, a control experiment was designed, yielding further evidence for the ring-opening mechanism.

The second project focused on the mechanistic investigation of a Cu^{II}-catalyzed aniline synthesis from aryl chlorides in aqueous ammonia. DFT investigations showed that deprotonation of an initial Cu^{II}-ammine complex yields the active form of the catalyst, a Cu^{II}-amido complex. The aniline formation proceeds via a nucleophilic aromatic substitution mechanism. Product liberation proceeds by subsequent ligand exchanges. These results led to the design of spectroscopic control experiments, giving indications for the deprotonated Cu^{II}-amido complex.

In the third project, the reaction of acetylene with formaldehyde was investigated, selectively yielding propargyl alcohol while suppressing the second reaction to butynediol. Optimization studies established a Cu^{I} catalyst with a cheap and air-stable phenanthroline ligand. Quantum-chemical investigations on phenylacetylene conducted in this work suggest that the reaction mechanism is preferably mediated by a mononuclear active species. The mechanism was transferred to the acetylene system. Kinetic modeling indicated that the selectivity to propargyl alcohol primarily results from concentration effects.

The fourth project describes computational studies for a bismuth-catalyzed C–N coupling. Experimentally, a mixture of a C–N and a C–O coupled product was observed, where the selectivity depends on the catalyst. Detailed DFT studies showed that the reductive elimination is the selectivity-determining step. Multiple pathways were found for the reductive elimination, with the energetic order depending on the catalyst. Statistical modeling was performed to achieve an interpretable multivariate linear regression model. The model enabled the analysis of how ligand electronic and steric properties affect reductive elimination by stabilizing a cationic substructure.

Previous Publications and Patents

Three of the four projects covered in this thesis have been published in or submitted to peer-reviewed academic journals. Additionally, a patent application was filed for two of the projects. All experiments presented in this thesis were conducted by the coauthors listed in the corresponding publications.

Organocatalytic Isomerization of *exo*- to *endo*-Vinylene Carbonates

Chang Qiao,[+] Philipp D. Engel,[+] Levi A. Ziegenhagen, Frank Rominger, Ansgar Schäfer, Peter Deglmann, Peter Rudolf, Peter Comba, A. Stephen K. Hashmi, Thomas Schaub, An Organocatalytic Route to *endo*-Vinylene Carbonates from Carbon Dioxide-Based *exo*-Vinylene Carbonates. *Adv. Synth. Catal.* **2024**, *366*, 291.

Thomas Schaub, Philipp D. Engel, Peter Rudolf, A. Stephen K. Hashmi, Chang Qiao, Process for preparing *endo*-unsaturated 1,3-dioxol-2-ones. WO2025021955A1, **2025** (Priority Date: 27.07.2023).

Cu^{II}-Catalyzed Amination of Aryl Chlorides in Aqueous Ammonia

Lucas S. Mello,[+] Philipp D. Engel,[+] Patrizio Orecchia, Katharina Bleher, Frank Rominger, Kailaskumar Borate, Roland Goetz, Peter Deglmann, Ansgar Schäfer, Christian Winter, Michael Rack, Peter Comba, A. Stephen K. Hashmi, Thomas Schaub, Copper(II)-Catalyzed Amination of Aryl Chlorides in Aqueous Ammonia. *Chem. Eur. J.* **2024**, e202403023.

Thomas Schaub, Roland Goetz, Christian Winter, Michael Rack, Kailaskumar Borate, A. Stephen K. Hashmi, Lucas dos Santos Mello, Process for preparing aromatic amines from aryl chlorides. WO2025073702A1, **2025** (Priority Date: 02.10.2023).

Ligand-Controlled Chemodivergent Bismuth Catalysis

Lucas Mele,[+] Philipp D. Engel,[+] Jamie A. Cadge, Vytautas Peciukenas, Hoonchul Choi, Matthew S. Sigman, Josep Cornella, Ligand-Controlled Chemodivergent Bismuth Catalysis. *J. Am. Chem. Soc.* **2025**, accepted DOI: 10.1021/jacs.5c11854.

[+] these authors contributed equally.

Use of Artificial Intelligence

The following artificial intelligence (AI) tools were used for spelling, grammar, and style corrections:

AI Tool	Purpose of Use and Prompt Used	Thesis Section
Microsoft Copilot	Use of "Rephrase" button to automatically check for spelling, grammar mistakes, and style corrections	Entire thesis

AI tools were employed to refine the text by correcting spelling and grammar mistakes and improving its style. After employing these tools, all modifications were carefully reviewed and manually edited as necessary. At no point was AI employed to generate text from scratch. The use of these tools was conducted transparently and in coordination with the primary examiner, Prof. Dr. Peter Comba.

Table of Contents

List of Abbreviations

AC	acetylene
AFQMC	auxiliary-field quantum Monte Carlo
a.u.	arbitrary units
av	average
BHT	butylated hydroxytoluene
b.l.	barrierless
Bn	benzyl
BYD	butynediol
CaRLa	catalysis research laboratory
CBS	complete basis set
CDI	carbonyl diimidazole
COSMO	conductor-like screening model
COSMO-RS	conductor-like screening model for real solvents
DCP	diphenyl carbonate
CPCM	conductor-like polarizable continuum model
CT	charge transfer
DABCO	1,4-diazabicyclo[2.2.2]octane
DBU	1,8-diazabicyclo[5.4.0]undec-7-ene
DFT	density functional theory
DID	dispersion interaction density
DLPNO	domain-based local pair natural orbital
DMAP	4-dimethylaminopyridine
DMSO	dimethyl sulfoxide
DOSY-NMR	diffusion-ordered nuclear magnetic resonance
e.q.	equivalent
EPR	electron paramagnetic resonance
FWHM	full width at half maximum
GGA	generalized gradient approximation

HF	Hartree-Fock
IRC	intrinsic reaction coordinate
LED	local energy decomposition
LFER	linear free energy relationship
LLM	large language model
LMCT	ligand to metal charge transfer
LOO	leave-one-out
LP	lone pair
MAE	mean absolute error
MEP	minimum energy pathway
MGSM	molecular growing string method
ML	machine learning
MLIP	machine learning interatomic potential
MLR	multivariate linear regression
MOF	metal-organic framework
MWFQ	microwave frequency
NBO	natural bond orbital
n.d.	not defined
NEt_3	triethylamine
NFSI	N-fluorobenzenesulfonimide
NMP	N-methyl-2-pyrrolidone
NMR	nuclear magnetic resonance
NN	neural network
NPA	natural population analysis
NSI	N-benzenesulfonimide
OTf	triflate
OTFA	trifluoroacetate
OTs	tosylate
PA	propargyl alcohol
PES	potential energy surface

PhAC	phenylacetylene
PNO	pair natural orbital
PPA	phenyl propargyl alcohol
QSAR	quantitative structure-activity relationship
QRO	quasi-restricted orbital
QZ	quadruple-zeta
RE	reductive elimination
RF	random forest
RI	resolution of the identity
RMSD	root mean square deviation
Sel	selectivity
SMD	solvation model based on solute electron density
SSE	sum of squared errors
TB	tight-binding
TBD	1,5,7-triazabicyclo[4.4.0]dec-5-ene
TD-DFT	time-dependent density functional theory
TEMPO	2,2,6,6-tetramethylpiperidinyloxyl
TS	transition state
TZ	triple-zeta
UV-vis-NIR	ultraviolet-visible-near-infrared
VC	vinylene carbonate
WBI	Wiberg bond index
wt%	weight percent
xTB	extended tight-binding

1
Introduction

Catalysis is a key concept in modern synthetic chemistry. It allows for better control over stereo- and chemoselectivity while increasing reaction efficiency. Using a catalyst opens alternative reaction pathways with lower activation barriers (Figure 1.1). Additionally, catalysts can selectively accelerate reactions leading to desired products, thereby effectively controlling selectivity. Catalysts, by definition, are regenerated after the reaction, thus only affecting the kinetics and not the thermodynamics of the reaction. As a result, even a small quantity of catalyst can convert large amounts of reactants, often under milder conditions. Catalysis can be broadly divided into two types: homogeneous (same phase as the reactant) and heterogeneous (different phase than the reactant) catalysis. This thesis focuses on homogeneous catalysis. Based on the characteristics of the catalyst, homogeneous catalysis can be categorized into several subgroups: transition metal catalysis, main-group catalysis (using *s*- and *p*-block elements as catalysts), and organocatalysis (utilizing organic molecules as a catalyst).[1-3] Examples representing each of these subcategories are discussed in this work.

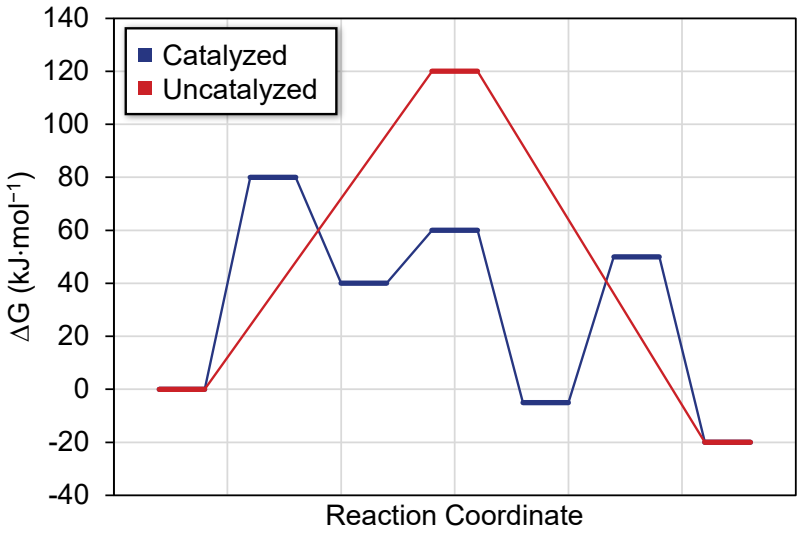

Figure 1.1: Schematic visualization of a hypothetical reaction scheme of a concerted, uncatalyzed reaction (red) and a stepwise, catalyzed reaction (blue).

Catalytic processes often involve complex, multi-step mechanisms with short-lived intermediates at low concentrations. This creates challenges for optimizing the catalytic system or pursuing rational design, as a comprehensive understanding of the catalytic cycle, including non-productive pathways, is required. The rapid timescales of the elementary reactions, in combination with not all intermediates being isolatable, make *in situ* spectroscopic evidence (via e.g., NMR, UV-vis, vibrational spectroscopy, or

EPR) difficult to sometimes impossible to obtain. Other experimental methods for investigating reaction mechanisms, such as kinetic studies, intermediate trapping, byproduct analysis, isotope labeling, or substrate variation, often provide only indirect evidence regarding the detailed mechanism at the atomistic level. Additionally, certain lab setups, such as the use of autoclaves, can limit spectroscopic investigations under reaction conditions without special equipment.[1-3]

In this context, computational chemistry has become a useful tool to study elementary reactions and full catalytic cycles.[2-3] It provides detailed information about the structures of resting states, intermediates, and transition states. With continuing advances in computational hardware and software, it has become possible to perform quantum-chemical calculations on molecules of relevant size (up to 200−300 atoms)[4] with little to no structural simplification.[5] The choice of the computational method depends on the specific characteristics of the system studied and the level of accuracy required. A variety of tools is available, from highly accurate models (e.g., coupled cluster) to options that require less computational power but offer lower accuracy (e.g., semiempirical methods).[3] Density functional theory (DFT) is widely used in quantum chemistry, enabling the realistic modeling of complex chemical transformations.[6] In recent years, data-driven approaches have been increasingly combined with mechanistic calculations to uncover interpretable structure–activity relationships and to develop predictive models.[7]

Nevertheless, a comprehensive strategy combines advances in synthesis, spectroscopy, experimental studies of reaction mechanisms, and computational chemistry.[3] The integration of experimental and computational chemistry within the same group is implemented at the Catalysis Research Laboratory (CaRLa) in Heidelberg, a joint laboratory of Heidelberg University and BASF SE. Research at CaRLa is primarily focused on industrially relevant homogeneous catalysis, with the goal of uniting academic and industrial experts within a single laboratory environment. This approach promotes effective technology transfer from fundamental research to potential industrial applications. The teamwork between experimental and computational chemistry offers significant benefits to both sides. Fast thermochemistry screening enables informed decisions, e.g., regarding the experimental testing of substrate variations. In particular, the close collaboration has been instrumental in designing targeted spectroscopic and control experiments, providing valuable insights to support mechanistic hypotheses. Furthermore, the ongoing alignment between theory and experiment allows the adjustment of computational models to better represent laboratory scenarios.

The goal of this thesis is to utilize state-of-the-art computational chemistry techniques across different projects to achieve detailed mechanistic insights in the area of homogeneous catalysis. In total, four projects are described. Three of these projects were conducted at CaRLa, while one was performed during a stay abroad with the Sigman group. The first project (Chapter 3) presents DFT studies on the organocatalyzed isomerization of *exo*- to *endo*-vinylene carbonates, focusing on the role of the co-catalyst phenol. In the second project (Chapter 4), DFT computations were carried out for a Cu^{II}-catalyzed route to anilines from widely available aryl

chlorides. Due to constraints imposed by the autoclave setup, spectroscopic experiments under reaction conditions could not be performed. Consequently, quantum-chemical insights into the reaction mechanism proved particularly valuable. The third project (Chapter 5) involved DFT calculations on the selective conversion of acetylene and formaldehyde into propargyl alcohol, while effectively suppressing the undesired formation of butynediol. The computations identified the reactive catalyst form and elucidated its mode of action. Finally, in the fourth project (Chapter 6), in-depth computational studies were conducted to develop a mechanistic hypothesis for a bismuth-catalyzed C–N coupling, with the ligand controlling selectivity. The mechanistic investigations were complemented by an interpretable machine learning model, providing insights into a complex system featuring multiple competing reaction pathways.

2
Theoretical Background

2.1 Methodology

2.1.1 Density Functional Theory

The central computational methodology used in this thesis is DFT. Since the primary focus of this work lies in the application of computational chemistry to practical problems rather than on developing new methods, a detailed derivation of DFT is not included here. Readers interested in the theoretical foundations are directed to standard references in the literature.[8-11] Instead, this chapter outlines key methodological aspects required to obtain reliable and accurate DFT results, highlighting important practical considerations. Reliability strongly depends on selecting an appropriate level of theory, performing thorough conformational screening (Section 2.1.2), and solvation treatment (Section 2.1.3).

Choosing the level of theory involves selecting both a DFT functional and basis set for geometry optimizations and single point energy calculations, each tailored to the chemical system under study.[4] It is important to find an appropriate balance between computational efficiency and accuracy. A common strategy is to use less computationally intensive methods for geometry optimizations (such as GGAs, meta-GGAs, or composite methods), while applying more accurate functionals (such as hybrid, range-separated hybrid, or double-hybrid functionals) for accurate single point electronic energy calculations. Additionally, a dispersion correction should be used. Benchmarking against experimental data or highly accurate calculations guides the process of method selection. Comprehensive benchmark studies, such as those published by the Grimme group (e.g., GMTKN),[12] may also be considered.

2.1.2 Conformational Screening

A primary objective of computational chemistry is the accurate modeling of molecular structure.[13] The three-dimensional shape of non-rigid molecules cannot be easily determined from connectivity alone, as multiple conformations must be considered.[14-15] Conformational flexibility often arises from the presence of multiple linearly connected covalent single bonds, which allow relatively unrestricted rotation. As system size increases, the number of possible conformers grows rapidly. Conformers have unique energy minima that are often connected by shallow barriers, typically associated with particular torsional angles or weak noncovalent interactions. Since molecular properties, including the Gibbs Free energy and various spectroscopic characteristics, are highly sensitive to molecular conformation, comprehensive conformational screening is essential to ensure accurate results. Depending on the

application, either the lowest energy conformer is chosen after screening, or a Boltzmann-weighted ensemble is used for further analysis.[14]

CREST,[15-16] developed by the Grimme group, is an automated program package for conformational screening. Metadynamics simulations are the core of CREST's conformational sampling workflow. These simulations apply a biasing potential based on the root-mean-square deviation (RMSD) of atomic positions relative to previously sampled molecular structures. This RMSD-based bias helps the system to escape local minima on the potential energy landscape by discouraging revisiting already explored conformations. The development of the semiempirical extended tight-binding (xTB) and force field methodologies[17-19] enabled the efficient screening for systems with a wide range of chemical compositions. DFT level refinement of the initial conformer ensemble (xTB level of theory) can be done either by manually optimizing geometries or automatically through the CENSO[14] workflow. Alongside CREST, an in-house developed workflow was employed for this thesis. This program systematically performs rotations around all rotatable bonds, enabling comprehensive conformational sampling at the DFT level of theory.

2.1.3 Solvation Treatment

Solvation is an important factor in chemistry and is particularly relevant in homogeneous catalysis.[20] The energy derived from a typical quantum-chemical calculation is evaluated in the gas phase, treating the isolated molecule without any surrounding species. For solvation treatment, there are two options: explicit solvation, which involves adding explicitly calculated solvent molecules, or implicit solvation.[4] Fully explicit solvation in molecular dynamics (MD) simulations is regarded as a thorough method for simulating solvent effects, but with current computational resources, this approach is not practical at the DFT level because it requires a large number of solvent molecules.[21] In contrast to this, implicit solvation is a (computationally undemanding) correction on top of the gas phase energy. Most implicit solvation methods, such as SMD,[22] CPCM,[23] and COSMO,[24] are continuum electrostatic models. These models treat the solvent as a homogeneous dielectric medium, characterized by a constant permittivity (ε), interacting with the solute via its cavity surface.[4]

COSMO simplifies solvation modeling by treating the solvent as an ideal conductor ($\varepsilon = \infty$), rather than a dielectric medium with finite permittivity. This approximation allows COSMO to calculate surface polarization charges efficiently: it places induced charges on the cavity surface to cancel the solute's electric field. These screening charges reflect the solute's polarity and are compiled into a screening charge density profile, also referred to as the σ-profile. The interaction between the solute's electrostatic potential and these surface charges yields the electrostatic component of the Gibbs free energy of solvation. COSMO ($\varepsilon = \infty$) was employed in this thesis for solvation treatment during geometry optimization.[4,24-25]

Dielectric continuum solvation methods have a notable limitation: they cannot differentiate between solvents that share the same permittivity, even if their properties vary considerably, as is the case with cyclohexane vs. benzene, or methoxyphenol vs. heptanone. This drawback led to the development of a more sophisticated method, the conductor-like screening model for real solvents (COSMO-RS).[26-28] COSMO-RS merges COSMO with statistical thermodynamics to model surface interactions. In an iterative process, the model calculates the chemical potential in solution using the σ-profiles from COSMO calculations for both solute and solvent. The interaction energy between solute and solvent includes components such as electrostatic interactions, hydrogen bond energies, and van der Waals interactions. It is parameterized using available thermochemical data. The chemical potentials can be applied to calculate activity coefficients, solubility, vapor pressures, or the free energy of solvation (ΔG_{solv}, Equation 2.1). ΔG_{solv} is calculated using the chemical potential at infinite dilution (μ_s) and in the ideal gas state (μ_{ig}), along with a correction term that includes the solvent's density (ρ_s), molar volume (V_{ig}), and molecular weight (M_s). [26-29]

$$\Delta G_{solv} = \mu_s - \mu_{ig} - R \cdot T \cdot \ln\left(\frac{\rho_s V_{ig}}{M_s}\right) \qquad 2.1$$

This correction term can be added to the Gibbs free energy in the gas phase to yield the Gibbs free energy in solution (Equation 2.2). For details about the thermochemical corrections ΔG_{therm}, see exemplarily [10].

$$G_{solution} = G_{gasphase} + \Delta G_{solv} = E_{elec} + \Delta G_{therm} + \Delta G_{solv} \qquad 2.2$$

COSMO-RS is a widely used method for modeling solvation effects, especially in reactions involving charge separation or recombination.[30] It should be noted that besides the implementation by the original author Andreas Klamt,[26-28] other versions, such as openCOSMO-RS[31] or COSMO-SAC,[32] are available. Adding solvent molecules explicitly to stabilize ions may be appropriate when the solvent molecules are strongly coordinated.[4]

2.1.4 Reaction Path Finding

Quantum chemistry helps to identify intermediates and transition states linking reactants to products. A key challenge is obtaining comprehensive knowledge of all relevant species on the potential energy surface (PES) to identify the minimum energy pathway (MEP). Therefore, it is necessary to compare various reaction mechanisms instead of depending only on the anticipated pathway. This also involves the analysis of side and decomposition reactions.[33-36] The investigation of elementary reaction steps is crucial for understanding reaction mechanisms, as it enables the identification

of rate- and selectivity-determining processes. In the context of homogeneous catalysis, such mechanistic insights help rationalize catalyst function and offer opportunities for performance optimization.[35]

A particular hurdle in finding reaction pathways is the geometry optimization of transition states. Obtaining an initial guess structure for a successful optimization typically involves several iterations and relies on chemical intuition. Subsequent intrinsic reaction coordinate (IRC) calculations are conducted to determine the minimum structures connected via the transition state (Figure 2.1A).[35] Tools such as the molecular growing string method (MGSM)[37-39] facilitate the search for transition states and pathways. With MGSM, it is possible to conduct single-ended searches by specifying reactants and bond changes (Figure 2.1B), as well as double-ended searches where both reactants and products are provided (Figure 2.1C). Single-ended MGSM requires proper reactant orientation, which can be set manually or using an automated precomplex builder.[40] MGSM results in a guess for a transition state optimization, which is optimally close to the optimized geometry. xTB may be used together with MGSM for rapid pathway screening, while DFT level calculations are suitable when higher accuracy is required. Single-ended MGSM, when paired with reaction rules from chemical heuristics or databases, can automate the search for reaction pathways. However, these rules depend on bond order and valence, limiting their applicability to organic chemistry.[34]

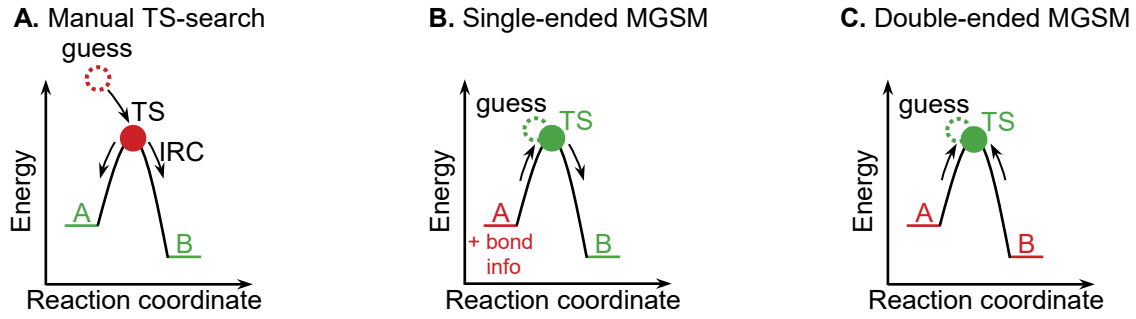

Figure 2.1: Schematic visualization of a manual TS search followed by an IRC calculation (A), a single-ended MGSM calculation starting from the reactant and information about the bond changes (B), and a double-ended MGSM calculation starting from the reactant and product side (C); MGSM optimally results in guesses close to the actual TS geometry; the starting point is marked in red, the result is marked in green.

Reaction path screening for reactions involving organometallic complexes presents several challenges. For all intermediates and transition states, it is necessary to consider not only different conformers but also alternating coordination modes or e.g., varying metal to ligand ratios.[41] Additionally, depending on the metal and ligand, e.g., dinuclear complexes may also need to be considered, further increasing complexity.[42] Finally, depending on the nature of the transition metal and its oxidation state, several possible spin states might be relevant.[43]

The (effective) Gibbs free energy of activation (in this thesis, consequently denoted as ΔG_A) at temperature T can be converted to a rate constant k using the Eyring

equation[44] (Equation 2.3), which enables direct comparison to measured kinetics. The transmission coefficient κ is typically set to one, assuming that no back-reaction originates from the product.

$$k = \frac{\kappa k_B T}{h} e^{-\frac{\Delta G_A}{RT}} \qquad 2.3$$

Practical assessments regarding the plausibility of a computed Gibbs free energy of activation for (pseudo) first-order reactions may be performed using either the half-life (Equation 2.4) or, alternatively, the reaction time required to achieve a particular conversion x (Equation 2.5).[45]

$$\tau_{1/2} = \frac{\ln(2)}{k} \qquad 2.4$$

$$\tau_x = \frac{\ln\left(\frac{1}{1-x}\right)}{k} \qquad 2.5$$

Since established by Marco Hermsen,[46] a common technique in our group is to visually study the plot of the reaction time vs. the Gibbs free energy of activation at a specific temperature for full conversion (x = 0.99). This provides a straightforward way to estimate the expected Gibbs free energy of activation for a reaction given its reaction time and temperature. The plot (Figure 2.2) is zoomed in on a region of several seconds (0.001 h = 3.6 s) to several days (100 h = 4.2 d).

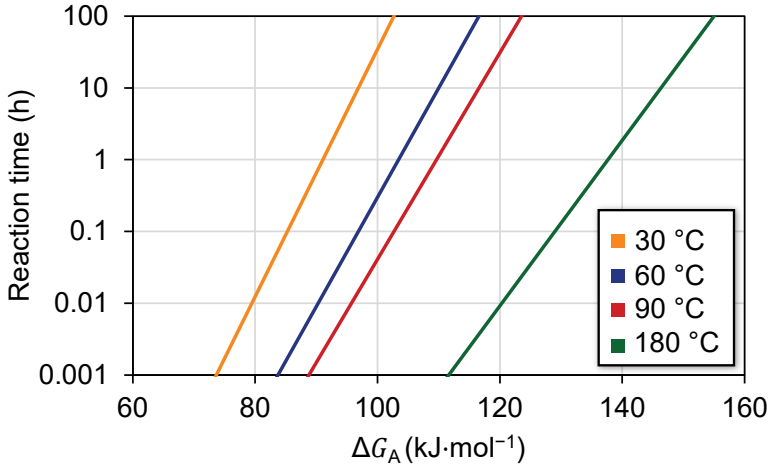

Figure 2.2: Reaction times in hours vs. Gibbs free energy of activation for a conversion of 99%; temperatures are chosen according to the reaction temperatures in the different chapters: 30 °C in orange, 60 °C in blue, 90 °C in red, 180 °C in green.

2.2 Statistical Modeling: Multivariate Linear Regression

2.2.1 Introduction to Multivariate Linear Regression

Linear free energy relationships (LFERs) link molecular structure to function and have been used to understand mechanisms and predict reaction outcomes since Hammett's pioneering work in the 1930s.[47-51] A quantitative correlation between an experimental reaction outcome (y) and molecular descriptors (x) obtained from empirical data or computational models is established.[7] When a single independent variable does not adequately correlate with the observation, multiple descriptors (x_i) can be employed in a multivariate linear regression (MLR, Equation 2.6). As such, MLR is a supervised machine learning model because it uses labeled training data with both features and the response variable.[52] Commonly used measures of experimental outcomes include selectivities (such as enantio-, regio-, or chemoselectivity),[7] turnover frequencies,[53-54] reaction rates,[55] and yields.[56] A variety of steric, geometrical, and electronic parameters are applied as molecular descriptors. The MLR approach differs from classical quantitative structure activity relationship (QSAR) by selecting and using physically meaningful molecular descriptors rather than only topological descriptors.[57-58]

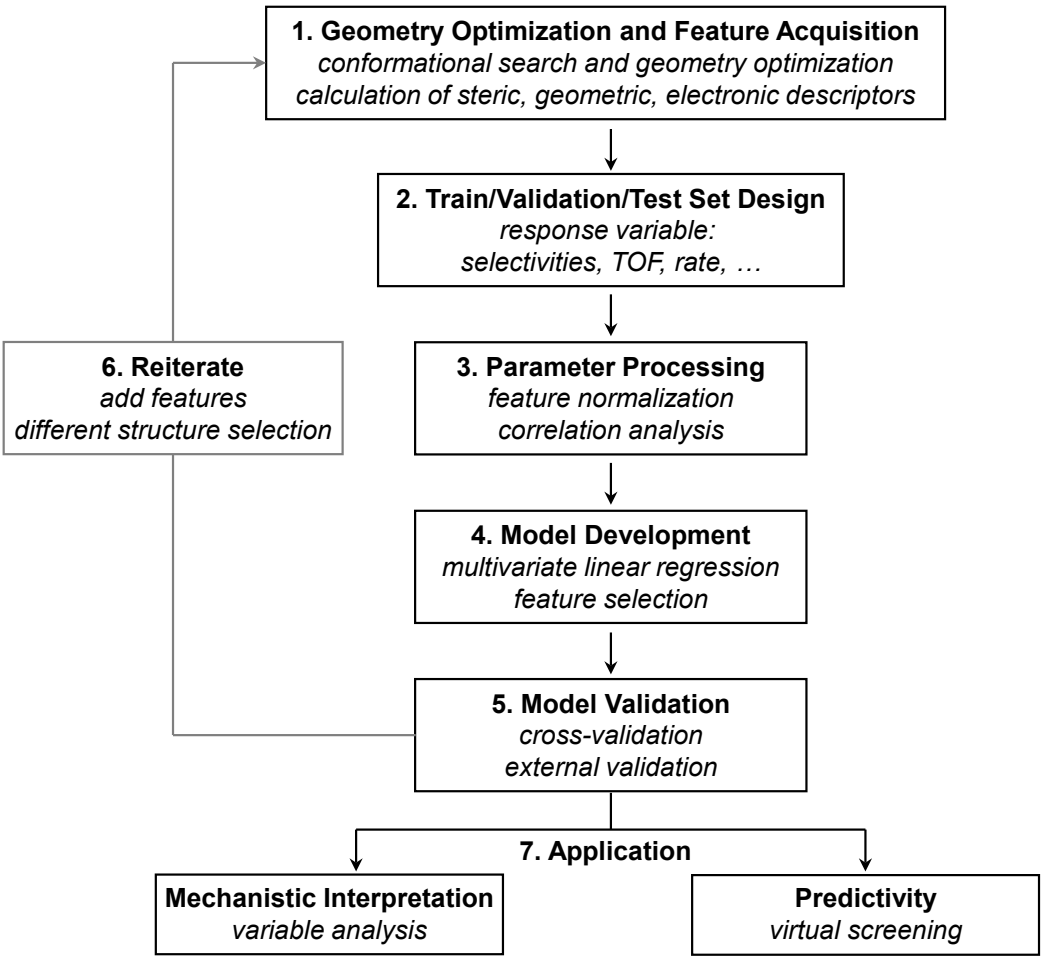

Figure 2.3: Schematic visualization of an MLR workflow.

$$y = \beta_0 + \sum_{i=1} \beta_i \cdot x_i \qquad 2.6$$

A general workflow for the development of an MLR model is depicted in Figure 2.3. In the following sections, each step will be explained in detail.

2.2.2 Structure Selection and Feature Acquisition

The representation of molecules is an important aspect to consider. Given that the MLR models performed for this thesis are based exclusively on molecular descriptors, the subsequent discussion will concentrate on this methodology. The selection of the structure for featurization is key to achieving a good MLR model. In the specific case of homogeneous catalysis, this may be a ligand, a substrate, the catalyst's precursor or resting state, an intermediate, or even a transition state.[59-60] Commonly, a conformational search is performed to generate a conformer ensemble. The approach for handling the ensemble, however, depends on the system. For more rigid systems, it is often adequate to featurize only the lowest energy conformer.[61] However, this approach may not be appropriate for more flexible systems. In such cases, features can be computed for the conformer ensemble within a defined energy window (e.g., 3 kcal·mol^{-1} ≙ 12.6 kJ·mol^{-1}), applying Boltzmann-weighted averages, along with the minimum and maximum feature values.[61]

2.2.3 Steric Descriptors

Steric effects, which are nonbonding interactions, influence molecular conformation, chemical reactivity, and can play a key role in, e.g., inducing asymmetry in catalysis.[7,62] A variety of descriptors are employed to quantify these effects, such as the Taft parameter,[63] Charton parameter,[64] Sterimol values,[65] Tolman cone angle,[66] and buried volumes,[67] in addition to geometric features including bond lengths, bond angles, torsion angles, and bite angles. As not all of these parameters were used in this thesis, only the descriptors that were applied are discussed.

Sterimol parameters are a set of steric measurements that capture different spatial dimensions rather than summarizing all information in one value (Figure 2.4A). Key Sterimol parameters are *L* (distance along the bond axis), *B1* (minimum radius perpendicular to the bond), and *B5* (maximum radius).[65] Nolan and Cavallo introduced the percent buried volume ($\%V_{bur}$) as a steric parameter. $\%V_{bur}$ indicates how much of an abstract sphere around an atom's center is filled by the ligand (Figure 2.4B).[67-69]

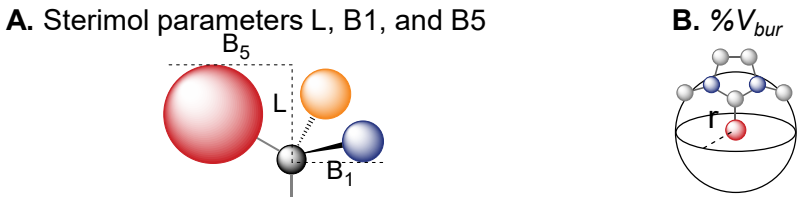

Figure 2.4: Schematic drawing of the Sterimol parameters L, B1, and B5 (A) and buried volume (%Vbur, B).

2.2.4 Electronic Descriptors

Tuning a catalyst's electronic properties can greatly affect its selectivity and efficiency. Electronic descriptors commonly used to evaluate these effects include HOMO-LUMO gaps, Hammett parameters, atomic charges, redox potentials, infrared frequencies and intensities, as well as NMR chemical shifts, coupling constants, and shielding tensors. It should be noted that most parameters used to assess electronic effects account not only for electronic properties but also include structural information.[7]

The Hammett parameter (σ) is a metric to quantify the electronic effects of various *para*- (σ_{para}) and *meta*-substituents (σ_{meta}) on a benzene ring.[47-50] Originally, Hammett used this empirically derived value to build LFERs to relate reaction constants (ρ) to equilibrium constants for the deprotonation of benzoic acid derivatives. In Equation 2.7, K_R denotes the equilibrium constant for the substituent of interest, while K_H is the reference constant for hydrogen as a substituent. Literature reports, such as those by Jacobsen,[70-71] demonstrated that this descriptor can be applied more broadly.

$$\sigma \cdot \rho = \log\left(\frac{K_R}{K_H}\right) \qquad 2.7$$

Whereas the Hammett equation utilizes a single substituent constant to represent electronic influences on reaction rates, more sophisticated models such as the Swain-Lupton equation differentiate these effects into distinct field inductive (F) and resonance (R) components.[72]

Atomic charges are important features in descriptor modeling.[73] As the assignment of atomic charges involves arbitrarily partitioning electron density, they are not strictly quantum-chemical observables. Several methods for calculating atomic charges have been proposed, including Mulliken,[74] Löwdin,[75] NPA (derived from a natural population analysis),[76] Bader's AIM (atoms in molecules),[77] Hirshfeld,[78] or CHELPG charges (derived from a fit to the electrostatic potential).[79] Although these methods rely on different theoretical foundations, the resulting charges can sometimes be correlated with each other.[73] The method selected for calculating atomic charges depends on the specific system and can differ, as demonstrated in studies by Seybold *et. al.*[73] and Sigfridsson *et. al.*[80]

All the descriptors mentioned above are just a few examples. Existing mechanistic knowledge helps guide parameter selection. This presents an opportunity to introduce mechanism-informed features; however, the choice of which features are calculated can also introduce bias into statistical models.[7]

2.2.5 Train/Validation/Test Set Design

The foundation for a successful statistical modeling is a properly distributed experimental dataset. The distribution should be assessed by analyzing a histogram of the measured output against the number of measurements. For regression tasks, the dataset distribution should ideally be well distributed (Figure 2.5). While regression algorithms are unsuitable for bimodal data, classification, e.g., to model whether a catalyst is active or not, may be appropriate. Skewed distributions, which can arise from uneven or biased data, may pose challenges for statistical modeling and require careful consideration. To address such issues, datasets can be optimized by applying data transformations, such as logarithmic or square root functions. Generally, it is important to also incorporate negative results, such as low yields, for the modeling process to ensure a good distribution. [60,81]

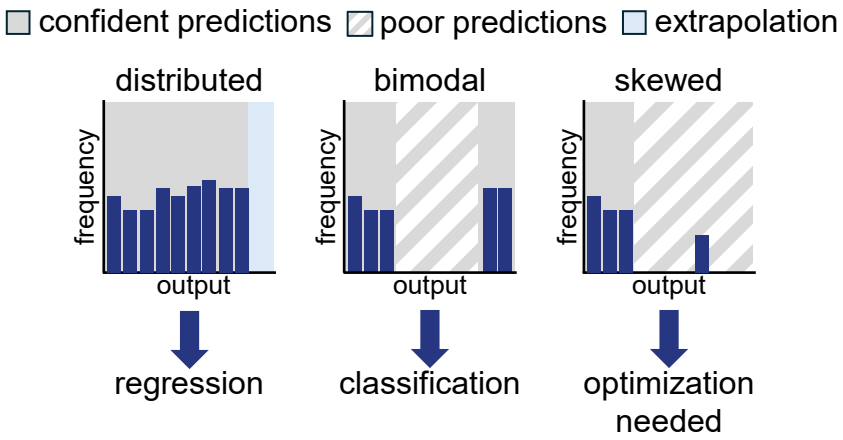

Figure 2.5: Schematic visualization of a distributed, bimodal, skewed data distribution.

Datasets are split into training, validation, and test sets to ensure models perform well on both seen and unseen data.[82-84] The training set is used to build the model, and the validation set is applied to measure the model's predictive performance during model selection. The test set is then used at the final stage to evaluate the model's generalizability in an unbiased manner. In small data regimes, often only a training/test split is used. The splitting is either performed in a random manner, based on the distribution of data points (y-equidistant), or based on descriptor variance[85] (Kennard-Stone algorithm).[60]

2.2.6 Parameter Processing

Feature refinement enables building more interpretable models. Usually, features (P) are scaled (Equation 2.8).[86] The sample is centered by subtracting the mean (μ_P) and subsequently scaled by dividing by the standard deviation (σ_P).[87] This is necessary for a direct comparison and interpretation of the coefficients in the final MLR model.[7]

$$P_{norm} = \frac{P - \mu_P}{\sigma_P} \tag{2.8}$$

Furthermore, an intercorrelation analysis is performed to prevent using correlated parameters in the same model. High intercorrelation among model parameters causes the model to learn parameter differences and magnify random noise, resulting in unreliable coefficients and reduced model accuracy.[88] This process is typically conducted by automatically applying a threshold (in the Sigman lab, a cutoff of R^2 = 0.5 is commonly utilized)[89] or may be facilitated by visually examining a correlation map.[7]

2.2.7 Model Development

Many different model types are available, ranging from simple MLR to more complex machine learning architectures like random forest (RF),[90-91] or neural networks (NN).[92-94] For algorithm selection, it is important to consider that data sets in chemical research are typically small. In these situations, MLR is often chosen for its simplicity.[60] Furthermore, a good balance is often achieved between accurately fitting the training data and avoiding overfitting to not-generalizable patterns or noise, while keeping interpretability.[95] As this thesis dealt with small datasets, only MLR was applied.

Constructing an MLR model is a multidimensional optimization problem. In ordinary least-squares linear regression, the best fit minimizes the sum of squared errors (SSE) or cost function (Equation 2.9). Here, y_i represents the measured value for the ith data point, and $\hat{y}_i$ refers to the predicted value. This approach identifies the optimal model coefficients for a given set of descriptors.[96]

$$SSE = \sum_{i=1}^{n} (y_i - \hat{y}_i)^2 \tag{2.9}$$

Using least-squares linear regression, a model is trained with a specific set of features. Nevertheless, optimizing the number and choice of features is important for good model performance. This is achieved through various methods for automatic feature selection. In a forward stepwise algorithm, features with the highest univariate

correlation are selected first. Then, further molecular descriptors are added to build bi-, tri-, or higher-order multivariate models up to a user-defined parameter limit.[60,95,97] Alternatively, a backward feature elimination method can be used. In this method, all parameters are initially included in the model and then removed individually if they are found to be statistically insignificant.[7,95] A third approach can be applied when models have a small number of maximal features, such as two features. In this case, all possible models can be created using a brute-force method.[98]

Using too many features in a model can cause overfitting and reduce generalizability.[99-100] Empirical guidelines in the literature suggest that having approximately eight to ten data points per feature is a reasonable standard.[60] Some techniques, such as LASSO, which is an advanced least-squares linear regression model, apply a penalty for each additional feature.[101] This approach reduces the number of features in the model, balancing predictive performance and interpretability.

2.2.8 Model Evaluation

The quality of the resulting model can be evaluated using various statistical metrics, with the most common being the R^2 value (Equation 2.10) and the mean absolute error (MAE, Equation 2.11). R^2, also known as the coefficient of determination, is used to assess how well the model explains the variation in the data. Dividing SSE (variance which is not explained by the model) by the total sum of squares (SST, total variance in the data) gives the unexplained variance, and subtracting this value from 1 yields R^2. A strong linear correlation is indicated by an R^2 value close to 1 and a low MAE.[102-103] In Equation 2.10 and Equation 2.11, $\hat{y}_i$ is the predicted value and $\bar{y}$ the mean of all measured values.

$$R^2 = 1 - \frac{SSE}{SST} = 1 - \frac{\sum_{i=1}^{n}(y_i - \hat{y}_i)^2}{\sum_{i=1}^{n}(y_i - \bar{y})^2} \quad 2.10$$

$$MAE = \frac{1}{n}\sum_{i=1}^{n}|y_i - \hat{y}_i| \quad 2.11$$

These statistical metrics are assessed on the training set to determine the model's goodness of fit. Performance on the validation and external test sets is used to evaluate the model's predictive ability. Besides external validation, a common method for further model verification is cross-validation. Cross-validation is performed on the training set by dividing the data into k parts, selecting one part as a holdout sample, and retraining a model using the remaining data.[83-84] The model's performance is then evaluated on the reserved subset by calculating statistical metrics. This process is repeated for every split, and the results are averaged. In leave-one-out (LOO), k matches the number of data points, with each holdout set containing one data point

(Figure 2.6). For LOO, the averaged R^2 is typically depicted as Q^2.[102] Models that show a significant reduction in training Q^2 or test R^2 compared to training R^2 suggest limited generalizability, reduced predictive accuracy, and insufficient statistical validity. Such outcomes are characteristic of overfitting. A visual representation of the LOO analysis can be helpful to assess the impact of individual data points on the model. A significant deviation in LOO cross-validation shows that a single data point has a major impact on the model equation.[7]

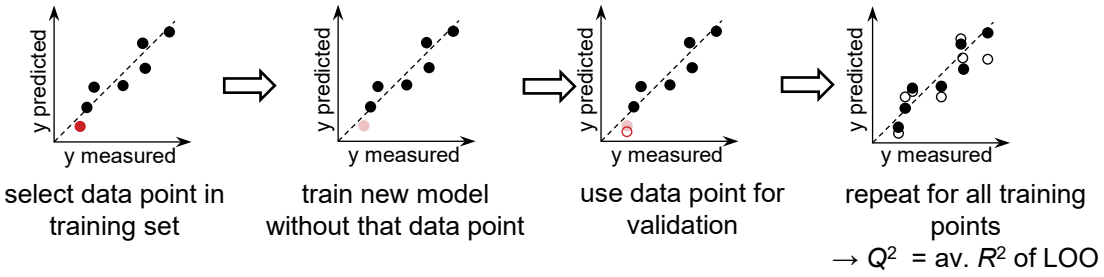

Figure 2.6: Schematic visualization of LOO cross-validation; LOO is plotted with unfilled circles.

2.2.9 Reiterate

If none of the models meet the required statistical metrics, the statistical modeling process should be repeated. The reasons for not finding suitable models can be diverse. However, it is important to note that in some cases an appropriate model may not exist due to limitations in the data or the underlying system being modeled.[7,60]

Outliers. When most of the data set is accurately predicted except for a few points, these points are identified as outliers. Potential causes may be related to experimental factors such as non-comparable conditions, side reactions, decomposition processes, changes in mechanism, or computational issues, including incorrect conformations. Possible solutions involve refining the parameters or removing the outliers from the data set.[7,60]

Mechanism changes. Unique structural features may cause the reaction to follow an alternative pathway. Such cases can be treated with mechanism-specific models or by finding appropriate descriptors that capture the change in mechanism.[60,104]

Unrepresentative training set. As described in Section 2.2.5, the training set should be carefully selected to avoid bias. Training sets that lack diversity, have a limited range, are clustered, or contain outliers may not be ideal for effective model development.[7,60]

Insufficient parameter space. The acquired features might not entirely capture the complexity of the reaction being modeled. Additional features incorporating mechanistic knowledge could be included. Furthermore, different structures for featurization, such as important intermediates or transition states, can also be selected.[7,60]

Unsuitable algorithm choice. Especially when using MLR, it is important to assess whether the data can be adequately described by linear models. If not, transitioning to more advanced machine learning approaches, such as RF or NNs, may be a viable alternative.[60]

Unmodelable data. It is not always possible to achieve successful statistical modeling for every data set. If attempts to enhance model quality fail, collecting more or chemically more diverse data may be required. Furthermore, it is important to consider not only the amount of data but also its quality and comparability. All data points should be measured under consistent experimental conditions.[60]

2.2.10 Application

Once a robust model is obtained, it can be utilized for predictions, interpretation, or both. In a virtual screening approach, e.g., new catalysts can be calculated, and their performance can be predicted using a previously established MLR model. For this computational screening, it is important to consider both the feasibility of synthesis and the commercial availability of starting materials.[7] Averaging predictions from several models may improve accuracy.[7,105] The structures should fall within the model's generalizable region, showing similarity to training set entries. Major differences not represented in the training data may cause prediction errors.[7,106]

Analysis of the sign and magnitude of feature coefficients can provide mechanistic insights.[7] With normalized features, the magnitude equals the feature importance. This straightforward nature of interpretation is a key reason why MLR is a preferred algorithm when interpretability is a primary objective. If the purpose of interpretation is to support the development of mechanistic hypotheses, it is necessary for the selected descriptors to be chemically interpretable. Considering this during feature acquisition may help to maintain simplicity in model construction. Furthermore, choosing an optimal structure for featurization is essential for ensuring interpretability, as key intermediates or transition states may yield the most valuable insights.[104] When interpretability is prioritized over predictivity, models with more interpretable descriptors may be selected instead of those with better statistical metrics.[7,60]

3

Organocatalytic Isomerization of *exo*- to *endo*-Vinylene Carbonates

This chapter was reproduced in part with permission from Chang Qiao, Philipp D. Engel, Levi A. Ziegenhagen, Frank Rominger, Ansgar Schäfer, Peter Deglmann, Peter Rudolf, Peter Comba, A. Stephen K. Hashmi, Thomas Schaub, An Organocatalytic Route to *endo*-Vinylene Carbonates from Carbon Dioxide-Based *exo*-Vinylene Carbonates. *Adv. Synth. Catal.* **2024**, *366*, 291.[107] Copyright 2024 Wiley-VCH GmbH.

All experiments presented were conducted by Chang Qiao and Levi A. Ziegenhagen.

Note: The numbering of calculated and experimental structures restarts at the beginning of each chapter.

3.1 Motivation and Goal

Endo-vinylene carbonates (*endo*-VCs) have a wide range of possible applications. These include the use as additives in lithium-ion battery electrolytes,[108] as monomers for polymers,[109-110] and as intermediates in drug synthesis.[111-112] However, synthetic approaches to produce substituted *endo*-VCs remain limited. Existing methodologies typically depend on chlorination/dehydrochlorination sequences,[113-114] or utilize toxic[115-117] or atom-inefficient[118-119] carbonyl sources. Additionally, dedicated starting materials are required, which limits the range of substrates that can be used.[120-121] The limited substrate scope and unsustainable carbonyl sources have prevented the use of substituted *endo*-VCs on a larger scale.[107]

The overall objective of this project was to develop a more sustainable method for synthesizing a wide range of substituted *endo*-VCs. Building on a strategy previously developed at CaRLa for producing substituted *exo*-vinylene carbonates (*exo*-VCs) from primary propargyl alcohols with CO_2,[122] the new methodology aimed to achieve regioisomerization of the *exo*-cyclic double bond to an *endo*-cyclic double bond.[107] As a catalyst, an N-heterocyclic base in combination with phenol was used. This method uses a green carbonyl source, is atom-efficient, and operates under moderate reaction conditions. To gain a deeper understanding of the catalytic system, control experiments were conducted. However, the interpretation of these results was initially not straightforward. Therefore, DFT calculations were performed to provide insights into the elementary steps of the reaction. While the experimental studies provide the necessary context, the focus in the following chapter is on computational chemistry, aiming to elucidate the reaction mechanism and rationalize the observed outcomes.

Central questions concern whether the transformation proceeds via a ring-retaining or a ring-opening pathway and how substrate substitutions influence these routes. A further objective is to examine the role of phenol as a co-catalyst, specifically by investigating how the pK_a value affects reactivity. Computational chemistry is used alongside control experiments, thereby providing a solid foundation for mechanistic interpretation and supporting the patenting process.

3.2 Experimental Background

The reactions of CO_2 with primary,[122-125] secondary,[126-128] and tertiary[129-130] propargyl alcohols to produce *exo*-VCs have been developed and optimized over the last decades. These methods offer high atom economy by avoiding reagents such as phosgene and utilizing CO_2 as a widely available reactant. For *endo*-VCs, on the other hand, equivalent strategies are still rare.

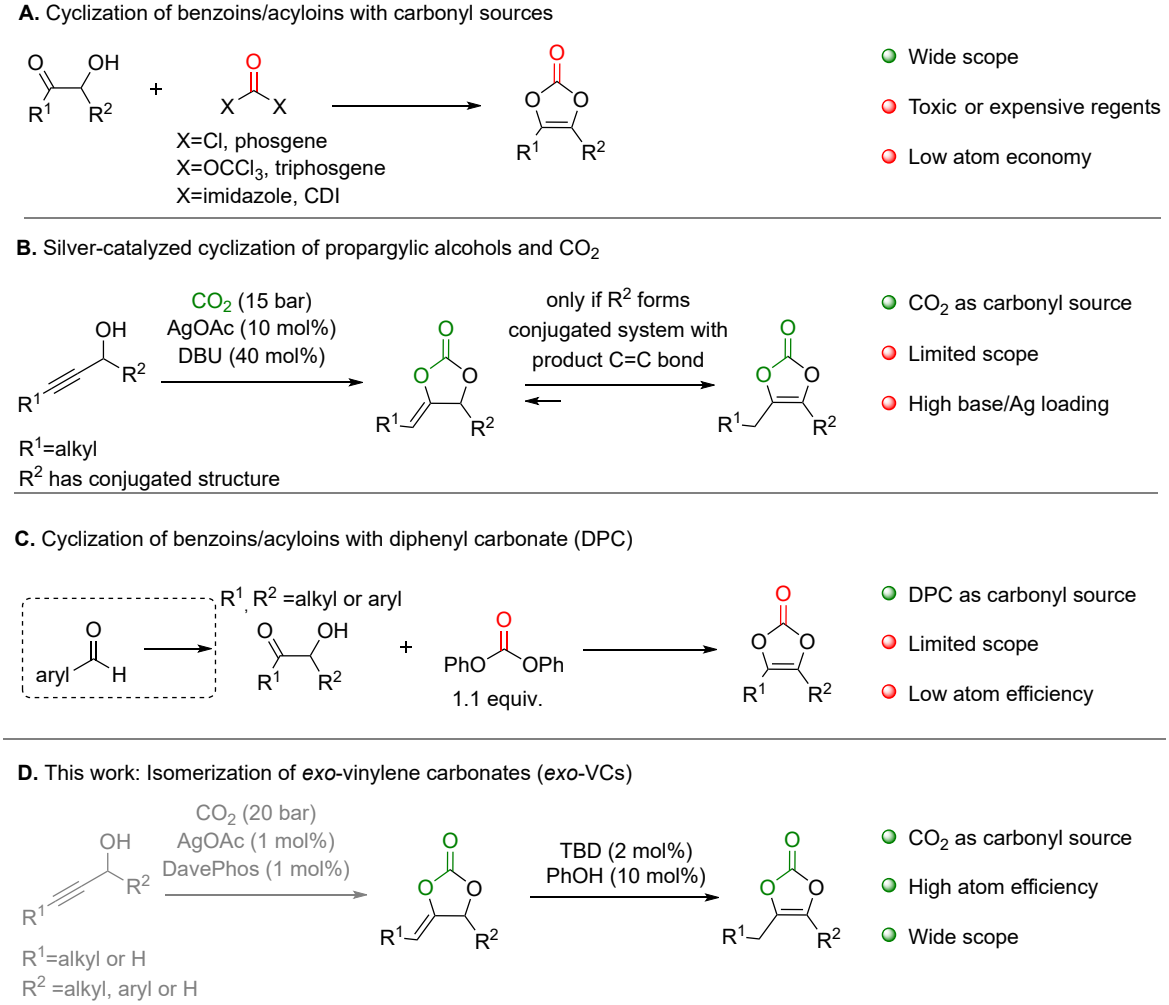

Figure 3.1: Synthetic strategies to synthesize *endo*-VCs; previous reports for the cyclization of benzoins/acyloins with different carbonyl sources (A),[118-119] silver-catalyzed cyclization of propargyl alcohol and CO_2 (B),[120] cyclization of benzoins/acyloins with DPC (C),[121] and this work (D).[107]

Until a decade ago, synthetic methods primarily relied on either chlorination/dehydrochlorination sequences[113-114] or toxic and atom-inefficient carbonyl sources, such as phosgene,[115-116] triphosgene,[117] or carbonyl diimidazole[118-119] (Figure 3.1A). In 2014, Yamada and coworkers first described a silver-catalyzed method using CO_2 to access *endo*-VCs (Figure 3.1B).[120] This approach requires a high loading of both the catalyst and base, and is limited to substrates with an aryl substituent. Duguet and coworkers developed a method using diphenyl carbonate (DPC) as a carbonyl source[121] and (partly *in situ* formed[131]) α-

hydroxy ketones to synthesize *endo*-VCs (Figure 3.1C). These transformations utilize secondary propargyl alcohol precursors for the synthesis of disubstituted *endo*-VCs. However, methodologies using primary propargyl alcohol precursors to synthesize monosubstituted *endo*-VCs remained undeveloped.

Table 3.1: Optimization study of the isomerization of *exo*-VC **S1** to *endo*-VC **P1**.[a]

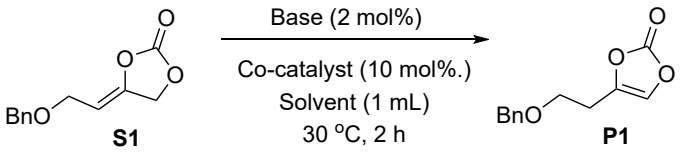

Entry	Base [2 mol%]	Co-catalyst [10 mol%] (4-R-PhOH)	pK_a[b]	Conv.	Yield
1	TBD	–	–	<5%	0
2	–	R=H	18.0	0	0
3	TBD	R=H	18.0	Full	82% (80%)[c]
4[d]	TBD	R=H	18.0	Full	65%
5	DBU	R=H	18.0	53%	22%
6	DABCO	R=H	18.0	0	0
7	DMAP	R=H	18.0	0	0
8	NaOH	–	18.0	20%	0
9	TBD	R=OH	14.9[e]	15%	0
10	TBD	R=CF_3	15.3	0	0
11	TBD	R=Br	15.5[e]	11%	0
12	TBD	R=Cl	16.7	70%	43%
13	TBD	R=F	18.0	Full	84% (82%)[e]
14	TBD	R=Me	18.9	Full	84% (82%)[e]

[a] Reaction conditions: substrate **S1** (0.2 mmol), base (2 mol%), co-catalyst (10 mol%), CH_2Cl_2 (1 mL), 30 °C, 2 h, inert atmosphere; conversions and yields were measured by ^1H NMR using CH_2Br_2 as internal standard; [b] taken from [132]; [c] given within brackets is the yield of isolated **P1**; [d] CH_3CN as solvent; [e] calculated pK_a values (M06-2X-D3ZERO/def2-QZVPP//M06-L-D3ZERO/def2-SVP; COSMO-RS (DMSO)).

Building on a previously developed approach at CaRLa for synthesizing substituted *exo*-VCs from primary propargyl alcohols using CO_2,[122] the new methodology was designed to achieve regioisomerization of the *exo*-cyclic double bond to the *endo*-cyclic double bond (Figure 3.1D). The experimental screening studies were guided by

combining two ideas, which were already present in the literature. It has been described that ketone-carbonate species are key intermediates in the preparation of *endo*-VCs.[121,131] These intermediates have also been reported to result from the ring-opening of *exo*-VCs with suitable nucleophiles.[122,130] Based on this knowledge, the hypothesis was that an appropriate alcohol/base catalytic system for reversible ring-opening could convert *exo*-VCs into their corresponding *endo*-VCs. Experimental screening studies were performed for the benchmark substrate **S1**. Selected entries are shown in Table 3.1.

The studies revealed that both the base and the phenol are necessary for the isomerization (Entries 1−3). The reaction proceeds well in chloroform, but also highly polar solvents (MeCN, Entry 4) are suitable for this reaction, which can be beneficial to dissolve more complex starting materials. Several N-heterocyclic and hydroxy bases were evaluated with phenol as a co-catalyst. Imine-structured N-heterocyclic bases such as TBD and DBU demonstrated a strong influence on both the yield of **P1** and overall chemoselectivity (Entries 3–5), compared to other nitrogen-containing bases (DABCO and DMAP, Entries 6 and 7). Utilizing a simple inorganic base (NaOH, Entry 8) did not result in the formation of the *endo*-product, highlighting the importance of the N-heterocyclic base. Furthermore, a variety of substituted phenols were screened, featuring different pK_a values (Entries 9−14). Interestingly, only phenols with pK_a values between 16.7 and 18.9 yielded the desired product **P1**. In particular, phenols with a pK_a in the range of 18.0 and 18.9 resulted in very good yields of **P1**. These results emphasize the important role of the co-catalyst's acidity and nucleophilicity. Based on these findings, in-depth quantum-chemical investigations were performed to elucidate the reaction mechanism, study the catalytic system, and further investigate the observed trends related to the acidity of the co-catalyst.

3.3 Computational Details

All geometry optimizations and Hessian calculations were conducted with the TURBOMOLE software package (version 7.5.2).[133] The meta-GGA functional M06-L[134] together with the def2-SVP[135] basis set was employed, including Grimme's D3 dispersion correction using zero-damping.[136] Geometry optimizations were performed using the COSMO solvation model with standard parameters and an infinite dielectric constant.[24] Verification of stationary points was achieved by analyzing the vibrational frequencies at the same computational level. Single point electronic energies were computed using the M06-2X functional[137] in combination with the def2-QZVPP[135,138] basis set. Throughout all calculations, the resolution-of-identity (RI) approximation[139-142] and matching auxiliary basis sets were utilized.

For Gibbs free energy calculations, zero-point vibrational energies and thermochemical corrections were derived at the level of geometry optimization (T = 298.15 K, p = 1 bar). Solvation correction was calculated using the COSMO-RS model[26,28] implemented in COSMOtherm[143] (Version 18.0.0; Revision 4360), assuming infinite dilution in acetonitrile and employing the FINE parametrization. pK_a values were computed for the solvent DMSO.

Reaction pathways and potential energy surfaces were explored using the MGSM approach[37-39] combined with a precomplex builder routine.[40] Extensive conformational sampling for minima and transition states was carried out with the CREST program package[15-16] developed by Grimme and co-workers. Selected conformers were refined by DFT optimization and single point energy evaluation to establish a consistent ranking of free energies on the single point level. In addition, two in-house programs were employed for complementary conformational screening. Only the lowest energy conformers are discussed and shown in the figures. Mechanistic studies were conducted for benchmark substrate **S1** and for the phenyl-substituted derivative **S2**, while other substrates were utilized either for geometry validation or to examine key intermediates and transition states (see Figure 3.2 for substrate nomenclature). During the benchmark, additionally, the functionals BP86[144-145] and ωB97x-D[146-147] were tested. For clarity, C–H hydrogen atoms are omitted in the figures.

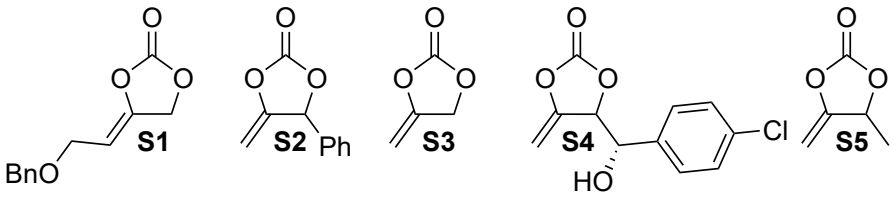

Figure 3.2: Substrate nomenclature; the substituent in **S4** is abbreviated as "R" in the following.

3.4 Results and Discussion

3.4.1 Geometry Benchmark

The geometrical accuracy of the DFT-calculated structures was assessed by comparing them with experimentally measured crystal structures. For this comparison, the ring bonds as well as the two exocyclic bonds were considered (Figure 3.3). The deviations from the experimentally measured structures were calculated in the form of an RMSD, where n is the number of bonds considered for each structure (Equation 3.1). To obtain a comparable RMSD for each DFT method, an overall RMSD was calculated, taking all bonds in all four benchmark structures into account (N in Equation 3.2).

$$RMSD_{structure} = \sqrt{\frac{\sum_{i=1}^{n}\left(r_{computed} - r_{measured}\right)^2}{n}} \qquad 3.1$$

$$RMSD_{functional} = \sqrt{\frac{\sum_{i=1}^{N}\left(r_{computed} - r_{measured}\right)^2}{N}} \qquad 3.2$$

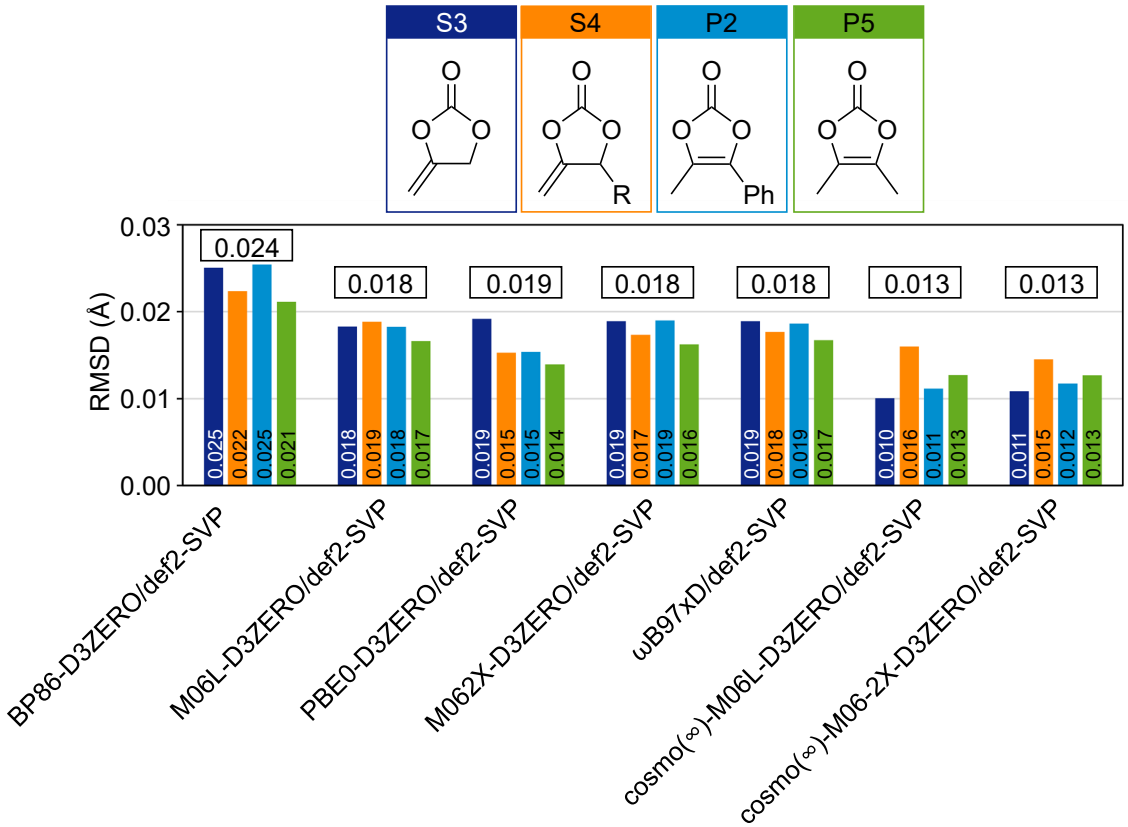

Figure 3.3: Geometry benchmark comparing four measured crystal structures with computed DFT structures; for all species, the ring bonds and the bond to the exocyclic substituents were considered; the overall RMSD is shown above each computational setup; for **S3**, the weighting differs because the C–H bond was excluded, resulting in one fewer bond length; crystal structure **S4** (R = *S*-4-chlorophenylhydroxymethyl) taken from [148].

For benchmarking, a small set of DFT functionals was employed, including two GGA functionals (BP86 and M06-L) and three hybrid functionals (PBE0, M06-2X, and ωB97x-D). All calculations were performed using a split valence double-ζ basis set (def2-SVP) and the Grimme D3 dispersion correction with zero damping. For simplification, the information about the basis set and dispersion correction is omitted in the following paragraphs. Overall, both starting materials (*exo*) and products (*endo*) are described equally accurately across all functionals, with a maximum difference in RMSD of 0.006 Å between two structures (COSMO(∞)-M06-L: RMSD(**S4**)–RMSD(**S3**)). Therefore, comparing the overall RMSDs is sufficient; it is not necessary to assess each structure individually. Comparing the two GGAs BP86 and M06-L to each other (optimization in the gas phase), M06-L shows a significantly higher accuracy with an RMSD of 0.018 Å compared to 0.024 Å. Interestingly, the RMSDs of the three hybrid functionals are identical to this (optimization in the gas phase, PBE0: 0.019 Å, M06-2X: 0.018 Å, and ωB97x-D: 0.018 Å). When applying an implicit solvation model (COSMO, $\varepsilon = \infty$), the deviation of the calculated structures from the crystal structures can be further reduced to an RMSD of 0.013 Å for the two functionals M06-L and M06-2X.

Based on this small functional comparison, M06-L in combination with COSMO(∞) was selected for the geometry optimizations in this project, since the accuracy of the hybrid functional M06-2X can be reached while maintaining the faster computation time[4] of the meta-GGA M06-L (full method for the optimization COSMO(∞)-M06-L-D3ZERO/def2-SVP). For accurate single point energies, the hybrid functional M06-2X was chosen based on literature studies, where this functional was shown to be capable of accurately describing reactions including charge separation and recombination steps.[149] Solvation treatment for the final Gibbs energies in solution was performed using COSMO-RS in the solvent acetonitrile. This results in the following level of theory: M06-2X-D3ZERO/def2-QZVPP//COSMO(∞)-M06-L/def2-SVP; COSMO-RS(MeCN).

3.4.2 Ring-Opening Mechanism

In line with the optimization of experimental conditions, **S1** was chosen as the benchmark substrate for mechanistic studies. For comparison with former work by Yamada and coworkers,[120] the isomerization mechanism was also studied for the phenyl substituted substrate (**S2**). The *exo*-VC **S1** can isomerize to the *endo*-cyclic double bond (**P1**) with a calculated exergonic ΔG_R of −6.9 kJ·mol^{-1}. In the case of substrate **S2**, the thermochemistry is significantly more exergonic with −29.0 kJ·mol^{-1}. The stronger thermodynamic driving force to **P2** might be explained by the product double bond being in conjugation with the aromatic system of the phenyl substituent. For the catalysis, two pathways were considered: one pathway involving ring-opened intermediate species upon combined TBD and phenol catalysis (Figure 3.4A, discussed in this section) and one only including TBD retaining the ring (Figure 3.4B, discussed in Section 3.4.3).

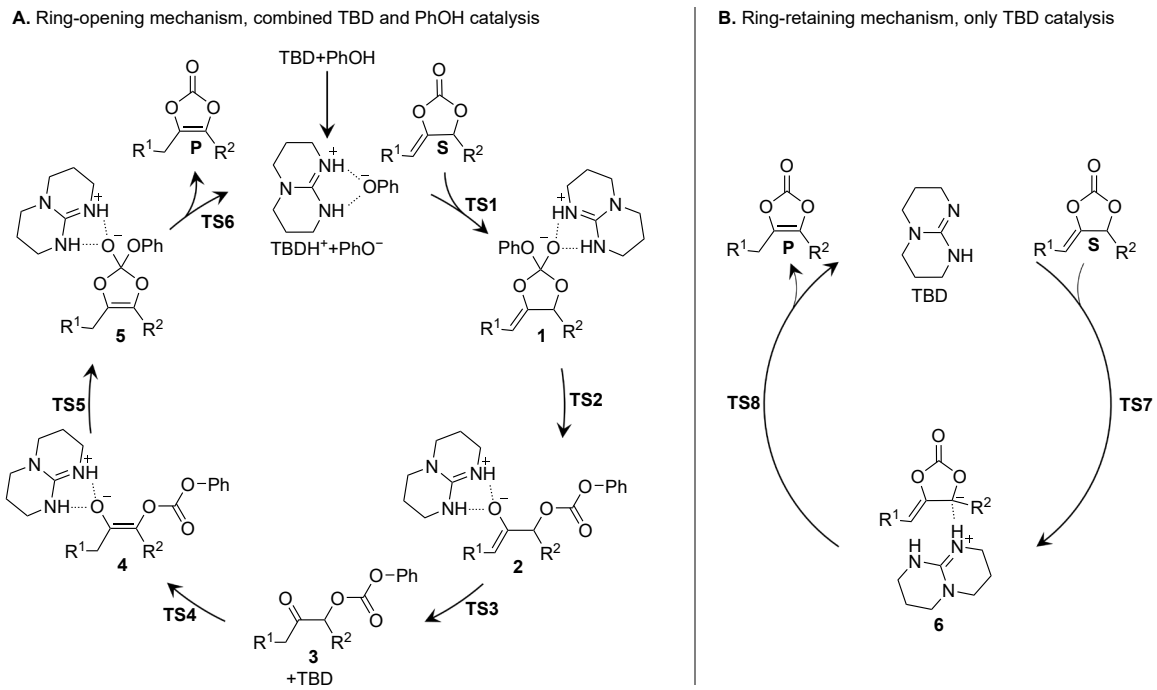

Figure 3.4: Proposed catalytic cycle for the ring-opening pathway upon combined TBD and phenol catalysis, showing all intermediates (A), and the ring-retaining pathway upon TBD catalysis (B).

Pathway A proceeds under combined TBD and phenol catalysis. The formation of the hydrogen-bonded complex of TBD and phenol is exergonic (−9.6 kJ·mol^{-1}). By barrierless proton transfer, the contact ion pair TBDH$^+$ and PhO$^-$ can be formed, acting as the catalyst's reactive form. The contact ion pair lies slightly higher in free energy than the hydrogen-bonded form (−7.0 kJ·mol^{-1}).

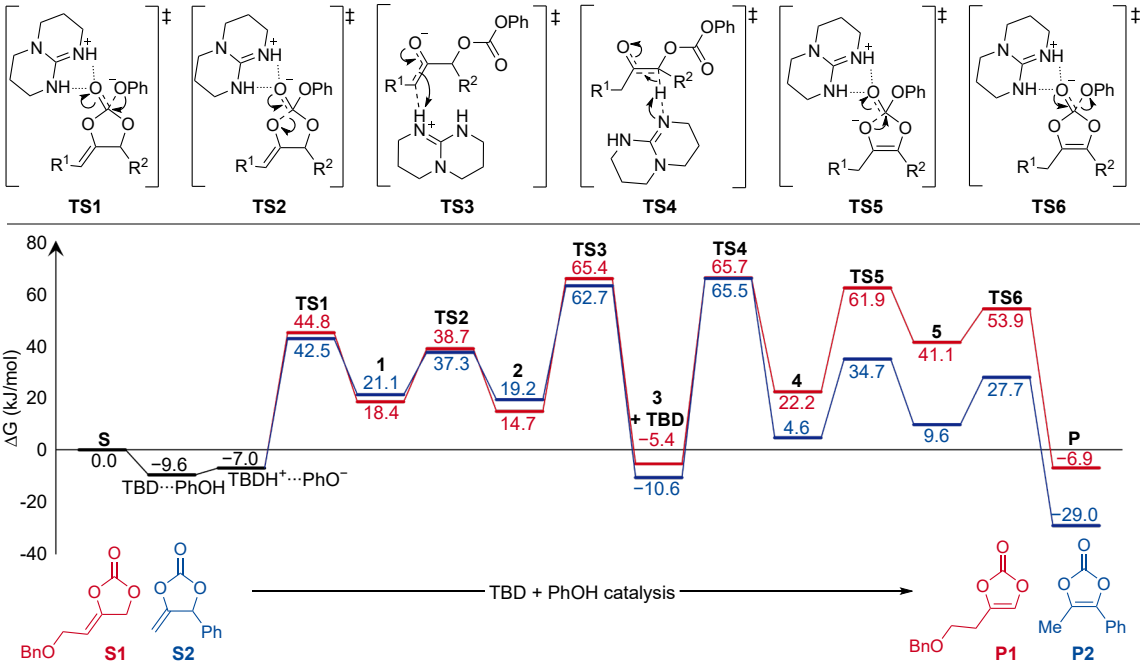

Figure 3.5: Energy diagram for the isomerization of substrates **S1** and **S2** to **P1** and **P2** upon combined TBD and phenol catalysis; ΔG^{303} in kJ·mol^{-1} relative to **S1** or **S2**, TBD and PhOH; M06-2X-D3ZERO/def2-QZVPP//M06-L-D3ZERO/def2-SVP; COSMO-RS (MeCN).

The first step of the multistep isomerization is the addition of phenolate to the carbonate C-atom (**TS1**), yielding intermediate **1**. This step exhibits low activation barriers for both substrates (**TS1**$_{S1}$: 44.8 kJ·mol^{-1} and **TS1**$_{S2}$: 42.5 kJ·mol^{-1}). Due to the phenyl substituent at the VC-ring in **S2**, there are two possibilities for the addition: *cis* or *trans* to the substituent. The *cis*-addition is preferred compared to the *trans*-addition (**TS1b**$_{S2}$: 53.5 kJ·mol^{-1}). While the TBDH$^+$ coordinated intermediates show low Gibbs free energies, this is not the case when the coordination is neglected. Coulomb interaction and hydrogen bonding of the cationic TBDH$^+$ lead to a stabilization of more than 40 kJ·mol^{-1} for certain intermediates (Figure 3.6). As a consequence, all charged species were calculated as contact ion pairs with TBDH$^+$. By treating charged species as contact ion pairs, steps that would involve full charge separation over infinite distances are excluded, thereby reducing possible errors.

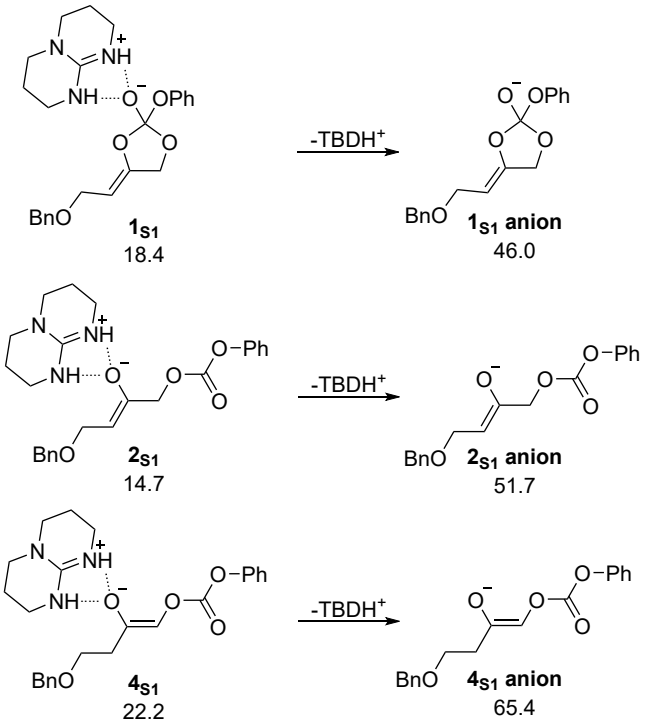

Figure 3.6: Comparison of the free energies of the intermediates **1**$_{S1}$, **2**$_{S1}$, and **4**$_{S1}$ with and without the coordination of TBDH$^+$ to show the stabilizing effect of coulomb interaction and hydrogen bonding through TBDH$^+$; no conformational screening was performed for the anions to ensure only coordination effects are considered in the energy comparison; ΔG^{303} in kJ·mol^{-1} relative to **S1**, TBD and PhOH; M06-2X-D3ZERO/def2-QZVPP//M06-L-D3ZERO/def2-SVP; COSMO-RS (MeCN).

The adduct of phenolate with the *exo*-VC can undergo ring-opening to yield the ring-opened enolate **2** via **TS2**. Protonation proceeds with a higher but still moderate barrier of 65.4 kJ·mol^{-1} (**TS3**$_{S1}$) and 62.7 kJ·mol^{-1} (**TS3**$_{S2}$), resulting in the exergonic formation of the ketone intermediate **3** (**3**$_{S1}$: −5.4 kJ·mol^{-1}, **3**$_{S2}$: −10.6 kJ·mol^{-1}). Intermediate **3** thus acts as a resting state in the catalytic cycle. Deprotonation of the ketone to the enolate **4** yields the product double bond and represents the overall rate-determining step for both substrates (**TS4**$_{S1}$: 65.7 kJ·mol^{-1}, **TS4**$_{S2}$: 65.5 kJ·mol^{-1}). This results in free effective activation barriers of 75.3 kJ·mol^{-1} for the transformation

of **S1** (relative to TBDH⁺ and PhO⁻) and 76.1 kJ·mol⁻¹ for **S2** (relative to $\mathbf{3}_{S2}$). Up to this step of the catalytic cycle, the differences between the two substrates remain small, particularly for the transition states. However, once the product double bond is formed, the free energies of the intermediates and the transition states decrease significantly in the isomerization process of substrate **S2** relative to **S1**. For substrate **S2**, the ring-closure transition state (**TS5**) lies 27.2 kJ·mol⁻¹, and the phenolate dissociation transition state (**TS6**) is 26.2 kJ·mol⁻¹ lower in free energy compared to the corresponding transition states in **S1**. The phenolate adduct of the product *endo*-VC (**5**) is even 31.5 kJ·mol⁻¹ more stable for **S2** compared to **S1**, which can be explained by a stabilizing conjugation of the VC-double bond with the aromatic substituent.

3.4.3 Ring-Retaining Mechanism

In addition to the mechanism that includes TBD and phenol, computations for the compounds **S1** and **S2** could also identify a ring-retaining, stepwise deprotonation and protonation sequence involving only TBD as a catalyst (Figure 3.4B for the catalytic cycle and Figure 3.7 for the energy diagram).

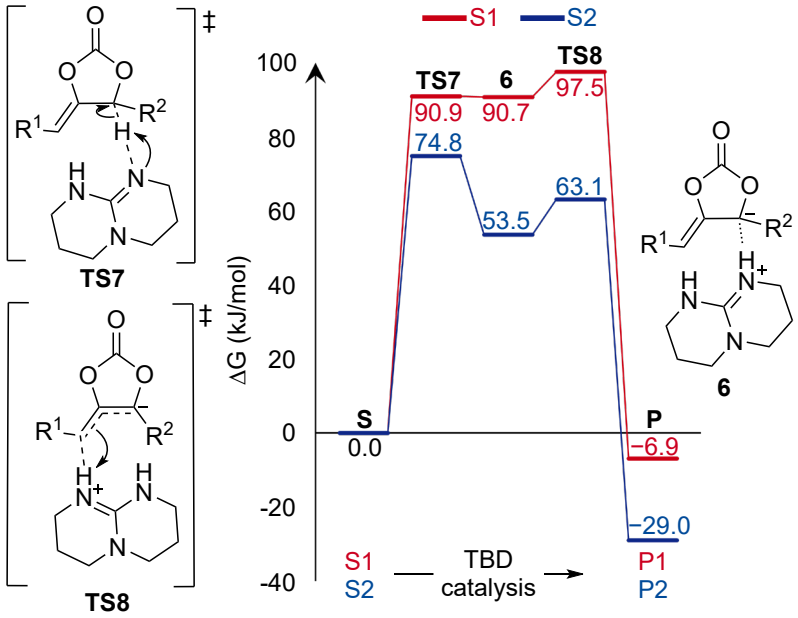

Figure 3.7: Energy diagram for the ring-retaining isomerization of substrates **S1** and **S2** under TBD catalysis; ΔG^{303} in kJ·mol⁻¹ relative to **S1** or **S2** and TBD; M06-2X-D3ZERO/def2-QZVPP//M06-L-D3ZERO/def2-SVP; COSMO-RS (MeCN).

Deprotonation of **S2** by TBD ($\mathbf{TS7}_{S2}$: 74.8 kJ·mol⁻¹) is significantly easier than the deprotonation of **S1** ($\mathbf{TS7}_{S1}$: 90.9 kJ·mol⁻¹). The differences for the anionic intermediates between $\mathbf{6}_{S1}$ and $\mathbf{6}_{S2}$ are even bigger (37.2 kJ·mol⁻¹). The subsequent protonation leading to the *endo*-VC exhibits a higher activation barrier than the preceding deprotonation in the case of **S1** ($\mathbf{TS8}_{S1}$: 97.5 kJ·mol⁻¹). Conversely, for **S2**, the subsequent protonation ($\mathbf{TS8}_{S2}$: 63.1 kJ·mol⁻¹) presents a lower free energy barrier compared to the initial deprotonation step.

Compared to this pathway, the mechanism under combined TBD and phenol catalysis is preferred for substrate **S1**, with a difference in the effective free activation energies of 22.2 kJ·mol^{-1} (ΔG_A = 75.3 kJ·mol^{-1} with TBD and PhOH vs. ΔG_A = 97.5 kJ·mol^{-1} with only TBD). For substrate **S2**, however, the Gibbs free energies of activation for the ring-opening and ring-retaining catalysis are almost identical within method uncertainties (ΔG_A = 76.1 kJ·mol^{-1} with TBD and PhOH vs. ΔG_A = 74.8 kJ·mol^{-1} with only TBD). The phenyl substituent in compound **S2** stabilizes the negative charge, resulting in lower Gibbs free energies for the ring-retaining pathway compared to the benchmark substrate. This result aligns with the experimental finding that isomerization does not occur for **S1** in the absence of phenol, whereas **S2** undergoes transformation even in the presence of only TBD. Nevertheless, the yield and selectivity are higher for compound **S2** when phenol is used, indicating a competition between both pathways. Having demonstrated the significance of the aryl substituent in enabling the ring-retaining pathway without phenol, it can be explained why Yamada and coworkers were able to synthesize only aryl-substituted *endo*-VCs using a silver-catalyzed reaction with just a base catalyst.[120] These findings support their hypothesis that the initially formed *exo*-VC directly isomerizes into the *endo*-VC.

3.4.4 Control Experiments

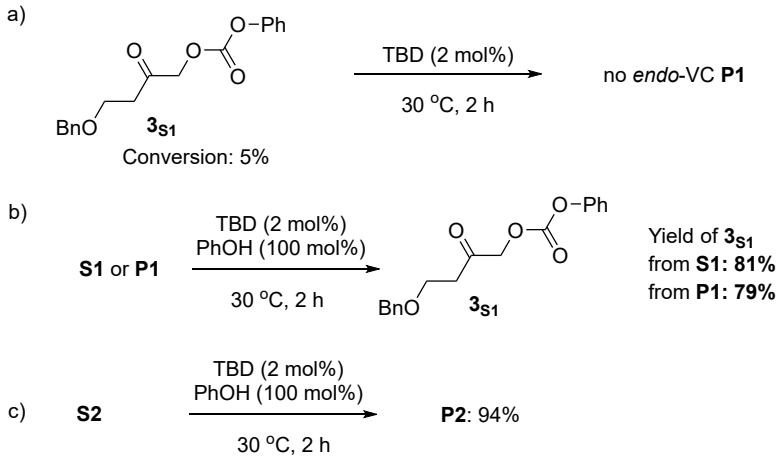

Figure 3.8: Control experiments to probe the ring-opening vs. ring-retaining catalysis; no reaction is observed for $\mathbf{3_{S1}}$ with catalytic amounts of TBD (a); **S1** and **P1** are converted to the ring-opened ketone intermediate with stoichiometric amounts of phenol (b); $\mathbf{3_{S2}}$ is not isolatable, the reaction proceeds directly to the product **P2** (c).

To experimentally prove the hypothesis of substrate **S1** only undergoing the ring-opening pathway under combined TBD and phenol catalysis, several control experiments were conducted. The first attempt was to transfer the isolated ketone-intermediate $\mathbf{3_{S1}}$ to the product **P1**. However, only a very low conversion of 5% was observed (Figure 3.8A). From the optimization studies, it was known that a low phenol concentration (10 mol%) favors product formation (**P1**), while a stoichiometric phenol concentration yields the ring-opened ketone intermediate $\mathbf{3_{S1}}$

(Figure 3.8B). The quantum-chemical calculations indicate that the equilibrium between the product side **P1** (+PhOH) and the ketone intermediate $\mathbf{3_{S1}}$ may be tunable, given the small free energy difference of 1.5 kJ·mol^{-1}. In fact, applying a stoichiometric phenol concentration yields the intermediate $\mathbf{3_{S1}}$ also from the product side (**P1**), being an indication that this is indeed an intermediate in the *exo* to *endo* isomerization. Similar reactivity was not observed for substrate **S2**, which, even under stoichiometric phenol concentration, directly yielded **P2**. This strong driving force from $\mathbf{3_{S2}}$ to **P2** is in line with the higher computed free energy difference of −18.4 kJ·mol^{-1} (Figure 3.8C).

3.4.5 Influence of the pK$_a$ of Phenol on the Reaction

The experimental screening study showed the importance of the pK$_a$ value of the used phenol. Only phenols with a pK$_a$ above 16.7 yielded the *endo*-VC (Table 3.1, entries 9–14). To further investigate this crucial dependency, the key steps of the ring-opening pathway (TBD···PhOH → TBDH$^+$···PhO$^-$ → $\mathbf{TS3_{S3}}$ → $\mathbf{3_{S3}}$ → $\mathbf{TS4_{S3}}$) were recalculated with different substituted phenols (Figure 3.9). As a comparison to unsubstituted phenol (pK$_a$ 18.0), two additional phenols were chosen: 4-CF$_3$-phenol as an example with a low pK$_a$ value (pK$_a$ 15.3), and 4-Me-phenol as an example with a high pK$_a$ value (pK$_a$ 18.9). To reduce the number of conformers in this qualitative investigation, the unsubstituted *exo*-VC **S3** is used as a model system (Figure 3.10).

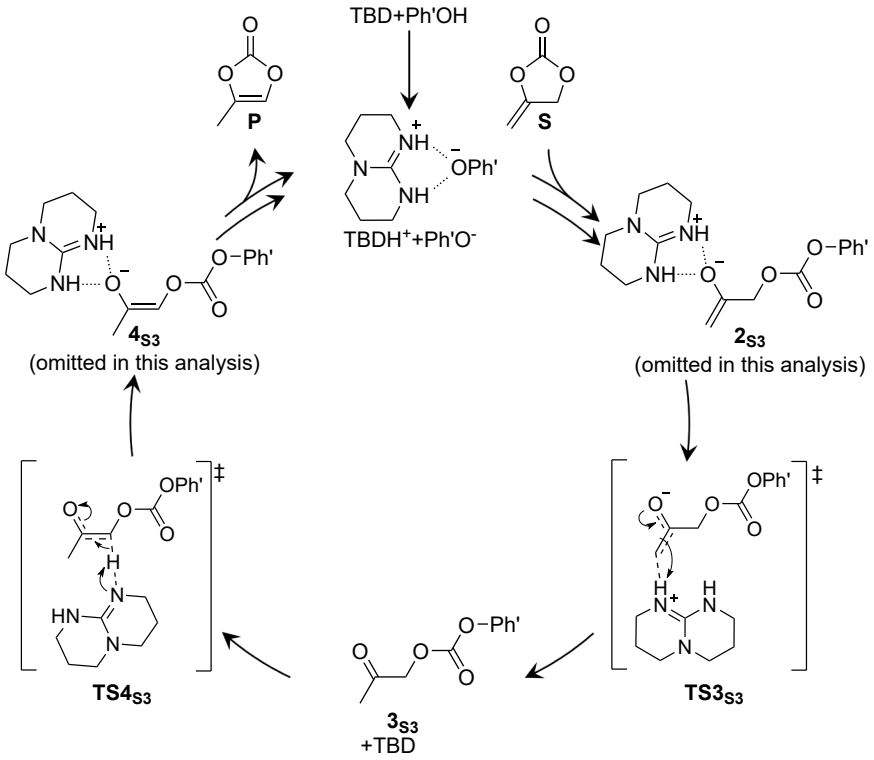

Figure 3.9: Catalytic cycle showing selected key species for the reaction of the unsubstituted *exo*-VC **S3** with TBD and different phenol derivatives (Ph'OH).

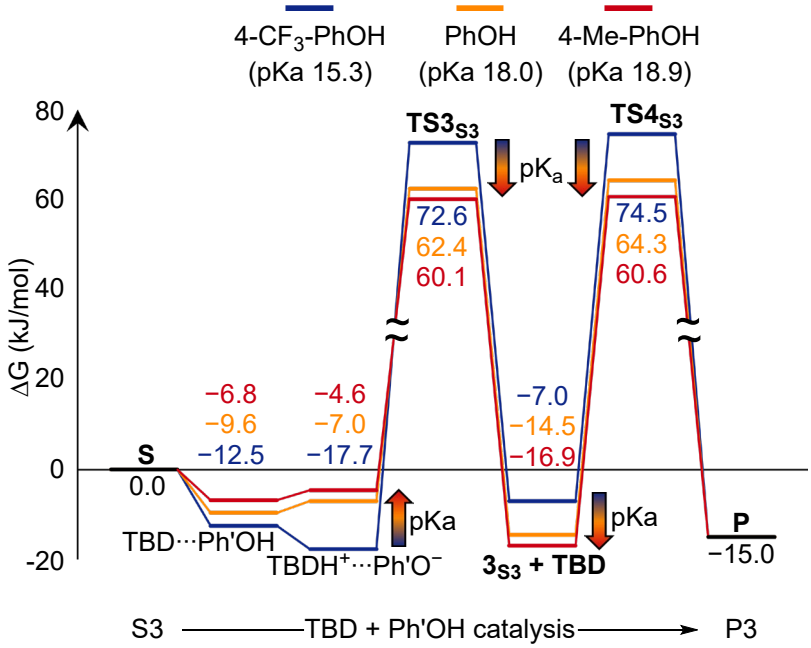

Figure 3.10: Energy diagram for selected key species for the reaction of the unsubstituted *exo*-VC **S3** with TBD and 4-CF_3-PhOH (blue), PhOH (orange), or 4-Me-PhOH (red); arrows pointing in the direction of rising pK_a values; ΔG^{303} in $kJ \cdot mol^{-1}$ relative to **S3**, TBD, and Ph'OH; M06-2X-D3ZERO/def2-QZVPP//M06-L-D3ZERO/def2-SVP; COSMO-RS (MeCN).

A decrease in pK_a value leads to the formation of a more exergonic hydrogen-bonded associate, as well as a more exergonic charged contact ion pair between TBD and phenol. In the case of 4-CF_3-phenol, the contact ion pair is more stable than the H-bonded associate due to its high acidity. Comparing the free energies of the transition states (**TS3** and **TS4**) as well as the ketone intermediate **3**, the trend is opposite. As the pK_a value decreases, the free energy rises, leading to higher Gibbs free energies of activation. This explains why catalysis only occurs when the pK_a of the phenol exceeds a specific threshold (16.7, Table 3.1).

3.4.6 Calculation of pK_a Values

The patent application for this project[150] includes the pK_a values in DMSO for all experimentally screened phenol derivatives, though some of these values were not previously reported in the literature. The missing pK_a values were therefore calculated using DFT (in DMSO) to allow ranking of the phenols according to their pK_a values. Although this task may initially appear straightforward, accurately simulating pK_a values is challenging due to the involvement of charged species. For this, a proton exchange scheme was employed.[151-152] The Gibbs free energy for the protonation of the reference structure (unsubstituted phenol) was determined in accordance with Equation 3.3. Subsequently, a corrected pK_a value relative to the reference pK_a was calculated using Equation 3.4.

$$\Delta G_{proton\ exchange} = G_{HRef} + G_{A^-} - G_{Ref^-} - G_{HA} \quad 3.3$$

$$pK_a(HA) = \frac{\Delta G_{proton\ exchange}}{RTln(10)} + pK_a^{exp}(HRef) \quad 3.4$$

Table 3.2: Calculated pK_a values; M06-2X-D3ZERO/def2-QZVPP//M06-L-D3ZERO/def2-SVP; COSMO-RS(DMSO); T = 25 °C.

Entry	Phenol Derivative R	Calculated pK_a	Experimental pK_a
1	4-OCH_3	19.8	19.1
2	4-CH_3	19.0	18.9
3	4-Cl	15.9	16.7
4	4-F	17.6	18.0
5	4-CF_3	12.8	15.3
6	4-OH	14.9	-
7	3-CH_3	17.5	-
8	2-CH_3	18.1	-
9	2,6-CH_3	19.0	-
10	4-Br	15.5	-

For four of the reference pK_a values (entries 1–4), the deviation between the experimental value and the calculated value is in the expected error range[152] with up to 0.8 pK_a, which equals a difference in free energy of 4.6 kJ·mol^{-1}. 4-CF_3-phenol (Entry 5) is considered an outlier with a higher deviation of 2.5 pK_a units (14.3 kJ·mol^{-1}). The calculated pK_a values were used to examine how the reaction outcome varies depending on the pK_a value (compare Section 3.4.5).

3.5 Summary and Outlook

As part of this chapter, a method evaluation was performed to identify a suitable DFT functional for accurate geometry optimizations. The comparison to experimentally measured crystal structures revealed that M06-L in combination with a split valence double-ζ basis set and the D3 dispersion correction with zero-damping and employing implicit solvation treatment results in a good balance between accuracy and computational cost. The solvation treatment was essential for achieving good geometrical accuracy. Based on literature reports, M06-2X was utilized for single point calculations due to its efficacy in describing reactions that involve charge separation steps.[149]

For the mechanism, two pathways were investigated: a pathway including ring-opened intermediates under combined catalysis of the N-heterocyclic base TBD and phenol (pathway A), as well as a ring-retaining pathway (pathway B) with only TBD as catalyst. The ring-opening mechanism proceeds with the charged contact ion pair of the catalysts $TBDH^+$ and PhO^-. Phenolate addition to the *exo*-VC enables the ring-opening. The ring-opened enolate can isomerize via the stable ketone intermediate **3** to the enolate featuring the product double bond. Ring-closure and subsequent phenolate dissociation yield the product endo-VC. In pathway B, TBD acts as a catalyst without phenol. A stepwise deprotonation, protonation sequence via an anionic intermediate takes place without opening the VC-ring.

In the case of the benchmark substrate **S1**, the ring-opening mechanism (A) is clearly favored over pathway B. For substrates featuring an aromatic substituent (**S2**), however, both pathways are essentially isoenergetic. This can be explained by the increased stability of deprotonated intermediates by conjugation with the aryl substituents.

Control experiments were conducted, proving the predicted shiftable equilibria between the product *endo*-VC **S1** and the ring-opened intermediary ketone $\mathbf{3_{S1}}$, as well as between the starting material *exo*-VC **S1** and $\mathbf{3_{S1}}$ under stoichiometric phenol concentration.

Experimental optimization showed that only phenols with a pK_a value above 16.7 are active for the catalysis. Investigations with three phenols (unsubstituted phenol, a more, and a less acidic derivative) showed that for very acidic phenols with a low pK_a value the charged contact ion pair of the catalysts ($TBDH^+$ and PhO^-) is very low in free energy in combination with higher transition states, leading to an increasing free activation barrier for more acidic phenols (lower pK_a).

Future computational studies could focus on expanding the mechanistic pictures to other experimentally used bases like MeTBD or DBU.

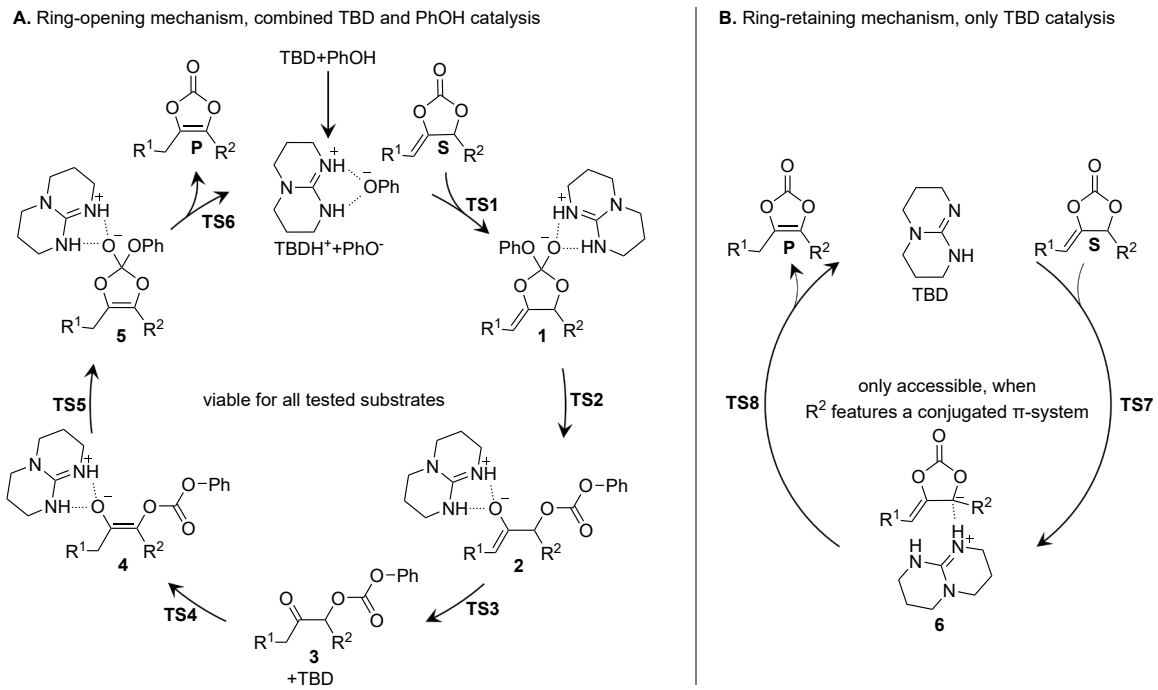

Figure 3.11: Summary showing the ring-opening (A) and ring-retaining pathway (B); the ring-retaining pathway is only viable for substrates bearing a conjugated structure at R^2.

4

Cu^{II}-Catalyzed Amination of Aryl Chlorides in Aqueous Ammonia

Reproduced in parts with permission from Lucas S. Mello,[+] Philipp D. Engel,[+] Patrizio Orecchia, Katharina Bleher, Frank Rominger, Kailaskumar Borate, Roland Goetz, Peter Deglmann, Ansgar Schäfer, Christian Winter, Michael Rack, Peter Comba, A. Stephen K. Hashmi, Thomas Schaub, Copper(II)-Catalyzed Amination of Aryl Chlorides in Aqueous Ammonia. *Chem. Eur. J.* **2024**, e202403023.[153]

All experiments presented were conducted by Lucas S. Mello, Patrizio Orecchia, Katharina Bleher, and Thomas Josephy. AFQMC calculations were performed by Michael Kühn.

Note: The numbering of calculated and experimental structures restarts at the beginning of each chapter.

4.1 Motivation and Goal

Anilines are key building blocks in industrial compounds, such as agrochemicals or pharmaceuticals.[154-155] They are also used in the production of dyes and act as intermediates in the synthesis of aromatic isocyanates, which are monomers for polyurethane production. Their global production reaches millions of tons annually. Metal-catalyzed cross-coupling reactions enable the arylation of ammonia with aryl halides in a selective and economic manner.[156] However, mostly aryl bromides and iodides are used.[156-157] While more reactive than aryl chlorides,[158] they are less available and costlier.[159] Moreover, commonly used organic solvents for this reaction, such as DMSO and NMP, are associated with toxicity and safety risks, making them less favorable for industrial use.[160-161]

The overall goal of this project was to find a method for synthesizing substituted anilines from aryl chlorides, using a catalyst based on an abundant metal like copper, ammonia as a nitrogen source, and water as a safer and more environmentally friendly solvent.[162-163] Moreover, selective amination of the C−Cl bond instead of the C−F bond was targeted in challenging substrates such as 3,4-difluoro-1-chlorobenzene. As a suitable catalytic system, a mixture of a Cu^{II} precursor with phenanthroline or bipyridine ligands in pure aqueous ammonia without additional organic solvent was found.[153] As an additional base, a potassium phosphate salt was added. The reaction was performed at 180 °C in a steel vessel suitable for the pressure build-up of up to 40 bar. These harsh conditions and the closed system prevented spectroscopic investigations at the reaction conditions. DFT computations, presented in this chapter, were needed to study the reaction pathway, especially since mechanisms based on Cu^{II} instead of Cu^{I} for such cross-couplings are rather scarce.[153,164]

As a starting point for the computational analysis, a benchmark study is included to identify a suitable DFT functional for obtaining accurate single point energies. A key objective is the study of the coordination chemistry of possible Cu^{II} complexes to identify species and equilibria possibly present in solution, including the potential deprotonation of coordinated ammonia ligands. In addition, the electronic structures of these complexes are characterized in detail. Based on these analyses, various mechanistic scenarios are examined and compared. To connect theory with experiment, EPR and UV-vis-NIR spectra are computed to rationalize and complement control experiments. Finally, the amination of C−Cl and C−F bonds is compared in order to clarify the origin of the experimentally observed selectivity trends.

4.2 Experimental Background

Classically, anilines are produced on a large scale by nitration of aromatic compounds followed by hydrogenation (Figure 4.1A). Drawbacks of this method are the formation of a high amount of byproducts, low selectivity, low functional group tolerance due to the harsh acidic and oxidative conditions, as well as safety issues.[165]

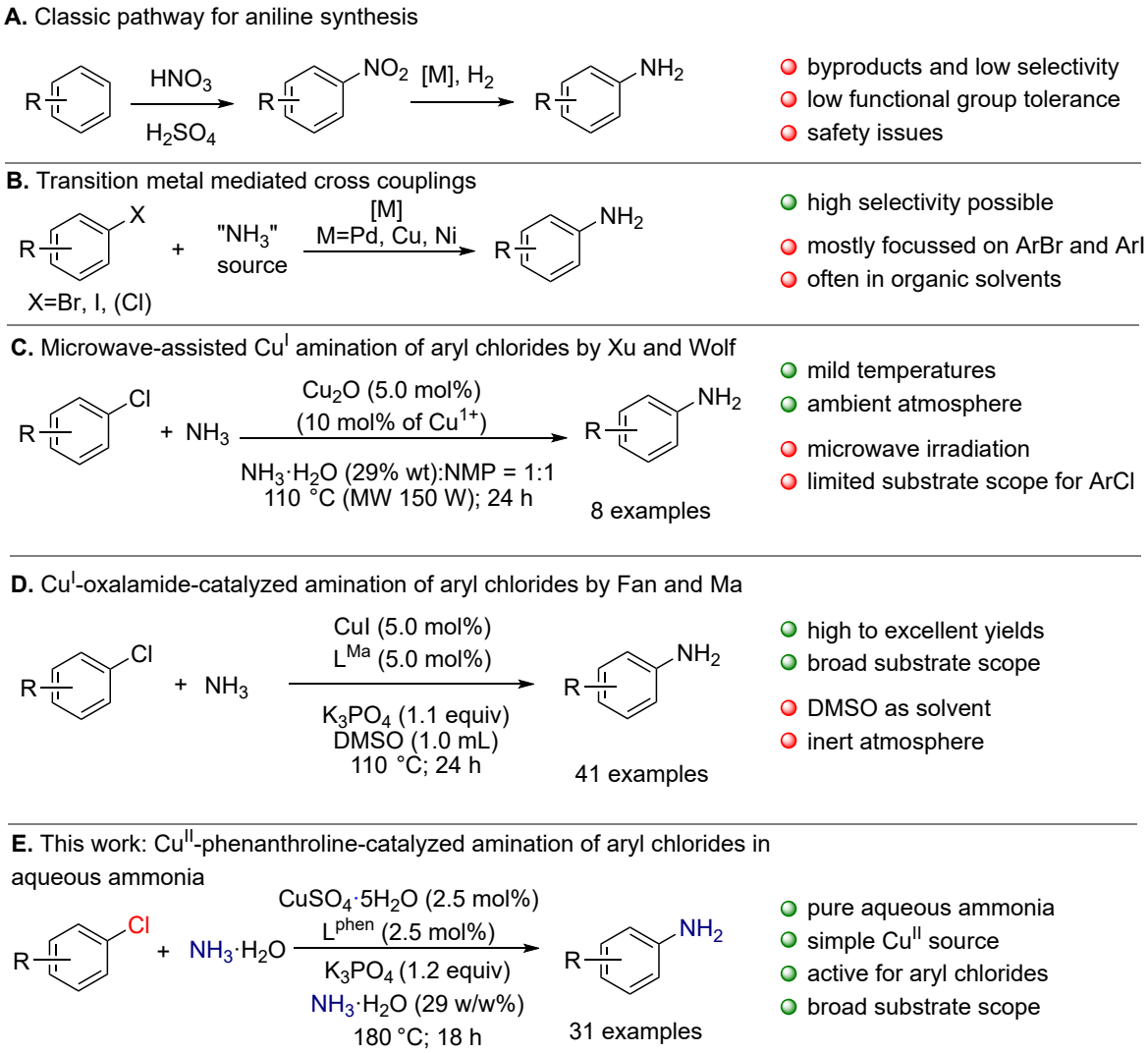

Figure 4.1: Selected reported examples for the synthesis of substituted anilines: classical pathway via nitration of benzene (A),[165] transition metal mediated cross couplings (B),[155,157,166-170] microwave-assisted Cu^{I}-catalyzed amination (C),[171] Cu^{I}-catalyzed amination of aryl chlorides using an arylated oxalamide ligand (D),[172] and Cu^{II}-catalyzed amination of aryl chlorides (E).[153]

Anilines can also be synthesized from aryl halides via direct nucleophilic substitution, but this requires high temperatures (up to 300 °C) and results in low selectivity.[154,156] Transition metal catalyzed direct mono-arylation of ammonia with aryl halides has been widely explored, using palladium,[155,166-167] copper,[157] and nickel[168-170] catalysts. However, most of these reports focused on the amination of aryl bromides and iodides, which are intrinsically more reactive but less available and more expensive than aryl chlorides (Figure 4.2).[156-159,173] Furthermore, the use of

predominantly hazardous organic solvents is not suitable for industrial applications due to toxicity and safety hazards.[160-161]

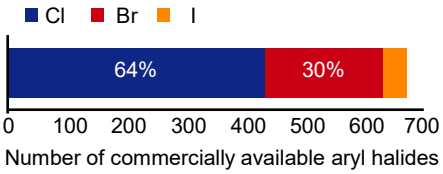

Figure 4.2: Number of commercially available aryl halides (in thousands); data taken from [173].

Xu and coworkers[171] reported the arylation of ammonia with aryl chlorides using Cu_2O as a catalyst in a H_2O:NMP mixture featuring mild temperatures and ambient conditions (Figure 4.1C). However, this process requires microwave irradiation and exhibits a limited substrate scope for aryl chlorides. Ma and colleagues[172] demonstrated that low Cu^I-loadings with an arylated oxalamide ligand enable efficient amination of aryl chlorides in DMSO, using aqueous ammonia to synthesize anilines in high to excellent yields across a broad range of substrates (Figure 4.1D). The need for an inert atmosphere (due to the use of Cu^I) and DMSO limits the potential industrial application. Few additional examples[174-178] of the mono-arylation of ammonia using aryl chlorides were described. However, these methods either have a limited substrate scope[174-178] or produce byproducts.[175-177]

To overcome these limitations, a method for a Cu^{II}-catalyzed direct synthesis of anilines from aryl chlorides in aqueous ammonia, achieving an adequate substrate scope, was developed at CaRLa (Figure 4.1E).[153] This methodology utilizes the metal precursor $CuSO_4$ and K_3PO_4 as the base, requiring no organic solvent and no exclusion of air during reagent handling. It offers an efficient alternative approach for synthesizing aniline building blocks, introducing this functionality at an early stage. The reactions were carried out in pure aqueous ammonia in stainless steel resealable tubes. Potassium phosphate was selected as the base because of its cost-effectiveness and its ability to facilitate the isolation of the final products as hydrochloride salts, while also preventing co-precipitation. $CuSO_4$ as the metal precursor was chosen for cost reasons. As a benchmark substrate for the condition optimizations, 3,4-difluoro-1-chlorobenzene was used. This substrate is considered challenging due to the presence of two C–F bonds, which can lead to side reactions through uncatalyzed aromatic nucleophilic substitutions at elevated temperatures.[156] The optimization conducted for this substrate aimed to determine the most broadly applicable conditions. Substituted phenanthroline and bipyridine ligands were shown to result in active catalysts (see [153] for results with bipyridine ligands; since the computational investigations focused on the phenanthroline ligands, only these are discussed here). Suitable phenanthroline ligands contain mesomeric donor substituents in the *para* position to the N-donor atom (Table 4.1, entries 1–4), with the methoxy-substituted phenanthroline being the most active (94% yield). Interestingly, using unsubstituted phenanthroline as well as methyl or hydroxymethyl substituents did not yield the product (Table 4.1, entries 5–7). Under these optimized conditions, a variety of aryl chlorides with electron-neutral, donating, or withdrawing substituents were tested.

Furthermore, the transformation of hetero- as well as several dichloro-substituted aromatics was achieved. Besides the di-fluoro substituted benchmark substrate, a tri-fluoro substituted aryl chloride was also selectively transferred to the tri-fluoro-aniline (see [153] for more examples and details).

Table 4.1: Optimization of the Cu-catalyzed amination of aryl chlorides in aqueous ammonia. Table excerpt adapted with permission from [153].

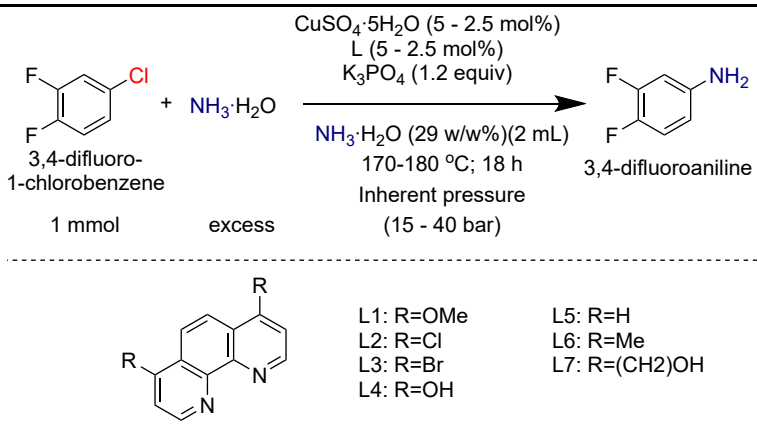

Entry	Ligand	Metal source	Metal/Ligand load (mol%)	Temp (°C)	Yield[c] (%)
1[a]	L1	$CuSO_4$	2.5	180	94%
2[a]	L2	$CuSO_4$	2.5	180	53%
3[b]	L3	$CuSO_4$	2.5	180	91%
4[a]	L4	$CuSO_4$	2.5	180	75%
5[a]	L5	$CuSO_4$	2.5	180	0
6[a]	L6	$CuSO_4$	2.5	180	0
7[a]	L7	$CuSO_4$	2.5	180	0
8[b]	L1	CuI	5.0	170	74%

General procedure: copper source (0.025-0.050 equivalents), ligand (0.025-0.050 equivalents), base (1.2 equivalents) and 3,4-difluoro-1-chlorobenzene (1.0 mmol) and 2 mL of 29 w/w% aqueous ammonia (30 equivalents), inherent pressure in a closed system (15—40 bar). [a]Copper sulfate pentahydrate as copper source under ambient atmosphere. [b]NEt_3 instead of K_3PO_4 used as base under argon atmosphere.

Besides the use of a Cu^{II} precursor, a Cu^{I} precursor resulted in an active catalyst. However, in the case of the Cu^{I} precursor, an induction period without any formation of aniline was observed. After the induction period, no change is visible compared to the reaction using the Cu^{II} precursor (Figure 4.3). This indicates that both precatalysts likely follow a Cu^{II}-catalyzed mechanism, with Cu^{I} oxidized to Cu^{II} under the non-inert conditions applied (due to potentially dissolved O_2 in aqueous ammonia).

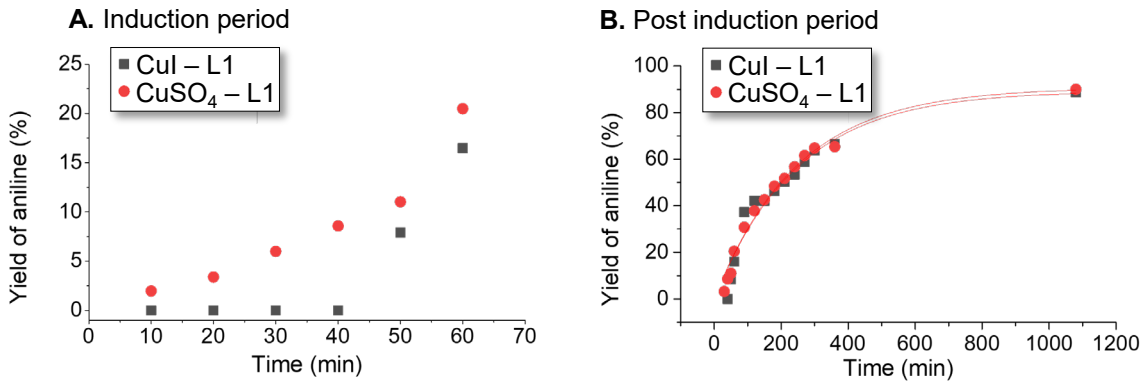

Figure 4.3: Reaction profiles for CuI and $CuSO_4$ precursors: first sixty minutes showing an induction period for the CuI precursor (A) and pseudo first order fitting for the 18 h reaction (B); results presented as mean of duplicates; reactions were set up under air as the initial atmosphere.

The Ullmann-type C–N coupling reaction, established for over a century, is typically described to proceed via a Cu^{I}–(formally)Cu^{III} oxidative addition pathway,[156-157] which rarely allows NH_3 as a nitrogen source. Contrarily, only a few examples are known for Cu^{II} catalysis.[164] Therefore, mechanistic studies, including detailed computational analyses of our system, are highly relevant.

4.3 Computational Details

Geometry optimizations and Hessian calculations were conducted using the TURBOMOLE[133] program package (version 7.5.2). The GGA functional TPSS[179] was employed together with the def2-SVP[135] basis set and the D3 dispersion correction with zero-damping.[136] Solvent effects during geometry optimization were incorporated through the COSMO model using default parameters and an infinite dielectric constant.[24] Verification of stationary points was performed through vibrational frequency analysis at the same level of theory.

Final single point electronic energies were determined using the range-separated hybrid functional ωB97x-D[146-147] in combination with the def2-QZVPP[135,138] basis set. The RI approximation[139-142] and corresponding auxiliary basis sets were consistently applied throughout. The choice of a robust GGA functional[180] for geometry optimizations and a range-separated hybrid functional for single point refinements was motivated by their demonstrated accuracy in benchmark studies.[181-182]

Thermochemical corrections to calculate Gibbs free energies were obtained at the level of theory of the geometry optimization (T = 453.15 K, p = 1 bar). Solvation treatment was performed using the COSMO-RS model[26,28] in COSMOtherm (Version 18.0.0; Revision 4360).[143] The calculations were carried out for infinite dilution in water employing the FINE parametrization and a reference state of 1 mol·L^{-1} at 453.15 K. Connections between transition states and local minima were confirmed by displacing the transition-state geometry along the imaginary mode, followed by geometry optimization. Barrierless processes were confirmed through relaxed scans. Molecular structures, molecular orbitals, and spin density plots were visualized with Cylview[183] and Chemcraft.[184] For clarity, C−H hydrogen atoms are omitted in the figures.

Exploration of reaction pathways was performed using the MGSM method[37-39] in combination with a precomplex builder.[40] Conformational sampling for all intermediates and transition states was carried out with the CREST[15-16] program package, followed by DFT optimization and single point energy evaluation of selected conformers to establish relative free energy rankings. For clarity, only the lowest energy conformers are discussed and shown in the figures.

Time-dependent DFT (TD-DFT) calculations of UV/Vis absorption spectra were carried out using ORCA[185-187] (version 5.0.4). The ωB97x-D functional[146-147] together with the def2-TZVP[135] basis set was employed, applying implicit solvation with the CPCM[188] model using water as solvent. Simulated spectra were plotted with a full width at half maximum (FWHM) of 11 nm. Electron paramagnetic resonance (EPR) parameters were computed at the same level of theory. Molecular orbital schemes were constructed using quasi-restricted orbitals (QROs)[189] obtained at the CPCM(H_2O)-ωB97x-D/def2-TZVP level of theory. Unless otherwise stated, all calculations were performed using methoxy-substituted phenanthroline and chlorobenzene as model systems.

For the benchmark study, auxiliary-field quantum Monte Carlo (AFQMC)[190] calculations were performed by Michael Kühn (BASF SE) using the ipie package (version 0.6.2)[191] interfaced with PySCF.[192] A restricted open-shell Hartree-Fock trial wave function was employed. The cc-pVDZ[193] and cc-pVTZ[193-195] basis sets were used, followed by extrapolation to the complete basis set limit. The frozen-core approximation was applied. 2000 walkers were employed for 7500 blocks. All additional computational parameters were selected in accordance with established literature standards (see [196] for more information). Additionally, DFT single point calculations were conducted using the TPSS, TPSSh,[179,197] B3LYP,[198-200] PBE0,[201] and CAM-B3LYP[202] functionals with the def2-QZVPP[135,138] basis set and D3 dispersion correction with zero-damping.[136] Furthermore, DLPNO-CCSD(T)[203] coupled cluster calculations were performed in ORCA[185-187] (version 5.0.4) with the cc-pVTZ[193-195] and the cc-pVQZ[193-195] basis sets, employing a two-point complete basis set extrapolation. The associated auxiliary basis sets were used.[204-205] A TPSS reference wavefunction was used. *TightSCF* and *NormalPNO* settings were applied.

4.4 Results and Discussion

4.4.1 Coordination Chemistry of *mono*-Phenanthroline Complexes

Different coordination geometries of the starting complex were systematically investigated to identify the species that are potentially present in solution (Figure 4.4).

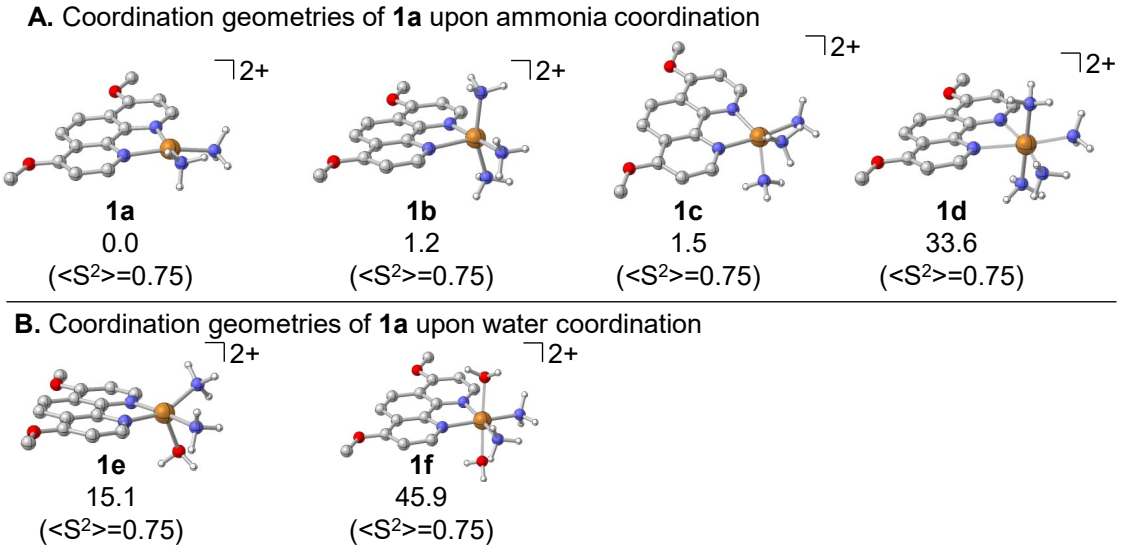

Figure 4.4: Coordination geometries of the *mono*-phenanthroline complex **1** in aqueous ammonia upon coordination of ammonia (A) and water (B); relative ΔG^{453} in kJ·mol^{-1}; ωB97x-D/def2-QZVPP//COSMO(∞)-TPSS-D3ZERO/def2-SVP; COSMO-RS (H_2O).

Given that the reaction is conducted in aqueous ammonia, both ammonia and water coordination are evaluated. For the *mono*-phenanthroline complexes, the lowest free energy is observed for the square planar structure coordinated by two ammine ligands (**1a**). In **1a**, the planarity is slightly disrupted with a N–N–N–N dihedral angle of 23°. The addition of a third ammine ligand proceeds nearly isoenergetically compared to **1a** (distorted square pyramidal **1b**: 1.2 kJ·mol^{-1}, trigonal bipyramidal **1c**: 1.5 kJ·mol^{-1}). Octahedral coordination with four ammine ligands is predicted to be energetically unfavorable (**1d**: 33.6 kJ·mol^{-1}). In comparison, water coordination results in higher free energies (**1e**: 15.1 kJ·mol^{-1}, **1f**: 45.9 kJ·mol^{-1}). Therefore, the square planar complex is considered as the resting state of the catalyst based on these static quantum-chemical calculations. For more accurate insights into the equilibria in solution, a molecular dynamics simulation would be needed, which is not part of this work. The spin density for all these complexes is mainly localized on the d^9 copper center in the $d_{x^2-y^2}$ orbital and the coordinated nitrogen atoms (Figure 4.5).

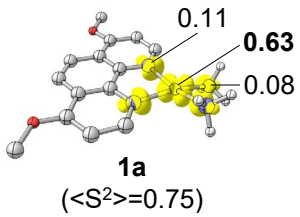

Figure 4.5: Spin density of **1a**, including Mulliken spin populations; exemplary for all species of **1**; spin density isosurfaces at ±0.005 $a_0^{-3/2}$; excess spin α shown in yellow; ωB97x-D/def2-QZVPP//COSMO(∞)-TPSS-D3ZERO/def2-SVP; COSMO-RS (H_2O).

Phosphate was used experimentally as a base. This led to the consideration of the deprotonation of a coordinated ammine ligand. To minimize potential errors in describing solvation effects for the trianionic phosphate ion, the hydroxide ion (OH^-) is modeled as the active base. To probe the importance of explicit solvation to stabilize the OH^- anion, coordination of one, two, and three explicit water molecules was evaluated (Figure 4.6).

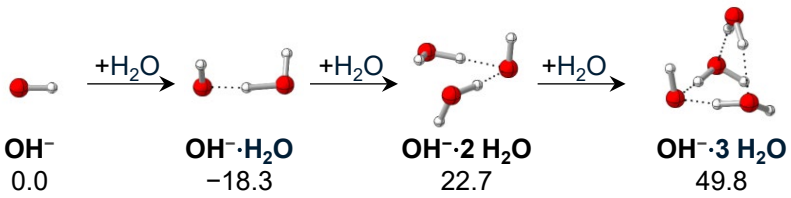

Figure 4.6: Explicitly solvated OH^-; ΔG^{453} in kJ·mol^{-1} relative OH^- and H_2O; ωB97x-D/def2-QZVPP//COSMO(∞)-TPSS-D3ZERO/def2-SVP; COSMO-RS (H_2O).

At the used level of theory, OH^- is found to be most stable when coordinated by one explicit water molecule (−18.3 kJ·mol^{-1} of stabilization relative to the uncoordinated ion). Consequently, an $OH^-·H_2O$ associate was used to model the thermodynamics in the step of deprotonation. As with **1**, various coordination geometries were computed for the deprotonated complexes **2** (Figure 4.7A).

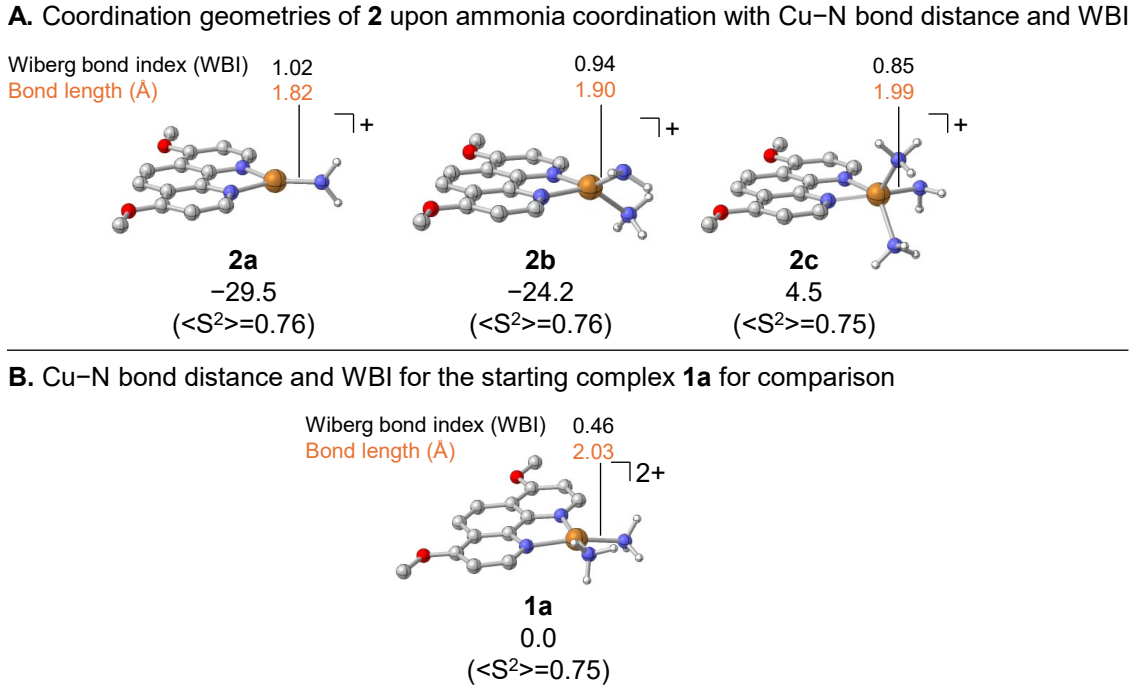

Figure 4.7: Coordination geometries of the deprotonated complex **2** upon ammonia coordination (A) with Cu−N Wiberg bond index (WBI, black) and bond distance (orange) and the starting *bis*-ammine complex **1a** for comparison (B); ΔG^{453} in kJ·mol^{-1} relative to **1a** and $OH^-·H_2O$; ωB97x-D/def2-QZVPP//COSMO(∞)-TPSS-D3ZERO/def2-SVP; COSMO-RS (H_2O).

The lowest energy complex is **2a** with a trigonal planar geometry and a significantly exergonic free energy of −29.5 kJ·mol^{-1}. Further ammonia coordination is unfavorable (**2b**: −24.2 kJ·mol^{-1} and **2c**: 4.5 kJ·mol^{-1}). Notably, the NH_2 group is only planar in **2a**, whereas it is pyramidal in both **2b** and **2c**. This indicates a stronger Cu–NH_2 π-interaction, as seen in the increased Cu–N Wiberg bond order and shorter bond distance for the deprotonated complex **2a** relative to **2b**, **2c**, and particularly compared to the starting complex **1a**, where such a π-interaction is not possible (Figure 4.7B).

The deprotonated complex **2a** with its Cu–N π-character is comparable to blue copper proteins, for which a highly covalent Cu–S π-interaction has been reported.[206] Blue copper proteins feature tetragonal pyramidal coordination with an axial donor, typically a methionine, about 2.9 Å away from the copper center.[207-209] Such distant interactions (>2.5 Å) are typically not considered as covalent bonds.[210-211] However, research on blue copper proteins and, e.g., copper-*tetrakis*-ammine complexes indicated that axial donors at these distances, including one or two axial water molecules in solution, may significantly influence the electronic properties.[212-214] For both the *bis*-ammine complex (square planar **1a**) and the deprotonated complex (trigonal planar **2a**), DFT-optimized geometries did not reveal any long-distance axial donor (water or ammonia). All attempts produced stronger coordination, where solvent molecules act as ligands (**1d**: d(Cu–$^{ax}NH_3$) = 2.06 Å; **1f**: d(Cu–$^{ax}H_2O$) = 2.36 Å). However, when calculating free energies, axial solvent interactions will be considered by the COSMO-RS solvation correction. Changing the DFT method used for geometry optimization to other GGA functionals, such as BP86, did not result in qualitative changes.

The electronic structure of the trigonal planar Cu^{II}-amido complex **2a** was investigated, particularly with respect to its Cu–NH_2 π-character. QROs were used, since in these α- and β-orbitals are identical and have the same energy, facilitating the interpretation. Relevant QROs were manually chosen, resembling the Cu–NH_2 σ- and π-bonding molecular orbitals, the corresponding anti-bonding molecular orbitals, and the copper-centered lone pairs (Figure 4.8). For this analysis, the z-axis is aligned along the Cu–NH_2 bond. It is noted that, while the choice of coordinate system does not affect the QROs, it can facilitate their interpretation; a direct influence on the orbitals occurs only when localization methods, such as natural bonding orbitals (NBOs), are employed.

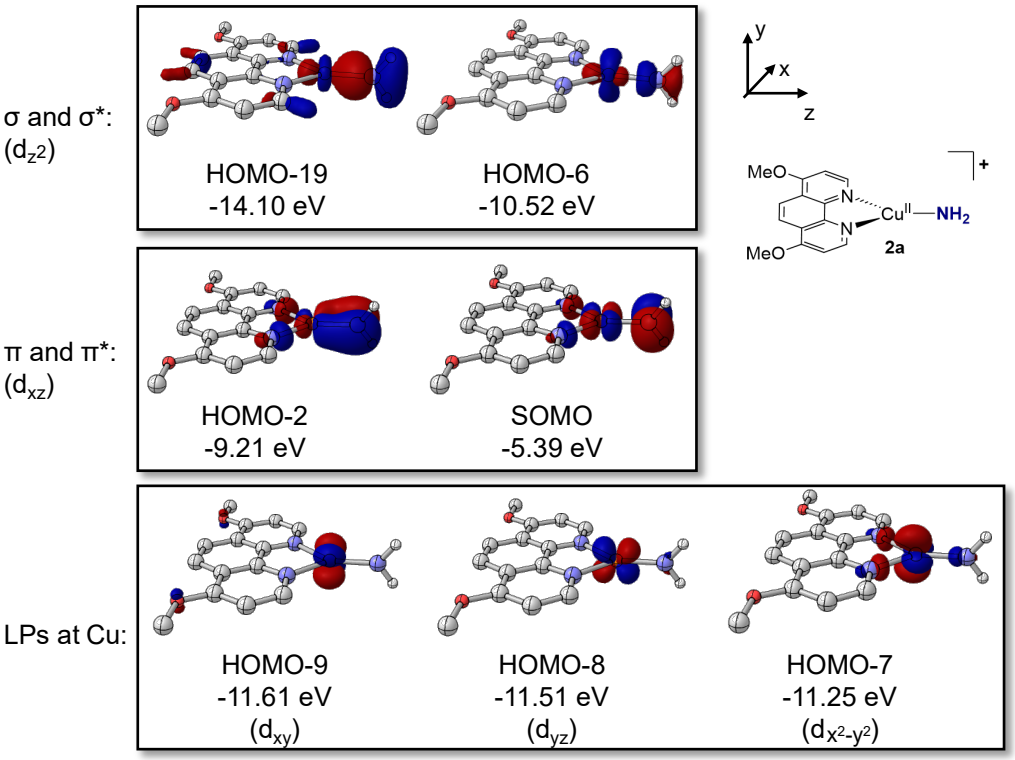

Figure 4.8: Relevant QROs of **2a** to show the σ- and π-interactions and the lone pairs (LPs) at the copper center; orbital energies in eV; isosurfaces at ±0.05 $a_0^{-3/2}$; CPCM(H_2O)-ωB97x-D/def2-TZVP//TPSS-D3ZERO/def2-SVP.

The σ-symmetric interaction originates from the overlap between the in-plane, doubly occupied d_z^2 orbital of the copper center and the sp^2-symmetric donor orbital of the NH_2^- fragment (HOMO−19). HOMO−6 displays the corresponding antibonding combination. A π-bond is formed by the singly occupied d_{xz} orbital and the NH_2-nitrogen atom's *p*-lone pair. The antibonding combination is represented in the SOMO. This 2-center, 3-electron interaction also leads to the planarity of the NH_2 fragment. Furthermore, three copper-centered lone pairs were found with the d_{xy}, d_{yz}, and $d_{x^2-y^2}$ orbitals. Based on these molecular orbitals, a fragment molecular orbital scheme can be generated showing the interaction of the NH_2^- unit with Cu^{II}-phenanthroline fragment (Figure 4.9).

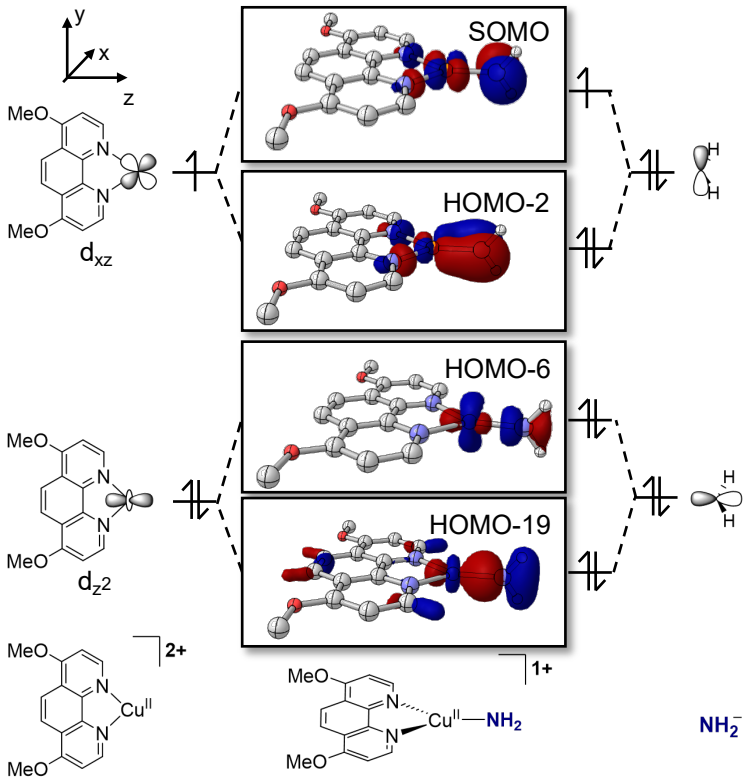

Figure 4.9: Qualitative fragment MO scheme of **2a**; using quasi-restricted molecular orbitals; isosurfaces at ±0.05 $a_0^{-3/2}$.

The canonical spin density of **2a** closely matches the SOMO from the quasi-restricted calculation (Figure 4.10), suggesting spin-polarization is not a major factor in this complex. Compared to the *bis*-ammine complex **1a**, spin is more delocalized from the copper to the NH_2-nitrogen atom in **2a**. Although the copper center in **2a** exhibits a reduced spin population of 0.41, the complex is more consistent with a Cu^{II}-amido rather than a Cu^{I}-aminyl species.

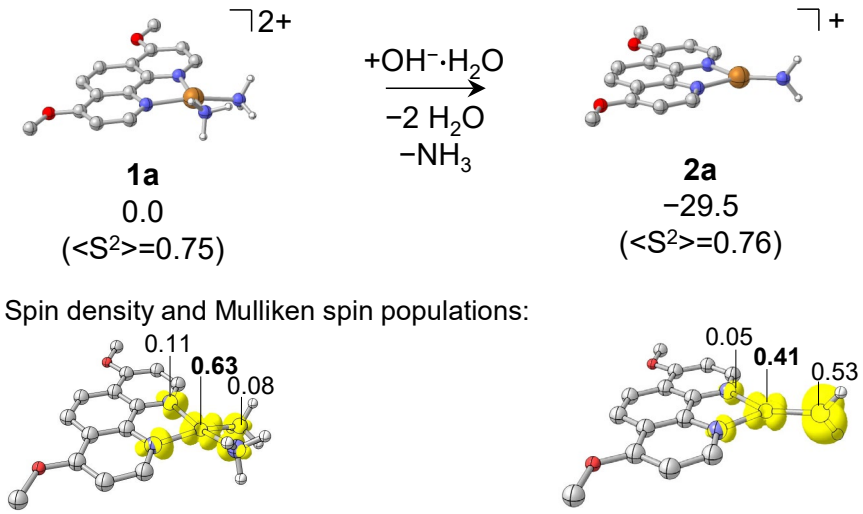

Figure 4.10: Spin densities and Mulliken spin populations of **1a** and **2a**; spin density isosurfaces at ±0.005 $a_0^{-3/2}$; excess spin α shown in yellow; ΔG^{453} in kJ·mol^{-1} relative to **1a** and $OH^-{\cdot}H_2O$; ωB97x-D/def2-QZVPP//COSMO(∞)-TPSS-D3ZERO/def2-SVP; COSMO-RS (H_2O).

4.4.2 Coordination Chemistry of *bis*-Phenanthroline Complexes

For completeness, the potential formation of a *bis*-phenanthroline complex was computationally examined as well. A ligand exchange process was calculated, leading to the *bis*-phenanthroline complex **1g** along with a copper-*tetrakis*-ammine species (Figure 4.11A). This transformation is modestly exergonic, exhibiting a free energy change of −3.7 kJ·mol^{-1}. Subsequent coordination of ammonia further decreases the free energy, yielding complex **1h** with a free energy of −19.9 kJ·mol^{-1} (Figure 4.11B). It should be noted that, similar to the *mono*-phenanthroline complexes, no weak solvent coordination in the axial position to the copper-*tetrakis*-ammine complex was found at the employed level of theory. Deprotonation of **1h** proceeds practically isoenergetically to **2d** (ΔG_R = +0.2 kJ·mol^{-1}, Figure 4.11C). Since the deprotonated *mono*-phenanthroline-amido complex **2a** (−29.5 kJ·mol^{-1}) is significantly more stable than the *bis*-phenanthroline-amido complex **2d** (−19.7 kJ·mol^{-1}), a phenanthroline dissociation would be expected; thus, the *bis*-phenanthroline complexes are excluded from the mechanistical analysis. This is in line with the experimental observation of the reaction getting less efficient upon increasing the phenanthroline concentration.

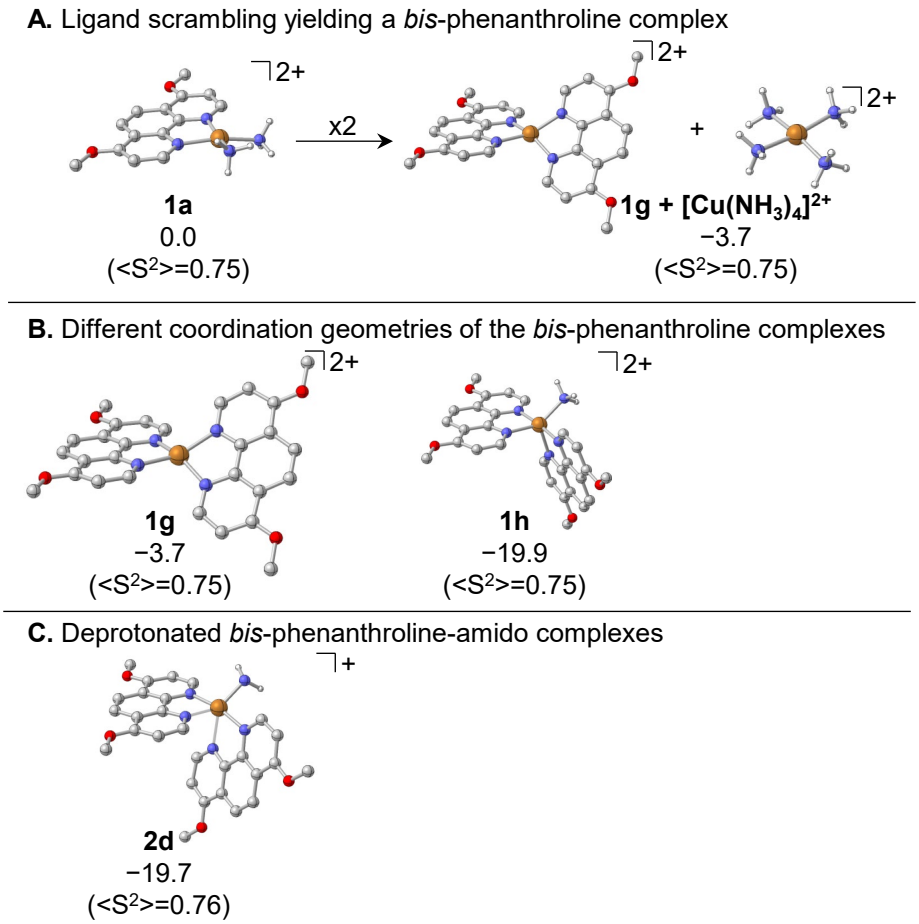

Figure 4.11. Ligand scrambling of **1a** to a *bis*-phenanthroline complex (A); coordination geometries of the *bis*-phenanthroline complex **1g** and **1h** (B); the deprotonated *bis*-phenanthroline-amido complex **2d** (C); ΔG^{453} in $kJ \cdot mol^{-1}$ relative to **1a** and $OH^- \cdot H_2O$; ωB97x-D/def2-QZVPP//COSMO(∞)-TPSS-D3ZERO/def2-SVP; COSMO-RS (H_2O).

4.4.3 Mechanistic Investigations

Four mechanistic scenarios involving a Cu^{II} catalyst were considered: a mechanism involving free organic radicals, an oxidative addition pathway, a σ-bond metathesis, and an S_NAr type reaction (Figure 4.12). These pathways align with those discussed in the literature.[164] As a model substrate for the mechanistic calculations, chlorobenzene was used.

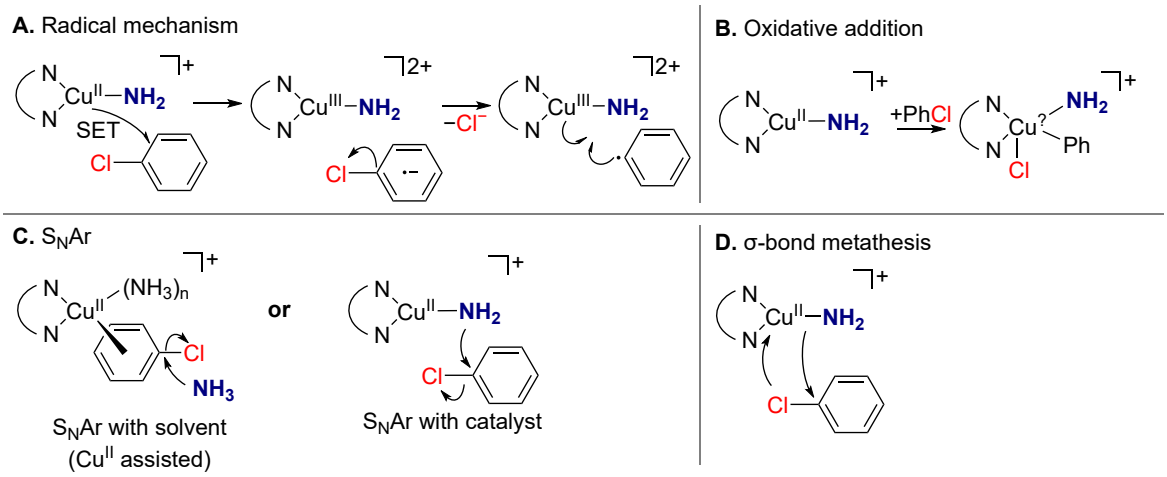

Figure 4.12: Possible mechanistic pathways; mechanism including free, organic radicals (A); oxidative addition pathway (B); S_NAr pathways (C); σ-bond metathesis (D).

Pathway A, which involves free organic radicals, was excluded based on experimental evidence, as the addition of radical scavengers (TEMPO and BHT) did not affect the reaction yield. In addition, when the amination was performed using the radical clock olefin 1-(3-buten-1-yl)-2-chlorobenzene, only the corresponding aniline was obtained, without detection of the product expected from a radical pathway. The DFT calculations indicate that oxidative addition of the aryl chloride to the Cu^{II} catalyst (pathway B) does not occur, as the resulting intermediate with a formally Cu^{IV} center is not accessible (Figure 4.13A). Two possibilities of an S_NAr reaction are plausible: substitution by a solvent molecule (NH_3), followed by deprotonation or substitution by a copper-coordinated NH_2-group. The transition state for the solvent-S_NAr is inaccessible (**TS1**: 219.0 kJ·mol^{-1}, Figure 4.13B).

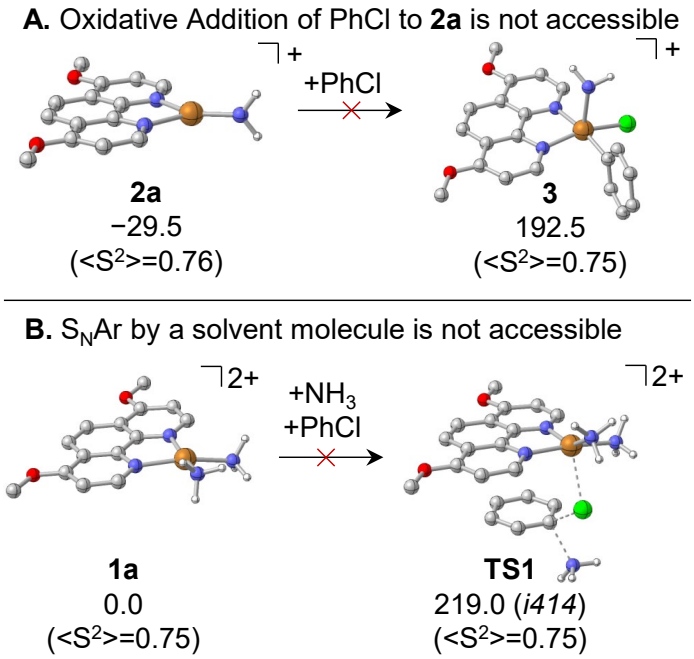

Figure 4.13: Neither oxidative addition of PhCl to **2a** (A) nor S_NAr reaction with a solvent molecule (B) is accessible; ΔG^{453} in kJ·mol^{-1} relative to **1a** and $OH^-{\cdot}H_2O$; ωB97x-D/def2-QZVPP//COSMO(∞)-TPSS-D3ZERO/def2-SVP; COSMO-RS (H_2O).

From the trigonal-planar Cu^{II}-amido complex **2a**, a transition state (**TS2a**, Figure 4.14) with an effective Gibbs free energy of activation of 150.9 kJ·mol^{-1} relative to the active catalyst **2a** is found, which is accessible at the given reaction conditions. Upon distortion of the transition state towards the product and subsequent geometry optimization, the chloride atom dissociates spontaneously and binds to the copper center to yield intermediate **4**. Since this dissociation does not appear in the vibrational mode associated with the imaginary frequency and is highly asynchronous, this transition state aligns more with an S_NAr reaction (pathway C) than with a σ-bond metathesis (pathway D). A synchronous transition state involving simultaneous C–Cl bond dissociation and Cu–Cl bond formation in the transition state mode, as seen in classic σ-bond metathesis, could not be found.

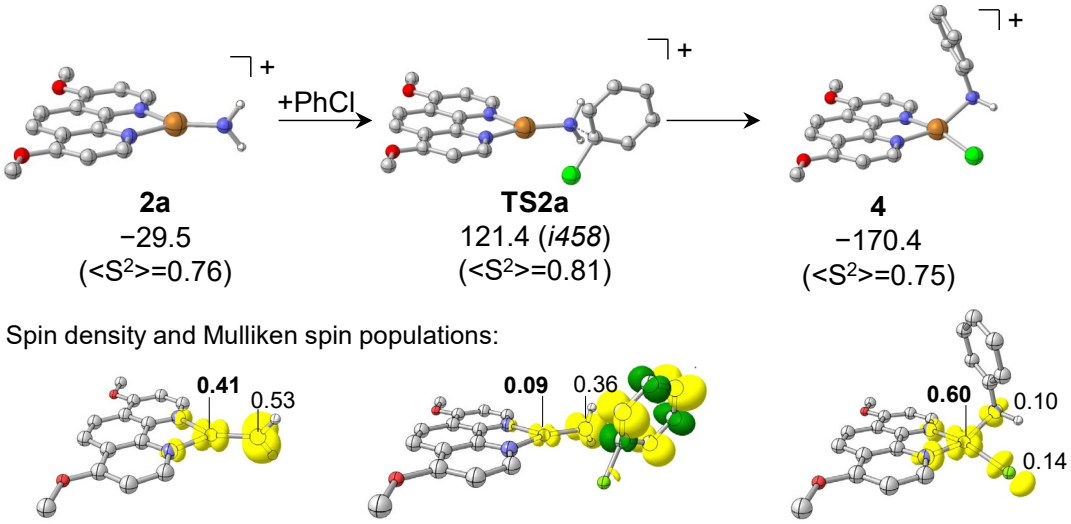

Figure 4.14: Nucleophilic aromatic substitution (S_NAr) via **TS2a**; spin density including Mulliken spin populations (spin density isosurfaces at ±0.005 $a_0^{-3/2}$, excess spin α shown in yellow and excess spin β shown in green); ΔG^{453} in kJ·mol^{-1} relative to **1a** and $OH^-{\cdot}H_2O$; ωB97x-D/def2-QZVPP//COSMO(∞)-TPSS-D3ZERO/def2-SVP; COSMO-RS (H_2O).

The analysis of the spin density for **TS2a** shows a minimal spin population of 0.09 at the copper center. The spin density is highly delocalized over the NH_2 ligand and the aromatic system of the aryl chloride. This suggests that, effectively, a Cu^I-aminyl radical attacks the chlorobenzene. Therefore, the reaction proceeds via a radical-mediated S_NAr pathway rather than a conventional S_NAr mechanism. Intermediate **4**, which follows the transition state, again exhibits a clear Cu^{II} center with a spin population of 0.60. For the transition state **TS2**, several geometries with coordinated ammonia molecules were calculated (Figure 4.15). However, the lowest transition state remains **TS2a**. Consequently, **2a** was found to be the active form of the catalyst.

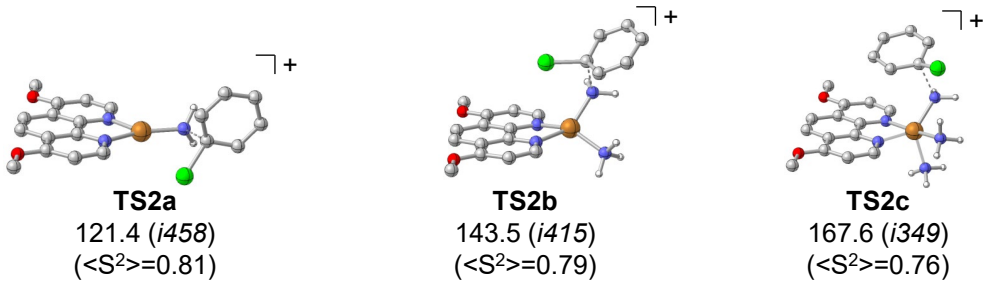

Figure 4.15: TS2 with zero, one and two coordinated ammonia molecules; ΔG^{453} in kJ·mol^{-1} relative to **1a**, PhCl and $OH^-{\cdot}H_2O$; ωB97x-D/def2-QZVPP//COSMO(∞)-TPSS-D3ZERO/def2-SVP; COSMO-RS (H_2O).

Via the transition state **TS2a**, the aniline- and chlorido-bound intermediate **4** is formed strongly exergonically (−170.4 kJ·mol^{-1}, Figure 4.16). A Meisenheimer complex[215] was not found with chlorobenzene as substrate. The regeneration of complex **1a** and subsequent product release proceeds through barrierless, sequential solvent exchange processes: ammonia coordinates to **4**, leading to the dissociation of aniline and formation of **5** (−189.3 kJ·mol^{-1}). This is followed by coordination of an additional molecule of ammonia and dissociation of a chloride ion, resulting in the regeneration of **1a** (**1a'**: −181.2 kJ·mol^{-1}). The free energy of **1a** for the second cycle includes the reaction free energy of the produced aniline and is therefore denoted as **1a'**. While **1a'** is slightly endergonic compared to **5**, the active form of the catalyst **2a'** is regenerated in an exergonic manner (−210.7 kJ·mol^{-1}). This results in the full catalytic cycle depicted in Figure 4.16.

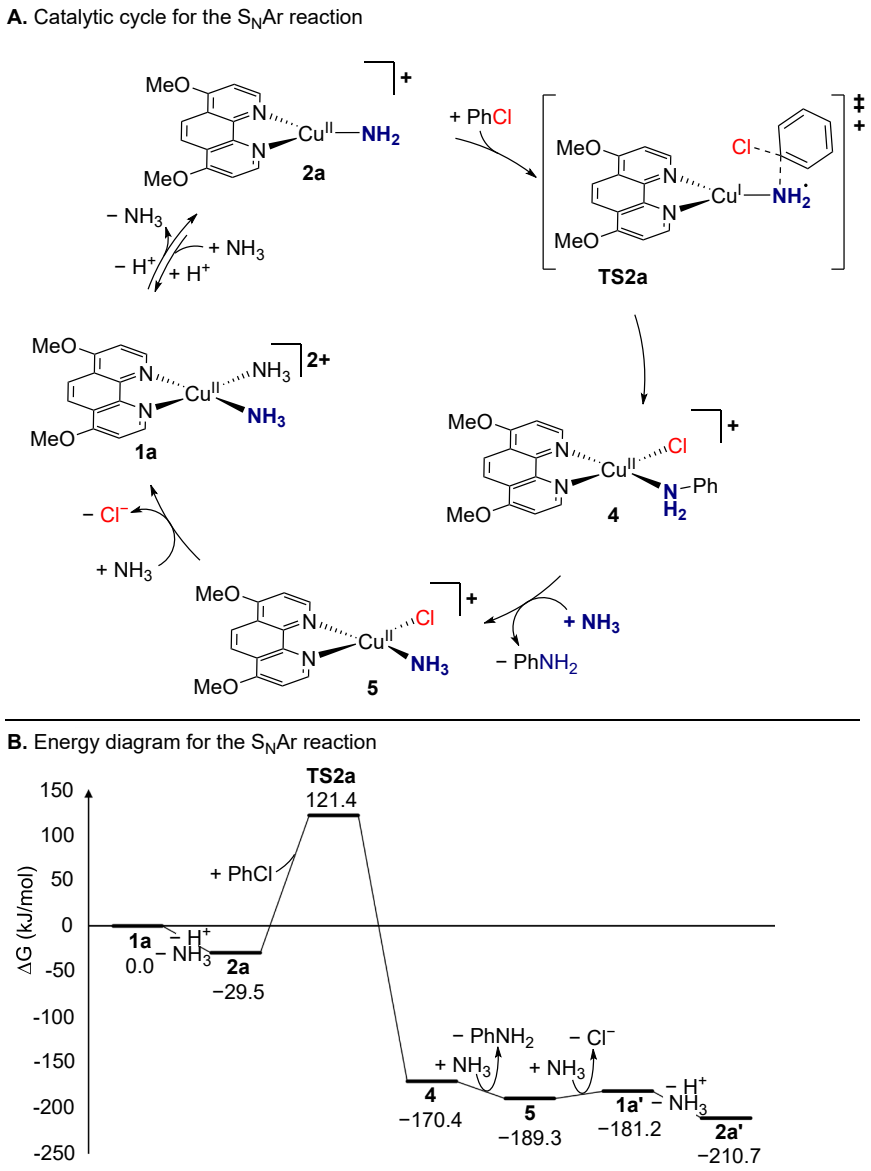

Figure 4.16: Proposed catalytic cycle and energy diagram for the amination of chlorobenzene; **1a'** and **2a'** refer to the second catalytic cycle; protonation and deprotonation were modeled with $OH^-{\cdot}H_2O$ as active base; ΔG^{453} in $kJ{\cdot}mol^{-1}$ relative to **1a** and $OH^-{\cdot}H_2O$; ωB97x-D/def2-QZVPP//COSMO(∞)-TPSS-D3ZERO/def2-SVP; COSMO-RS (H_2O).

4.4.4 Control Experiments: UV-vis-NIR

Based on these computational results indicating deprotonation of a coordinated ammonia ligand, UV-vis-NIR spectroscopic investigations were conducted with the aim of finding evidence for the formation of the deprotonated Cu^{II}-amido complex **2a**. Due to the autoclave setup and the high temperatures for the experiments, these studies could not be conducted at the reaction conditions. To study the deprotonation of the ammine-phenanthroline-complex in solution, additional base (triethylamine) was titrated to a solution of a Cu^{II}-precursor and 4,7-dimethoxy-1,10-phenanthroline in methanolic ammonia. During the titration, UV-vis-NIR spectra were recorded (Figure 4.17).

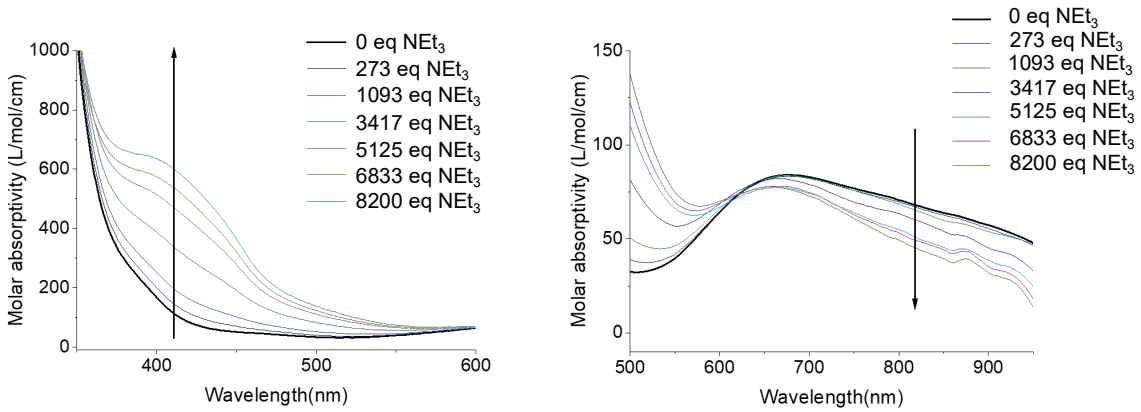

Figure 4.17: UV-Vis-NIR spectra (205–950 nm) of a solution of $Cu(OTF)_2$ and 4,7-dimethoxy-1,10-phenanthroline in methanolic ammonia under *in situ* titration of triethylamine (NEt_3); UV-vis-NIR area on the left and Vis-NIR area on the right.

The experimental spectra show two main trends: an increasing band at 400–450 nm and decreasing intensity at higher wavelength in the Vis-NIR region. TD-DFT calculations were conducted to get further insights into the nature of the characteristic band at 400–450 nm. Notably, the calculated UV-vis-NIR spectrum of the Cu^{II}-amido species shows an isolated band at 410 nm (Figure 4.18). The nature of this band is a transition of the Cu–NH_2 π-bonding orbital into the corresponding π*-antibonding orbital and effectively a $p(N) \rightarrow d_{xy}(Cu^{II})$ ligand to metal charge transfer (LMCT) transition. This transition is in line with former literature reports on comparable Cu^{II} complexes.[206,216-217]

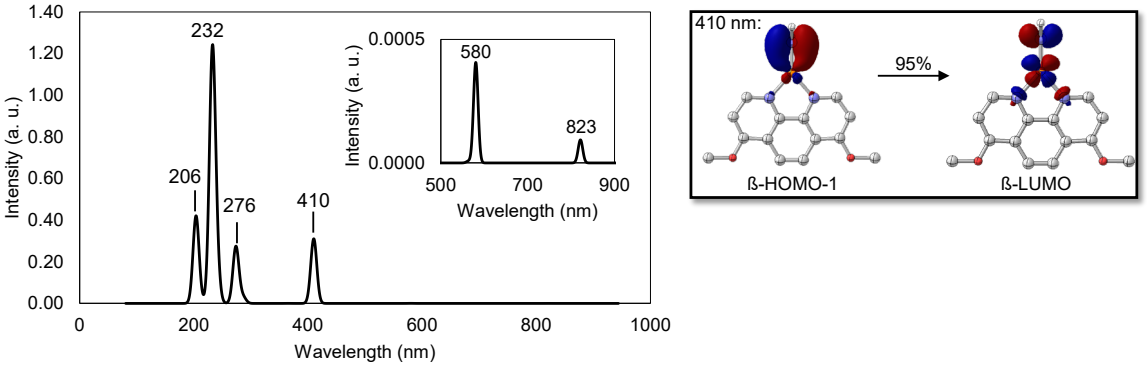

Figure 4.18: TD-DFT-calculated UV-vis-NIR spectrum of **2a** and the canonical MOs mainly contributing to the transition at 410 nm; 11 nm FWHM Gaussian Broadening; molecular orbital isosurfaces at ±0.05 $a_0^{-3/2}$; CPCM(H_2O)-ωB97x-D/def2-TZVP//COSMO(∞)-TPSS-D3ZERO/def2-SVP.

In the calculated UV-vis-NIR spectrum of the *bis*-ammine starting complex, no band is observed in this region (Figure 4.19). The area corresponding to *d-d* transitions is more challenging to simulate, as it does not present as a single band like the 410 nm transition. Benchmarking the applied TD-DFT method would be necessary for a detailed comparison between the calculated *d-d* bands and experimental data but this was beyond the scope of this work.

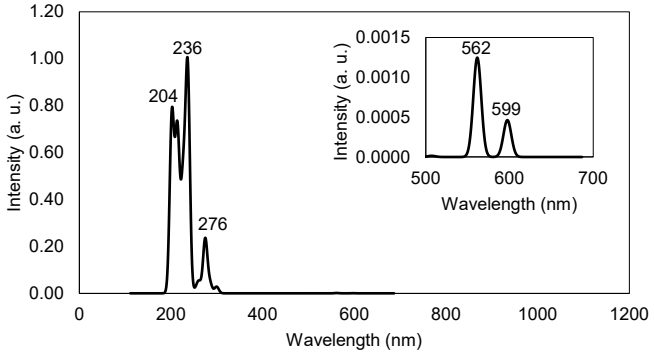

Figure 4.19: TD-DFT-calculated UV-vis-NIR spectrum of **1a**; 11 nm FWHM Gaussian Broadening; CPCM(H_2O)-ωB97x-D/def2-TZVP//COSMO(∞)-TPSS-D3ZERO/def2-SVP.

Solely based on the TD-DFT calculations, the 4- and 5-coordinate species **2b** and **2c** cannot fully be excluded (Figure 4.20 exemplarily shows the calculated spectrum for **2b**), since they feature a comparable transition at 382 nm (**2b**) and 355 nm (**2c**). Due to the weaker Cu–NH_2 π-interactions compared to **2a** in combination with more distorted coordination spheres, the transitions involve more molecular orbitals for **2b** and **2c**. The analysis of the difference electron density, however, suggests the same nature as the LMCT transition as in **2a**. Nevertheless, the calculated Gibbs free energies of activation suggest a preference for the trigonal planar form (compare discussion in Section 4.4.3).

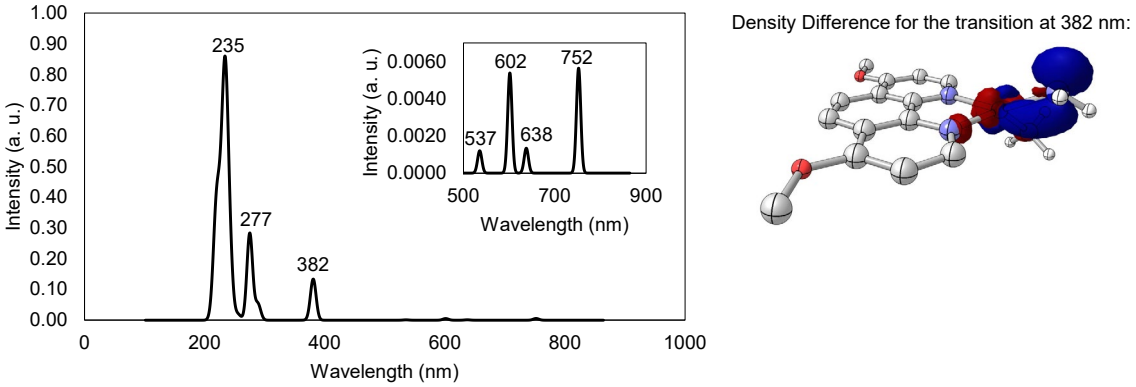

Figure 4.20: TD-DFT-calculated UV-vis-NIR spectra of **2b** showing a more complex CT-transition at 382 nm than in the case of **2a**; 11 nm FWHM Gaussian broadening; density difference for the LMCT, isosurfaces at ±0.05 $a_0^{-3/2}$; CPCM(H_2O)-ωB97x-D/def2-TZVP//COSMO(∞)-TPSS-D3ZERO/def2-SVP.

The titration experiments demonstrate that complete deprotonation could not be achieved under the conditions applied. Based on the expected[206,216,218] extinction coefficient for the LMCT transition at 410 nm of approximately 2000–5000 $l \cdot mol^{-1} \cdot cm^{-1}$, only 10–30% of the deprotonated species is formed.

4.4.5 Control Experiments: EPR

To further investigate the deprotonation, EPR studies were performed. For this, a solution of *in situ* formed Cu^{II}-ammine-*mono*-phenanthroline was treated with 3000 equivalents of triethylamine or roughly 1000 eq KOH (Figure 4.21).

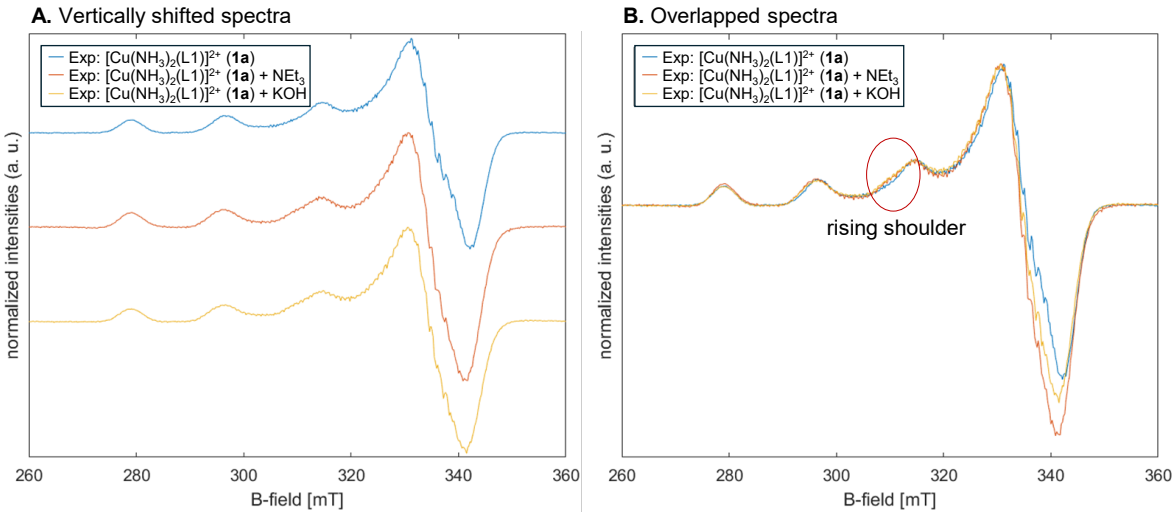

Figure 4.21: EPR spectra (260–360 mT, 10 K, MeOH) for *in situ* formed $[Cu(NH_3)_2(L1)]^{2+}$ (**1a**, assumed based on computations) (blue MWFQ = $9.629949 \cdot 10^9$ Hz) and the mixtures with a deprotonated complex (**2a**, assumed based on computations) in the presence of roughly 3000 eq NEt_3 (orange line, MWFQ = $9.631071 \cdot 10^9$ Hz) or 1000 equivalents of KOH (yellow line, MWFQ = $9.629803 \cdot 10^9$ Hz); vertically shifted (A) and overlapped spectra (B); L1 = 4,7-dimethoxy-1,10-phenanthroline.

The appearance of a shoulder in the hyperfine coupling of the Cu^{II} center indicates an equilibrium between two species. To further interpret the EPR spectra and get more insights into the possibly formed species, they were simulated using EasySpin (version 6.0.0)[219], assuming axial g- and A-tensors. Only the hyperfine coupling of copper was fitted for each species, while possible superhyperfine couplings with nitrogen were ignored. The fitted spectra are shown in Figure 4.22, fitted parameters in Table 4.2, and DFT-computed EPR parameters in Table 4.3.

While the simulation of the ammine-phenanthroline complex shows a good agreement with the measured peak position and form, the simulation of the spectra upon base addition is less accurate. The observed formation of a new band around 315 mT is not reproduced well in a simulation including only one species (Figure 4.22B). Thus, in the next step, the simulation of a mixture between two species (protonated and deprotonated) was attempted (Figure 4.22C). DFT calculations indicated that the deprotonated amido complex is likely to feature a trigonal planar geometry (**2a**) along with a significantly reduced spin density at the copper center in comparison to the ammine-phenanthroline complex. For such species (e.g., [Cu^{II}]-anilides in [217], [Cu^{II}]-peroxido complexes in [216], or blue copper proteins in [206]), clearly reduced copper hyperfine couplings ($A_{\parallel}$) are reported. This is also consistent with the DFT-computed copper hyperfine coupling for **2a** (−419.4 MHz), which is clearly decreased (in absolute value) compared to the protonated species (**1a**, −618.4 MHz, Table 4.3).

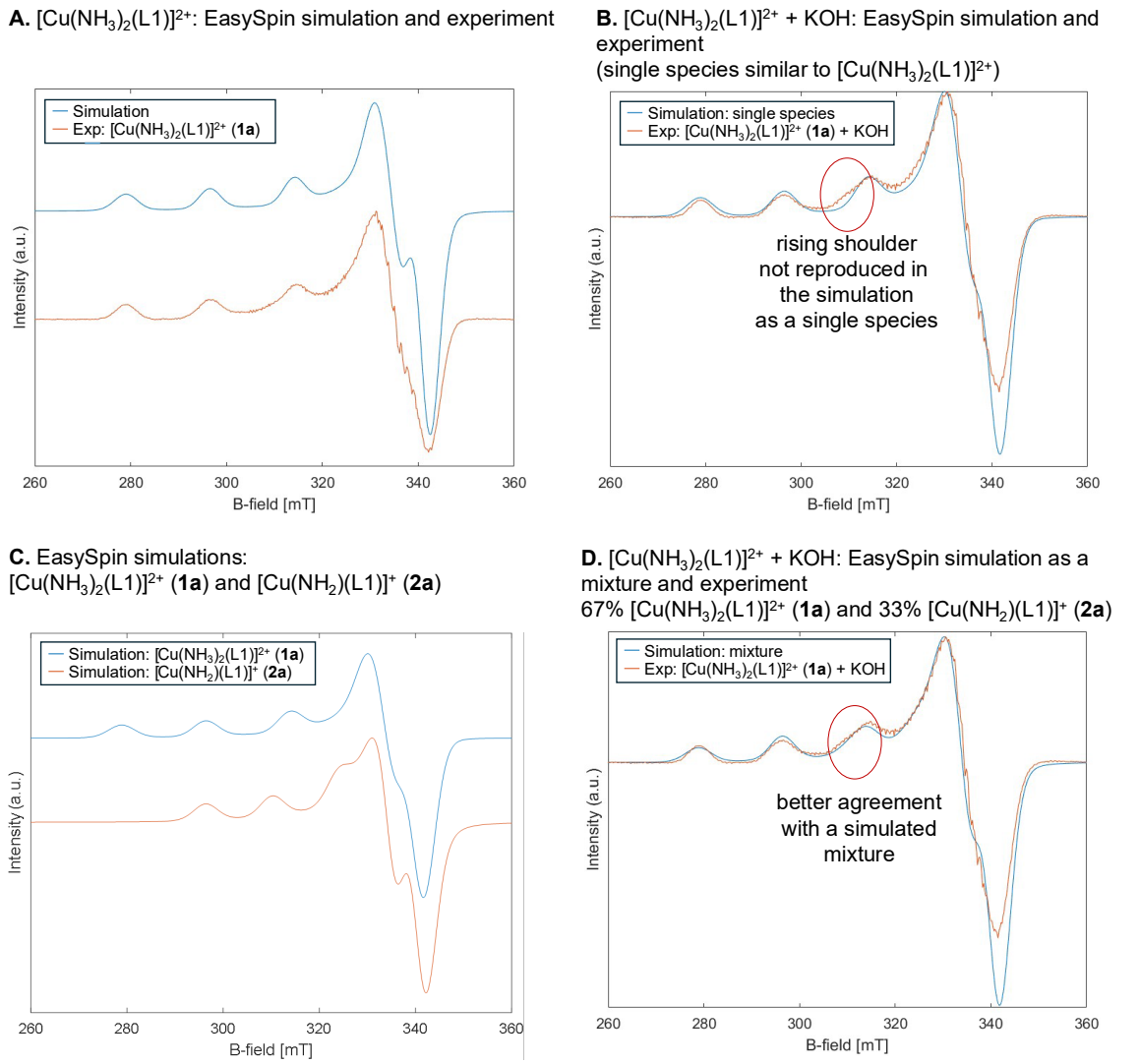

Figure 4.22: EasySpin simulations were performed for $[Cu(NH_3)_2(L1)]^{2+}$ without base addition (A), upon KOH addition, simulated a single species (B); since the agreement with the experiment remained unsatisfactory, an equilibrium with a deprotonated species was considered (EasySpin simulations in C); the simulation as a mixture with 33% contribution of a species with lower copper hyperfine coupling reproduced the rising shoulder better (D); L1 = 4,7-dimethoxy-1,10-phenanthroline.

The intensity of the extinction coefficient of the charge transfer band in the UV-vis-NIR spectrum indicated that roughly 33% of the deprotonated species is formed. Consequently, a 67%:33% ratio was assumed for the EasySpin simulation. The simulation for this mixture yields a better agreement with the form of the bands, especially around 310–320 mT. This result supports an equilibrium between Cu^{II}-ammine and Cu^{II}-amido complexes, consistent with the DFT computations and UV–vis–NIR experiments.

Table 4.2: Parameters of *EasySpin* simulation for $[Cu(NH_3)_2(L1)]^{2+}$, $[Cu(NH_3)_2(L1)]^{2+}$ + KOH fitted as a single species as well as a potential $[Cu(NH_2)(L1)]^{+}$ with a low hyperfine coupling; L1 = 4,7-dimethoxy-1,10-phenanthroline; g-factors and copper hyperfine couplings were fitted as axial matrices.

Species	$[g_\perp\ g_\parallel]$	A_{Cu} (MHz) $[A_\perp\ A_\parallel]$	lw (mT) [Gaussian Lorentzian]
$[Cu(NH_3)_2(L1)]^{2+}$	[2.052 2.253]	[47 542]	[4.8 0.8]
$[Cu(NH_3)_2(L1)]^{2+}$ + KOH (single species)	[2.058 2.254]	[43 542]	[5.8 0.5]
Potential $[Cu(NH_2)(L1)]^{+}$	[2.055 2.169]	[20 420]	[5.0 2.0]

Table 4.3: EPR parameters obtained from DFT calculations for $[Cu(NH_3)_2(L1)]^{2+}$ (**1a**) and $[Cu(NH_2)(L1)]^{+}$ (**2a**); L1 = 4,7-dimethoxy-1,10-phenanthroline; CPCM(H_2O)-ωB97x-D3/def2-TZVP//COSMO(∞)-TPSS-D3ZERO/def2-SVP.

Species	$[g_x\ g_y\ g_z]$	A_{Cu} (MHz) $[A_x\ A_y\ A_z]$
$[Cu(NH_3)_2(L1)]^{2+}$ (**1a**)	[2.054 2.055 2.178]	[−9.0 −9.2 −618.4]
$[Cu(NH_2)(L1)]^{+}$ (**2a**)	[2.043 2.053 2.145]	[−19.7 −39.9 −419.4]

4.4.6 Reactivity Comparison between PhCl and PhF

During the experimental screening, no catalytic activity was observed when fluorobenzene was used as the substrate, whereas chlorobenzene was converted under the same reaction conditions. Similarly, for 3,4-difluoro-1-chlorobenzene, amination occurs selectively at the C–Cl bonds. This trend is the opposite of that reported in the literature[156,220-221] for (uncatalyzed) S_NAr reactions, where fluoroarenes typically react faster than chloro-, bromo-, or iodoarenes. Notably, this is inverted to the $^{Ar}C–X$ bond strengths, as C–F is the strongest. The explanation lies in the rate-determining step of the uncatalyzed reaction, which is the nucleophilic addition to the aryl halide and not the halide ion dissociation (Figure 4.23). This addition depends on C–X polarization, which matches the reactivity order in uncatalyzed S_NAr reactions (C–F > C–Cl > C–Br > C–I).[156,220-221]

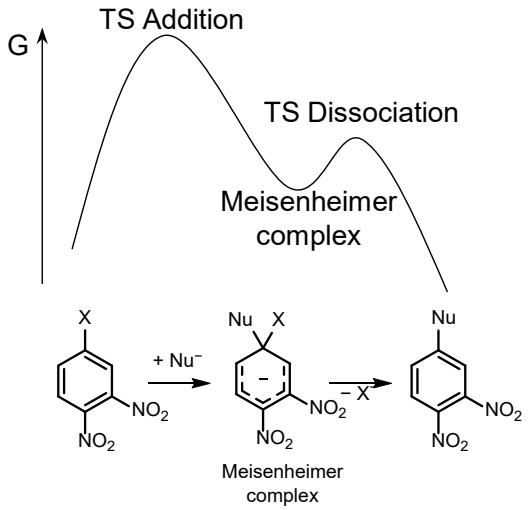

Figure 4.23: Schematic energy diagram of an uncatalyzed S_NAr reaction; oriented at [221].

Compared to this mechanism, the Cu^{II}-catalyzed radical-mediated S_NAr reaction in this case proceeds via a concerted transition state, without a Meisenheimer complex. To further investigate the effects of the halide, the transition state **TS2a** and key intermediates were calculated with fluorobenzene in comparison to chlorobenzene (Figure 4.24).

The transition state **TS2a** for the substitution at fluorobenzene is 4.8 kJ·mol^{-1} lower in free energy than for chlorobenzene – a rather small difference for a qualitative change in reactivity. In the following intermediates, however, bigger differences are observed with intermediate **5** being even lower in free energy than the active form of the catalyst **2a**. Consequently, the regeneration of the active catalyst is 22.7 kJ·mol^{-1} endergonic, and the fluorido-bound complex **5** acts as a thermodynamic sink. For the second catalytic cycle, this regeneration energy has to be considered, leading to a higher effective Gibbs free energy of activation (G_A = 168.8 kJ·mol^{-1}) for fluorobenzene compared to that with chlorobenzene (150.9 kJ·mol^{-1}), explaining the experimentally observed differences between these model systems. Future studies should focus on whether this trend also holds true for the more complex case of the experimental benchmark substrate 3,4-difluoro-1-chlorobenzene.

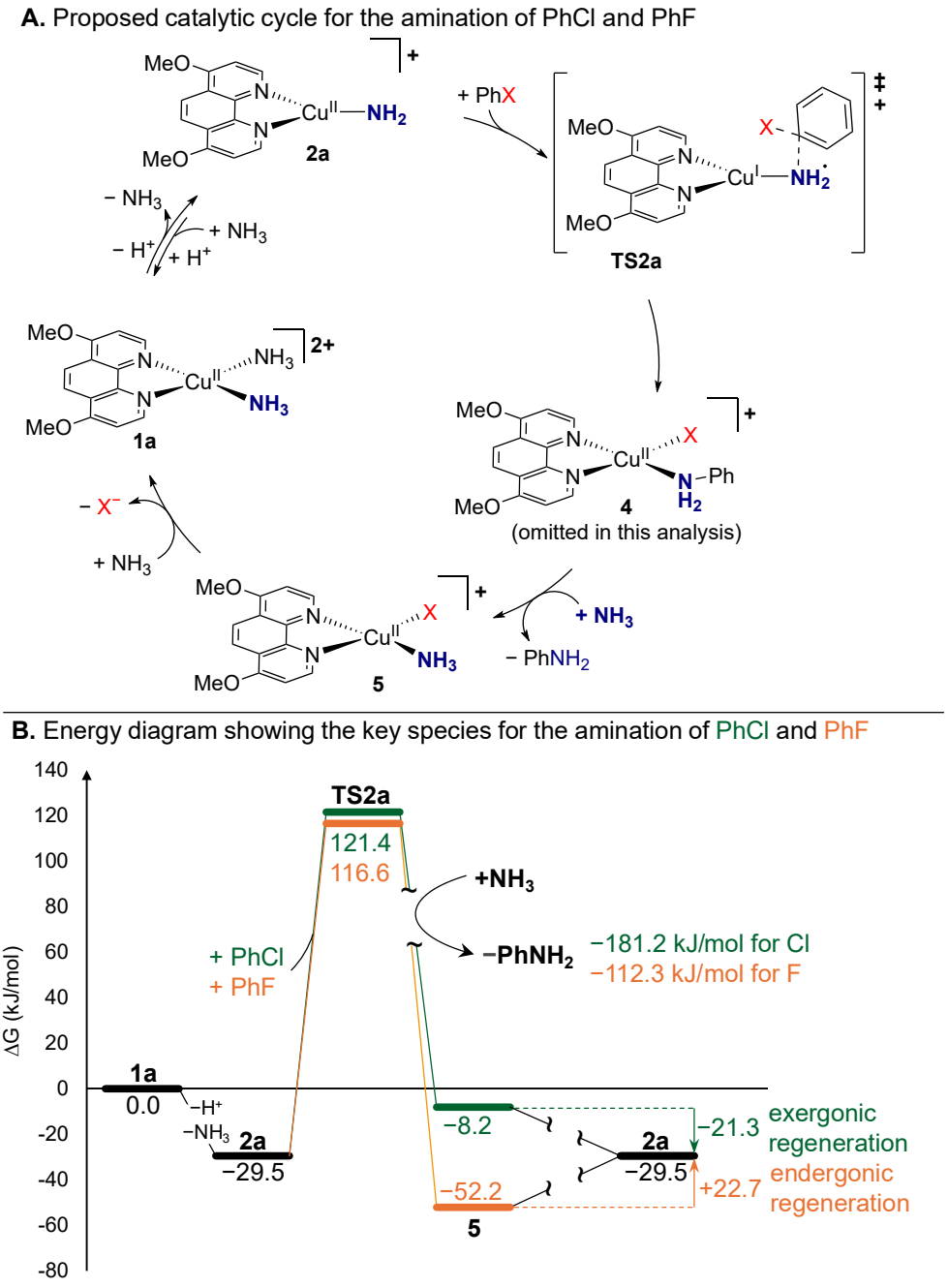

Figure 4.24: Transition state **TS2a** and selected key species for the amination of chlorobenzene (green) and fluorobenzene (orange); catalytic cycle (A) and energy diagram (B); complex **4** and **1a** of the second cycle are omitted for clarity; ΔG^{453} in kJ·mol^{-1}; ωB97x-D/def2-QZVPP//COSMO(∞)-TPSS-D3ZERO/def2-SVP; COSMO-RS (H_2O).

4.4.7 Benchmark of the Single Point Method

Since the treatment of open-shell systems with DFT is challenging, especially for 3*d* metals like copper,[222-223] a small benchmark was performed to identify a DFT method capable of providing reliable electronic energies. As a benchmark reaction, the amination of chlorobenzene by the deprotonated complex **2b** via **TS2b** was investigated.

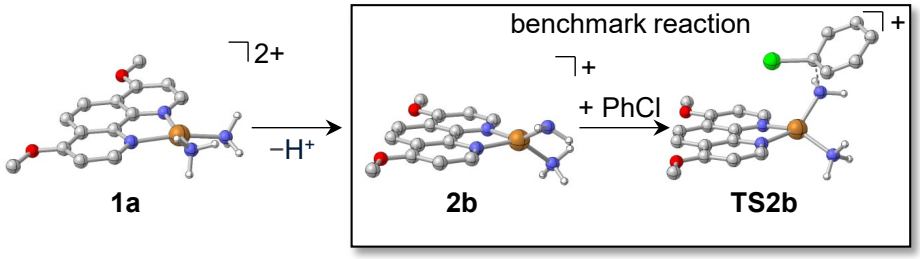

Figure 4.25: Model system for the benchmark; it should be noted that **2b** and **TS2b** act as a model compounds, while **2a** gives a lower activation energy via **TS2a** (compare Section 4.4.1); for the benchmark, only the effective activation energy between **TS2b** and **2b** was investigated.

For geometry optimizations, the robust[180] GGA functional TPSS was chosen. As a high-accuracy energy reference, auxiliary-field quantum Monte Carlo calculations (AFQMC)[224] were taken. AFQMC is particularly well-suited for electronically challenging cases like open-shell 3*d* metals.[196,225] Furthermore, DLPNO-CCSD(T)[203] coupled cluster calculations with TPSS reference wavefunction were performed. A variety of DFT functionals were tested. As a representative for GGA functionals, the DFT functional of the geometry optimization was chosen (TPSS). Furthermore, single point calculations with three hybrid functionals (TPSSh,[179,197] B3LYP,[198-200] PBE0[201]) as well as two range-separated hybrid functionals (ωB97x-D, CAM-B3LYP[202]) were performed (Table 4.4).

The GGA TPSS (Entry 1) yields the lowest activation energy for the model transition state, and with that also the strongest deviation from the high accuracy benchmark energy of AFQMC (Entry 8). Among the hybrid functionals (Entries 2–6), an increase in Hartree-Fock exchange is associated with higher activation energies. In addition, spin contamination also rises with higher Hartree-Fock exchange, as shown by increasing $\langle S^2 \rangle$ values. However, $\langle S^2 \rangle$ values of up to 0.8 are within the acceptable range despite deviating from the ideal 0.75. The range-separated hybrids (Entries 5–6) align best with the benchmark energy. CAM-B3LYP matches AFQMC's barrier closely, but the functional is rather optimized for the simulation of UV-vis spectra than for electronic energies.[202] ωB97x-D slightly overestimates the activation barrier with an $\Delta E_{A,gas}$ of 94.0 kJ·mol^{-1} compared to 87.4±4.9 kJ·mol^{-1}, yet the functional is also literature-known to produce accurate energies also in electronically difficult cases.[181-182] Consequently, ωB97x-D was chosen as the single point method.

Table 4.4: Benchmarking of the activation barrier for the S_NAr of PhCl with **2b** as catalyst; it should be noted that while **2b** acts as a model compound for this benchmark, **2a** gives a lower activation energy (compare Section 4.4.1); $\Delta E_{A,gas}$ of **TS2b** relative to **2b** in $kJ \cdot mol^{-1}$ in gas phase, as well as $<S^2>$, and % Hartree-Fock (HF) exchange (SR for short range HF exchange and LR for long range HF exchange); the AFQMC calculations served as highly accurate reference energies and were performed by Dr. Michael Kühn (BASF SE); for all DFT-calculations the D3ZERO dispersion correction was used, with the exception of the ωB97x-D functional, where the default correction was employed.

Entry	Level of theory	$\Delta E_{A,gas}$ (**TS2b**) ($kJ \cdot mol^{-1}$)	$<S^2>$ (**TS2b**)	% HF exchange
1	TPSS-D3ZERO/def2-QZVPP	48.2	0.76	0%
2	TPSSh-D3ZERO/def2-QZVPP	59.5	0.77	10%
3	B3LYP-D3ZERO/def2-QZVPP	72.4	0.77	20%
4	PBE0-D3ZERO/def2-QZVPP	72.9	0.78	25%
5	CAM-B3LYP-D3ZERO/def2-QZVPP	90.8	0.80	19% SR 65% LR
6	ωB97x-D/def2-QZVPP	94.0	0.79	16% SR 100% LR
7	DLPNO-CCSD(T)/3-4 CBS(TPSS)	76.5	0.75	–
8	AFQMC	87.4±4.9	–	–

With a deviation of 10.9 $kJ \cdot mol^{-1}$, the DLPNO-CCSD(T) coupled cluster calculation underestimates the activation barrier significantly. A standard PNO grid was utilized, and a complete basis set extrapolation (TZ–QZ) was conducted. Initial attempts using Hartree-Fock reference wavefunctions revealed significant spin delocalization; consequently, a TPSS reference wavefunction was employed (Figure 4.26). The significant deviation from the highly accurate AFQMC activation energy could indicate a problem in the description of the open-shell Cu^{II} center in the DLPNO-CCSD(T) calculation.

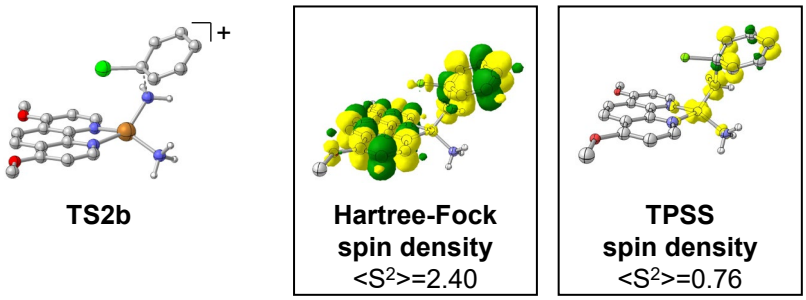

Figure 4.26: Comparison of the spin densities of **TS2b** on Hartree-Fock and on TPSS level of theory; spin density isosurfaces at ±0.005 $a_0^{-3/2}$; excess spin α shown in yellow and ß shown in green.

4.5 Summary and Outlook

For all calculations, chlorobenzene was used as a model system. The evaluation of different coordination geometries of Cu^{II}-phenanthroline complexes revealed that the square planar *bis*-ammine-*mono*-phenanthroline form (**1a**) is predicted to be in equilibrium with a square-pyramidal (**1b**) or trigonal-bipyramidal *tris*-ammine complex (**1c**). Water coordination was found to be unfavorable. A potential drawback of the DFT method in the geometry optimization was uncovered, since the optimization of long-distance (roughly 2.9 Å) coordinating axial solvent molecules was not found, and all molecules were always bound as ligands (shorter than 2.5 Å), contrary to literature reports.[212-214]

It was shown that **1a** can undergo an exergonic deprotonation. The resulting Cu^{II}-amido complex **2a** likely features a trigonal-planar coordination environment with a significant Cu–NH_2 π-bond character. Analysis of the spin density revealed a reduced spin population on the copper center. Mechanistic investigations indicated an S_NAr reaction in which the Cu^{II}-amido complex **2a** serves as the active catalyst. In the transition state, the spin density at the copper center vanishes due to strong delocalization. Thus, the attack was considered a radical-mediated S_NAr reaction with effectively a Cu^{I}-aminyl complex. After the transition state, however, all intermediates were shown to have clear Cu^{II} character.

Control experiments were performed to find experimental indications for the Cu^{II}-amido complex in solution. A characteristic LMCT band was found in UV-vis-NIR titration experiments. The origin of this band was shown to be a π to π* transition of the Cu–NH_2 π-bond. EPR experiments coupled with *EasySpin* and DFT simulations indicated an equilibrium with a species with a low Cu-hyperfine coupling, in line with a deprotonated complex featuring a reduced spin population on the copper center (**2a**).

Unlike typical uncatalyzed S_NAr reactions, where C–F is more reactive than C–Cl upon amination, our system showed an opposite trend: PhF was not converted in the catalysis, while PhCl was reactive. DFT calculations indicate that, for fluorobenzene, the effective free energy of activation for the first catalytic cycle is slightly lower than for chlorobenzene; however, the subsequent formation of the fluorido-bound intermediate **5** constitutes a thermodynamic sink, leading to catalyst deactivation.

To ensure accurate electronic energies, a method evaluation was conducted to identify a suitable DFT functional for single point calculations. Among the tested functionals, range-separated hybrid functionals performed best; therefore, the ωB97x-D functional was selected.

The computational results could guide future ligand optimizations to improve catalytic efficiency at lower temperatures by tailoring the electronic properties of the Cu^{II}-amido complex to facilitate its conversion to a Cu^{I}-aminyl species for the radical-mediated S_NAr reaction.

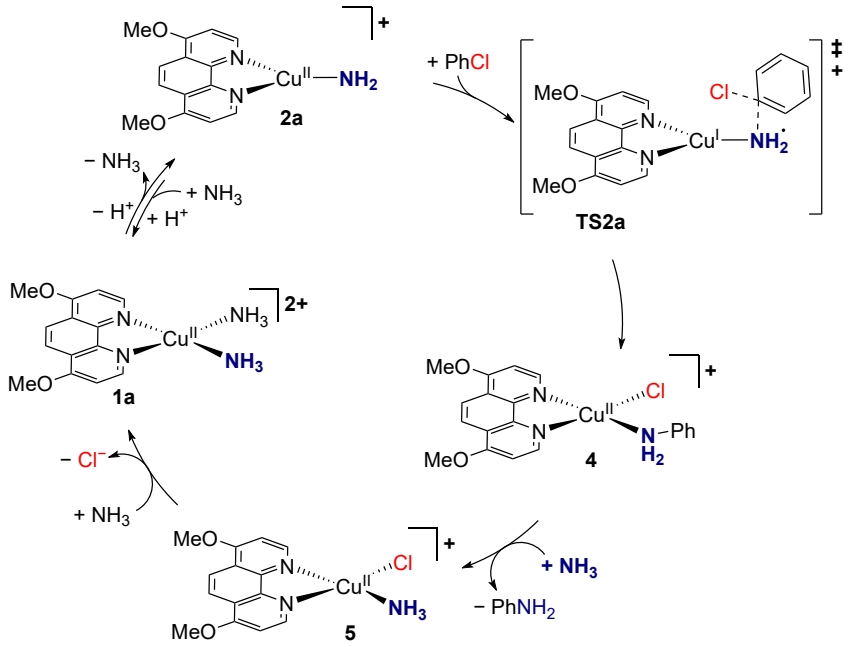

Figure 4.27: Proposed catalytic cycle and energy diagram for the amination of chlorobenzene via a radical-mediated S_NAr reaction.

5

Cu^{I}-Catalyzed Alkynylations

Reproduced in part from Leo Saputra, Philipp D. Engel, Frank Bienewald, Grigory A. Shevchenko, Ansgar Schäfer, Peter Deglmann, Peter Comba, A. Stephen K. Hashmi, Thomas Schaub, Jaroslaw Mormul, *manuscript in preparation* **2025**.[226]

All experiments presented were conducted by Leo Saputra.

Note: The numbering of calculated and experimental structures restarts at the beginning of each chapter.

5.1 Motivation and Goal

Propargyl alcohol (PA) is a useful building block in organic synthesis, e.g., in the formation of heterocyclic compounds[227-232] or as a corrosion inhibitor.[233] Since the early 1900s, the alkynylation of carbonyl compounds has been widely used to synthesize PAs.[234] Despite PA being the industrially most relevant alkynyl alcohol derivative,[235] it is only produced as a byproduct in the large-scale synthesis of 1,4-butynediol (BYD).[236] Until a few years back, all known examples for its synthesis either resulted in bad selectivities,[236] needed stoichiometric amounts of base,[237-238] or used unstable catalysts.[239] A prior publication by researchers at CaRLa showed a promising Cu^{I} catalyst with a good selectivity; however, an expensive and air-sensitive ligand was used.[240]

Based on this publication, the objective of this project was to optimize the catalytic system to function efficiently with more cost-effective and air-stable ligands. A Cu^{I}-phenylacetylide precursor with cheap and air-stable phenanthroline ligands efficiently and selectively converts both phenylacetylene (PhAC) and acetylene (AC) with formaldehyde to the corresponding propargyl alcohols. PhAC was used for experimental condition optimization and mechanistic investigations, because of the easier handling as a liquid compared to the gas acetylene.

This chapter describes the computational investigation aimed at further explaining and complementing the experimental findings for both the model substrate and AC. The first objective is to benchmark single point methods to ensure accurate relative energies for the complexes. A further focus is the analysis of the coordination chemistry in solution, with particular attention to the comparison between mononuclear and dinuclear species. Finally, different mechanistic pathways are evaluated in order to identify the most plausible reaction mechanism.

5.2 Experimental Background

PA is industrially produced only as a side product, with a yield of 1-2%, in the production of 1,4-butynediol from AC and formaldehyde using a heterogeneous catalyst.[236] Walter Reppe first described this process in 1955 (Figure 5.1A),[241] and it is still used today with minimal changes.[242] Even when applying a higher AC pressure and lower formaldehyde concentration, only a PA yield of 5% can be achieved.[235]

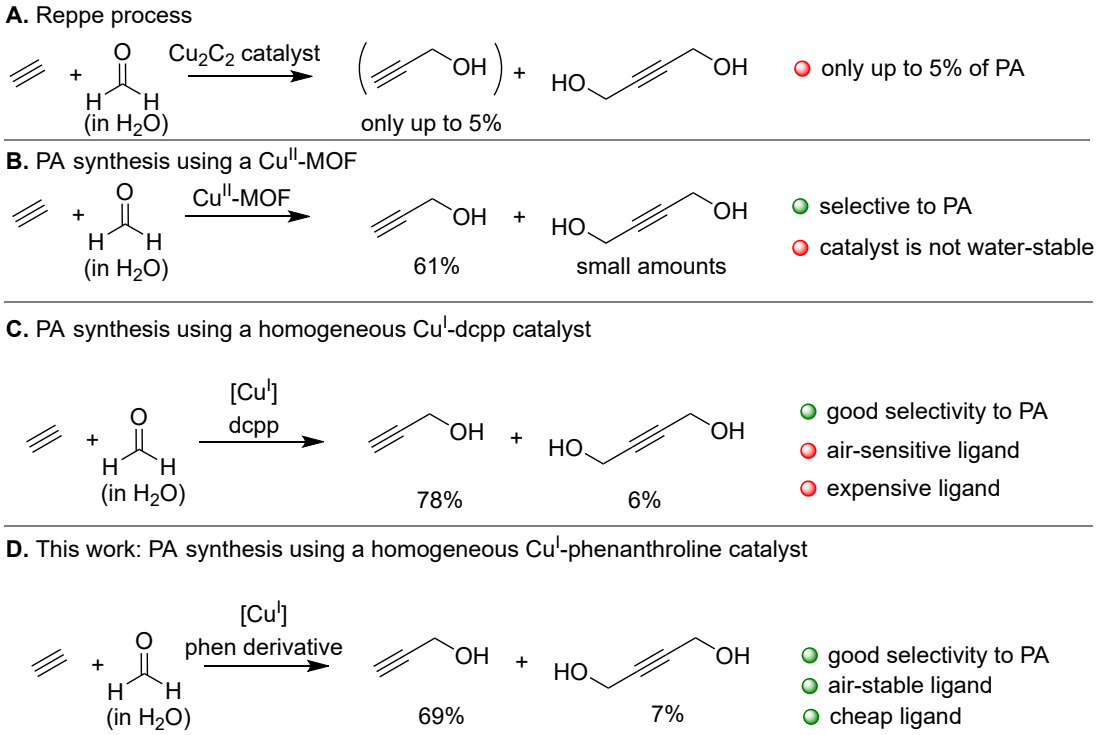

Figure 5.1: Selected literature reports for the synthesis of propargyl alcohol using a heterogeneous Cu_2C_2 catalyst (A),[236] a Cu^{II} metal-organic framework (B),[239] a homogeneous Cu^{I}-dcpp catalyst (C),[240] and a homogeneous Cu^{I}-phenanthroline catalyst (D);[226] dcpp = 1,3-*bis*(dicyclohexylphosphino)-propane; phen derivative in this example is 1,10-phenanthroline.

Different routes either used stoichiometric amounts of base[237-238] or resulted in only moderate yields.[243] Additionally, significant salt waste is generated, making it unsuitable for industrial use.[240,243] More recently, a Cu^{II} metal-organic framework (MOF) demonstrated high efficiency in the ethynylation of aqueous formaldehyde, achieving a good PA yield of 61% with only minor formation of BYD side-product (Figure 5.1B). However, this catalyst could not be recovered because it was sensitive to water.[239] A previous report by CaRLa used AC at atmospheric pressure for the alkynylation of aqueous formaldehyde with a base-free homogeneous Cu^{I} catalyst (Figure 5.1C). Using the bisphosphine ligand dcpp (1,3-bis(dicyclohexylphosphino)propane), a good yield of 69% to PA was found with 21% of BYD as byproduct.[240] However, the applied bisphosphine ligand is costly and air-sensitive. For industrial purposes, a more cost-effective and air-stable alternative is preferred.[244]

In this project, a catalytic system was developed at CaRLa to address this challenge by replacing the bisphosphine ligand with phenanthrolines, which are less expensive and resistant to air. Furthermore, the bisphosphine ligand is water-sensitive, preventing effective catalyst regeneration. PhAC was chosen as the model substrate for preliminary screening due to its liquid state, which facilitates handling compared to gaseous AC. The corresponding product is 3-phenyl-2-propin-1-ol (phenyl propargyl alcohol, PPA). A variety of (mainly) N-donor ligands were tested, resulting in yields of up to 98% (**L2**); a selection is shown in Figure 5.2. The introduction of methyl groups adjacent to the nitrogen atoms resulted in no conversion (**L3**), indicating that steric factors around the nitrogen atoms affect the outcome.

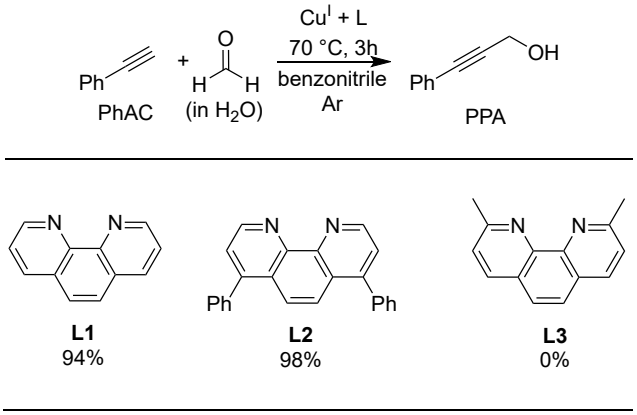

Figure 5.2: Examples from the ligand screening of different phenanthrolines for the alkynylation of formaldehyde, using PhAC as substrate; *Reaction conditions*: Cu^{I}-phenylacetylide as copper source 0.025 mmol (10 mol%, 5 mM), ligand 0.1 mmol, PhAC 0.25 mmol, H_2CO/H_2O (37 wt%) 0.5 mmol (2 e.q.), benzonitrile 5 mL, 70 °C, 3 h, Ar.

Besides the ligand, different metal precursors were screened. It was shown that Cu^{II} precursors did not yield active catalysts. The best results were achieved using Cu^{I}-phenylacetylide with a phenanthroline ligand, prepared either *in situ* or as a preformed complex. The optimized conditions were then transferred to the ethynylation of formaldehyde, the reaction in which acetylene is used as alkyne. For this starting material, various phenanthroline ligands were assessed, with selected examples shown in Figure 5.3.

A selectivity for PA of up to 89% (**L4**, PA yield 69%) was reached. The unsubstituted phenanthroline (**L1**) produced a lower yield but maintained an equally high selectivity of 73%. Similar to the alkynylation using PhAC as substrate, the dimethyl-substituted ligand next to the nitrogen atoms gave no conversion (**L3**). Based on these experimental results, DFT calculations were performed to get insights into the reaction mechanism of the alkynylation. Unsubstituted phenanthroline (**L1**) was used for all computations.

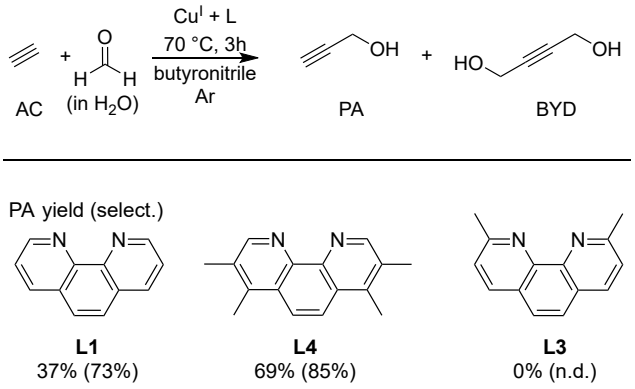

Figure 5.3: Examples from the ligand screening of different phenanthrolines for the ethynylation of formaldehyde; *Reaction conditions*: Cu^{I}-phenylacetylide as copper source 0.025 mmol (1.25 mol%, 5 mM), ligand 0.1 mmol, AC (sat. solution, ca. 2.0 mmol), H_2CO/H_2O (37 wt%) 2.7 mmol (1.35 e.q.), butyronitrile 5 mL, 100 °C, 3 h, Ar.

5.3 Computational Details

Geometry optimizations and Hessian calculations were performed using the TURBOMOLE program package (version 7.5.2).[133] The GGA functional TPSS[179] was applied together with the def2-SVP[135] basis set and Grimme's D3 dispersion correction, including a three-body term and zero-damping.[136] Solvation effects were included during geometry optimization with the COSMO model using default parameters and an infinite dielectric constant.[24] Verification of stationary points was achieved through analysis of vibrational frequencies at the same level of theory. Final electronic single point energies were calculated employing the range-separated hybrid functional ωB97x-D[146-147] in combination with the def2-QZVPP[135,138] basis set. The RI approximation,[139-142] along with the appropriate auxiliary basis sets, was used throughout all computations.

Thermochemical corrections to calculate Gibbs free energies were obtained at the level of theory of the geometry optimization (T = 343.15 K, p = 1 bar). Solvation corrections were determined using the COSMO-RS model[26,28] implemented in COSMOtherm (Version 18.0.0; Revision 4360).[143] This was performed for infinite dilution in acetonitrile, applying the FINE parametrization and a reference state of 1 mol·L^{-1} at 343.15 K. Connections between transition states and adjacent minima were confirmed by following the transition mode and subsequent geometry optimization. Barrierless reactions were validated by relaxed potential energy surface scans. Visualizations of molecular structures were generated with Cylview[183], and molecular orbital representations were produced using Chemcraft.[184] For clarity, all C–H hydrogen atoms are omitted in the figures except those of formaldehyde.

Exploration of reaction pathways was conducted using the MGSM approach[37-39] in combination with a precomplex builder routine.[40] Conformational sampling for all intermediates and transition states was performed with the CREST[15-16] program package developed by Grimme and co-workers. Selected structures were further refined by DFT optimization and single point energy calculation to establish a consistent ranking of relative Gibbs free energies. For clarity, only the most stable conformers are discussed and shown in the figures.

For molecular orbital diagrams, single point calculations were carried out in ORCA[185-187] (version 5.0.4) using the ωB97x-D functional together with the def2-TZVP[135] basis set. Implicit solvation was described using CPCM[188] with acetonitrile as solvent.

Dispersion interactions were visualized using the London dispersion component obtained from a local energy decomposition (LED)[245-246] analysis. Dispersion interaction density (DID)[247-248] plots were generated and mapped onto the electron density. For this purpose, domain-based local pair-natural orbital coupled-cluster (DLPNO-CCSD)[203] single point calculations were carried out in ORCA[185-187] (version 5.0.4) using the cc-pVTZ[193-195] basis set and associated auxiliary basis sets.[204-205] *TightSCF* and *NormalPNO* settings were applied. Noncovalent interaction (NCI) plots were created with MultiWFN.[249] For the benchmark study, DLPNO-CCSD(T)[203] calculations were performed with the cc-pVTZ[193-195] and the cc-pVQZ[193-195] basis sets employing a two-point complete basis set extrapolation.

5.4 Results and Discussion

5.4.1 Benchmark of the Single Point Method

The robust and well-tested[180] GGA TPSS was applied for geometry optimizations in this project. A small benchmark study was conducted (Table 5.1) to select an appropriate DFT functional for accurate single point energies. For this purpose, the activation energy for the insertion of formaldehyde into the Cu^{I}–phenylacetylide bond was evaluated by applying different single point methods. For all single points, the def2-QZVPP basis set along with the D3ZERO dispersion correction was used, except for ωB97M-V and ωB97x-D, where the implemented[146-147] dispersion correction was applied. For accurate benchmark energies, a DLPNO-CCSD(T) calculation was performed, with a two-point complete basis set extrapolation (TZ–QZ) and using a *normal* PNO-grid. A variety of DFT functionals were applied, including three GGA (BP86,[144-145] TPSS, BLYP[144,250]) and five hybrid functionals (TPSSh,[179,197] PBE0,[201] B3LYP,[198-200] ωB97M-V,[251] ωB97x-D).

Table 5.1: Benchmark of the single point method; activation barrier for the insertion of formaldehyde into the Cu–C(phenylacetylide) bond; it should be noted that while **TS1** is the model for this benchmark, this TS is not in the final lowest energy reaction pathway (compare Section 5.4.3); for all DFT-calculations the D3ZERO dispersion correction was used, only for the functional ωB97x-D and ωB97M-V the functional-specific dispersion correction were employed; sorted in ascending order of Gibbs free energy of activation; geometry optimization: COSMO(∞)-TPSS-D3ZERO/def2-SVP.

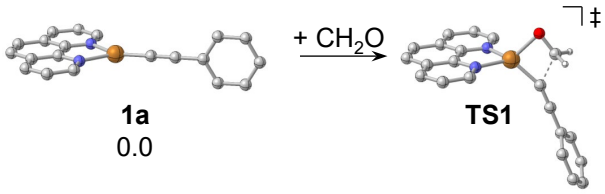

Entry	Singlepoint Method	ΔG‡ (**TS1**) (kJ·mol^{-1})
1	BP86/def2-QZVPP	85.2
2	TPSS/def2-QZVPP	86.0
3	TPSSh/def2-QZVPP	93.3
4	PBE0/def2-QZVPP	100.0
5	BLYP/def2-QZVPP	113.2
6	B3LYP/def2-QZVPP	122.9
7	ωB97M-V/def2-QZVPP	126.0
8	ωB97x-D/def2-QZVPP	128.2
9	DLPNO-CCSD(T)/CBS-3/4	134.6

The GGA functionals BP86 (deviation of 49.4 kJ·mol^{-1}, Entry 1) and TPSS (deviation of 48.6 kJ·mol^{-1}, Entry 2) predict the lowest Gibbs free energies of activation, resulting in the largest discrepancies from the more accurate benchmark DLPNO-CCSD(T) reference calculation. While the GGA functional BLYP demonstrates improved accuracy with a lower deviation of 21.4 kJ·mol^{-1}, its performance remains unsatisfactory. Similarly, the hybrid functionals TPSSh and PBE0 exhibit limited accuracy, with deviations of 41.3 kJ·mol^{-1} (Entry 3) and 34.6 kJ·mol^{-1} (Entry 4), respectively. B3LYP deviates by 11.7 kJ·mol^{-1}, which falls within the typically acceptable[252] accuracy range for DFT functionals (2–3 kcal·mol^{-1} ≙ 8.4–12.6 kJ·mol^{-1}). Only the range-separated hybrid functionals ωB97M-V and ωB97x-D, with 8.6 kJ·mol^{-1} and 6.4 kJ·mol^{-1}, get closer to the DLPNO-CCSD(T) calculation. Based on these results, the best-performing functional ωB97x-D was selected for single point calculations.

5.4.2 Coordination Chemistry of Cu^{I}-Phenylacetylide

The mononuclear Cu^{I}-phenylacetylide complex features a trigonal planar coordination geometry (**1a**, Figure 5.4). While axial formaldehyde coordination (d(Cu–O) = 2.33 Å) is unfavorable with an increase in free energy of 36.8 kJ·mol^{-1} (**1b**), this complex may play a role as an intermediate in coordinating formaldehyde prior to a reaction. Upon simplifying the nitrile solvent to acetonitrile, no nitrile-coordinated complex was found. A dinuclear complex is slightly lower in free energy (**1c**, −1.6 kJ·mol^{-1}) than the mononuclear complex and is predicted to be in equilibrium with the mononuclear species.

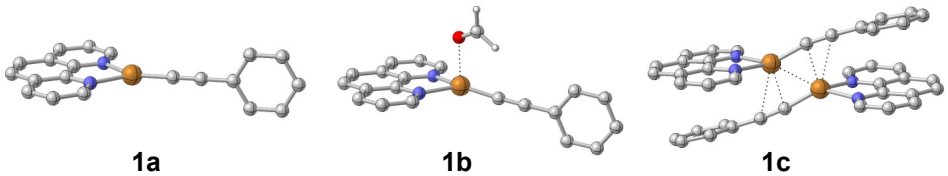

Figure 5.4: Selected key structures of **1**; ΔG^{343} in kJ·mol^{-1}; ωB97x-D/def2-QZVPP//COSMO(∞)-TPSS-D3ZERO/def2-SVP; COSMO-RS (MeCN).

Experimental DOSY-NMR studies supported this hypothesis, showing a good agreement with the molecular weight of the dinuclear complex in solution. Temperature-dependent NMR investigations revealed a temperature dependency of the equilibrium between **1a** and **1c** with a preference for the mononuclear species at higher temperatures. This is in line with the close free energies (difference of only −1.6 kJ·mol^{-1}).

The computed geometry of the dinuclear complex **1c** features a bent bonding of the phenylacetylide units. This bending does not appear in the crystal structure of a similar dinuclear complex with a bulky bisphosphine ligand previously published (Figure 5.5).[240] A fundamental difference between the complexes is the steric bulk. While the phenanthroline ligands are planar, the bisphosphine ligand features bulky cyclohexyl

substituents, prohibiting a bent structure. Additionally, unlike phenanthroline, the bisphosphine ligand lacks an aromatic backbone.

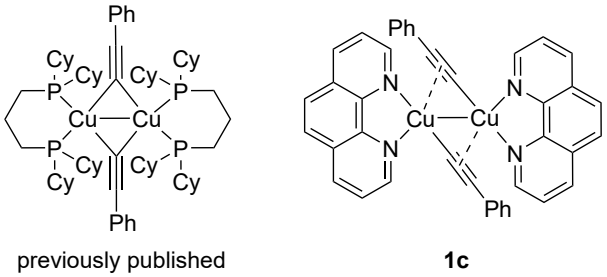

Figure 5.5: Comparison of the binding modes in the previously published[240] crystal structure of a dinuclear complex with bisphosphine ligands and the DFT-computed geometry of **1c**; COSMO(∞)-TPSS-D3ZERO/def2-SVP.

This clarifies why the published complex does not exhibit a bent binding mode, the cause of the bending observed with phenanthroline was not clear. Consequently, a detailed investigation was carried out to determine the source of the bending. The electronic structure of **1c** was analyzed to identify interactions that may stabilize the bent coordination (Figure 5.6).

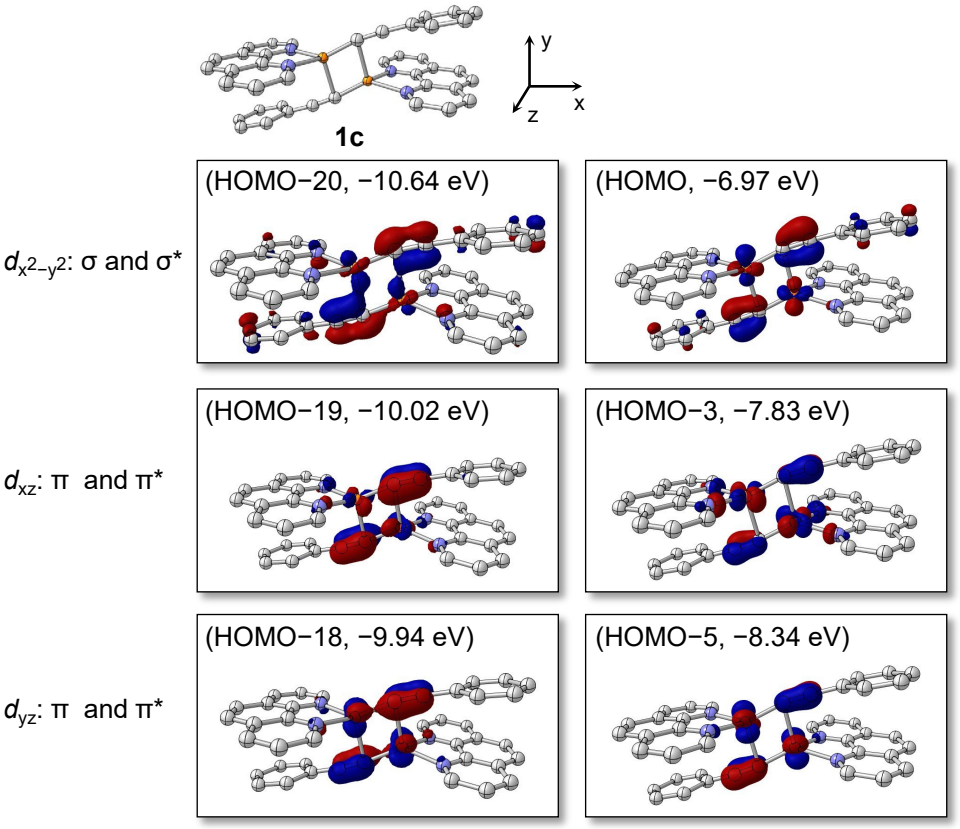

Figure 5.6: Selected canonical molecular orbitals of the dinuclear complex **1c**; isosurfaces at ±0.05 $a_0^{-3/2}$; CPCM(MeCN)-ωB97x-D/def2-TZVP//COSMO(∞)-TPSS-D3ZERO/def2-SVP.

All depicted interactions involve two doubly occupied molecular orbitals, specifically, the π-orbital of the C≡C bond and a copper-centered *d*-orbital. The interaction with the $d_{x^2-y^2}$ orbital is σ-symmetric. Both d_{xz} and d_{yz} interact in a π-symmetric fashion. However, the overlap for these interactions is rather low, which is why non-covalent interactions were also studied. In fact, substantial non-covalent interactions, mainly dispersion-driven, are observed in the dinuclear complex **1c** (Figure 5.7).

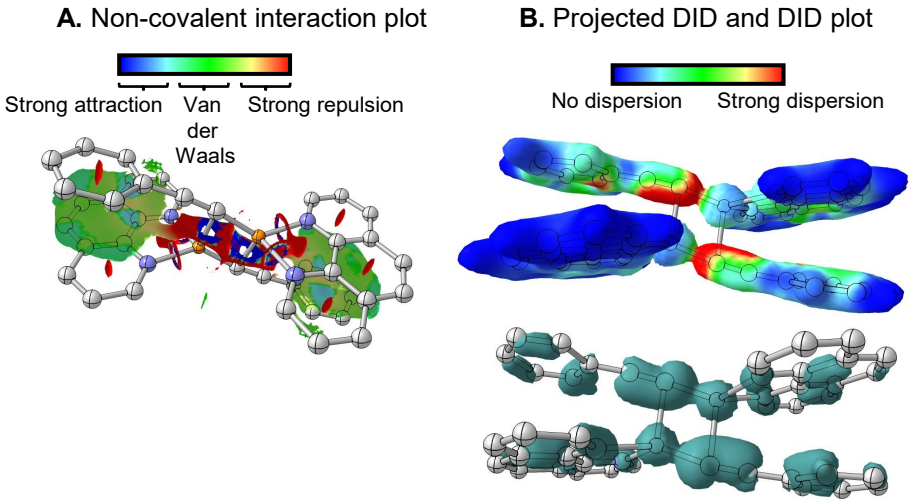

Figure 5.7: Non-Covalent-Interaction Plot (a) and projected dispersion interaction density (DID) as well as the DID plot for the dinuclear complex **1c** to show dispersion interactions; COSMO(∞)-TPSS-D3ZERO/def2-SVP geometries and DLPNO-CCSD/cc-PVTZ single point for the DID analysis.

The NCI plot (Figure 5.7A) shows Van-der-Waals interactions (depicted in green), specifically dispersive π-π-stacking, occurring between the phenyl substituent and the phenanthroline. The projection plot of the dispersion interaction density (DID) on the electron density (Figure 5.7B) provides additional support for this observation, since red regions at the phenyl ring and brighter regions in the middle of the phenanthroline are visible. A strong dispersion contribution is also observed around the C≡C triple bond, which may represent the dispersive component in its interaction with the copper centers. Notably, the combination of these two methods enables the interpretation of dispersion contribution on two different levels of theory: while the NCI analysis is based on the level of theory for the geometry optimization, the DID plot is based on a DLPNO-CCSD coupled cluster calculation. Consequently, for the NCI plots, dispersion is described using the empirical dispersion correction (D3ZERO), and for the DID plot via electron correlation[253] in the coupled cluster method.

Summing up, complex **1c** exhibits bending primarily because of its capability for π-π stacking interactions between the phenanthroline ligand and the phenyl ring. This interaction is not possible for the bisphosphine complex. Steric effects likely also affect the extent of bending. These factors account for the differences in coordination motifs observed between the phenanthroline and bisphosphine dinuclear complexes.

5.4.3 Mechanistic Investigations: Mononuclear Pathway

Experimental and computational results indicated an equilibrium between the mononuclear and dinuclear complexes. Accordingly, the mechanistic investigations assessed possible pathways involving both types of complexes.

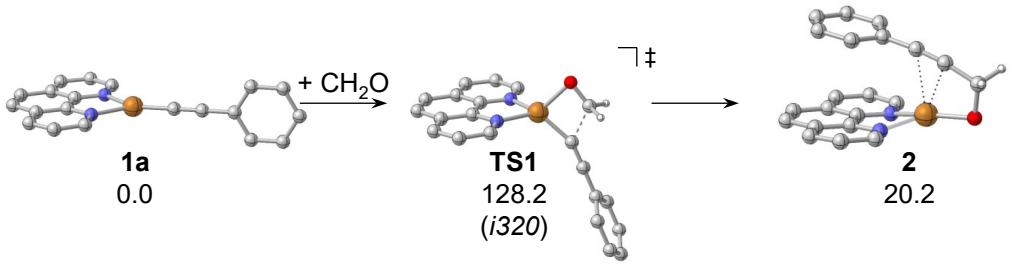

Figure 5.8: A direct insertion of formaldehyde into the Cu–C bond is not accessible; ΔG^{343} in kJ·mol^{-1}; ωB97x-D/def2-QZVPP//COSMO(∞)-TPSS-D3ZERO/def2-SVP; COSMO-RS (MeCN).

Insertion of formaldehyde into the Cu–C bond of the mononuclear complex is not accessible at the reaction temperature of 70 °C with a Gibbs free energy of activation of 128.2 kJ·mol^{-1} (Figure 5.8). To investigate further possible pathways with a mononuclear active compound, different phenylacetylide coordination modes were examined. The phenylacetylide unit can also coordinate in a side-on $\eta^2(\pi)$ fashion (Figure 5.9). Notably, this coordination is also encountered in a reported crystal structure.[254]

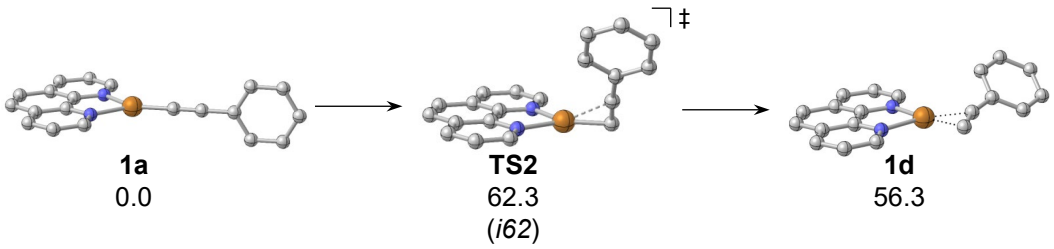

Figure 5.9: The phenylacetylide unit can coordinate side-on (**1d**) via **TS2**; ΔG^{343} in kJ·mol^{-1}; ωB97x-D/def2-QZVPP//COSMO(∞)-TPSS-D3ZERO/def2-SVP; COSMO-RS (MeCN).

Side-on coordination is with 56.3 kJ·mol^{-1} clearly endergonic and thus **1d** is not predicted to be detectable. **TS2**, representing the bend of the phenylacetylide, is with 62.3 kJ·mol^{-1} just slightly higher in free energy than intermediate **1d**. This moderate barrier is in line with a low-lying bending mode at 14 cm^{-1} in the mononuclear complex **1a**. The nucleophilic attack by the acetylide carbon atom in **1d** on formaldehyde results in a viable pathway at 70 °C (Figure 5.10).

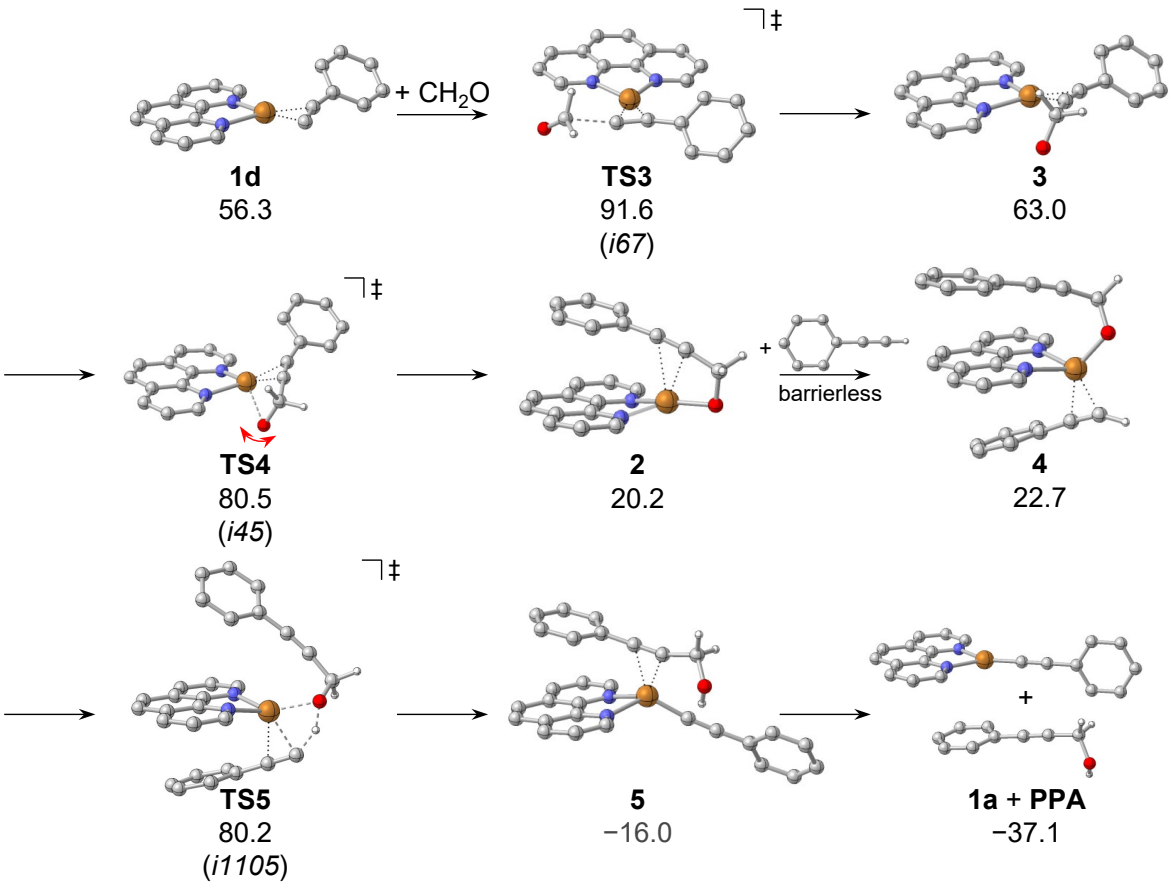

Figure 5.10: Reaction pathway for the nucleophilic attack of a side-on coordinated Cu^{I}-phenylacetylide unit in **1d** on formaldehyde; ΔG^{343} in kJ·mol^{-1} relative to **1a**; ωB97x-D/def2-QZVPP//COSMO(∞)-TPSS-D3ZERO/def2-SVP; COSMO-RS (MeCN).

The reaction proceeds via **TS3** (91.6 kJ·mol^{-1}) with an effective activation free energy of 93.2 kJ·mol^{-1} relative to the resting state **1c**, which is the rate-limiting transition state. The resulting intermediate **3** (63.0 kJ·mol^{-1}) features the same bonding motif as **1d** with an $\eta^2(\pi)$-bound propargyl alcoholate. An uncoordinated equivalent of PhAC can protonate the alkoxide to yield the product; however, this must proceed from the σ-bound phenylacetylide complex **2** to prevent the formation of a free carbanion. This rearrangement happens by rotation around the newly formed C–C bond (**TS4**). Addition of PhAC proceeds barrierless to **4**. A subsequent proton transfer exergonically yields the product-coordinated complex **5** (−16.0 kJ·mol^{-1}). Releasing the product and regenerating the starting complex further lowers the free energy to −37.1 kJ·mol^{-1}.

The high reactivity of the $\eta^2(\pi)$-coordinated complex **1d** can be rationalized by analyzing HOMO−1 (Figure 5.11). This molecular orbital shows the constrictive π-interaction between the C–C σ-orbital of phenylacetylide with the copper d_{yz} orbital. The σ-donor orbital is strongly polarized and points in the direction of the attacked formaldehyde carbonyl C in **TS3**, facilitating the nucleophilic attack on formaldehyde.

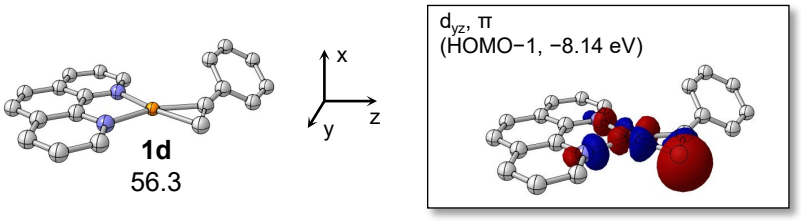

Figure 5.11: High-lying canonical donor orbital of **1d**; ΔG^{343} in kJ·mol^{-1} relative to **1a**; isosurfaces at ±0.05 $a_0^{-3/2}$; CPCM(MeCN)-ωB97x-D/def2-TZVP//COSMO(∞)-TPSS-D3ZERO/def2-SVP.

5.4.4 Mechanistic Investigations: Dinuclear Pathway

Having shown that the dinuclear complex **1c** is slightly lower in free energy than the mononuclear complex **1a**, **1c** was also considered as the active species. For simplification, the dinuclear complexes are shown as Lewis structures (Figure 5.12).

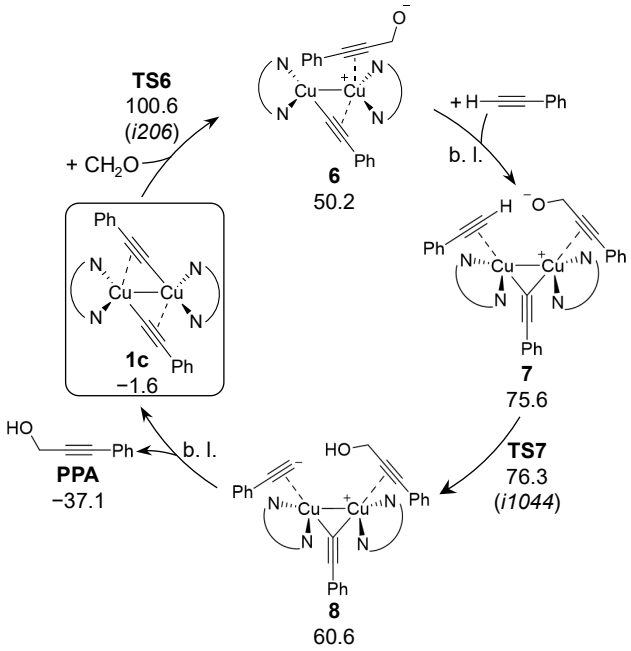

Figure 5.12: Proposed catalytic cycle with a dinuclear complex as active species (pathway B); barrierless transformations are abbreviated with b. l.; ΔG^{343} in kJ·mol^{-1} relative to **1a**; ωB97x-D/def2-QZVPP//COSMO(∞)-TPSS-D3ZERO/def2-SVP; COSMO-RS (MeCN).

The nucleophilic attack on formaldehyde occurs through **TS6** (100.6 kJ·mol^{-1}) with an effective barrier of 102.2 kJ·mol^{-1} relative to **1c**. This step is rate-limiting. The following intermediate **6** displays an $\eta^2(\pi)$-coordinated propargyl alcoholate, as also seen in the mononuclear species **3**. Barrierless addition of PhAC yields intermediate **7**. Interestingly, the geometry of **7** does not exhibit the bent binding motif of the unreacted phenylacetylide as observed in **1c**. This could be explained by the high steric pressure due to the coordination of PhAC. Protonation of the alcoholate by PhAC through **TS7** (76.3 kJ·mol^{-1}) yields the product (**PPA**: −37.1 kJ·mol^{-1}) in an exergonic step.

A comparison of pathway A, which involves a mononuclear active species, and pathway B, which involves a dinuclear active species, shows that the mononuclear pathway is favored by 9.0 kJ·mol^{-1}. Consequently, the dinuclear species is predicted to be the resting state, and the reaction is likely to undergo the pathway with the mononuclear complex **1a** as the active species. A competition between the pathways remains possible, given that the difference in free energy falls within the typical error margin of 8–12 kJ·mol^{-1}.[252] This results in the full catalytic cycle shown in Figure 5.13.

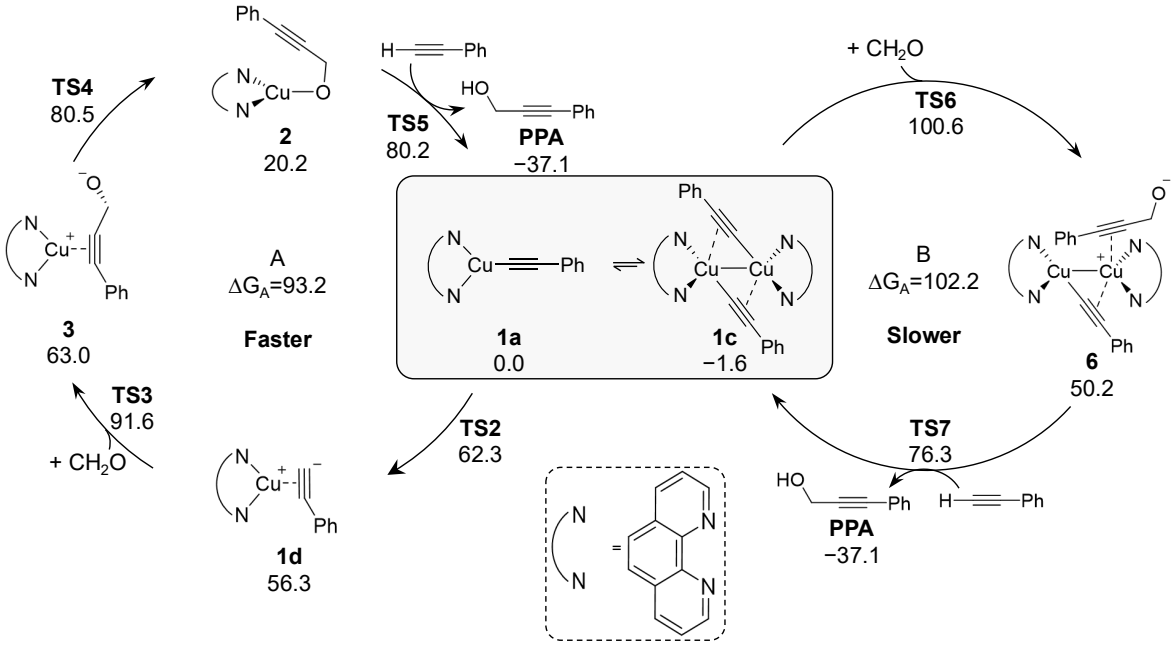

Figure 5.13: Proposed catalytic cycle with a mononuclear (pathway A) and a dinuclear complex as active species (pathway B); only the most important intermediates are shown; barrierless transformations are abbreviated with b. l.; ΔG^{343} in kJ·mol^{-1}; ωB97x-D/def2-QZVPP//COSMO(∞)-TPSS-D3ZERO/def2-SVP; COSMO-RS (MeCN).

5.4.5 Comparison of Different Substrates

Experimentally, various substrates besides formaldehyde (**S1**) were tested (Figure 5.14A). Of these, only the highly activated ketone 2,2,2-trifluoroacetophenone (**S2**) was successfully converted to the corresponding PPA derivative. In contrast, acetophenone (**S3**) and acetaldehyde (**S4**) showed no conversion. To study these substrate effects, the rate-limiting transition state (**TS3**) and the following intermediate **3** were calculated for these substrates (Figure 5.14B). Up to this point, the substrate designation (**S1** for formaldehyde) has been omitted for simplicity, as formaldehyde was the only substrate discussed. With the introduction of additional substrates, explicit notation is now used.

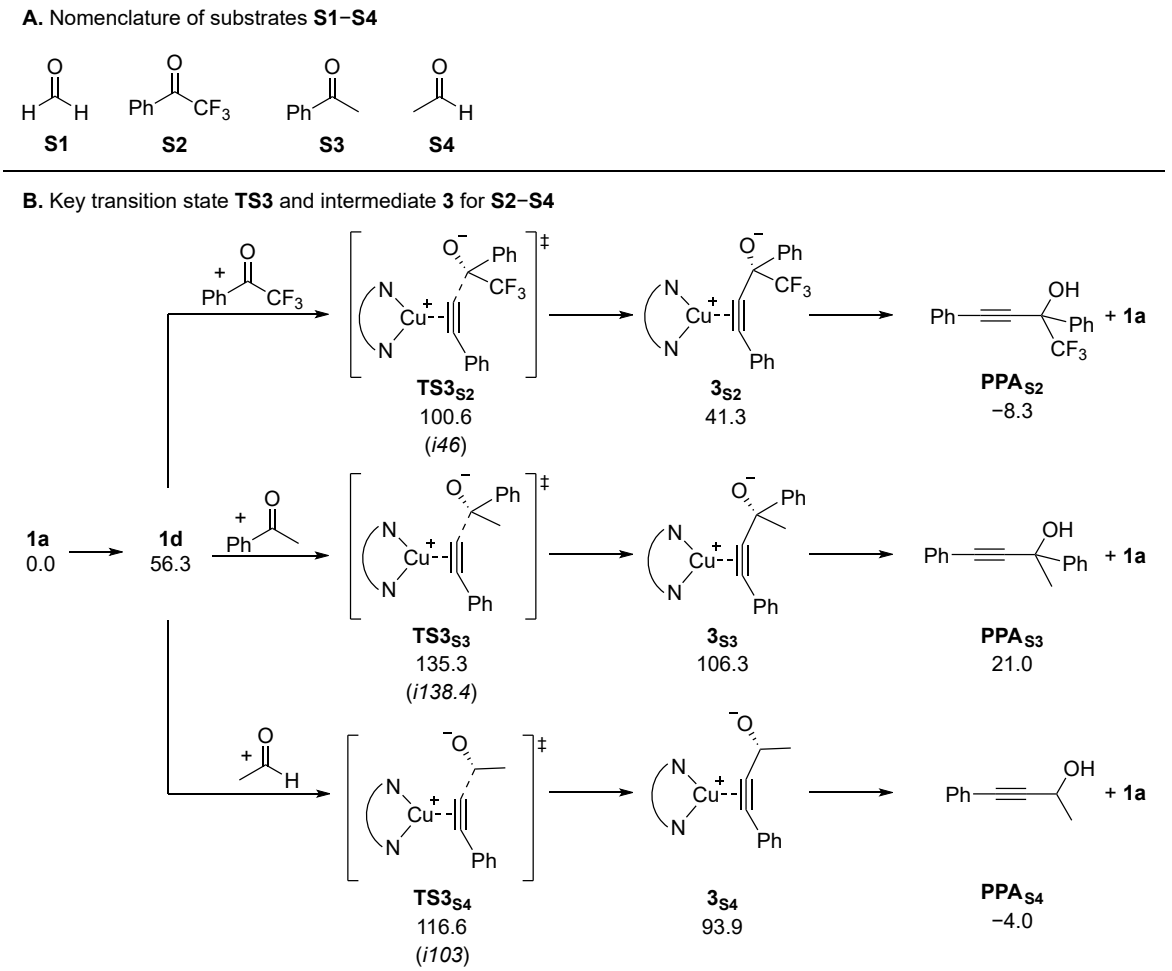

Figure 5.14: Nomenclature (A) of the substrates formaldehyde (**S1**), 2,2,2-trifluoroacetophenone (**S2**), acetophenone (**S3**), and acetaldehyde (**S4**); pathways for the alkynylation starting from the mononuclear complex **1a** (B); **1d** is the reactive intermediate, in which the phenylacetylide is coordinated side-on; ΔG^{343} in kJ·mol^{-1}; ωB97x-D/def2-QZVPP//COSMO(∞)-TPSS-D3ZERO/def2-SVP; COSMO-RS (MeCN).

The free energy of the transition state for the nucleophilic attack of the acetylide carbon atom on the carbonyl carbon in **S2** (**TS3$_{S2}$**: 100.6 kJ·mol^{-1}, G_A relative to **1c**: 102.2 kJ·mol^{-1}) is higher than that for formaldehyde (**TS3$_{S1}$**: 91.6 kJ·mol^{-1}, G_A = 93.2 kJ·mol^{-1}). Nevertheless, it remains accessible at a reaction temperature of 70 °C. It is noteworthy that intermediate **3$_{S2}$** (41.3 kJ·mol^{-1}) shows a significantly lower free energy than in the case of **S1** (**3$_{S1}$**: 63.0 kJ·mol^{-1}). The thermodynamic driving force for the product formation is much lower for **S2** (PPA_{S2}: −8.3 kJ·mol^{-1}) compared to **S1** (PPA_{S1}: −36.1 kJ·mol^{-1}). The transition state for the nucleophilic attack on **S3** (**TS3$_{S3}$**: 135.3 kJ·mol^{-1}, G_A = 136.9 kJ·mol^{-1}) is not accessible at the given conditions. Furthermore, product formation is strongly endergonic (PPA_{S3}: 21.0 kJ·mol^{-1}), preventing the reaction. For acetaldehyde (**S4**), the effective activation free energy (**TS3$_{S4}$**: 116.6 kJ·mol^{-1}, G_A = 118.2 kJ·mol^{-1}) is slightly too high to be easily accessible at 70 °C. Additionally, the free energies of the starting materials and product are nearly isoenergetic (PPA_{S4}: −4.0 kJ·mol^{-1}), providing only a minimal thermodynamic driving force for product formation.

These results are consistent with the experimental observation that product formation occurs only when formaldehyde or an activated substrate such as **S2** is used. For acetophenone (**S3**), product formation is limited by kinetic and thermodynamic factors. In contrast, for acetaldehyde (**S4**), the reaction is primarily hindered by kinetic factors, however, the thermodynamic driving force is also very small. Consequently, even the use of an alternative or optimized catalyst that affects reaction kinetics is unlikely to enable product formation in the case of **S3** or **S4**.

5.4.6 Ethynylation

The learnings from the model system PhAC were transferred to AC to study the competition between the formation of PA and BYD. Thermodynamically, BYD is favored over PA (PA: −66.3 kJ·mol^{-1}, BYD: −104.1 kJ·mol^{-1}). Assuming a similar reactivity as for PhAC, the most relevant intermediates and transition states for a pathway involving mononuclear species were calculated (Figure 5.15).

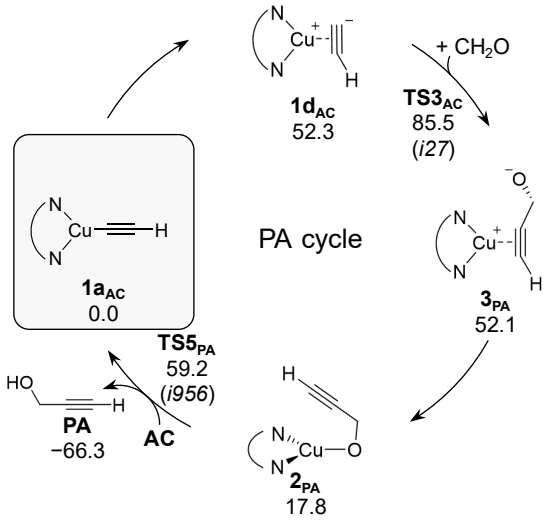

Figure 5.15: Catalytic cycle with key transition states and intermediates for the generation of PA; ΔG^{343} in kJ·mol^{-1}; ωB97x-D/def2-QZVPP//COSMO(∞)-TPSS-D3ZERO/def2-SVP; COSMO-RS (MeCN).

The Cu^{I}-acetylide complex, similar to Cu^{I}-phenylacetylide, features an $\eta^2(\pi)$ side-on coordinated intermediate at a moderate free energy of 52.3 kJ·mol^{-1} (**1d$_{AC}$**). The nucleophilic attack on formaldehyde occurs with a Gibbs free activation energy of 85.5 kJ·mol^{-1} (**TS3$_{AC}$**). The $\eta^2(\pi)$-coordinated propargyl alcoholate complex (**3$_{PA}$**) can undergo isomerization to an O-bound form (**2$_{PA}$**) in which the alcoholate coordinates through its oxygen atom. Subsequent protonation by AC via **TS5$_{PA}$** yields the product and regenerates the starting complex (Figure 5.16, top). This step has a lower activation barrier than the nucleophilic attack on formaldehyde via **TS3$_{AC}$**, making **TS3$_{AC}$** the rate-limiting transition state, similar to the cycle with PhAC. Alternatively, an already synthesized PA equivalent can protonate the alcoholate in place of AC (Figure 5.16, bottom). This competition gives access to a pathway for the formation of BYD.

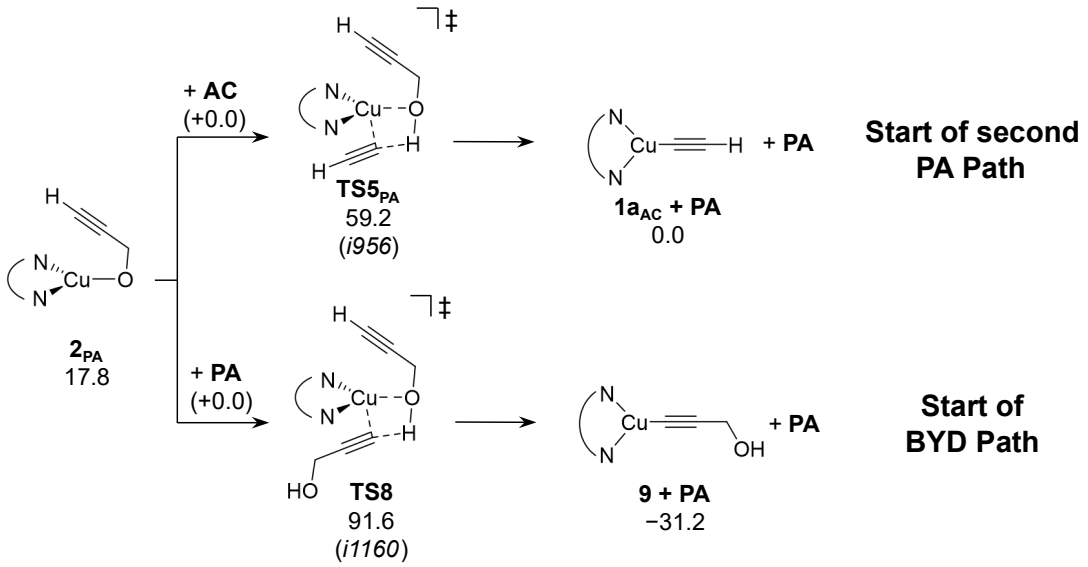

Figure 5.16: Protonation of $\mathbf{2_{PA}}$ by AC compared to PA, generating the starting complex for the generation of BYD; the thermochemistry of **PA** for the protonation is not included for clarity, since the **PA** is regenerated; ΔG^{343} in kJ·mol^{-1} relative to $\mathbf{1a_{AC}}$; ωB97x-D/def2-QZVPP//COSMO(∞)-TPSS-D3ZERO/def2-SVP; COSMO-RS (MeCN).

Protonation by PA occurs with an effective Gibbs free energy of activation of 91.6 kJ·mol^{-1} (**TS8**). In the resulting complex **9** (−31.2 kJ·mol^{-1}), the propargyl alcoholate is coordinated with the carbon atom. This coordination is clearly favored compared to O-coordination ($\mathbf{2_{PA}}$: 17.8 kJ·mol^{-1}). With **9**, a starting complex for BYD formation is available (Figure 5.17).

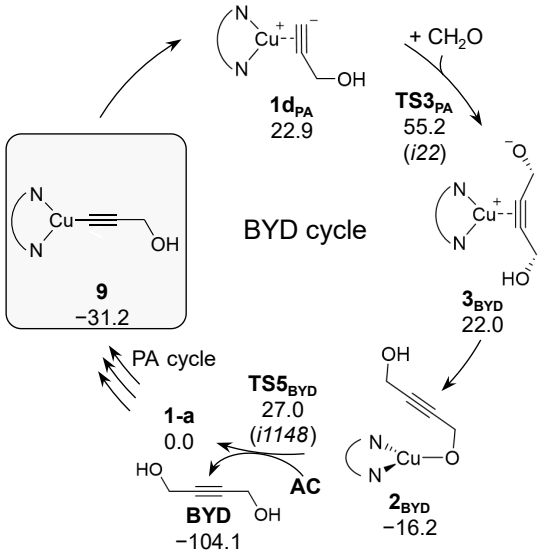

Figure 5.17: Catalytic cycle with key transition states and intermediates for the generation of butynediol (BYD); ΔG^{343} in kJ·mol^{-1} relative to $\mathbf{1a_{AC}}$; ωB97x-D/def2-QZVPP//COSMO(∞)-TPSS-D3ZERO/def2-SVP; COSMO-RS (MeCN).

A similar reactivity as for the PA formation was found for the second reaction with formaldehyde (BYD formation). The nucleophilic attack of the $\eta^2(\pi)$-coordinated intermediate **1d$_{PA}$** on formaldehyde proceeds with an effective activation barrier of 86.4 kJ·mol^{-1} (**TS3$_{PA}$**), which is lower than that observed for the ligand exchange from the O- to the C-bound propargyl alcoholate. Consequently, the preparation of the starting complex for the BYD pathway **9** is rate-limiting. Product generation through protonation by AC goes along with the regeneration of the Cu^{I}-acetylide starting complex with a moderate effective Gibbs free energy of activation of 58.2 kJ·mol^{-1} (**TS5$_{BYD}$**: 27.0 kJ·mol^{-1}). The starting complex for the BYD cycle **9** is regenerated by a PA cycle followed by ligand exchange through protonation.

Comparing the PA and the BYD cycle, the selectivity-determining step is the protonation of the O-bound Cu^{I} propargyl alcoholate complex (**2$_{PA}$**). If protonation and ligand exchange occur with AC, the PA cycle restarts, while in the case of protonation by PA, the BYD cycle begins. For this step, the effective barrier for the protonation by AC is significantly lower (**TS5$_{PA}$**: 59.2 kJ·mol^{-1}) than that observed for PA (**TS8**: 91.6 kJ·mol^{-1}). A comparison of the overall Gibbs free energy of activation (**TS3$_{AC}$** for PA and **TS8** for BYD formation), however, indicates that PA formation is favored by only 6.1 kJ·mol^{-1} over BYD formation. While a kinetic factorization of PA formation is visible in this comparison, the small difference may be in the range of error limits of the applied methods.

Attempts to optimize a stable dinuclear resting state failed and only gave an endergonic, unsymmetrical complex (**1b$_{AC}$**: 37.0 kJ·mol^{-1}, Figure 5.18). Higher-order oligomeric clusters were not examined but remain possible.

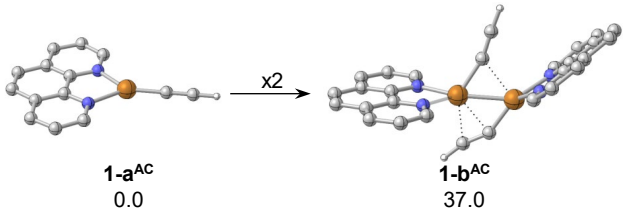

Figure 5.18: Only an unsymmetrical, endergonic dinuclear complex was found for Cu^{I}-acetylide; ΔG^{343} in kJ·mol^{-1}; ωB97x-D/def2-QZVPP//COSMO(∞)-TPSS-D3ZERO/def2-SVP; COSMO-RS (MeCN).

5.4.7 Kinetic Modeling for the Ethynylation

As a plausibility check for the predicted small difference in activation barriers for the synthesis of PA and BYD of only 6.1 kJ·mol^{-1}, kinetic modeling was performed, neglecting side reactions and assuming a constant catalyst concentration. The reaction scheme for converting AC to PA and BYD (Figure 5.19) yields four rate equations: two for substrate consumption (Equations 5.1 and 5.2) and two for product formation (Equations 5.3 and 5.4).

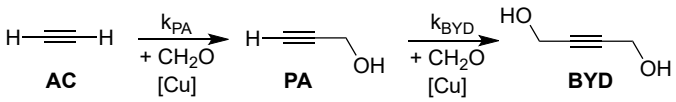

Figure 5.19: Reaction scheme for the kinetic model; irreversible, pseudo second order reactions are assumed; for the modeling, the fitted rate constants pseudo second order are denoted as k'.

$$-\frac{d[AC]}{dt} = k'_{PA} \cdot [AC][CH_2O] \tag{5.1}$$

$$-\frac{d[CH_2O]}{dt} = k'_{PA} \cdot [AC][CH_2O] + k'_{BYD} \cdot [PA][CH_2O] \tag{5.2}$$

$$\frac{d[PA]}{dt} = k'_{PA} \cdot [AC][CH_2O] - k'_{BYD} \cdot [PA][CH_2O] \tag{5.3}$$

$$\frac{d[BYD]}{dt} = k'_{BYD} \cdot [PA][CH_2O] \tag{5.4}$$

For the kinetic model, discrete time intervals of one minute were utilized. The initial concentrations of formaldehyde and AC were set according to experimental conditions from the ligand screening ($c_0(CH_2O)$ = 540 mM and $c_0(AC)$ = 400 mM). The rate constants k'_{PA} and k'_{BYD} were fitted using the Solver add-in implemented in Excel[255] to reach the measured yields of 37% PA and 14% BYD (selectivity of 73%). It was assumed that the reaction proceeds until the end of the simulation (3 h). It is noted that the fitted rate constants (k') are pseudo second order rate constants, since the catalyst concentration is assumed to be constant.

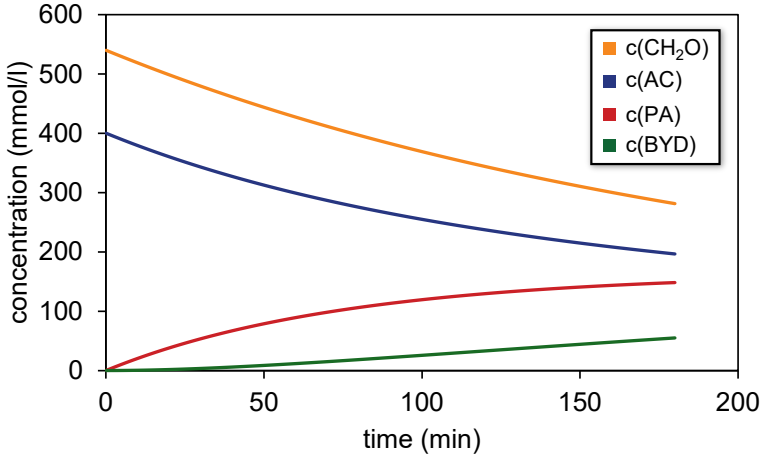

Figure 5.20: Kinetic model for the ethynylation of formaldehyde; discrete time steps of 1 minute were used; side reactions were neglected, and a constant catalyst concentration was assumed; the experimental start and end concentrations were utilized to fit reaction rates pseudo second order.

The resulting concentration-time profiles (Figure 5.20) indicate that the formation of PA is predominant at the initial stage. After 25 minutes, BYD slowly starts to form; however, clearly slower than the formation of PA. The rate constant for PA formation ($k'_{PA} = 1.00 \cdot 10^{-6}$ L·mol^{-1}·s^{-1}) is 1.2 times faster than for BYD formation ($k'_{BYD} = 0.84 \cdot 10^{-6}$ L·mol^{-1}·s^{-1}). This corresponds to a difference in effective Gibbs free energy of activation of only 0.6 kJ·mol^{-1}. This indicates that selectivity is primarily determined by concentration effects rather than differences in activation energies. With a DFT-computed difference of 6.1 kJ·mol^{-1} between the Gibbs free energies of activation for PA and BYD formation, the energetic preference appears slightly overestimated. However, the deviation remains within the typical error range of the DFT methods employed.[252]

5.5 Summary and Outlook

To ensure an accurate energy prediction, an energy benchmark was conducted. ωB97x-D in combination with the def2-QZVPP basis set performed the best compared to the DLPNO-CCSD(T) reference calculation employing an extrapolation to the complete basis set limit. For the Cu^{I}-phenylacetylide-phenanthroline complexes, it was shown that coordination with either the starting material (formaldehyde) or the solvent is unfavorable. The dinuclear species (**1c**) and the mononuclear complex (**1a**) are nearly identical in free energies, consistent with experimental indications for a temperature-dependent equilibrium between them. The computed geometry of **1c** features bent phenylacetylide units. Electronic structure analysis revealed minimal orbital interactions, while notable attractive dispersion interactions were identified.

An insertion of formaldehyde into the Cu–C bond was found to be impossible at the reaction temperature. The phenylacetylide unit in **1a** can bend and coordinate in an $\eta^2(\pi)$ fashion. This reactive form can undergo a nucleophilic attack on formaldehyde with a barrier that can be overcome at the given conditions. A similar transition state was found for the dinuclear complex, but with higher barriers. Therefore, the dinuclear complex was identified as the (concentration and temperature dependent) resting state and the mononuclear complex as the active species.

The comparison of different substrates reproduced experimental trends, that reactions occurred only with formaldehyde and 2,2,2-trifluoroacetophenone, but not with acetophenone or acetaldehyde. For acetophenone, the computations indicated that the reaction is highly endergonic, whereas for acetaldehyde, the reaction is predominantly hindered by kinetic factors.

The mononuclear pathway was calculated for acetylene as a substrate. A similar reactivity for the reaction with formaldehyde was revealed as for the model system phenylacetylene (propargyl alcohol (PA) pathway). The generation of a starting complex for the second reaction with formaldehyde (butynediol (BYD) formation) was shown to proceed via ligand exchange of an O- to a C-coordinated propargyl alcoholate. This step is rate-limiting for the BYD formation and determines the selectivity between PA and BYD. The C-coordinated complex reacts in a similar manner to the model system and the PA pathway. With only a difference of 6.1 $kJ \cdot mol^{-1}$ in the effective activation barriers of PA compared to BYD, PA is kinetically favored; however, this difference is close to the error limits of the applied methods.

An equivalent to the dinuclear resting state of Cu^{I}-phenylacetylide was not found for Cu^{I}-acetylide, only unsymmetric and endergonic complexes were found. Future investigations could focus on exploring possibilities of higher oligomeric structures.

A basic kinetic model was employed to reproduce the experimentally measured yields and selectivity. The rate constants fitted for PA and BYD formation indicated that the reaction for PA formation is 1.2 times faster, with Gibbs free energies of activation that are nearly equal for both processes. This matches the small difference in Gibbs free energy of activation found by DFT, suggesting that selectivity is mainly driven by concentration effects.

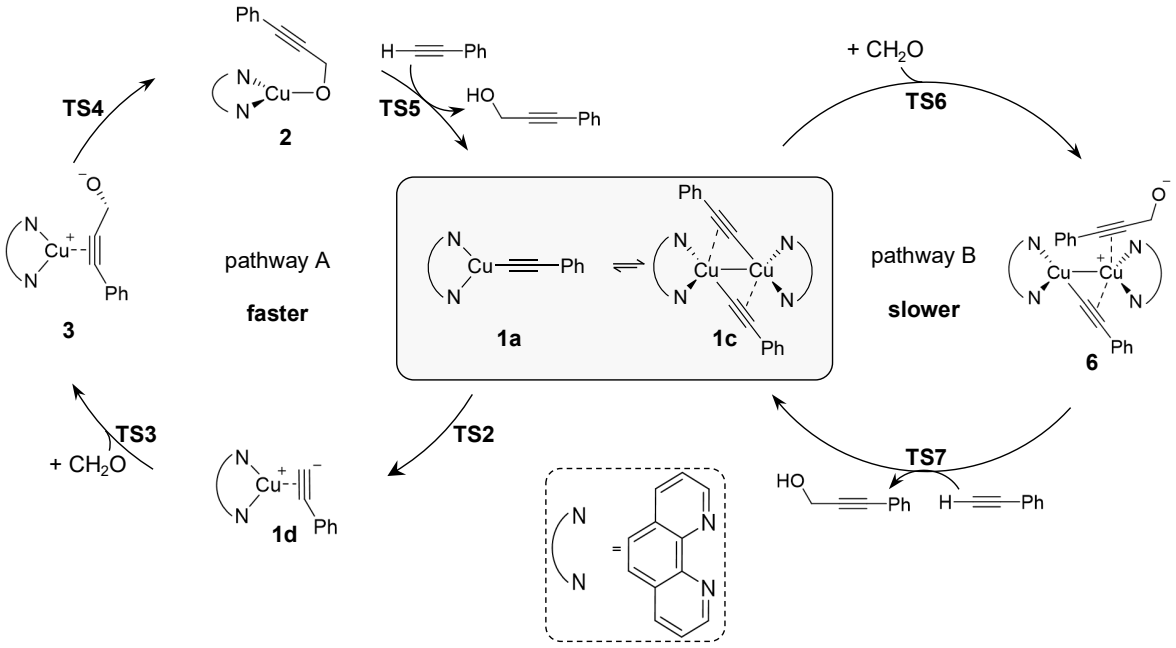

Figure 5.21: Proposed catalytic cycle with a mononuclear (pathway A) and a dinuclear (pathway B) complex as active species; only the most important intermediates are shown.

6

Ligand-Controlled Chemodivergent Bismuth Catalysis

Reproduced in part with permission from Lucas Mele, Philipp D. Engel, Jamie A. Cadge, Vytautas Peciukenas, Hoonchul Choi, Matthew S. Sigman, Josep Cornella, Ligand-Controlled Chemodivergent Bismuth Catalysis. *J. Am. Chem. Soc.* **2025**, manuscript accepted DOI: 10.1021/jacs.5c11854.[256]

All experiments presented were conducted by Lucas Mele, Vytautas Peciukenas, and Hoonchul Choi. Jamie A. Cadge co-supervised computational analysis.

Note: The numbering of calculated and experimental structures restarts at the beginning of each chapter.

6.1 Motivation and Goal

Recent years have shown a broader trend in catalysis toward more sustainable strategies. While much of this effort has centered on earth-abundant, first-row transition metals,[257-258] the present chapter highlights an example for an alternative approach that exploits transition metal-like reactivity in *p*-block elements,[259-262] opening new avenues for sustainable and versatile catalyst design. An established concept in transition metal catalysis is *ligand-controlled chemodivergence*, where simple modification of the ligand enables access to distinct reaction pathways and products from the same starting material under the same conditions.[263] However, examples in main group catalysis have typically involved variations of additives or substrates rather than solely changing the ligand.[264-270]

The Cornella group optimized a bismuth-catalyzed coupling between arylboronic acids and N-fluorosulfonimide (NFSI) derivatives, achieving selective formation of either C(sp^2)–N or C(sp^2)–O bonds. The selectivity is controllable by changing the ligand.[256]

Given that ligand-controlled chemodivergence is a recent development in main group catalysis, an in-depth understanding of ligand effects is required, which is explored in this chapter through DFT computations and complementary statistical analyses. A central objective is to perform mechanistic calculations to study the catalytic cycle, with a particular focus on the selectivity-determining step. Insights gained from calculations on a model catalyst are extended to different catalyst backbones and counterions to understand experimental trends. Additionally, MLR models are developed to identify interpretable descriptors that help rationalize the observed ligand effects.

6.2 Experimental Background

It is well established that the electronic and steric characteristics of ligands coordinated to transition metal centers significantly affect the outcomes of catalytic processes.[271-274] As a result, ligand design has become an important aspect of method development, contributing to control over reaction pathways and stabilization of the metal center. Ligand-controlled chemodivergent reactions demonstrate that two different products can be generated from the same starting material under similar reaction conditions, solely by changing the ligand.[263] This approach enables the selective formation of important bonds, including C(sp^2)–N and C(sp^2)–O (Figure 6.1A).[275] C(sp^2) functionalization has typically involved transition metals with supporting ligands. However, recent years have demonstrated that main group chemistry and catalysis can also achieve these types of transformations using electrons in frontier *p*-orbitals.[259,276-280] Without the involvement of *d*-orbitals in bonding, main group catalysts often depend on structural distortion enforced by their ligand frameworks to steer reactivity. This constraint makes it difficult to adjust the ligand structure in order to control selectivity and efficiency in main group chemistry.[256]

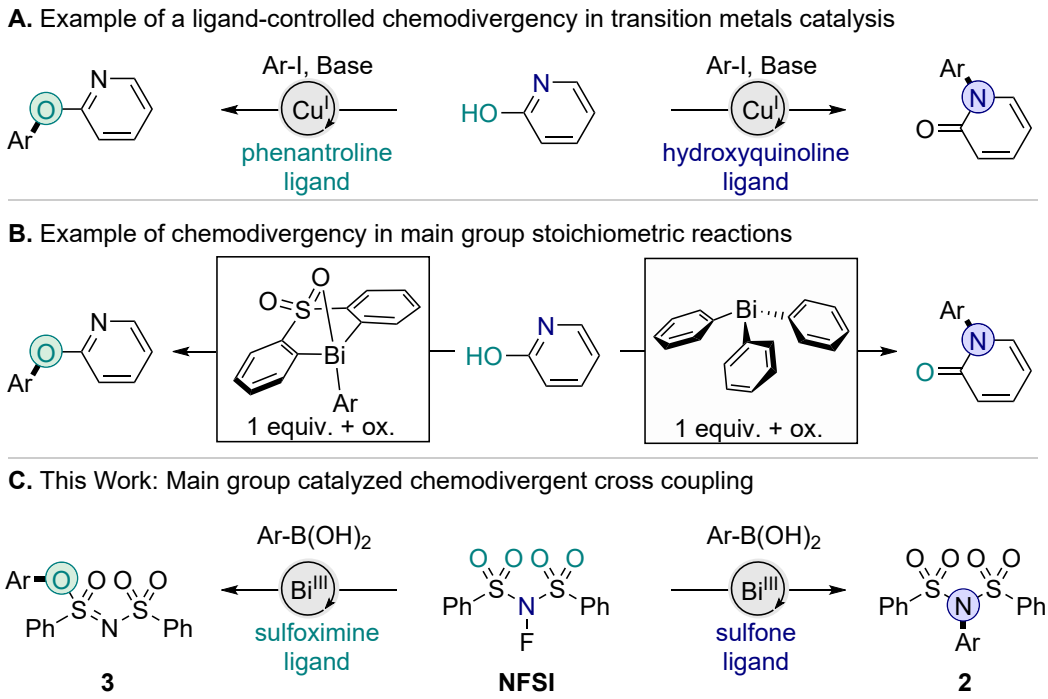

Figure 6.1: An example for a Cu-catalyzed ligand-controlled chemodivergent coupling of 2-hydroxypyridine with aryl iodide (**A**),[275] stoichiometric oxidative arylbismuth chemodivergent coupling with 2-hydroxypyridine, using selectfluor as an additive oxidant (**B**),[281] and bismuth-catalyzed ligand-controlled chemodivergent coupling of NFSI with arylboronic acids (**C**).[256]

Some examples for chemodivergent transformations with main group reagents have been reported, typically steered by the additives or substrate type.[264-270] Only a limited number of stoichiometric reactions involve control via ligand structure. Corresponding catalytic processes have not yet been developed. Mukaiyama's group used high-valent bismuth reagents from homoleptic triarylbismuthine for a selective

N-arylation of 2-hydroxypyridine. More recently, the Ball group reversed this selectivity to favor O-arylation on the same substrate by using a stoichiometric diarylsulfone bismuth reagent (Figure 6.1B).[281] Other attempts did not yield reactivities that could be modified solely through ligand replacement.[282]

Building on prior research,[262,281,283-287] the Cornella group initiated their investigations by treating NFSI with a stoichiometric amount of the Bi^{III} complex $\mathbf{1}_{L1}$-***t*BuPh**, which features a bis-anionic aryl ligand and a linking sulfonyl or sulfoximine group in the backbone (Figure 6.1C, Figure 6.2A).[256] The experiment produced a 77:23 (3.3:1) mixture, with the C–N coupled product **2** preferred over the C–O coupled compound **3**. A catalytic system was optimized to efficiently couple arylboronic acids with NFSI derivatives, enabling unprecedented bismuth-catalyzed C(sp^2)–N bond formation. By changing the substitution at the ligand backbone, selectivity is tunable, achieving N- or O-arylation. Under optimized conditions for C–N coupling, a C–N:C–O selectivity ratio of up to 78:22 can be achieved. Modification of the ligand while keeping other conditions, such as the solvent, constant directs the selectivity toward the O-product, yielding a C–N:C–O ratio of 43:57 (Figure 6.2B).

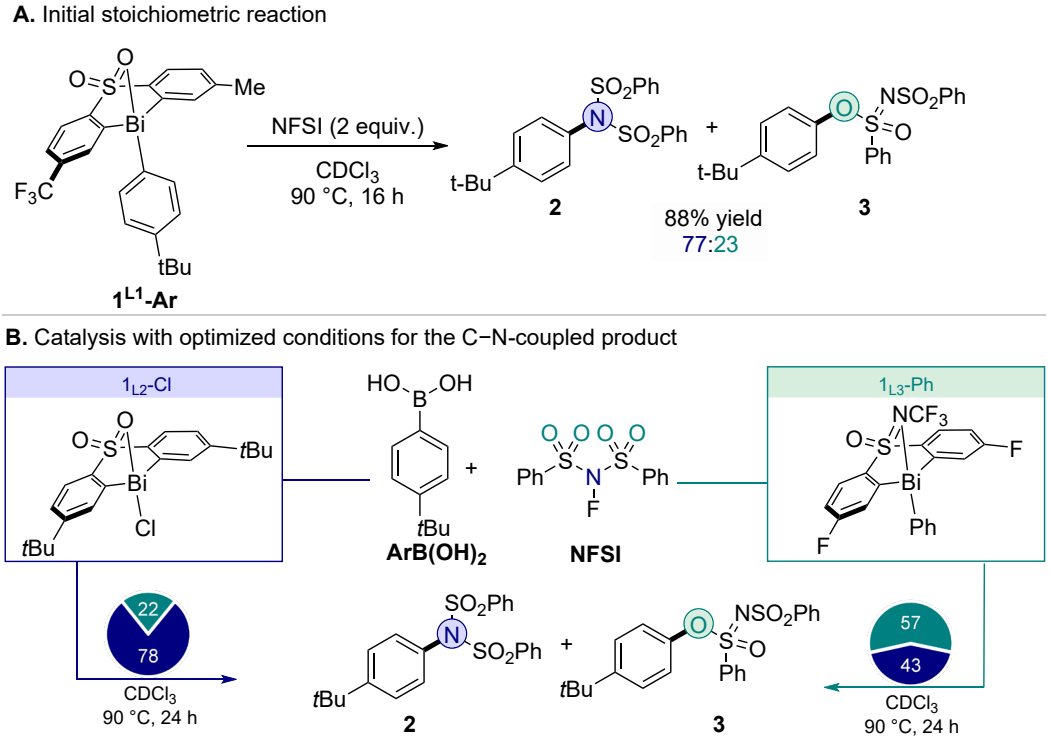

Figure 6.2: Initial stoichiometric experiments (**A**) and optimized catalysis for the C–N coupled species as the major product (**B**); 20 mol% *p*CF_3-stillbene as an additive to improve yields.

6.3 Computational Details

Geometry optimizations and Hessian calculations were performed using the TURBOMOLE[133] program (version 7.5.2). The GGA functional BP86[144-145] was employed together with the def2-TZVP[135] basis set and the D4[288] dispersion correction. The standard effective core potential (ECPs) for Bi was applied.[289] The implicit solvation model COSMO with default parameters and an infinite dielectric constant was used for the geometry optimization.[24] Stationary points were confirmed by vibrational frequency analyses at the same level of theory. Final single point electronic energies were obtained with the hybrid functional B3LYP[198-200,250] in combination with the def2-TZVP[135] basis set, including the D4[288] dispersion correction. The RI approximation[139-142] and corresponding auxiliary basis sets were used throughout all calculations.

Thermochemical corrections to calculate Gibbs free energies were obtained at the level of theory of the geometry optimization (T = 363.15 K, p = 1 bar). Solvation correction was calculated using the COSMO-RS model[26,28] implemented in COSMOtherm (Version 18.0.0; Revision 4360).[143] An infinite dilution in chloroform was assumed, and the FINE parametrization with a reference state of 1 mol·L^{-1} at 363.15 K was used. Transition states were connected to corresponding minima by following the transition mode and subsequent geometry optimization or by intrinsic reaction coordinate (IRC) calculations. IRC analyses were conducted with Gaussian16,[290] using energies, gradients, and force constants provided by TURBOMOLE as external input. Barrierless processes were verified via relaxed potential energy surface scans.

Reaction pathway exploration was performed with the MGSM method[37-39] combined with a precomplex builder routine.[40] Extensive conformational searches for intermediates and transition states were carried out using the CREST[15-16] program package developed by Grimme and co-workers, followed by DFT optimization of selected conformers to establish ranking based on Gibbs free energies on single point level of theory. For clarity, only the lowest energy conformers are discussed and shown in the figures.

For property calculations, single point computations were performed in ORCA[185-187] (version 5.0.4) using the B3LYP[198-200,250] functional and the def2-TZVP[135] basis set on the lowest energy conformer. Implicit solvation was treated with the CPCM[188] model employing chloroform as solvent. From these calculations, NMR chemical shifts and HOMO–LUMO parameters were obtained. The MORFEUS[291] tool was used to determine buried volume and Sterimol parameters. Wiberg bond indices and natural population analysis (NPA)[76] charges were extracted from the TURBOMOLE[133] calculations at the optimization level. Hammett substituent constants were taken from the literature for the arene substituents.[50]

Different coordination motifs were manually screened, followed by automated conformational screening within each coordination mode for all complexes. Descriptor calculations were carried out only for the lowest energy conformer. This automated workflow was also applied to the species used in the mechanistic analysis (**1$_{L4}$-OTFA**,

1$_{L2}$-Cl, and **1$_{L2}$-OTFA**), which resulted in slightly different, but within error identical, conformers compared to those used in the mechanistic study.

For properties derived from the arene ligands, average, minimum, and maximum values were computed over the atoms of both aromatic rings, yielding the descriptors av-, min-, and max-, respectively. Molecular descriptors were generated using a Python script developed in the Sigman group.[292] Atom labeling for descriptor nomenclature was standardized, and atom mapping was carried out via substructure searches using RDKit.[293]

MLR modeling was performed with a Python script, developed in the Sigman group,[89] based on the scikit-learn library.[294] A collinearity filter was applied with a cutoff of $R^2 = 0.5$ to avoid correlated features within the same model. Feature values were normalized to enable direct interpretation of regression coefficients. A brute-force feature selection strategy was employed, constructing and evaluating all possible models containing one or two features. To assess model performance, the dataset was divided into training and validation subsets using a 12:3 ratio. Validation points were selected to be evenly distributed across the dependent variable. Cross-validation using the leave-one-out (LOO) method was applied to test model robustness and detect potential overfitting. For both datasets and cross-validation, R^2 (Q^2 for LOO) and MAE values were calculated. It should be noted that the purpose of the linear modeling was interpretative rather than predictive, aiming to reproduce experimental data and identify factors influencing chemoselectivity.

Molecular structures were visualized using Cylview.[183] For clarity, C–H hydrogen atoms are omitted in the figures. Additionally, the C–N and C–O coupled products are simplified according to Figure 6.3.

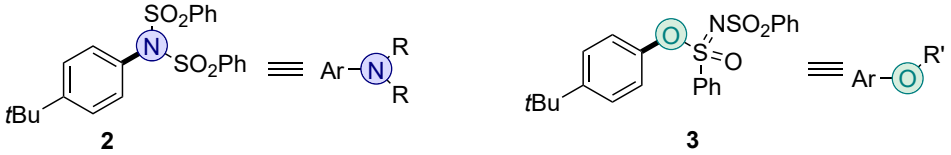

Figure 6.3: Abbreviation of the C–N (**2**) and C–O (**3**) coupled products.

6.4 Results and Discussion

6.4.1 Oxidative Addition and Transmetalation

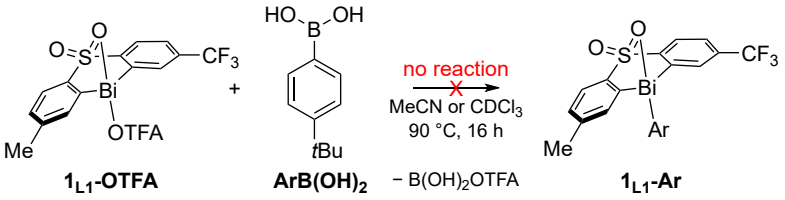

Figure 6.4: Addition of stoichiometric amounts of boronic acid derivative leads to no reaction, indicating that transmetalation is not the first step of the catalytic cycle.

Previous studies on Bi^{III}/Bi^{V} catalysis indicated that transmetalation occurs as the initial step.[262,287] However, with this system, the addition of stoichiometric amounts of a boronic acid derivative to the Bi^{III} complex resulted in no observable reaction (Figure 6.4). This suggests that transmetalation is unlikely to be the initial step in the catalytic process. Based on this observation, experimental and computational studies examined the oxidative addition process as the initial step. Cyclic voltammetry indicated that a one-electron oxidative addition step involving a Bi^{IV} species does not occur and suggested a stepwise two-electron process.

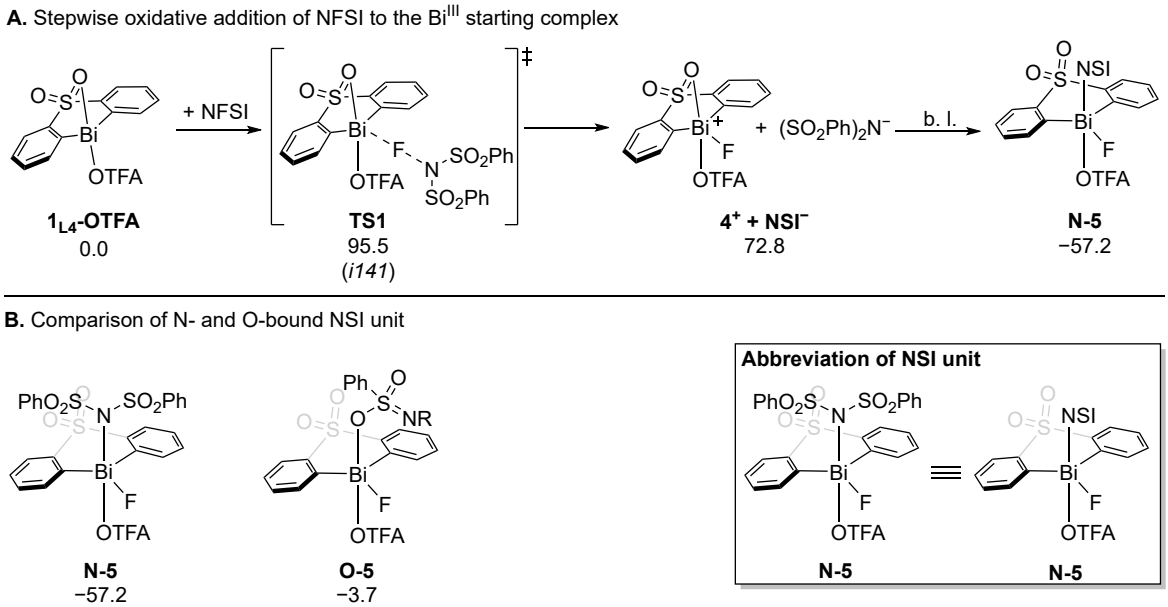

Figure 6.5: Stepwise oxidative addition of NFSI to **1_{L4}-OTFA** (**A**), as well as the comparison of N- vs. O-binding mode of the NSI unit; N-bound NSI unit is abbreviated as NSI; ΔG^{363} in kJ·mol^{-1}; B3LYP-D4/def2-TZVP//COSMO(∞)-BP86-D4/def2-TZVP; COSMO-RS (chloroform).

DFT computations revealed a viable pathway for the stepwise oxidative addition of the substrate NFSI to the Bi^{III} starting complex (Figure 6.5A). Initially, a fluoronium is transferred (**TS1**: 95.5 kJ·mol^{-1}), yielding an intermediary ion pair (**4**$^{+}$ and **NSI**$^{-}$). This energetically high-lying ion pair (72.8 kJ·mol^{-1}) can recombine in a barrierless and

strongly exergonic reaction to the Bi^V complex **N-5** (−57.2 kJ·mol^{-1}). In this nomenclature, the prefix *N* refers to the binding mode of the substrate NSI. Binding via one of the oxygen atoms is thermodynamically less favored (**O-5**: −3.7 kJ·mol^{-1}, Figure 6.5B). Based on this, it was concluded that oxidative addition and transmetalation proceed only from the thermodynamically more stable N-bound intermediates.

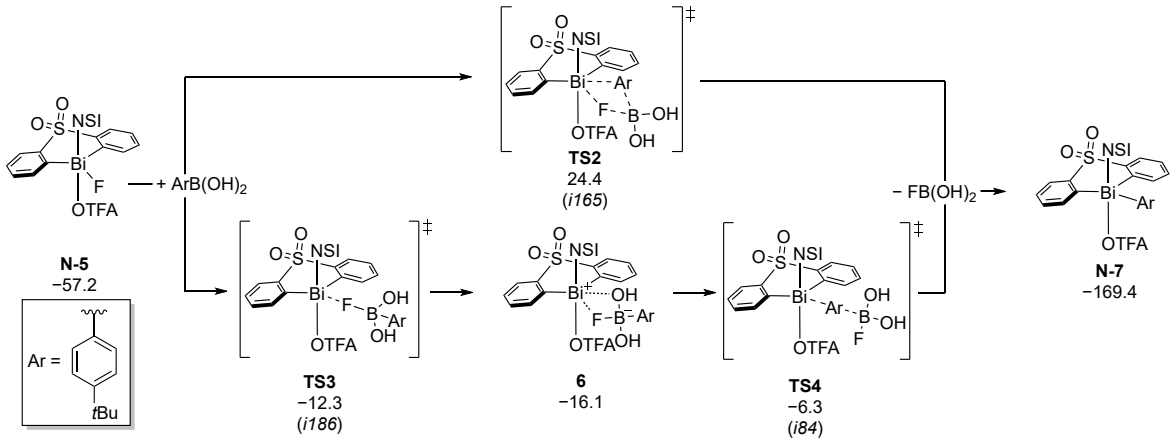

Figure 6.6: Comparison of concerted (**TS2**) and stepwise (**TS3**, **TS4**) transmetalation; ΔG^{363} in kJ·mol^{-1} relative to $\mathbf{1_{L4}}$**-OTFA**; B3LYP-D4/def2-TZVP//COSMO(∞)-BP86-D4/def2-TZVP; COSMO-RS (chloroform).

Two pathways for the transmetalation by the arylboronic acid were computed: a concerted and a stepwise pathway (Figure 6.6). The concerted pathway over **TS2** exhibits an effective activation Gibbs free energy of 81.7 kJ·mol^{-1} relative to **N-5**. Stepwise transmetalation starts with the transfer of a fluoride to the boronic acid derivative (**TS3**: −12.3 kJ·mol^{-1}), yielding the contact ion pair **6** (−16.1 kJ·mol^{-1}). After the transfer of the aryl substituent to the bismuth center (**TS4**: −6.3 kJ·mol^{-1}), the Bi^V intermediate **N-7** is produced in a strongly exergonic manner (−169.4 kJ·mol^{-1}). For this pathway, the effective Gibbs free energy of activation is 51.0 kJ·mol^{-1}, significantly lower than for the concerted reaction. Consequently, stepwise transmetalation is favored.

6.4.2 Reductive Elimination

Reductive elimination (RE), as the last step in the catalysis, is regarded as the selectivity-determining step. To explain why the C–N coupled product (**2**) forms preferentially over the C–O coupled product (**3**), three possible mechanistic scenarios were examined using a combination of experimental and computational methods (Figure 6.7).

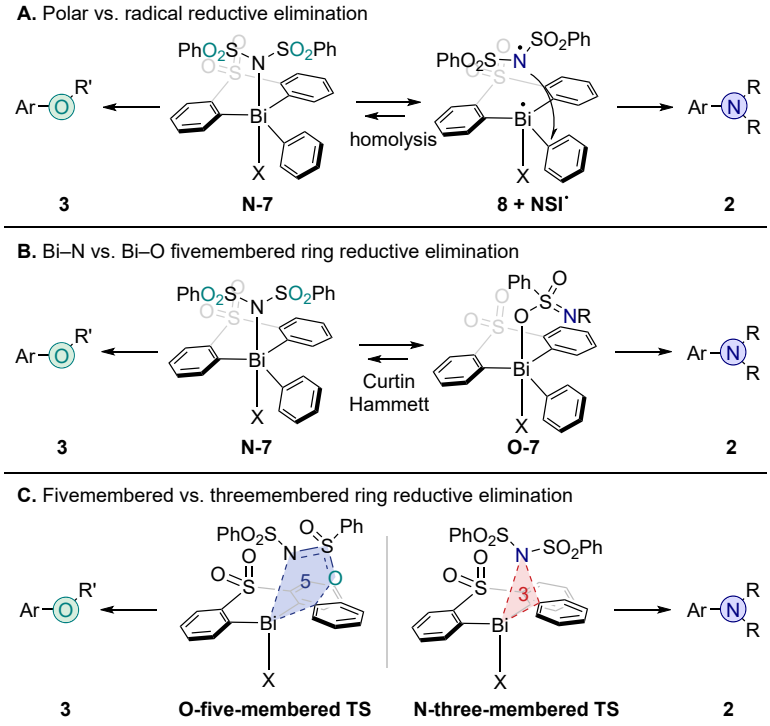

Figure 6.7: Overview of three different possibilities for the RE: Polar vs. radical RE (A), RE following the Curtin Hammett principle (B), and a scenario incorporating a three- and a five-membered ring transition state (C); X represents the counterion, R and R' are defined as shown in Figure 6.3.

Pathway A considers a polar vs. radical reductive elimination mechanism.[295-297] The O-product results from a polar five-membered ring transition state from the Bi^V intermediate **N-7**. In contrast, the N-product is formed by homolytic cleavage of the Bi–NSI bond followed by *ipso*-substitution through the N-centered radical. However, DFT computations ruled out this pathway: the radical pair after the homolytic cleavage (**8** + **NSI**•) lies 199.5 kJ·mol^{-1} higher in free energy than the Bi^V intermediate, making this process energetically inaccessible at the reaction temperature (Figure 6.8).

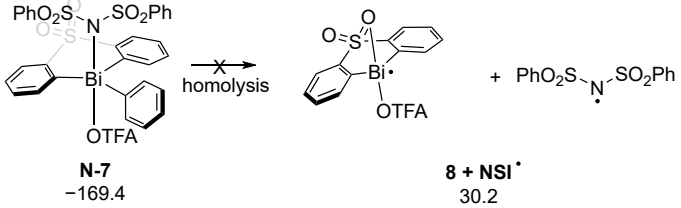

Figure 6.8: A radical RE (pathway A) is discarded since the homolysis of **N-7** is inaccessible; the *t*Bu group at the aryl substituent is not shown for clarity; ΔG^{363} in kJ·mol^{-1} relative to $\mathbf{1_{L4}}$**-OTFA**, $ArB(OH)_2$ and NFSI; B3LYP-D4/def2-TZVP//COSMO(∞)-BP86-D4/def2-TZVP; COSMO-RS (chloroform).

Pathway B (Figure 6.7B) involves a Curtin-Hammett scenario in which two rapidly interconverting intermediates (**N-7** and **O-7**) generate the two products through reductive elimination via polar five-membered ring transition states. The resulting product distribution is determined by the difference in the free energies of the transition states. In contrast, pathway C proposes a competition between a three-membered and a five-membered ring transition state (Figure 6.7C). Both originate from the N-bound Bi^{V} complex (**N-7**): the N-product forms via a three-membered transition state (**N-TS5b**), while the O-product forms through a five-membered transition state (**O-TS5a**). To evaluate whether pathway B or pathway C is predominant, all four transition states were computed and systematically compared (Figure 6.9, **TS5a** in blue, **TS5b** in red).

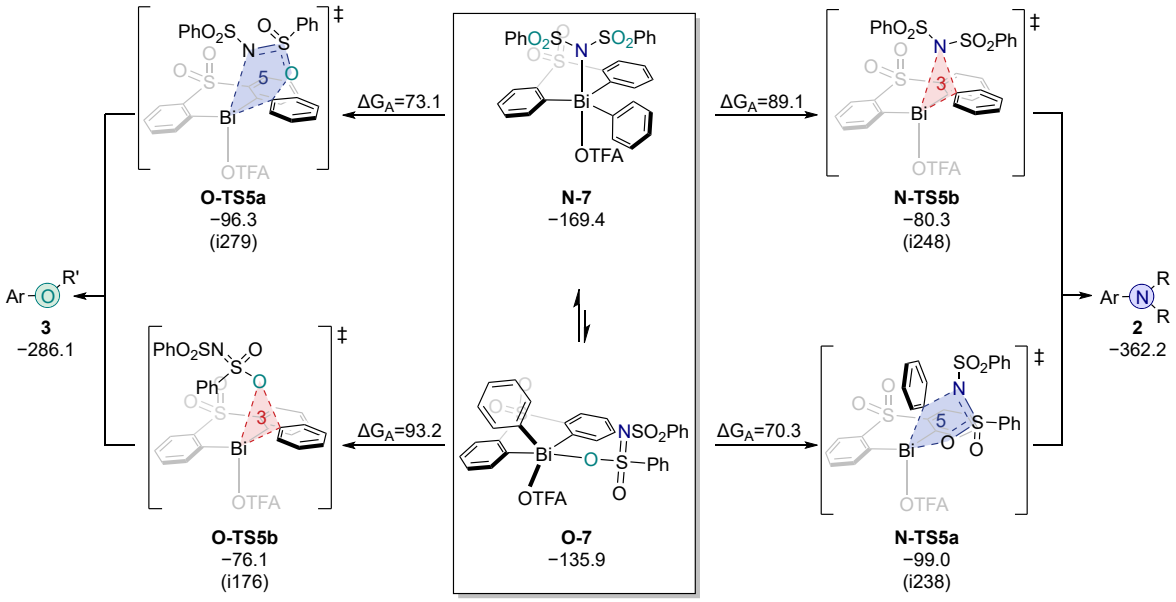

Figure 6.9: Reductive elimination for the model catalyst (**1$_{L4}$-OTFA**) via five-membered (**TS5a**, blue) and three-membered (**TS5b**, red) ring transition states; the *t*Bu group at the aryl substituent is not shown for clarity; R and R' are defined as shown in Figure 6.3; ΔG^{363} in kJ·mol^{-1} relative to **1$_{L4}$-OTFA**, $ArB(OH)_2$ and NFSI; B3LYP-D4/def2-TZVP//COSMO(∞)-BP86-D4/def2-TZVP; COSMO-RS (chloroform).

The N-bound intermediate (**N-7**) is significantly more stable than the O-bound intermediate (**O-7**) with a difference in free energy of 33.4 kJ·mol^{-1}. For the model catalyst, the three-membered ring transition states **TS5b** have higher free energies than the five-membered ring **TS5a**. **TS5a** is preferred over **TS5b** by 18.7 kJ·mol^{-1} in the case of C–N and 20.2 kJ·mol^{-1} in the case of C–O coupling. With such a big difference, a competition between these pathways for the model catalyst is unlikely. Consequently, pathway B is preferred. The effective Gibbs free energy of activation relative to intermediate **N-7** is 2.7 kJ·mol^{-1} lower for the formation of the N-product.

Reductive elimination via three-membered ring transition states has been reported to proceed asynchronously in pentacoordinate pnictogens, preventing symmetry-forbidden ligand couplings.[287,298-300] Motivated by this, the IRCs were studied for the transition states forming the N-product. Selected bond lengths were plotted at each IRC step (Figure 6.10). For the five-membered ring transition state (**N-TS5a**, Figure 6.10A),

all bonds involved in the transition mode change in a largely synchronous fashion, with only minor deviations. For the three-membered ring transition state (**N-TS5b**, Figure 6.10B), however, the Bi–N bond cleaves more rapidly than the C–N bond forms. Thus, the NSI unit partially dissociates before attacking the aryl group, resulting in an asynchronous three-membered transition state.

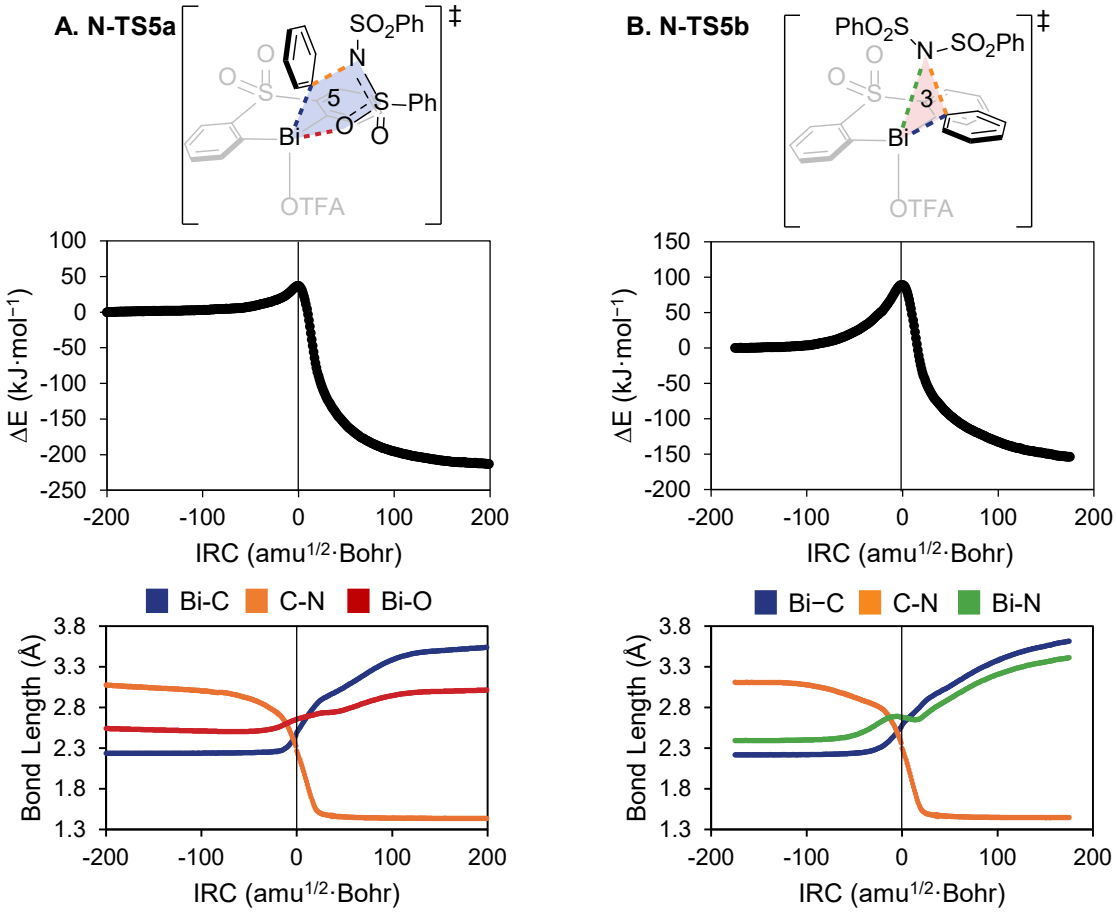

Figure 6.10: IRC calculation for the five-membered (**A**, **N-TS5a**) and three-membered ring transition state to the N-product (**B**, **N-TS5b**); energy as well as the bonds involved in the transition state; COSMO(∞)-BP86-D4/def2-TZVP.

In the extreme case, this asynchronous transition could become a stepwise, outer-sphere S_NAr-type mechanism (Figure 6.11). In this scenario, NSI^- first dissociates heterolytically, then attacks the *ipso*-carbon of an intermediate bismuthonium cation (**9⁺**).[301-302] The heterolytic dissociation is 71.3 kJ·mol^{-1} endergonic relative to intermediate **N-7**. Product formation proceeds with an effective Gibbs free energy of activation of 98.7 kJ·mol^{-1} to the N- and 112.7 kJ·mol^{-1} to the O-product. With that, the formation of the N-product is clearly favored. Comparing steps that involve charge separation with those in which charge is retained is challenging due to uncertainties in the appropriate treatment of solvation. To avoid potentially misleading conclusions, the outer-sphere attack will therefore not be directly compared to the concerted transition states **TS5a** and **TS5b**.

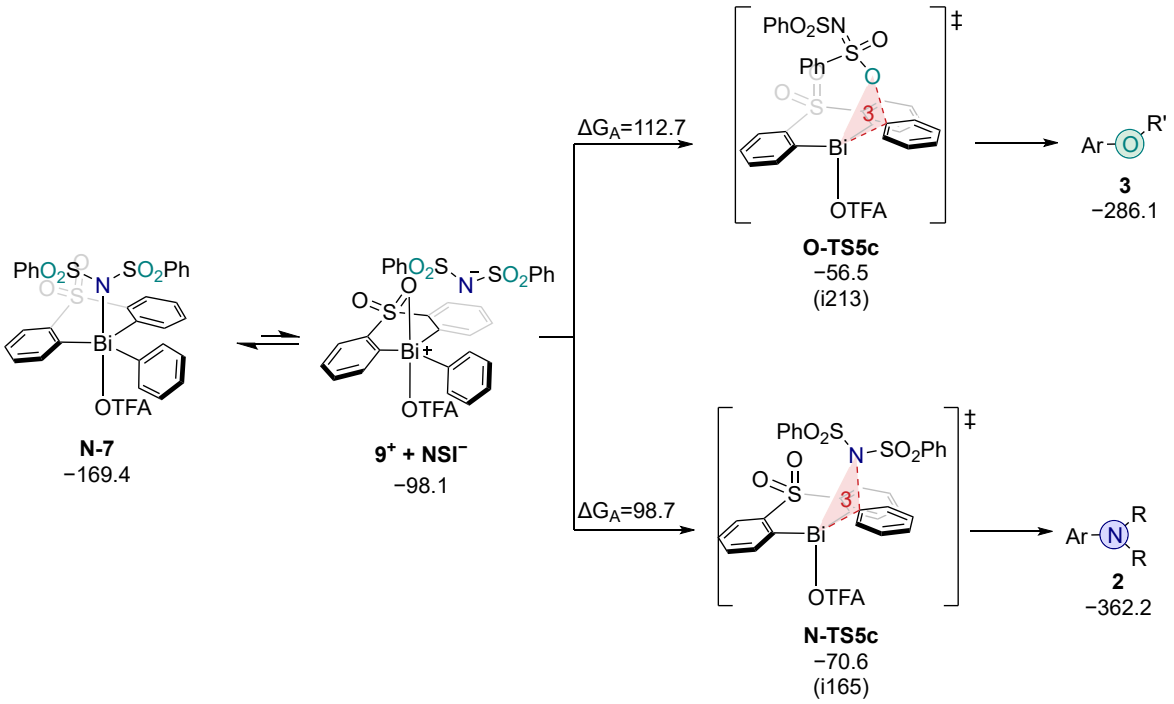

Figure 6.11: Reductive elimination for the model catalyst (**1$_{L4}$-OTFA**) via an outer sphere transition state (**TS5c**, red); the *t*Bu group at the aryl substituent is not shown for clarity; R and R' are defined as shown in Figure 6.3; ΔG^{363} in kJ·mol^{-1} relative to **1$_{L4}$-OTFA**, ArB(OH)$_2$ and NFSI; B3LYP-D4/def2-TZVP//COSMO(∞)-BP86-D4/def2-TZVP; COSMO-RS (chloroform).

To further investigate a possible competition between pathways B and C, the key transition states (**TS5a** and **TS5b**) and intermediates (**7**) were computed for selected other catalysts (see Figure 6.12A). The model catalyst (**1$_{L4}$-OTFA**, Sel(C–N:C–O): 2.13) was compared to the most N-selective catalyst (**1$_{L2}$-Cl**, Sel(C–N:C–O): 3.65) and to an analogous system with OTFA as counterion (**1$_{L2}$-OTFA**, Sel(C–N:C–O): 2.82). This comparison helps to separate the effects of ligand substitution and the change of counterion. Ligand **L2** features *t*Bu groups in *meta* position to the bismuth center. In Figure 6.12, the intermediates **O-7** are not shown for clarity. Instead, the equilibria with **O-7** are only indicated with a dotted line. (Figure 6.12B–D).

With the model catalyst (**1$_{L4}$-OTFA**), the five-membered transition state (**TS5a**) is favored for both N- and O-products. Compared to this, the most N-selective catalyst (**1$_{L2}$-Cl**) shows qualitative differences. For the formation of the O-product, the five-membered transition state (**O-TS5a**) remains favored by 28.3 kJ·mol^{-1}. In contrast, for the generation of the N-product, the three-membered transition state (**N-TS5b**) is preferred by 4.8 kJ·mol^{-1}. With that, a competition between pathway B and pathway C is expected for this catalyst. The higher selectivity to the N-product compared to the model catalyst is not reproduced with identical effective Gibbs free energies of activation for the C–N (ΔG_A = 62.8 kJ·mol^{-1}) and C–O coupling (ΔG_A = 62.7 kJ·mol^{-1}).

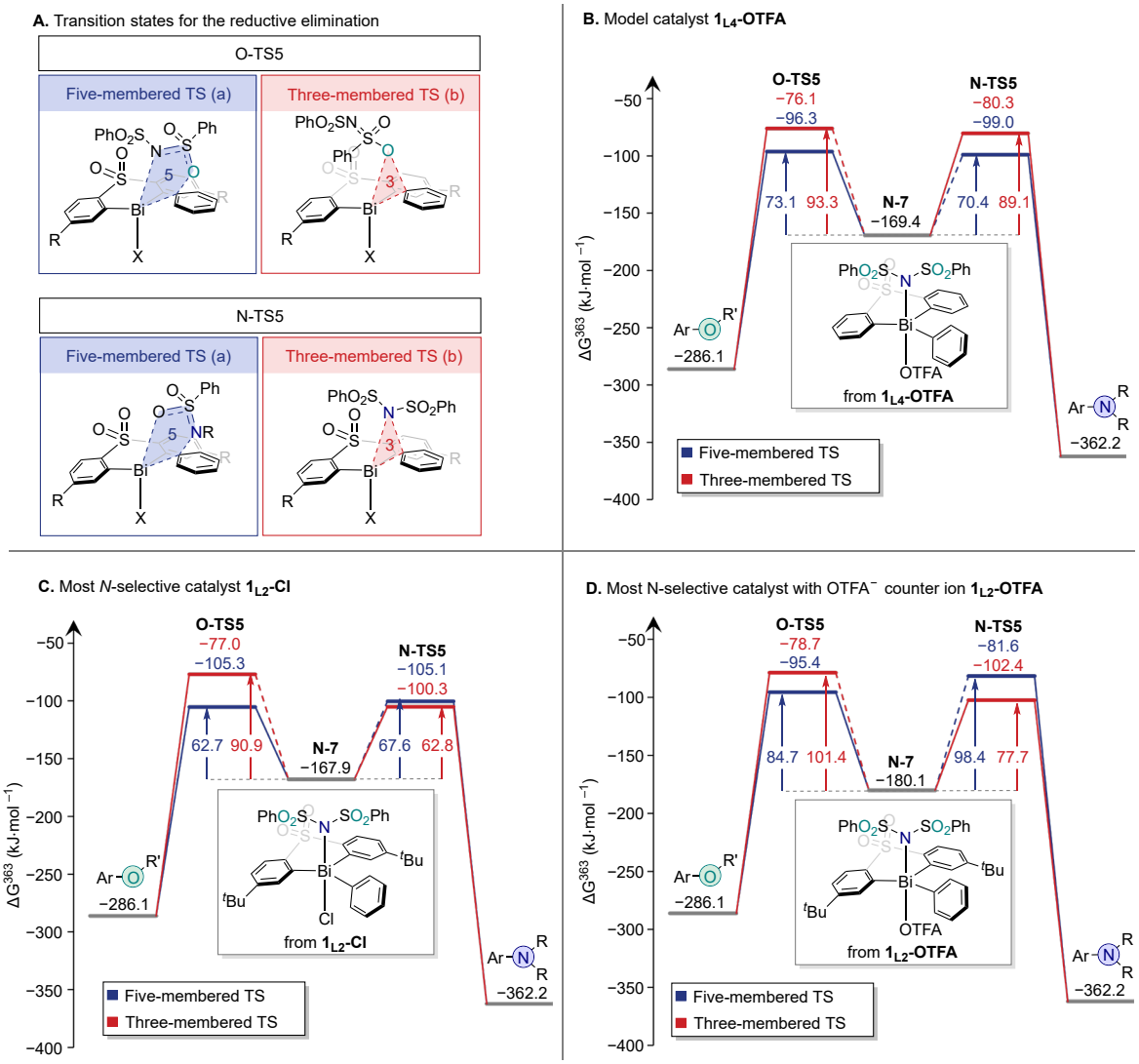

Figure 6.12: Exemplary coordination geometries for the five-membered and three-membered ring transition states (**A**) of the reductive elimination; X represents the counterion; R and R' are defined as shown in Figure 6.3; free energy diagrams for the model catalyst **1$_{L4}$-OTFA** (B), the most N-selective catalyst **1$_{L2}$-Cl** (C), and the most N-selective catalyst with OTFA as counterion **1$_{L2}$-OTFA** (D); for simplification the equilibria to **O-7** are not shown in the Figure and indicated by a dotted line; the *t*Bu group at the aryl substituent is not shown for clarity; ΔG^{363} in kJ·mol^{-1} relative to **1$_{L4}$-OTFA**, $ArB(OH)_2$ and NFSI; B3LYP-D4/def2-TZVP//COSMO(∞)-BP86-D4/def2-TZVP; COSMO-RS (chloroform).

With the step from **1$_{L4}$-OTFA** to **1$_{L2}$-Cl**, two properties of the catalyst were changed at the same time: the backbone (*t*Bu substitution instead of hydrogen atoms) as well as the counterion (Cl^- instead of $TFAO^-$). To investigate the isolated role of the ligand substitution on the changing mechanism while excluding effects by the counterion, **1$_{L2}$-OTFA** was investigated as well (Figure 6.12D). C–O coupling still proceeds through the five-membered ring transition state (**O-TS5a** is 16.7 kJ·mol^{-1} more stable than **O-TS5b**), whereas C–N coupling occurs preferentially via the three-membered transition state (**N-TS5b** is 20.8 kJ·mol^{-1} more stable than **N-TS5a**). The effective Gibbs free energy of activation for the formation of the N-product is 7.0 kJ·mol^{-1} lower than that for the O-product, qualitatively reproducing the experimental trend.

These findings emphasize the critical role of ligand substitution on the catalyst backbone. While the model catalyst mainly follows pathway B, introducing *t*Bu groups shifts the preference toward pathway C. The studied counterion changes, by contrast, exert little influence on the qualitative mechanism. Accurate modeling of C–N:C–O selectivities was shown to be challenging, with even the highest measured selectivity falling within the error limits of the computational methods. For instance, the most favorable ratio of 3.65:1.00 corresponds to a $\Delta\Delta G^{\ddagger}$ of only 3.9 kJ·mol^{-1}, which is below the threshold of chemical accuracy (1 kcal·mol^{-1} ≙ 4.2 kJ·mol^{-1})[252] and thus within the uncertainty of the applied theoretical methods. These constraints, combined with difficult conformational screening and multiple competing pathways, prevent the use of these calculations for predicting product distributions.

6.4.3 Full Catalytic Cycle

Combining the information for the individual steps, the full catalytic cycle can be closed (Figure 6.13).

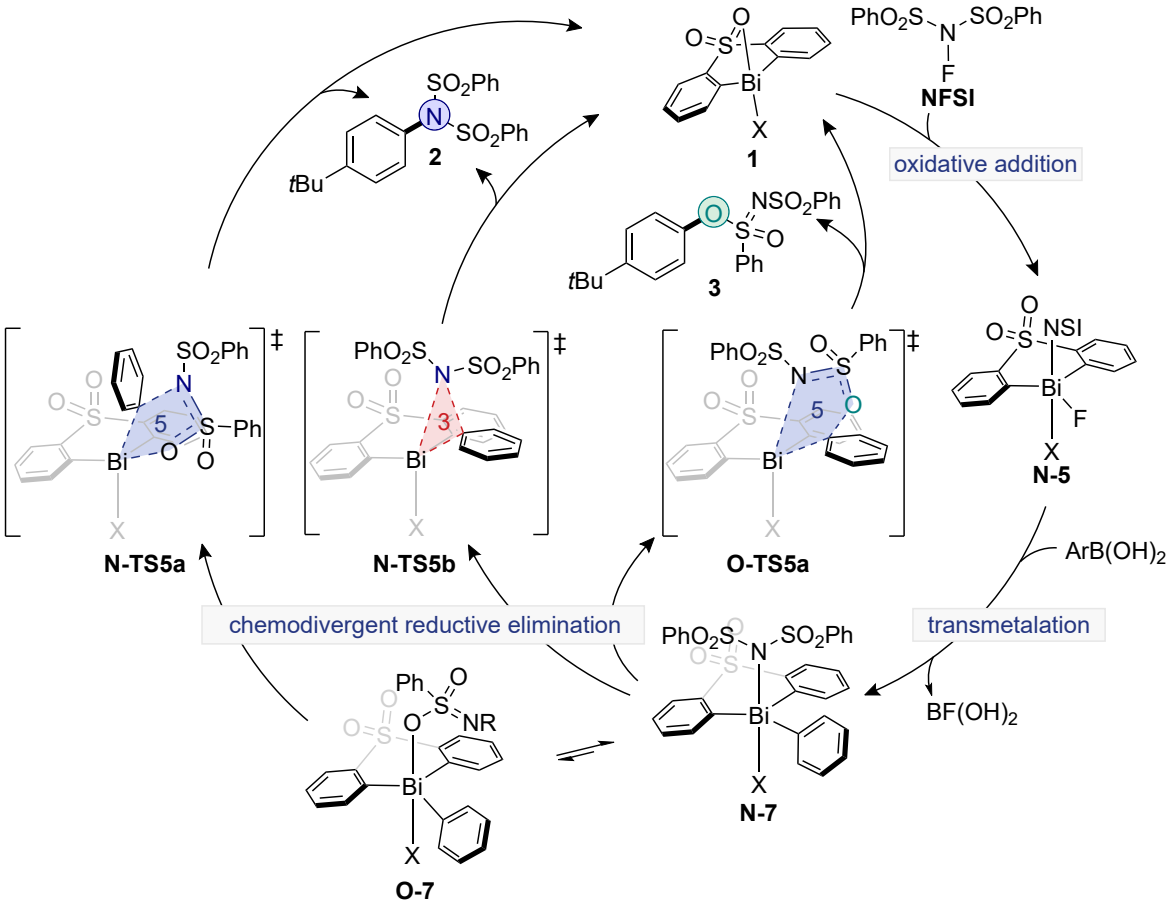

Figure 6.13: Proposed catalytic cycle for the Bi^{III}/Bi^{V} C–N/C–O chemodivergent coupling; X is a placeholder for the counterion; the *t*Bu groups at the aryl substituent are omitted for clarity.

Initially, the Bi^{III} resting state **1** gets oxidized in a stepwise, two-electron oxidative addition process of the substrate NFSI, forming the first Bi^{V} intermediate **N-5**.

Experimental NMR studies suggested that an exchange of the counterion to NSI could happen at this step of the catalytic cycle. After transmetalation with a boronic acid, the aryl substituent is introduced, yielding the N-bound intermediate **N-7**, which is in equilibrium with the O-bound form **O-7**. The transition states for the reductive elimination are accessible from these two intermediates. For the generation of the C–O coupled product **3**, only a five-membered ring transition state (**O-TS5a**) is expected. For the formation of the C–N coupled product **2**, however, a competition between a five- and three-membered ring transition state is possible.

6.4.4 Statistical Modeling

To overcome the challenges faced in the mechanistic studies, statistical modeling was performed, since typically small selectivity differences can be reproduced, often achieving sub-kcal accuracy.[7,303] The experimental results obtained in chloroform were selected for this analysis because that dataset contained the most data. As the response variable, the selectivity was used; however, to directly relate the selectivity to the difference in Gibbs free energy of activation, the selectivity was transformed into a measured ΔΔG term (Equation 6.1). The values obtained for the different complexes (Figure 6.14) are listed in Table 6.1.

$$\Delta\Delta G^{\ddagger}_{measured} = \Delta G^{\ddagger}_{N} - \Delta G^{\ddagger}_{O} = -R \cdot T \cdot \ln(Sel) \qquad 6.1$$

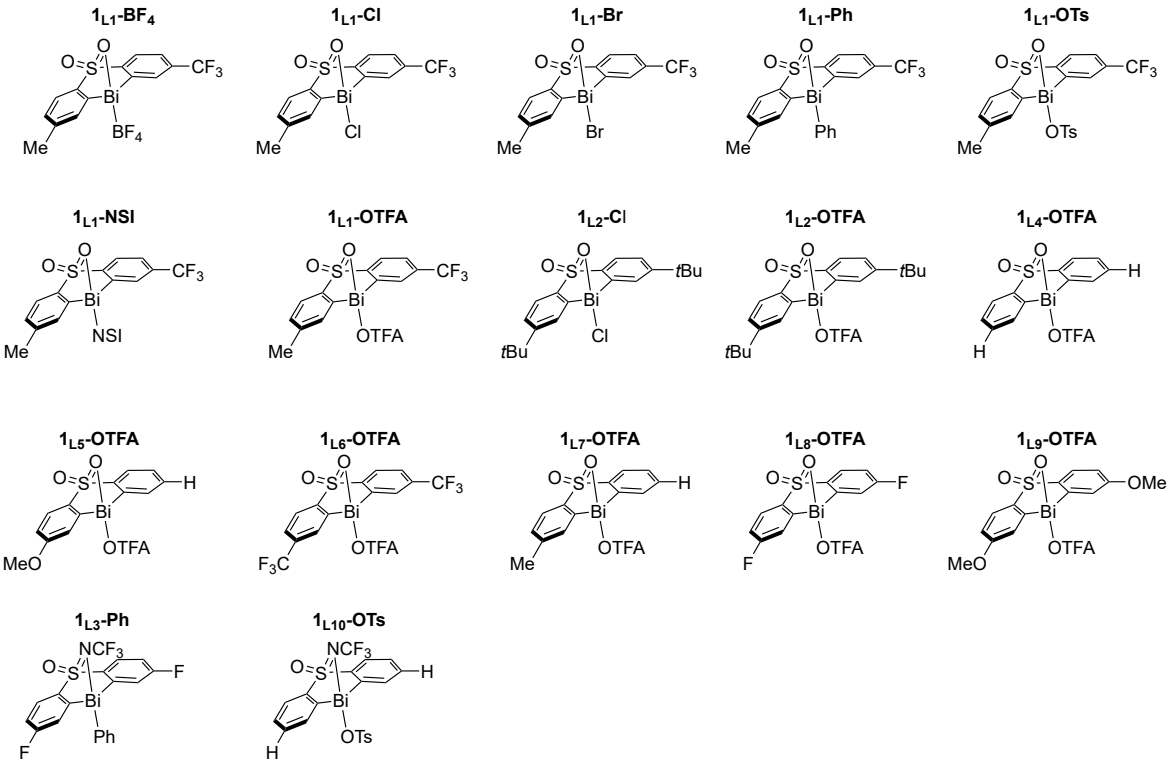

Figure 6.14: Ligand nomenclature; selectivities and assignment to training or validation set are documented in Table 6.1.

Table 6.1: Complex names, experimental selectivities Sel(C–N:C–O) and $\Delta\Delta G^{\ddagger}$(N–O) obtained from $\Delta\Delta G^{\ddagger} = -R \cdot T \cdot \ln(sel)$; as well as whether the point is in the training (train.) or validation (valid.) set or considered as an outlier.

Complex	Sel (C–N:C–O)	$\Delta\Delta G^{\ddagger}_{measured}$ ($kJ \cdot mol^{-1}$)	Train./valid. or outlier
1_{L1}-Cl	3.0	−3.3	train.
1_{L1}-Br	2.2	−2.4	train.
1_{L1}-Ph	2.5	−2.7	train.
1_{L1}-OTs	2.0	−2.0	valid.
1_{L1}-NSI	2.4	−2.6	train.
1_{L1}-BF_4	1.9	−2.0	train.
1_{L1}-OTFA	2.1	−2.2	train.
1_{L2}-Cl	3.7	−3.9	valid.
1_{L2}-OTFA	2.8	−3.1	train.
1_{L4}-OTFA	2.1	−2.3	train.
1_{L5}-OTFA	2.1	−2.3	train.
1_{L6}-OTFA	1.6	−1.4	train.
1_{L7}-OTFA	2.7	−3.0	valid.
1_{L8}-OTFA	1.8	−1.8	train.
1_{L9}-OTFA	1.9	−2.0	train.
1_{L3}-Ph	0.8	0.8	outlier
1_{L10}-OTs	1.0	−0.1	outlier

When plotting the data distribution (Figure 6.15 left), two outliers were identified and excluded: **1_{L13}-OTs**, which produced approximately a 1:1 mixture, and **1_{L3}-Ph**, which yielded more O-product than N-product, contrary to the excess of the N-product observed with all other catalysts. Structurally, these catalysts feature sulfoximine rather than sulfone backbones. After excluding the outliers, the dataset was split into a training and a validation set employing a 12:3 split (Figure 6.15 right). For this, an equidistant splitting across output values was used.

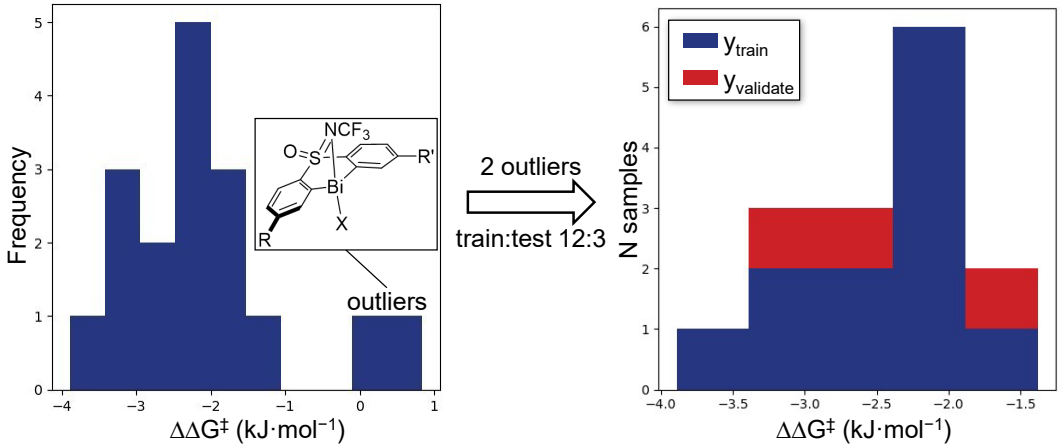

Figure 6.15: Two outliers were ignored, and a train:validation splitting of 12:3 was applied.

The first attempt was to build models based on the Bi^{III} starting complexes **1** (Figure 6.16). However, the statistical measures for the best found model are not satisfactory, with an R^2 of 0.63 for the training, a significantly decreased Q^2 (0.35), and a validation R^2 of 0.54. Furthermore, two steric parameters were used ($\%V_{bur}$ at C^4 and C^1). Using only steric parameters without electronic descriptors is uncommon, as this approach cannot capture the combined effects of steric and electronic factors.[304] These findings indicate that the features of the Bi^{III} resting state do not adequately capture the complexity of the selectivity-determining reductive elimination step.

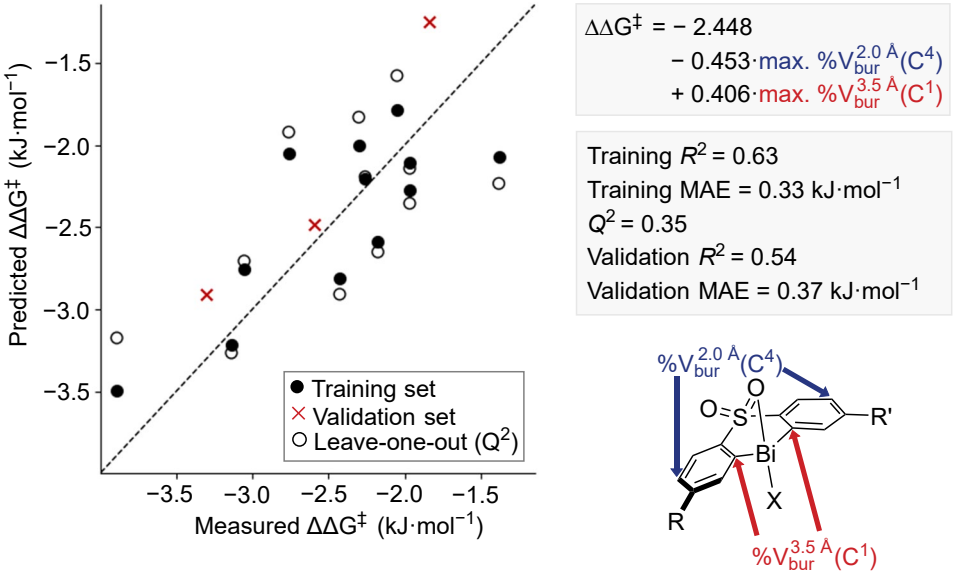

Figure 6.16: Best multivariate linear regression model for the Bi^{III} starting complex **1**; R, R', and X are placeholders for the individual complexes and are defined as shown in Figure 6.14.

In the next step, the Bi^{V} complexes **N-7** were used for the feature calculation. As a key intermediate, this structure may capture the reductive elimination better than the starting complex. Indeed, a model with better statistical measures was found (Figure 6.17). The training R^2 of 0.80, paired with a decently decreased Q^2 of 0.64, is acceptable for an explanatory model. The validation set is predicted fairly well (R^2 = 0.69).

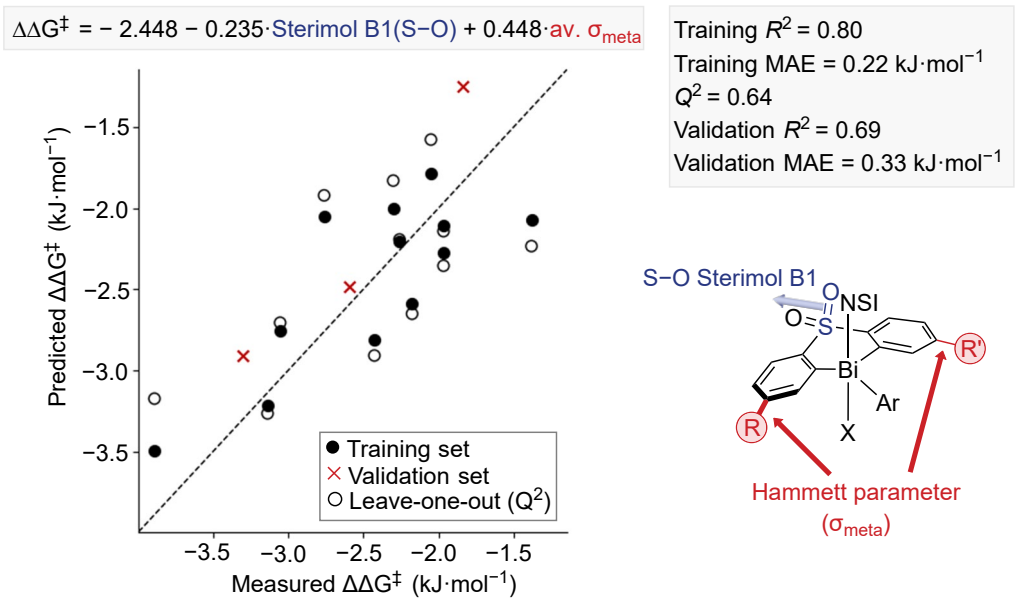

Figure 6.17: Best multivariate linear regression model for the Bi^{V} intermediate **N-7**; R, R', and X are placeholders for the individual complexes and are defined as shown in Figure 6.14.

The features present in the best found MLR model for the intermediate **N-7** are a Hammett parameter (σ_{meta}) for the backbone substitution in combination with a Sterimol B1 value (S–O bond, see Figure 6.17). Upon further inspection of these features in a plot of the response variable ($\Delta\Delta G^{\ddagger}_{measured}$) vs. features, it becomes clear that both features are highly classifying (Figure 6.18). While this is in the nature of the Hammett parameter, this is unexpected for the Sterimol feature. Effectively, the Hammett parameter classifies the backbone substitution, and the Sterimol parameter the counterion. As a result, the MLR model only learns the backbone/counterion combination, limiting its usefulness for obtaining chemical insights.

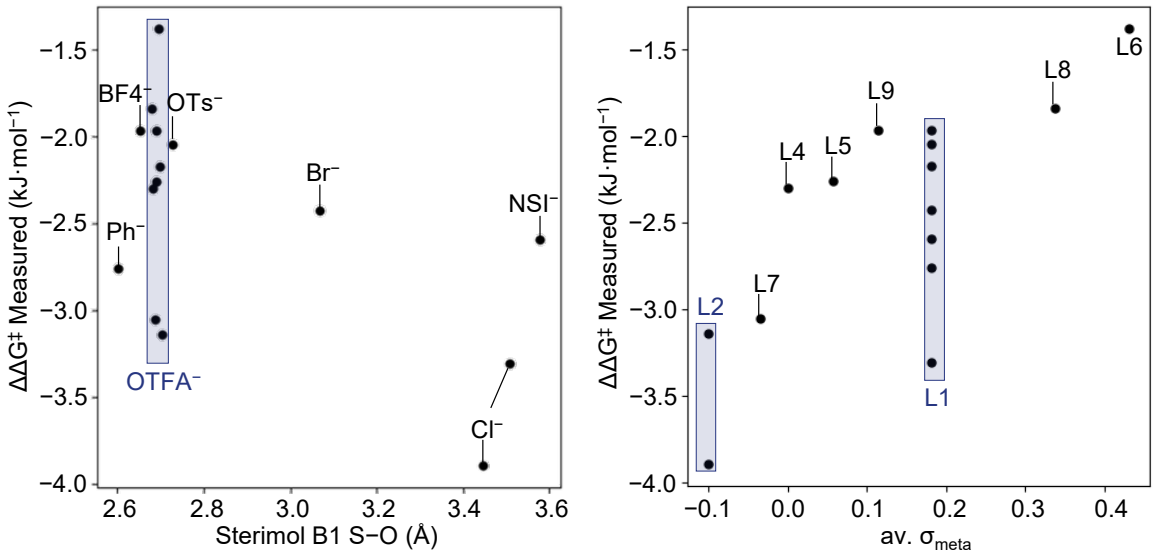

Figure 6.18: Plot of $\Delta\Delta G^{\ddagger}$ vs. the features for the Bi^{V} intermediate **N-7**; unscaled features were used for this plot; the Sterimol plot is labeled with the counterions, and the plot for the Hammett parameter with the ligand names.

The search for a meaningful intermediate within the catalytic cycle to enable statistical modeling led to the bismuthonium complex **9**$^+$ (Figure 6.19A). The connection between a species with a dissociated ambident nucleophile and selectivity is not immediately clear. However, the bismuthonium intermediate may mimic the asynchronous three-membered ring transition state of the reductive elimination. As described in Section 6.4.2, asynchrony arises from the dissociation of the Bi–NSI bond, which occurs mainly before changes in other bond lengths, leading to a buildup of positive charge on the Bi center. In the extreme scenario of the asynchrony, the stepwise outer-sphere reaction results in the formation of an intermediary bismuthonium complex.

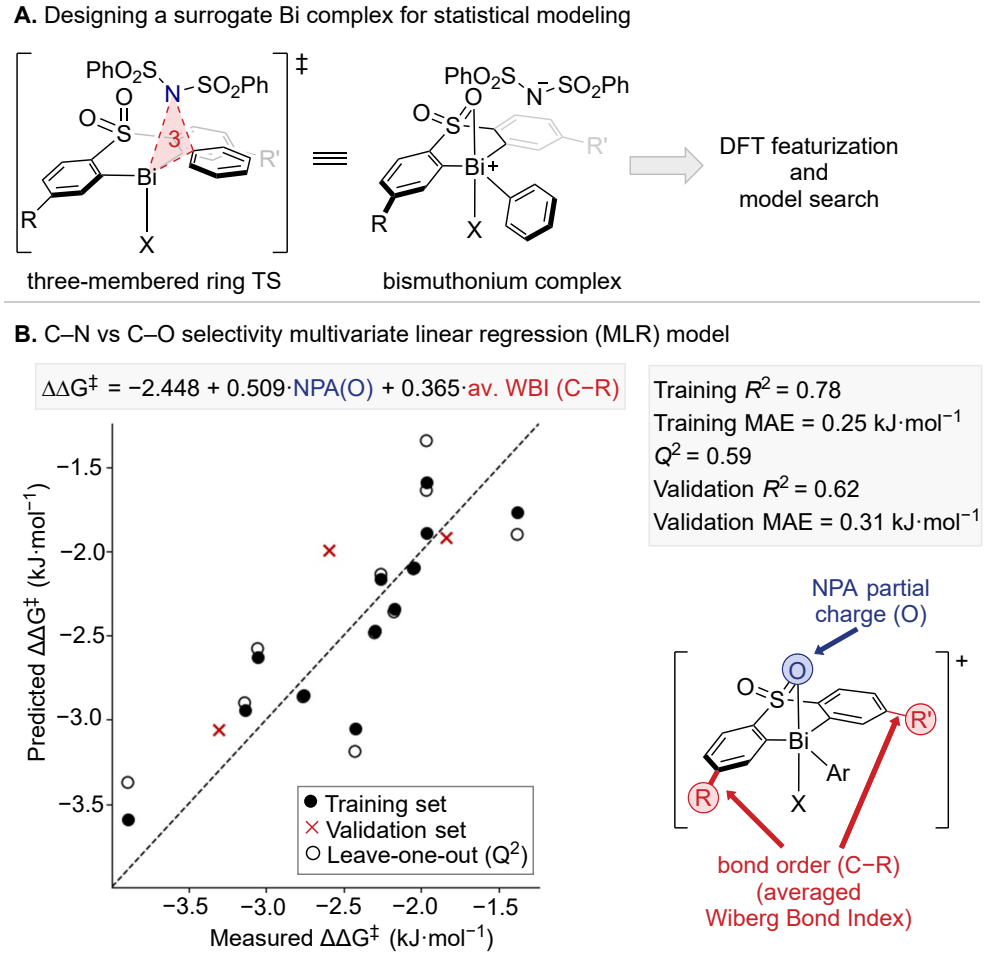

Figure 6.19: Surrogate complex to mimic the three-membered ring transition state for the reductive elimination (**A**) and best multivariate linear regression model for the bismuthonium intermediate **9**$^+$ (**B**); R, R', and X are placeholders for the individual complexes and defined as shown in Figure 6.14.

A good MLR model was found using the features of the bismuthonium complex with adequate training and cross-validation statistics (R^2 = 0.78; MAE = 0.25 kJ·mol^{-1}, leave-one-out cross-validation Q^2 = 0.59). Additionally, the validation set was predicted with moderate accuracy, yielding an R^2 value of 0.62 and an MAE of 0.31 kJ·mol^{-1}. The MLR model uses as molecular features the atomic partial charge of the oxygen atom coordinated to bismuth (NPA charge from a natural population analysis) and the average Wiberg bond index (WBI) of both ligand sides of the C–R bond, *meta* to bismuth

on the ligand aryls. Both features of the MLR model have positive coefficients; consequently, a more negative O partial charge and a smaller WBI lead to a more negative $\Delta\Delta G^{\ddagger}$ and hence higher selectivity for formation of the C–N coupled product **2**.

The mechanism calculations indicated that the three-membered ring transition state is increasingly important for complexes yielding high selectivity to product **2**. Aligning these findings with the outcome of the MLR analysis, the more negative partial charge on the oxygen atom could lead to enhanced coordination of the sulfone group to Bi. This may result in a higher stability of a three-membered reductive elimination transition state, which is structurally and electronically close to a bismuthonium intermediate. The WBI probes the bond order of the ligand substitutions. Furthermore, it intrinsically reflects the steric bulk of the substituent, correlating strongly ($R^2 = 0.92$) with two Sterimol parameters that measure substituent length and width (Figure 6.20). Thus, the WBI feature incorporates bond order and steric information without needing a model with more features.

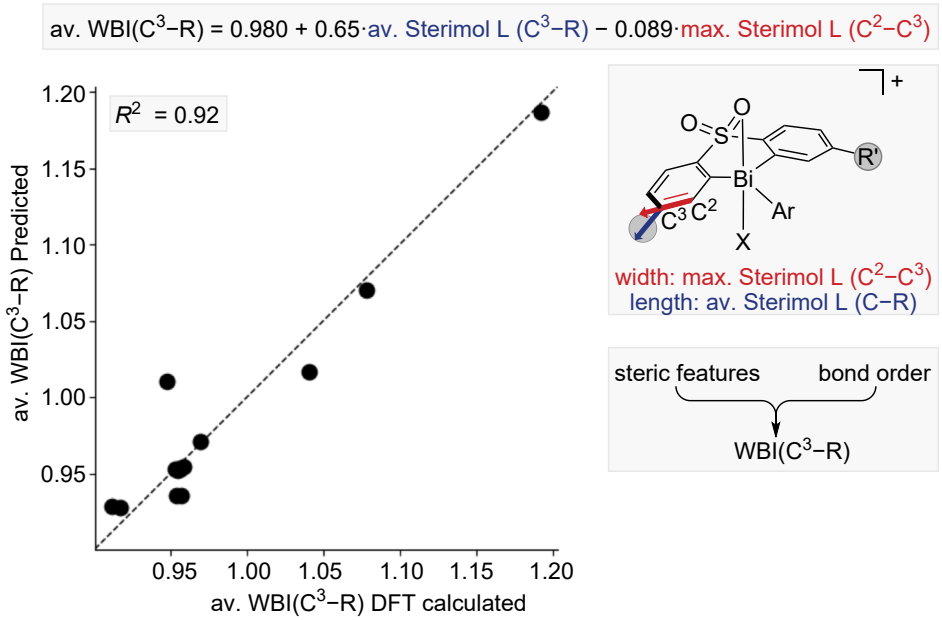

Figure 6.20: Regression of the WBI feature revealed two steric features, which are incorporated in the bond order, effectively measuring the length and width of the substituents R (hidden for clarity) and R'; R, R', and X are placeholders for the individual complexes and defined as shown in Figure 6.14.

An analysis of the relationship between the response variable and the WBI feature reveals its highly classifying nature (Figure 6.21 left), which is not observed for the corresponding plot of the response variable against the NPA charge (Figure 6.21 right).

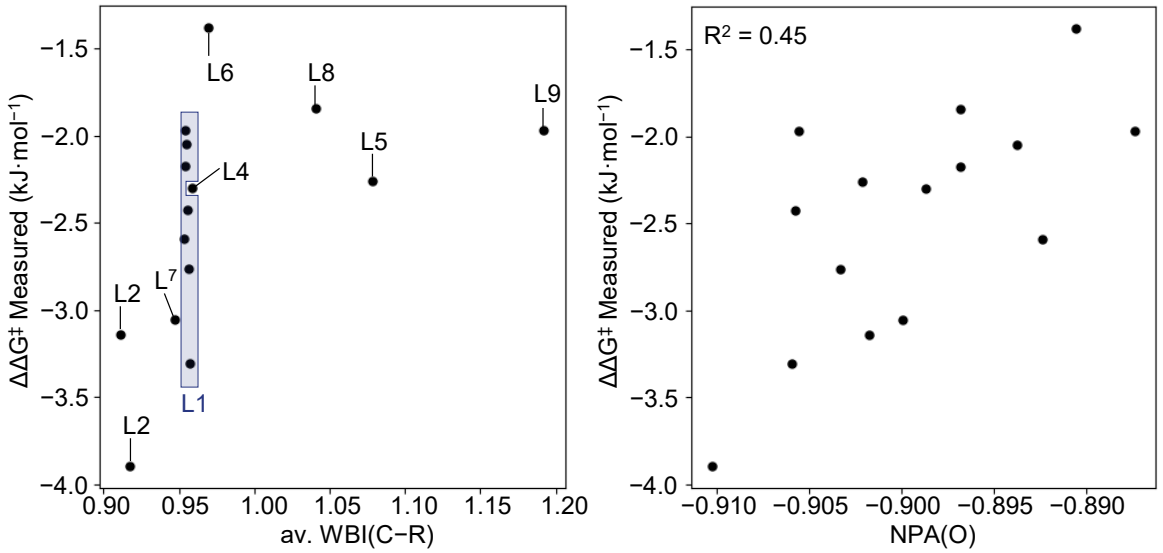

Figure 6.21: ΔΔG‡ vs. feature plot for the best multivariate linear regression model for the bismuthonium complexes **9**⁺; unscaled features were used for this plot.

To further test this MLR model on the predictivity of unseen, external data, a train/validation/test split (9:3:3 data points) was applied (Figure 6.22). While retaining comparable accuracy for the training set (R^2 = 0.80, MAE = 0.25 kJ·mol^{-1}, Q^2 = 0.53), the model showed reasonable predictivity for the validation set (R^2 = 0.61, MAE = 0.32 kJ·mol^{-1}) as well as the test set (R^2 = 0.64, MAE = 0.22 kJ·mol^{-1}). This result underpins the robustness of this model.

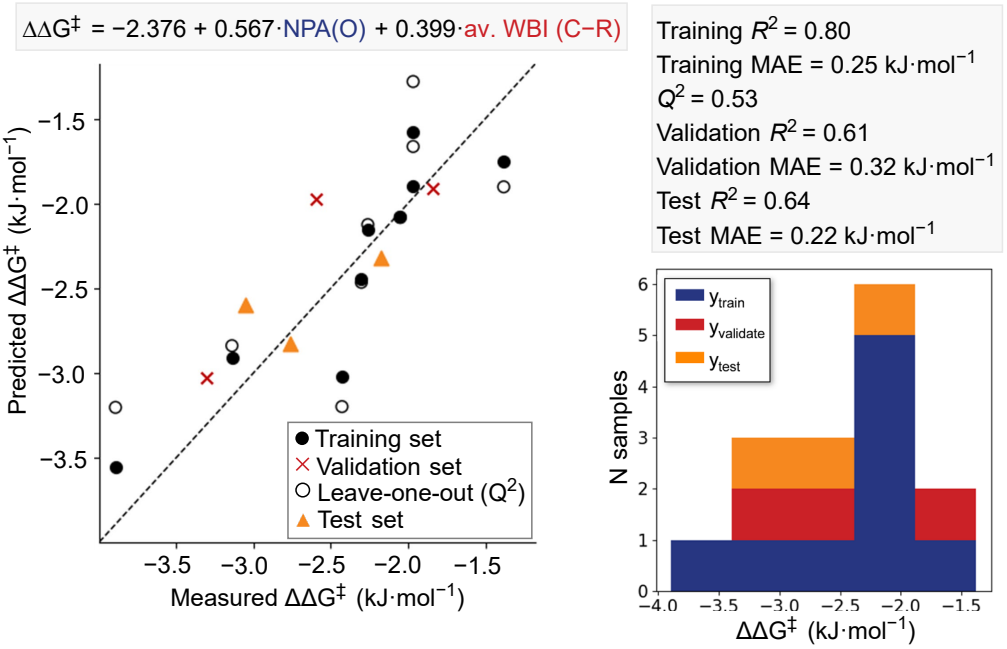

Figure 6.22: Train/validation/test split of 9:3:3 to ensure the robustness of the model, as well as the resulting MLR model.

The success of the featurization and statistical modeling based on the bismuthonium species (**9**$^{+}$) is most consistent with a three-membered ring reductive elimination transition state, favoring the generation of the N-product **2** (pathway C). This pathway becomes more important for catalysts with suitable electronic (NPA at oxygen) and steric (WBI C–R) properties to stabilize a bismuthonium substructure in a three-membered transition state more effectively, resulting in a higher predicted selectivity to product **2**. With that, the statistical modeling is capable of reading out the tendency of this pathway getting more relevant compared to the pathway exclusively via five-membered ring transition states (pathway B).

6.5 Summary and Outlook

DFT computations revealed a stepwise, two-electron oxidative addition process. This was determined as the rate-limiting step. After the oxidative addition, transmetalation with the aryl boronic acid can take place. The reductive elimination was identified as the selectivity-determining step. For the reductive elimination, different scenarios were investigated. A pathway involving open-shell Bi^{IV} species was ruled out by DFT. A Curtin-Hammett scenario based on an equilibrium between an N- and O-bound Bi^{V} intermediate and five-membered ring transition states was shown not to explain the chemodivergence for every catalyst. Comparison of different catalysts showed that, in cases of higher selectivity for the N-product, the three-membered ring transition state becomes competitive or even dominant for the C–N coupling. For the formation of the O-product, the three-membered ring transition state was never predicted to be competitive with the five-membered ring. The five-membered ring transition state was shown to proceed in a synchronous and the three-membered ring transition state in an asynchronous manner. An outer-sphere reaction was studied as well, but due to difficulties of the description of charge separation processes, no direct comparison to the concerted transition states was performed.

Statistical modeling was conducted to reproduce the experimentally observed C–N/C–O selectivities and relate them to interpretable molecular descriptors. Model building using features from the Bi^{III} resting state did not result in satisfactory models. Similarly, incorporating features from the Bi^{V} intermediate involved in the reductive elimination step did not yield readily interpretable models, since the catalysts were only classified based on ligand substitution and counterion type without using chemically interpretable descriptors. A bismuthonium intermediate was identified as an important substructure in the three-membered ring transition state. In fact, a convincing model was found for this species. The MLR model included the NPA charge at the oxygen atom coordinated to bismuth, along with the WBI bond order of the ligand substitutions. The latter one was also shown to resemble the steric properties of the substituents. Catalysts with suitable electronic and steric properties likely stabilize a bismuthonium substructure better and thus lead to a preference for a three-membered ring transition state. With that, the tendency of the mechanism for the reductive elimination, changing from exclusively via five-membered ring transition states to three-membered ring transition states yielding the N-product, was captured by the MLR model. This MLR model could be the foundation for future studies, including ligand optimization to achieve improved yields for the N-product. While this computational study focused on the sulfone ligands, future research may also include the sulfoximine ligands.

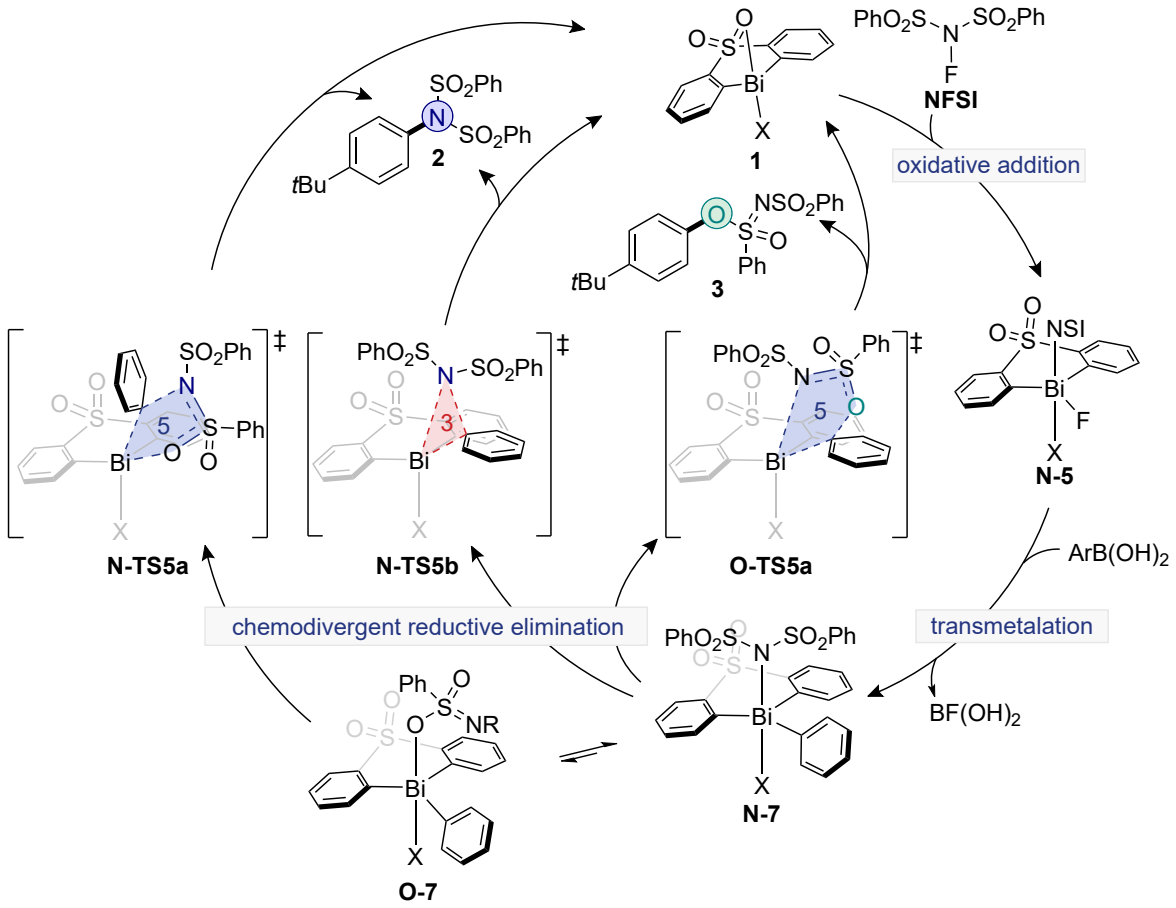

Figure 6.23: Proposed catalytic cycle for the Bi^{III}/Bi^{V} C–N/C–O chemodivergent coupling; X is a placeholder for different counterions; the *t*Bu groups at the aryl substituent are omitted for clarity.

7

Summary and Perspective

7.1 Summary

In this thesis, four projects were presented, showcasing the use of computational chemistry for mechanistic investigations in homogeneous catalysis. Each chapter concludes with its own, more detailed summary.

Organocatalytic Isomerization of *exo*- to *endo*-Vinylene Carbonates:

In the first project, mechanistic studies for the organocatalytic isomerization of *exo*- to *endo*-vinylene carbonates were performed. The catalytic system consists of an organic base and a phenol. The active form of the catalyst was shown to be a charged contact ion pair of $TBDH^+$ with PhO^-. In a ring-opening mechanism, the phenolate enables the ring-opening, and TBD acts as a proton shuttle. Additionally, a ring-retaining pathway was found, which is only accessible for substrates bearing an aryl substituent. A central computational challenge tackled in this project was the accurate modeling of charge separation and recombination processes, for which proper solvation treatment and the consideration of contact ion pairs were key to achieving accurate results. Based on these quantum-chemical calculations, a control experiment was designed to obtain the ring-opened ketone from both the starting material and product, using excess phenol to shift the equilibrium.

Cu^{II}-Catalyzed Amination of Aryl Chlorides in Aqueous Ammonia:

For this project, quantum-chemical calculations were performed on a Cu^{II} catalytic system for the synthesis of substituted anilines as building blocks starting from widely available aryl chlorides and aqueous ammonia. The active catalyst was shown to transform chlorobenzene to aniline in a radical-mediated S_NAr reaction. Compared to free, anionic S_NAr reactions, C–F bonds are not aminated by the Cu^{II} system. The reason for this was investigated with fluorobenzene as a model system, showing poisoning of the catalyst with resulting Cu^{II}-fluorido complexes as a thermodynamic sink. The accurate description of Cu^{II} species turned out to be challenging and strongly functional-dependent. Among the tested (single point) methods, ωB97x-D turned out as a reasonable choice. In this project, DFT demonstrated limitations in modeling weakly bound solvent molecules, as it identified only strong coordination or no coordination at all, which is inconsistent with previous findings.[212-214] Tailored spectroscopic experiments were conducted to obtain evidence for the involvement of a Cu^{II}-amido species in solution. UV/vis spectra revealed an isolated charge-transfer band, characteristic of Cu^{II}-amido complexes, as confirmed by DFT calculations.

Future studies could examine the selectivity of amination at C–Cl versus C–F bonds in substrates containing both bond types within a single molecule. The insights gained

from DFT can help guide the design of new ligands, improving the efficiency of the catalysis at reduced temperatures.

Cu^{I}-Catalyzed Alkynylations:

In this project, mechanistic studies were carried out for the selective synthesis of propargyl alcohol starting from acetylene and formaldehyde using a Cu^{I}-phenanthroline catalyst, while suppressing the double reaction to butynediol. Phenylacetylene was used for the screening of reaction mechanisms as a model alkyne. A dinuclear Cu^{I}-phenylacetylide complex was found to be a resting state. The mononuclear Cu^{I}-phenylacetylide complex can undergo a nucleophilic attack on formaldehyde after performing a bend of the σ-bound phenylacetylide to an $\eta^2(\pi)$-bound phenylacetylide unit. Protonation and product liberation proceed with phenylacetylene as the proton source. The mechanism was transferred to acetylene. The activation barriers for the first and second reactions with formaldehyde are close to each other. Kinetic modeling suggested that the selectivity is primarily steered by concentrations of acetylene and formaldehyde.

These results may form a basis for follow-up studies, including the exploration of other (activated) aldehydes or ketones as substrates. Additionally, future work could aim to achieve a detailed computational understanding of the resting states of the Cu^{I}-acetylide complexes and also include oligonuclear structures, representing a significant challenge.

Ligand-Controlled Chemodivergent Bismuth Catalysis:

The objective of this computational study was to understand the origin of selectivity in a bismuth-catalyzed coupling reaction between NFSI and an aryl boronic acid, which experimentally yields both C–N and C–O coupled products. A stepwise, two-electron oxidative addition process was identified as the rate-limiting step. The aryl substituent is introduced by a boronic acid derivative in a subsequent transmetalation. The reductive elimination is the selectivity-determining step. Comprehensive studies revealed two pathways for the reductive elimination, via a five- and a three-membered ring transition state. Depending on the catalyst, the primarily preferred pathway changes. While the C–O coupled product is exclusively formed via a five-membered ring transition state, highly C–N selective catalysts feature a competitive or even dominant three-membered ring transition state.

Accurately predicting small energy differences for a reaction involving complex conformational landscapes and competing mechanistic pathways posed significant computational challenges. These were overcome by employing statistical modeling, which enabled rationalization and reproduction of the observed C–N/C–O selectivity. A bismuthonium substructure in the three-membered ring transition state emerged as the key surrogate structure. An explanatory MLR model was found, capturing the switch from five- to three-membered ring transition states in reductive elimination. Future research may involve a virtual screening to optimize more selective catalysts.

7.2 Perspective

7.2.1 Future Challenges for Computational Chemistry

Computational chemistry is a rapidly evolving research field, with continuous advances in computational techniques. Despite significant progress, several limitations remain, in particular for organometallic chemistry.[1-3] This outlook highlights four main areas of active research and future challenges for method development: (i) faster and more reliable computational methods, (ii) automation of reaction network exploration, (iii) statistical modeling, and (iv) hardware advances (Figure 7.1).

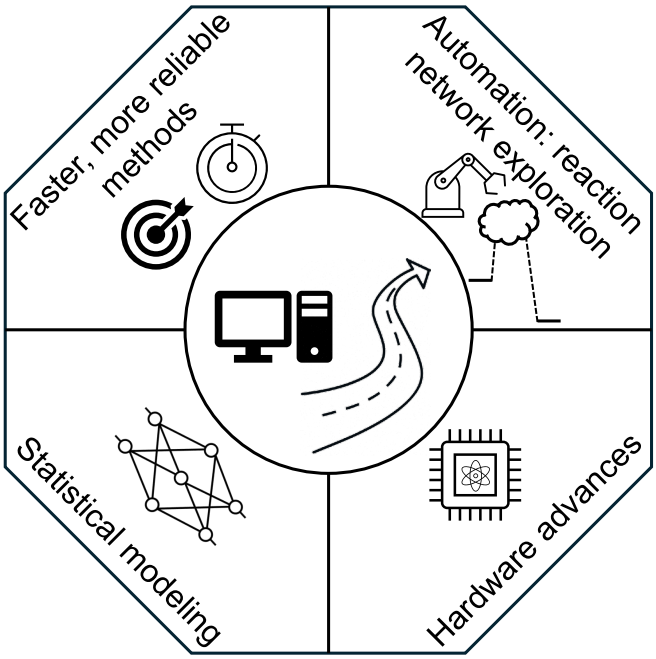

Figure 7.1: General outlook for the field of computational chemistry: four examples of promising ongoing method developments.

7.2.2 Faster and More Reliable Methods

A prevailing challenge in computational chemistry, particularly when metal atoms are present, is finding a balance between accuracy and computational efficiency. Ongoing method development is directed toward creating fast and reliable approaches. These methods include semiempirical quantum mechanical (SQM) methods and machine learning-based interatomic potentials (MLIPs).[18]

Physics-based SQM methods achieve computational efficiency by approximating the electronic structure problem with a minimal basis set and parameterized Hamiltonians.[18] Among other approaches (such as PM6[305-307] or DFTB[308-313]), extended tight binding (xTB) has emerged as the most prominent choice due to its broad applicability for all *s*-, *p*-, and *d*-block elements and its robustness.[17-18,314] xTB was heavily used in this thesis for the screening of potential energy surfaces (PES) and conformational search. Currently, a new version of xTB (general-purpose extended

tight-binding, g-xTB)[315] is under development, showing promising accuracy on a variety of benchmark sets, achieving the accuracy of medium-level DFT, with the promise of maintaining the low computational cost. Future studies will investigate the reliability of g-xTB. Nevertheless, limitations arise from the use of a minimal basis set.[316]

Compared to SQM, MLIPs have the same idea of application; however, they are purely data-based methods. MLIPs are trained on a database of typical density functional theory (DFT) calculations.[317] Highly parametrized neural network architectures are employed to map the energy and its first derivatives to the molecular structure. Most recent methodologies, such as MACE-OFF23,[318] AIMNet2[317], or STRUCTURES25[319] represent the first generation of MLIPs with broader applicability and transferability. While typically even faster than SQM, most MLIPs are only trained for organic molecules, not transition metals. Furthermore, the interpretability of the results is worse than with SQM, since no electronic structure is calculated.[316] Ongoing research focuses on the extension to more elements, thus enhancing the application range, which would enable broader use in modeling homogeneous catalysis.[317]

7.2.3 Automation of Reaction Network Exploration

A major hurdle in computational chemistry, particularly for organometallic complexes, is the automation of reaction network exploration.[2] While reaction-rule-based methods are often effective for organic compounds, they struggle to describe metal complexes accurately. Furthermore, conventional cheminformatic representations, such as SMILES[320] or SELFIES[321], cannot adequately capture complex coordination environments.[322-323] Although a few examples of fully automated PES screenings for homogeneous catalysis exist, such as those by the Zimmermann[324-326] or Reiher[327] groups, examples remain rare. Recent advances in large language models (LLMs) have introduced new opportunities for natural language controlled automation; however, they have not yet solved the underlying problem of accurately describing complex organometallic systems.[322] Consequently, method developments should not only focus on the employed level of theory (e.g., xTB) and transition state search strategies (e.g., MGSM), but also on improving the representation of organometallic complexes.

7.2.4 Statistical Modeling

Statistical modeling is used increasingly to bridge the gap between experimental and computational chemistry by correlating calculated descriptors to reaction outcomes, such as yields or selectivities.[7] Many literature reports (exemplarily [328-329] from the Sigman group) show that this approach enables extrapolation to new catalysts, offering predictive power beyond traditional mechanistic intuition. High-throughput experimentations can provide large, high-quality datasets that are crucial for training robust machine learning models; however, especially for transition metal catalysts, fewer datasets are available.[2] An example by Doyle and coworkers on C–N cross-coupling reactions showed potential for a broader applicability,[330] yet most reported

statistical models are restricted to the small chemical space they were trained on, showing limited transferability. Efforts to train neural networks on more diverse datasets from publications, patents, and electronic lab journals have not yet been successful.[331] While new machine learning models are advancing this field, challenges persist with data quality, availability, and model adaptability.[332-333]

7.2.5 Hardware Advances

The rapid advancements of computational resources have been fundamental to establishing computational chemistry as an important research field.[2] Historically, performance improvements were closely related to transistor scaling, as described by Moore's law,[334] which predicted that the number of transistors on a microchip would double every two years. In recent years, this trend, particularly for central processing unit (CPU) architectures, slowed down because of physical and economic constraints in transistor miniaturization. Consequently, performance gains are increasingly driven by innovations in processor architecture, software optimization, and parallelization.[335] As a result of this shift, graphics processing units (GPUs) gained importance. GPUs were initially designed for image processing, but their massively parallel architecture also makes them applicable to scientific computing. Nevertheless, exploiting the potential of GPUs requires dedicated software optimization.[336] While a promising acceleration was already shown, development is still ongoing.[335,337-339]

In 1982, Feynman noted that classical computers face fundamental limitations in simulating quantum mechanical systems, motivating the development of quantum computers.[340] Quantum computers are based on the exploitation of quantum effects, such as superposition or quantum interference, in fundamentally new ways. Nowadays, quantum hardware is still limited by low qubit counts and high error rates.[341] Yet, the emerging technology has already seen some promising developments, particularly for hybrid quantum-classical approaches. In the context of homogeneous catalysis, auxiliary-field quantum Monte Carlo methods have been proposed to use quantum hardware for generating trial wave functions, which could help address multireference problems.[342] While such applications remain largely conceptual and are not yet effective in practice, they illustrate how quantum computing may eventually impact molecular simulations in the future.[343]

8

References

[1] V. Butera, *Phys. Chem. Chem. Phys.* **2024**, *26*, 7950-7970.

[2] I. Funes-Ardoiz, F. Schoenebeck, *Chem.* **2020**, *6*, 1904-1913.

[3] C. Poree, F. Schoenebeck, *Acc. Chem. Res.* **2017**, *50*, 605-608.

[4] M. Bursch, J.-M. Mewes, A. Hansen, S. Grimme, *Angew. Chem. Int. Ed.* **2022**, *61*, e202205735.

[5] S. Ahn, M. Hong, M. Sundararajan, D. H. Ess, M.-H. Baik, *Chem. Rev.* **2019**, *119*, 6509-6560.

[6] J. N. Harvey, F. Himo, F. Maseras, L. Perrin, *ACS Catal.* **2019**, *9*, 6803-6813.

[7] C. B. Santiago, J.-Y. Guo, M. S. Sigman, *Chem. Sci.* **2018**, *9*, 2398-2412.

[8] J. Harvey, *Computational Chemistry*, Oxford University Press, Oxford, **2018**.

[9] F. Jensen, *Introduction to Computational Chemistry*, Wiley-VCH, Weinheim, **2017**.

[10] W. Koch, M. C. Holthausen, *A Chemist's Guide to Density Functional Theory*, Wiley-VCH, Weinheim, **2001**.

[11] A. Szabo, N. S. Ostlund, *Modern Quantum Chemistry*, McGraw-Hill, Inc., New York, **1989**.

[12] L. Goerigk, A. Hansen, C. Bauer, S. Ehrlich, A. Najibi, S. Grimme, *Phys. Chem. Chem. Phys.* **2017**, *19*, 32184-32215.

[13] K. Houk, F. Liu, *Acc. Chem. Res.* **2017**, *50*, 539-543.

[14] S. Grimme, F. Bohle, A. Hansen, P. Pracht, S. Spicher, M. Stahn, *J. Phys. Chem. A* **2021**, *125*, 4039-4054.

[15] P. Pracht, F. Bohle, S. Grimme, *Phys. Chem. Chem. Phys.* **2020**, *22*, 7169-7192.

[16] S. Grimme, *J. Chem. Theory Comput.* **2019**, *15*, 2847-2862.

[17] C. Bannwarth, E. Caldeweyher, S. Ehlert, A. Hansen, P. Pracht, J. Seibert, S. Spicher, S. Grimme, *Wiley Interdiscip. Rev. Comput. Mol. Sci.* **2021**, *11*, e1493.

[18] C. Bannwarth, S. Ehlert, S. Grimme, *J. Chem. Theory Comput.* **2019**, *15*, 1652-1671.

[19] S. Spicher, S. Grimme, *Angew. Chem. Int. Ed.* **2020**, *59*, 15665-15673.

[20] G. Norjmaa, G. Ujaque, A. Lledós, *Top. Catal.* **2022**, *65*, 118-140.

[21] S. Müller, T. Nevolianis, M. Garcia-Ratés, C. Riplinger, K. Leonhard, I. Smirnova, *Fluid Ph. Equilib.* **2025**, *589*, 114250.

[22] A. V. Marenich, C. J. Cramer, D. G. Truhlar, *J. Phys. Chem. B* **2009**, *113*, 6378-6396.

[23] V. Barone, M. Cossi, *J. Phys. Chem. A* **1998**, *102*, 1995-2001.

[24] A. Klamt, G. Schüürmann, *J. Chem. Soc., Perkin Trans. 2* **1993**, 799-805.

[25] A. Klamt, *Wiley Interdiscip. Rev. Comput. Mol. Sci.* **2011**, *1*, 699-709.

[26] A. Klamt, V. Jonas, T. Bürger, J. C. Lohrenz, *J. Phys. Chem. A* **1998**, *102*, 5074-5085.

[27] F. Eckert, A. Klamt, *AlChE J.* **2002**, *48*, 369-385.

[28] A. Klamt, *J. Phys. Chem.* **1995**, *99*, 2224-2235.

[29] A. Klamt, *Wiley Interdiscip. Rev. Comput. Mol. Sci.* **2018**, *8*, e1338.

[30] P. Deglmann, S. Schenk, *J. Comput. Chem.* **2012**, *33*, 1304-1320.

[31] T. Gerlach, S. Müller, A. G. de Castilla, I. Smirnova, *Fluid Ph. Equilib.* **2022**, *560*, 113472.

[32] S.-T. Lin, S. I. Sandler, *Ind. Eng. Chem. Res.* **2002**, *41*, 899-913.

[33] W. M. C. Sameera, S. Maeda, K. Morokuma, *Acc. Chem. Res.* **2016**, *49*, 763-773.

[34] G. N. Simm, A. C. Vaucher, M. Reiher, *J. Phys. Chem. A* **2019**, *123*, 385-399.

[35] A. L. Dewyer, A. J. Argüelles, P. M. Zimmerman, *Wiley Interdiscip. Rev. Comput. Mol. Sci.* **2018**, *8*, e1354.

[36] H. Ryu, J. Park, H. K. Kim, J. Y. Park, S.-T. Kim, M.-H. Baik, *Organometallics* **2018**, *37*, 3228-3239.

[37] P. Zimmerman, *J. Chem. Theory Comput.* **2013**, *9*, 3043-3050.

[38] P. M. Zimmerman, *J. Chem. Phys.* **2013**, *138*, 184102.

[39] P. M. Zimmerman, *J. Comput. Chem.* **2015**, *36*, 601-611.

[40] J. Geiger, V. Settels, P. Deglmann, A. Schäfer, M. Bergeler, *J. Comput. Chem.* **2022**, *43*, 1662-1674.

[41] T. A. Young, J. J. Silcock, A. J. Sterling, F. Duarte, *Angew. Chem. Int. Ed.* **2021**, *60*, 4266-4274.

[42] A. Matsuzawa, J. N. Harvey, F. Himo, *Top. Catal.* **2022**, *65*, 96-104.

[43] M. Swart, *Dealing with Spin States in Computational Organometallic Catalysis*, in *New Directions in the Modeling of Organometallic Reactions* (Eds.: A. Lledós, G. Ujaque), Springer International Publishing, Cham, **2020**, pp. 191-226.

[44] H. Eyring, *J. Chem. Phys.* **1935**, *3*, 107-115.

[45] P. W. Atkins, *Physikalische Chemie*, (Eds.: A. Höpfner, A. Schleitzer, M. Bär), Wiley, Weinheim, **1996**, pp. 813.

[46] M. Hermsen, PhD thesis, Heidelberg University, **2018**.

[47] L. P. Hammett, *Chem. Rev.* **1935**, *17*, 125-136.

[48] L. P. Hammett, *J. Am. Chem. Soc.* **1937**, *59*, 96-103.

[49] L. P. Hammett, *Trans. Faraday Soc.* **1938**, *34*, 156-165.

[50] C. Hansch, A. Leo, R. W. Taft, *Chem. Rev.* **1991**, *91*, 165-195.

[51] H. H. Jaffe, *Chem. Rev.* **1953**, *53*, 191-261.

[52] J. D. Hirst, S. Boobier, J. Coughlan, J. Streets, P. L. Jacob, O. Pugh, E. Özcan, S. Woodward, *Artif. Intell. Chem.* **2023**, *1*, 100006.

[53] V. Mougel, C. B. Santiago, P. A. Zhizhko, E. N. Bess, J. Varga, G. Frater, M. S. Sigman, C. Copéret, *J. Am. Chem. Soc.* **2015**, *137*, 6699-6704.

[54] E. Burello, D. Farrusseng, G. Rothenberg, *Adv. Synth. Catal.* **2004**, *346*, 1844-1853.

[55] C. S. Sevov, D. P. Hickey, M. E. Cook, S. G. Robinson, S. Barnett, S. D. Minteer, M. S. Sigman, M. S. Sanford, *J. Am. Chem. Soc.* **2017**, *139*, 2924-2927.

[56] K. Wu, A. G. Doyle, *Nat. Chem.* **2017**, *9*, 779-784.

[57] A. Cherkasov, E. N. Muratov, D. Fourches, A. Varnek, I. I. Baskin, M. Cronin, J. Dearden, P. Gramatica, Y. C. Martin, R. Todeschini, *J. Med. Chem.* **2014**, *57*, 4977-5010.

[58] P. Polishchuk, *J. Chem. Inf. Model.* **2017**, *57*, 2618-2639.

[59] M. S. Sigman, K. C. Harper, E. N. Bess, A. Milo, *Acc. Chem. Res.* **2016**, *49*, 1292-1301.

[60] B. C. Haas, D. Kalyani, M. S. Sigman, *Sci. Adv.* **2025**, *11*, eadt3013.

[61] A. V. Brethomé, S. P. Fletcher, R. S. Paton, *ACS Catal.* **2019**, *9*, 2313-2323.

[62] R. R. Knowles, E. N. Jacobsen, *Proc. Natl. Acad. Sci. USA* **2010**, *107*, 20678-20685.

[63] R. W. Taft, Jr., *J. Am. Chem. Soc.* **1952**, *74*, 2729-2732.

[64] M. Charton, *J. Am. Chem. Soc.* **1975**, *97*, 1552-1556.

[65] A. Verloop, *Drug Design*, Academic Press, New York, **1976**, pp. 165.

[66] C. A. Tolman, *Chem. Rev.* **1977**, *77*, 313-348.

[67] A. C. Hillier, W. J. Sommer, B. S. Yong, J. L. Petersen, L. Cavallo, S. P. Nolan, *Organometallics* **2003**, *22*, 4322-4326.

[68] H. Clavier, S. P. Nolan, *Chem. Commun.* **2010**, *46*, 841-861.

[69] A. Gómez-Suárez, D. J. Nelson, S. P. Nolan, *Chem. Commun.* **2017**, *53*, 2650-2660.

[70] E. N. Jacobsen, W. Zhang, M. L. Guler, *J. Am. Chem. Soc.* **1991**, *113*, 6703-6704.

[71] M. Palucki, N. S. Finney, P. J. Pospisil, M. L. Güler, T. Ishida, E. N. Jacobsen, *J. Am. Chem. Soc.* **1998**, *120*, 948-954.

[72] C. G. Swain, E. C. Lupton, *J. Am. Chem. Soc.* **1968**, *90*, 4328-4337.

[73] K. C. Gross, P. G. Seybold, C. M. Hadad, *Int. J. Quantum Chem.* **2002**, *90*, 445-458.

[74] S. M. Bachrach, *Rev. Comput. Chem.* **1994**, 171-228.

[75] P.-O. Löwdin, *On the nonorthogonality problem*, in *Advances in quantum chemistry, Vol. 5*, Elsevier, **1970**, pp. 185-199.

[76] A. E. Reed, R. B. Weinstock, F. Weinhold, *J. Chem. Phys.* **1985**, *83*, 735-746.

[77] F. Richard, R. Bader, *Atoms in molecules: a quantum theory*, Oxford University Press, Oxford, **1990**.

[78] F. L. Hirshfeld, *Theor. Chim. Acta.* **1977**, *44*, 129-138.

[79] C. M. Breneman, K. B. Wiberg, *J. Comput. Chem.* **1990**, *11*, 361-373.

[80] E. Sigfridsson, U. Ryde, *J. Comput. Chem.* **1998**, *19*, 377-395.

[81] F. Strieth-Kalthoff, F. Sandfort, M. Kühnemund, F. R. Schäfer, H. Kuchen, F. Glorius, *Angew. Chem. Int. Ed.* **2022**, *61*, e202204647.

[82] V. Consonni, D. Ballabio, R. Todeschini, *J. Chemom.* **2010**, *24*, 194-201.

[83] P. Gramatica, *QSAR Comb. Sci.* **2007**, *26*, 694-701.

[84] A. Tropsha, P. Gramatica, V. K. Gombar, *QSAR Comb. Sci.* **2003**, *22*, 69-77.

[85] R. W. Kennard, L. A. Stone, *Technometrics* **1969**, *11*, 137-148.

[86] R. Kiralj, M. M. Ferreira, *J. Chemom.* **2010**, *24*, 681-693.

[87] D. W. Marquardt, *J. Am. Stat. Assoc.* **1980**, *75*, 87-91.

[88] B. Slinker, S. Glantz, *Am. J. Physiol. Regul. Integr. Comp. Physiol.* **1985**, *249*, R1-R12.

[89] A. LeSueur, E. Peters, J. Crawford, J. Howard, python-modeling, **2025**. https://github.com/SigmanGroup/python-modeling (accessed: 03.09.2024).

[90] L. Breiman, *Mach. Learn.* **2001**, *45*, 5-32.

[91] A. Liaw, M. Wiener, *R. News* **2002**, *2*, 18-22.

[92] S. Dreiseitl, L. Ohno-Machado, *J. Biomed. Inform.* **2002**, *35*, 352-359.

[93] T. Hill, L. Marquez, M. O'Connor, W. Remus, *Int. J. Forecast.* **1994**, *10*, 5-15.

[94] J. V. Tu, *J. Clin. Epidemiol.* **1996**, *49*, 1225-1231.

[95] H. Shalit Peleg, A. Milo, *Angew. Chem. Int. Ed.* **2023**, *62*, e202219070.

[96] Z. Bursac, C. H. Gauss, D. K. Williams, D. W. Hosmer, *Source Code Biol. Med.* **2008**, *3*, 17.

[97] R. B. Bendel, A. A. Afifi, *J. Am. Stat. Assoc.* **1977**, *72*, 46-53.

[98] B. C. Haas, PhD thesis, University of Utah, **2024**.

[99] J. Lever, M. Krzywinski, N. Altman, *Nat. Methods* **2016**, *13*, 703-705.

[100] D. M. Hawkins, *J. Chem. Inf. Comput. Sci.* **2004**, *44*, 1-12.

[101] R. Tibshirani, *J. R. Stat. Soc. Ser. B Stat. Method.* **1996**, *58*, 267-288.

[102] A. Golbraikh, A. Tropsha, *J. Mol. Graphics Modell.* **2002**, *20*, 269-276.

[103] D. L. Alexander, A. Tropsha, D. A. Winkler, *J. Chem. Inf. Model.* **2015**, *55*, 1316-1322.

[104] J. M. Crawford, C. Kingston, F. D. Toste, M. S. Sigman, *Acc. Chem. Res.* **2021**, *54*, 3136-3148.

[105] J. C. Ianni, V. Annamalai, P. W. Phuan, M. Panda, M. C. Kozlowski, *Angew. Chem. Int. Ed.* **2006**, *45*, 5502-5505.

[106] A. G. Maldonado, G. Rothenberg, *Chem. Soc. Rev.* **2010**, *39*, 1891-1902.

[107] C. Qiao, P. D. Engel, L. A. Ziegenhagen, F. Rominger, A. Schäfer, P. Deglmann, P. Rudolf, P. Comba, A. S. K. Hashmi, T. Schaub, *Adv. Synth. Catal.* **2024**, *366*, 291-298.

[108] S. Park, S. Y. Jeong, T. K. Lee, M. W. Park, H. Y. Lim, J. Sung, J. Cho, S. K. Kwak, S. Y. Hong, N. S. Choi, *Nat. Commun.* **2021**, *12*, 838.

[109] C. Chauveau, S. Fouquay, G. Michaud, F. Simon, J.-F. Carpentier, S. M. Guillaume, *Eur. Polym. J.* **2019**, *116*, 144-157.

[110] R. Langer, A. Beckmann, A. Schulze Tilling, P. Wagner, L. Mleczko, S. Buchholz (Saltigo GmbH), WO2006119909_A1, **2006**.

[111] K. S. Babu, R. M. Srinivasa, T. A. Ravindranath, R. G. Srinivas, S. Sony, V. M. Satish, V. Gandu, B. Apurba, R. P. Pratap, R. V. Anand, *Synth. Commun.* **2008**, *39*, 291-298.

[112] S. Rádl, J. Černý, J. Stach, Z. Gablíková, *Org. Process Res. Dev.* **2013**, *17*, 77-86.

[113] M. S. Newman, R. W. Addor, *J. Am. Chem. Soc.* **1953**, *75*, 1263-1264.

[114] M. S. Newman, R. W. Addor, *J. Am. Chem. Soc.* **1955**, *77*, 3789-3793.

[115] H. M. Fischler, H. G. Heine, W. Hartmann, *Tetrahedron Lett.* **1972**, *13*, 1701-1704.

[116] M. Torres, J. Ribo, A. Clement, O. P. Strausz, *Can. J. Chem.* **1983**, *61*, 996-998.

[117] D. P. Sahu, *Indian J. Chem.* **2002**, *41B*, 1722–1723.

[118] M. M. Krayushkin, S. N. Ivanov, A. Y. Martynkin, B. V. Lichitsky, A. A. Dudinov, L. G. Vorontsova, Z. A. Starikova, B. M. Uzhinov, *Russ. Chem. Bull.* **2002**, *51*, 1731-1736.

[119] G. Papageorgiou, J. E. T. Corrie, *Tetrahedron* **1997**, *53*, 3917-3932.

[120] K. Sekine, T. Yamada, *Chem. Soc. Rev.* **2016**, *45*, 4524-4532.

[121] K. Onida, A. J. Haddleton, S. Norsic, C. Boisson, F. D'Agosto, N. Duguet, *Adv. Synth. Catal.* **2021**, *363*, 5129-5137.

[122] S. Dabral, B. Bayarmagnai, M. Hermsen, J. Schießl, V. Mormul, A. S. K. Hashmi, T. Schaub, *Org. Lett.* **2019**, *21*, 1422-1425.

[123] A. Cervantes-Reyes, K. Farshadfar, M. Rudolph, F. Rominger, T. Schaub, A. Ariafard, A. S. K. Hashmi, *Green Chem.* **2021**, *23*, 889-897.

[124] S. Dabral, U. Licht, P. Rudolf, G. Bollmann, A. S. K. Hashmi, T. Schaub, *Green Chem.* **2020**, *22*, 1553-1558.

[125] C. Johnson, S. Dabral, P. Rudolf, U. Licht, A. S. K. Hashmi, T. Schaub, *ChemCatChem* **2021**, *13*, 353-361.

[126] H.-F. Jiang, A.-Z. Wang, H.-L. Liu, C.-R. Qi, *Eur. J. Org. Chem.* **2008**, *2008*, 2309-2312.

[127] L. Ouyang, X. Tang, H. He, C. Qi, W. Xiong, Y. Ren, H. Jiang, *Adv. Synth. Catal.* **2015**, *357*, 2556-2565.

[128] X. Tang, C. Qi, H. He, H. Jiang, Y. Ren, G. Yuan, *Adv. Synth. Catal.* **2013**, *355*, 2019-2028.

[129] M. Li, S. Abdolmohammadi, M. S. Hoseininezhad-Namin, F. Behmagham, E. Vessally, *J. CO2 Util.* **2020**, *38*, 220-231.

[130] X. Li, A. Villar-Yanez, C. Ngassam Tounzoua, J. Benet-Buchholz, B. Grignard, C. Bo, C. Detrembleur, A. W. Kleij, *ACS Catal.* **2022**, *12*, 2854-2860.

[131] K. Onida, L. Ibrahimli, N. Duguet, *Eur. J. Org. Chem.* **2022**, *2022*, e202200153.

[132] https://organicchemistrydata.org/hansreich/resources/pka/#kaalcohol: (accessed 17th August 2023).

[133] TURBOMOLE V7.5.2 2021, a development of University of Karlsruhe and Forschungszentrum Karlsruhe GmbH, TURBOMOLE GmbH, available from http://www.turbomole.com.

[134] Y. Zhao, D. G. Truhlar, *J. Chem. Phys.* **2006**, *125*, 194101.

[135] F. Weigend, R. Ahlrichs, *Phys. Chem. Chem. Phys.* **2005**, *7*, 3297-3305.

[136] S. Grimme, J. Antony, S. Ehrlich, H. Krieg, *J. Chem. Phys.* **2010**, *132*, 154104.

[137] Y. Zhao, D. G. Truhlar, *Theor. Chem. Acc.* **2007**, *120*, 215-241.

[138] F. Weigend, F. Furche, R. Ahlrichs, *J. Chem. Phys.* **2003**, *119*, 12753-12762.

[139] P. Deglmann, K. May, F. Furche, R. Ahlrichs, *Chem. Phys. Lett.* **2004**, *384*, 103-107.

[140] K. Eichkorn, O. Treutler, H. Öhm, M. Häser, R. Ahlrichs, *Chem. Phys. Lett.* **1995**, *240*, 283-290.

[141] O. Vahtras, J. Almlöf, M. W. Feyereisen, *Chem. Phys. Lett.* **1993**, *213*, 514-518.

[142] F. Weigend, *Phys. Chem. Chem. Phys.* **2006**, *8*, 1057-1065.

[143] COSMOtherm Version 18.0.0 (Revision 4360), COSMOlogic GmbH & Co KG, available from http://www.cosmologic.de.

[144] A. D. Becke, *Phys. Rev. A* **1988**, *38*, 3098-3100.

[145] J. P. Perdew, *Phys. Rev. B* **1986**, *33*, 8822-8824.

[146] J.-D. Chai, M. Head-Gordon, *Phys. Chem. Chem. Phys.* **2008**, *10*, 6615-6620.

[147] J.-D. Chai, M. Head-Gordon, *J. Chem. Phys.* **2008**, *128*, 084106.

[148] M. Bigovic, V. Maslak, Z. Tokic-Vujosevic, V. Divjakovic, R. N. Saicic, *Org. Lett.* **2011**, *13*, 4720-4723.

[149] P. Deglmann, S. Schenk, *J. Comput. Chem.* **2012**, *33*, 1304-1320.

[150] Thomas Schaub, Philipp D. Engel, Peter Rudolf, A. Stephen K. Hashmi, C. Qiao (BASF SE), WO2025021955A1, **2023**.

[151] J. Ho, M. Z. Ertem, *J. Phys. Chem. B* **2016**, *120*, 1319-1329.

[152] J. Ho, V. E. Zwicker, K. K. Y. Yuen, K. A. Jolliffe, *J. Org. Chem.* **2017**, *82*, 10732-10736.

[153] L. S. Mello, P. D. Engel, P. Orecchia, K. Bleher, F. Rominger, K. Borate, R. Goetz, P. Deglmann, A. Schäfer, C. Winter, M. Rack, P. Comba, A. S. K. Hashmi, T. Schaub, *Chem. Eur. J.* **2024**, *30*, e202403023.

[154] P. F. Vogt, J. J. Gerulis, *Amines, Aromatic*, in *Ullmann's Encyclopedia of Industrial Chemistry*, Wiley-VCH Verlag GmbH & Co. KG, Weinheim, Germany, **2000**, pp. 703-705.

[155] G. D. Vo, J. F. Hartwig, *J. Am. Chem. Soc.* **2009**, *131*, 11049-11061.

[156] J. F. Hartwig, S. Shekhar, Q. Shen, F. Barrios-Landeros, *Synthesis of Anilines*, in *PATAI'S Chemistry of Functional Groups*, Wiley, Chichester, **2009**, pp. 3-7, 9-19, 38-42, 47-53.

[157] Q. Yang, Y. Zhao, D. Ma, *Org. Process Res. Dev.* **2022**, *26*, 1690-1750.

[158] J. Lindley, *Tetrahedron* **1984**, *40*, 1433-1456.

[159] G. Evano, A. Nitelet, P. Thilmany, D. F. Dewez, *Front. Chem.* **2018**, *6*, 114.

[160] F. P. Byrne, S. Jin, G. Paggiola, T. H. M. Petchey, J. H. Clark, T. J. Farmer, A. J. Hunt, C. Robert McElroy, J. Sherwood, *Sustain. Chem. Process.* **2016**, *4*, 7.

[161] Y. Deguchi, M. Kono, Y. Koizumi, Y.-i. Izato, A. Miyake, *Org. Process Res. Dev.* **2020**, *24*, 1614-1620.

[162] P. G. Jessop, *Green Chem.* **2011**, *13*, 1391-1398.

[163] D. Prat, A. Wells, J. Hayler, H. Sneddon, C. R. McElroy, S. Abou-Shehada, P. J. Dunn, *Green Chem.* **2016**, *18*, 288-296.

[164] C. P. Delaney, E. Lin, Q. Huang, I. F. Yu, G. Rao, L. Tao, A. Jed, S. M. Fantasia, K. A. Püntener, R. D. Britt, J. F. Hartwig, *Science* **2023**, *381*, 1079-1085.

[165] R. Calvo, K. Zhang, A. Passera, D. Katayev, *Nat. Commun.* **2019**, *10*, 3410.

[166] D. S. Surry, S. L. Buchwald, *J. Am. Chem. Soc.* **2007**, *129*, 10354-10355.

[167] K. Borate, R. Kaduskar, H. Shinde, R. Goetz (BASF SE), World WO 2021/204774 A1, **2021**.

[168] R. A. Green, J. F. Hartwig, *Angew. Chem. Int. Ed.* **2015**, *54*, 3768-3772.

[169] A. Borzenko, N. L. Rotta-Loria, P. M. MacQueen, C. M. Lavoie, R. McDonald, M. Stradiotto, *Angew. Chem. Int. Ed.* **2015**, *54*, 3773-3777.

[170] G. Song, J. Song, Q. Li, D.-Z. Nong, J. Dong, G. Li, J. Fan, C. Wang, J. Xiao, D. Xue, *Angew. Chem. Int. Ed.* **2023**, e202314355.

[171] H. Xu, C. Wolf, *Chem. Commun.* **2009**, 3035-3037.

[172] M. Fan, W. Zhou, Y. Jiang, D. Ma, *Org. Lett.* **2015**, *17*, 5934-5937.

[173] H.-J. Ai, S.-T. Kim, C. Liu, S. L. Buchwald, *J. Am. Chem. Soc.* **2024**, *146*, 25949-25955.

[174] M. Huang, X. Lin, X. Zhu, W. Peng, J. Xie, Y. Wan, *Eur. J. Org. Chem.* **2011**, *2011*, 4523-4527.

[175] M. R. G. Pews, J. A. Gall (Corteva Agriscience LLC), US5091580A, **1992**.

[176] R. He, J. Zhong, Y. Wang, Z. Zhang (Zhejiang Yongtai Technology Co. Ltd.), China CN101245020B, **2008**.

[177] Y. Wan, M. Huang, X. Zhu, L. Wang (National Sun Yat Sen University), China CN102557958A, **2012**.

[178] L. Sun, P. He, B. Xu, X. Xu, X. Wang, *RSC Adv.* **2013**, *3*, 5819–5823.

[179] J. Tao, J. P. Perdew, V. N. Staroverov, G. E. Scuseria, *Phys. Rev. Lett.* **2003**, *91*, 146401.

[180] F. Furche, J. P. Perdew, *J. Chem. Phys.* **2006**, *124*, 044103.

[181] L. R. Maurer, M. Bursch, S. Grimme, A. Hansen, *J. Chem. Theory Comput.* **2021**, *17*, 6134-6151.

[182] M. Müller, A. Hansen, S. Grimme, *J. Chem. Phys.* **2023**, *158*, 014103.

[183] C. Y. Legault, CYLview20, version 1.0b; Université de Sherbrooke, **2020**. http://www.cylview.org.

[184] G. A. Zhurko, D. A. Zhurko, ChemCraft: Tool for treatment of chemical data, **2005**.

[185] F. Neese, *WIREs Comput. Mol. Sci.* **2012**, *2*, 73-78.

[186] F. Neese, *WIREs Comput. Mol. Sci.* **2022**, *12*, e1606.

[187] F. Neese, F. Wennmohs, U. Becker, C. Riplinger, *J. Chem. Phys.* **2020**, *152*.

[188] V. Barone, M. Cossi, *J. Phys. Chem. A* **1998**, *102*, 1995-2001.

[189] F. Neese, *J. Phys. Chem. Solids* **2004**, *65*, 781-785.

[190] S. Zhang, H. Krakauer, *Phys. Rev. Lett.* **2003**, *90*, 136401.

[191] F. D. Malone, A. Mahajan, J. S. Spencer, J. Lee, *J. Chem. Theory Comput.* **2023**, *19*, 109-121.

[192] Q. Sun, T. C. Berkelbach, N. S. Blunt, G. H. Booth, S. Guo, Z. Li, J. Liu, J. D. McClain, E. R. Sayfutyarova, S. Sharma, S. Wouters, G. K.-L. Chan, *Wiley Interdiscip. Rev. Comput. Mol. Sci.* **2018**, *8*, e1340.

[193] T. H. Dunning, Jr., *J. Chem. Phys.* **1989**, *90*, 1007-1023.

[194] N. B. Balabanov, K. A. Peterson, *J. Chem. Phys.* **2005**, *123*, 064107.

[195] N. B. Balabanov, K. A. Peterson, *J. Chem. Phys.* **2006**, *125*, 074110.

[196] L. Hehn, P. Deglmann, M. Kühn, *J. Chem. Theory Comput.* **2024**, *20*, 4545-4568.

[197] V. N. Staroverov, G. E. Scuseria, J. Tao, J. P. Perdew, *J. Chem. Phys.* **2003**, *119*, 12129-12137.

[198] A. D. Becke, *J. Chem. Phys.* **1993**, *98*, 5648-5652.

[199] P. J. Stephens, F. J. Devlin, C. F. Chabalowski, M. J. Frisch, *J. Phys. Chem.* **1994**, *98*, 11623-11627.

[200] S. H. Vosko, L. Wilk, M. Nusair, *Can. J. Phys.* **1980**, *58*, 1200-1211.

[201] C. Adamo, V. Barone, *J. Chem. Phys.* **1999**, *110*, 6158-6170.

[202] T. Yanai, D. P. Tew, N. C. Handy, *Chem. Phys. Lett.* **2004**, *393*, 51-57.

[203] C. Riplinger, F. Neese, *J. Chem. Phys.* **2013**, *138*, 034106.

[204] J. G. Hill, J. A. Platts, *J. Chem. Phys.* **2008**, *128*, 044104.

[205] F. Weigend, A. Köhn, C. Hättig, *J. Chem. Phys.* **2002**, *116*, 3175-3183.

[206] E. I. Solomon, R. G. Hadt, *Coord. Chem. Rev.* **2011**, *255*, 774-789.

[207] H. B. Gray, B. G. Malmström, R. J. P. Williams, *J. Biol. Inorg. Chem.* **2000**, *5*, 551-559.

[208] S. Larsson, *J. Biol. Inorg. Chem.* **2000**, *5*, 560-564.

[209] U. Ryde, M. H. M. Olsson, B. O. Roos, J. O. A. De Kerpel, K. Pierloot, *J. Biol. Inorg. Chem.* **2000**, *5*, 565-574.

[210] P. Comba, *The Importance of Intra- and Intermolecular Weak Bonds in Transition Metal Coordination Compounds*, in *Intermolecular Interactions* (Eds.: W. Gans, J. C. A. Boeyens), Springer US, Boston, MA, **1998**, pp. 97-109.

[211] P. Comba, P. Jurisic, Y. D. Lampeka, A. Peters, A. I. Prikhod'ko, H. Pritzkow, *Inorg. Chim. Acta* **2001**, *324*, 99-107.

[212] P. Comba, T. W. Hambley, M. A. Hitchman, H. Stratemeier, *Inorg. Chem.* **1995**, *34*, 3903-3911.

[213] P. Comba, P. Hilfenhaus, B. Nuber, *Helv. Chim. Acta* **1997**, *80*, 1831-1842.

[214] P. Comba, H. Pritzkow, W. Schiek, *Angew. Chem. Int. Ed.* **2001**, *40*, 2465-2468.

[215] J. Meisenheimer, *Liebigs Ann.* **1902**, *323*, 205-246.

[216] P. Comba, B. Martin, A. Muruganantham, J. Straub, *Inorg. Chem.* **2012**, *51*, 9214-9225.

[217] E. S. Jang, C. L. McMullin, M. Käß, K. Meyer, T. R. Cundari, T. H. Warren, *J. Am. Chem. Soc.* **2014**, *136*, 10930-10940.

[218] K. Bleher, P. Comba, M. Gast, S. Kronenberger, T. Josephy, *Inorg. Chim. Acta* **2022**, *532*, 120752.

[219] S. Stoll, A. Schweiger, *J. Magn. Reson.* **2006**, *178*, 42-55.

[220] K. H. Lee, F. McPhee, J. J. DeVoss, C. S. Craik, P. R. Ortiz de Montellano, *J. Org. Chem.* **1994**, *59*, 6194-6199.

[221] J. F. Bunnett, E. W. Garbisch, Jr., K. M. Pruitt, *J. Am. Chem. Soc.* **1957**, *79*, 385-391.

[222] M. Reiher, *Faraday Discuss.* **2007**, *135*, 97-124.

[223] M. Reiher, *CHIMIA* **2009**, *63*, 140.

[224] These calculations were performed by Dr. Michael Kühn (BASF SE).

[225] J. Shee, B. Rudshteyn, E. J. Arthur, S. Zhang, D. R. Reichman, R. A. Friesner, *J. Chem. Theory Comput.* **2019**, *15*, 2346-2358.

[226] L. Saputra, P. D. Engel, F. Bienewald, G. A. Shevchenko, A. Schäfer, P. Deglmann, P. Comba, A. S. K. Hashmi, T. Schaub, J. Mormul, *manuscript in preparation* **2025**.

[227] T. Cao, J. Deitch, E. C. Linton, M. C. Kozlowski, *Angew. Chem. Int. Ed. Engl.* **2012**, *51*, 2448-2451.

[228] F. Fang, M. Vogel, J. V. Hines, S. C. Bergmeier, *Org. Biomol. Chem.* **2012**, *10*, 3080-3091.

[229] M. A. Franks, E. A. Schrader, E. C. Pietsch, D. R. Pennella, S. V. Torti, M. E. Welker, *Biorg. Med. Chem.* **2005**, *13*, 2221-2233.

[230] L. Wang, Q.-B. Liu, D.-S. Wang, X. Li, X.-W. Han, W.-J. Xiao, Y.-G. Zhou, *Org. Lett.* **2009**, *11*, 1119-1122.

[231] R. K. Kumar, X. Bi, *Chem. Commun.* **2016**, *52*, 853-868.

[232] X.-R. Song, Y.-F. Qiu, X.-Y. Liu, Y.-M. Liang, *Org. Biomol. Chem.* **2016**, *14*, 11317-11331.

[233] V. S. Muralidharan, A. M. Uduman Mohideen, R. Arun Mozhi Selvan, *Anti-Corros. Methods Mater.* **1995**, *42*, 17-20.

[234] A. E. Favorsky, *J. Russ. Phys.-Chem. Soc.* **1905**, *37*, 643-645.

[235] J. Falbe, H. Bahrmann, W. Lipps, D. Mayer, G. D. Frey, *Alcohols, Aliphatic*, in *Ullmann's Encyclopedia of Industrial Chemistry*, Wiley-VCH Verlag GmbH & Co. KGaA, Weinheim, Germany, **2000**, pp. 1.

[236] H. Gräfje, W. Körnig, H.-M. Weitz, W. Reiß, G. Steffan, H. Diehl, H. Bosche, K. Schneider, H. Kieczka, R. Pinkos, *Butanediols, Butenediol, and Butynediol*, in *Ullmann's Encyclopedia of Industrial Chemistry*, Wiley-VCH Verlag GmbH & Co. KGaA, Weinheim, Germany, **2000**, pp. 1–12.

[237] A. T. Boris, *Curr. Org. Chem.* **2002**, *6*, 1121-1162.

[238] B. A. Trofimov, A. I. Mikhaleva, R. N. Nesterenko, L. N. Sobenina, V. K. Stankevich, M. G. Voronkov (IR Instiute Organicheskoi), Russia RU1832674C, **1989**.

[239] W. Yang, W. Peng, H. Li, J. Mao, L. Qian, Q. Zhang, *New J. Chem.* **2024**, *48*, 9082-9089.

[240] N. A. Sitte, F. Ghiringhelli, G. A. Shevchenko, F. Rominger, A. S. K. Hashmi, T. Schaub, *Adv. Synth. Catal.* **2022**, *364*, 2227-2234.

[241] W. Reppe, *Liebigs Ann.* **1955**, *596*, 158-224.

[242] I.-T. Trotuş, T. Zimmermann, F. Schüth, *Chem. Rev.* **2014**, *114*, 1761-1782.

[243] J. H. Blumentha (Air Reduction), US2996552A, **1958**.

[244] B. Stewart, A. Harriman, L. J. Higham, *Organometallics* **2011**, *30*, 5338-5343.

[245] A. Altun, R. Izsák, G. Bistoni, *Int. J. Quantum Chem.* **2021**, *121*, e26339.

[246] G. Bistoni, *Wiley Interdiscip. Rev. Comput. Mol. Sci.* **2020**, *10*, e1442.

[247] A. Altun, F. Neese, G. Bistoni, *J. Chem. Theory Comput.* **2019**, *15*, 215-228.

[248] A. Wuttke, R. A. Mata, *J. Comput. Chem.* **2017**, *38*, 15-23.

[249] T. Lu, *J. Chem. Phys.* **2024**, *161*, 082503.

[250] C. Lee, W. Yang, R. G. Parr, *Phys. Rev. B* **1988**, *37*, 785-789.

[251] N. Mardirossian, M. Head-Gordon, *J. Chem. Phys.* **2016**, *144*.

[252] M. Bogojeski, L. Vogt-Maranto, M. E. Tuckerman, K.-R. Müller, K. Burke, *Nat. Commun.* **2020**, *11*, 5223.

[253] S. Lambie, D. Kats, D. Usvyat, A. Alavi, *J. Chem. Phys.* **2025**, *162*, 114112.

[254] M. Munakata, S. Kitagawa, I. Kawada, M. Maekawa, H. Shimono, *J. Chem. Soc., Dalton Trans.* **1992**, 2225-2230.

[255] Microsoft Corporation, Microsoft Excel, **2025**. https://office.microsoft.com/excel.

[256] L. Mele, P. D. Engel, J. A. Cadge, V. Peciukenas, H. Choi, M. S. Sigman, J. Cornella, *J. Am. Chem. Soc.* **2025**, accepted DOI: 10.1021/jacs.1025c11854.

[257] J. E. Zweig, D. E. Kim, T. R. Newhouse, *Chem. Rev.* **2017**, *117*, 11680-11752.

[258] B. Su, Z. C. Cao, Z. J. Shi, *Acc. Chem. Res.* **2015**, *48*, 886-896.

[259] R. L. Melen, *Science* **2019**, *363*, 479-484.

[260] C. Weetman, S. Inoue, *ChemCatChem* **2018**, *10*, 4213-4228.

[261] P. P. Power, *Nature* **2010**, *463*, 171-177.

[262] O. Planas, F. Wang, M. Leutzsch, J. Cornella, *Science* **2020**, *367*, 313-317.

[263] I. P. Beletskaya, C. Nájera, M. Yus, *Chem. Soc. Rev.* **2020**, *49*, 7101-7166.

[264] J. Cao, R. Fang, J. Y. Liu, H. Lu, Y. C. Luo, P. F. Xu, *Chem. Eur. J.* **2018**, *24*, 18863-18867.

[265] X.-Y. Chen, R.-C. Lin, S. Ye, *Chem. Commun.* **2012**, *48*, 1317-1319.

[266] X. Gao, Z. Li, W. Yang, Y. Liu, W. Chen, C. Zhang, L. Zheng, H. Guo, *Org. Biomol. Chem.* **2017**, *15*, 5298-5307.

[267] Y.-C. Ming, X.-J. Lv, C. Wang, Y.-K. Liu, *Org. Lett.* **2024**, *26*, 10853-10858.

[268] M. Viji, S. Lanka, J. Sim, C. Jung, H. Lee, M. Vishwanath, J.-K. Jung, *Catal.* **2021**, *11*, 1013.

[269] M. Wang, P. Y. Tseng, W. J. Chi, S. Suresh, A. Edukondalu, Y. R. Chen, W. Lin, *Adv. Synth. Catal.* **2020**, *362*, 3407-3415.

[270] Y. Zhang, Y. Sun, Y. Wei, M. Shi, *Adv. Synth. Catal.* **2019**, *361*, 2129-2135.

[271] A. L. Clevenger, R. M. Stolley, J. Aderibigbe, J. Louie, *Chem. Rev.* **2020**, *120*, 6124-6196.

[272] W. Fang, H. Zhu, Q. Deng, S. Liu, X. Liu, Y. Shen, T. Tu, *Synthesis* **2014**, *46*, 1689-1708.

[273] D. J. Gorin, B. D. Sherry, F. D. Toste, *Chem. Rev.* **2008**, *108*, 3351-3378.

[274] D. S. Surry, S. L. Buchwald, *Angew. Chem. Int. Ed.* **2008**, *47*, 6338-6361.

[275] D. Gelman, L. Jiang, S. L. Buchwald, *Org. Lett.* **2003**, *5*, 2315-2318.

[276] T. Chu, G. I. Nikonov, *Chem. Rev.* **2018**, *118*, 3608-3680.

[277] J. M. Lipshultz, G. Li, A. T. Radosevich, *J. Am. Chem. Soc.* **2021**, *143*, 1699-1721.

[278] M. Mato, J. Cornella, *Angew. Chem. Int. Ed.* **2024**, *63*, e202315046.

[279] H. W. Moon, J. Cornella, *ACS Catal.* **2022**, *12*, 1382-1393.

[280] C. Weetman, S. Inoue, *ChemCatChem* **2018**, *10*, 4213-4228.

[281] K. Ruffell, L. C. Gallegos, K. B. Ling, R. S. Paton, L. T. Ball, *Angew. Chem. Int. Ed.* **2022**, *61*, e202212873.

[282] J. He, F.-H. Du, C. Zhang, Y. Du, *Commun. Chem.* **2023**, *6*, 126.

[283] T. Faber, S. Engelhardt, J. Cornella, *Angew. Chem. Int. Ed.* **2025**, *64*, e202424698.

[284] A. Gagnon, J. Dansereau, A. Le Roch, *Synthesis* **2017**, *49*, 1707-1745.

[285] M. Jurrat, L. Maggi, W. Lewis, L. T. Ball, *Nat. Chem.* **2020**, *12*, 260-269.

[286] M. Magre, J. Cornella, *J. Am. Chem. Soc.* **2021**, *143*, 21497-21502.

[287] O. Planas, V. Peciukenas, J. Cornella, *J. Am. Chem. Soc.* **2020**, *142*, 11382-11387.

[288] E. Caldeweyher, S. Ehlert, A. Hansen, H. Neugebauer, S. Spicher, C. Bannwarth, S. Grimme, *J. Chem. Phys.* **2019**, *150*, 154122.

[289] B. Metz, H. Stoll, M. Dolg, *J. Chem. Phys.* **2000**, *113*, 2563-2569.

[290] M. J. Frisch, G. W. Trucks, H. B. Schlegel, G. E. Scuseria, M. A. Robb, J. R. Cheeseman, G. Scalmani, V. Barone, G. A. Petersson, H. Nakatsuji, X. Li, M. Caricato, A. V. Marenich, J. Bloino, B. G. Janesko, R. Gomperts, B. Mennucci, H. P. Hratchian, J. V. Ortiz, A. F. Izmaylov, J. L. Sonnenberg, Williams, F. Ding, F. Lipparini, F. Egidi, J. Goings, B. Peng, A. Petrone, T. Henderson, D. Ranasinghe, V. G. Zakrzewski, J. Gao, N. Rega, G. Zheng, W. Liang, M. Hada, M. Ehara, K. Toyota, R. Fukuda, J. Hasegawa, M. Ishida, T. Nakajima, Y. Honda, O. Kitao, H. Nakai, T. Vreven, K. Throssell, J. A. Montgomery Jr., J. E. Peralta, F. Ogliaro, M. J. Bearpark, J. J. Heyd, E. N. Brothers, K. N. Kudin, V. N. Staroverov, T. A. Keith, R. Kobayashi, J. Normand, K. Raghavachari, A. P. Rendell, J. C. Burant, S. S. Iyengar, J. Tomasi, M. Cossi, J. M. Millam, M. Klene, C. Adamo, R. Cammi, J. W. Ochterski, R. L. Martin, K. Morokuma, O. Farkas, J. B. Foresman, D. J. Fox, Gaussian 16 Rev. C.01, **2016**.

[291] K. Jorner, L. Turcani, Morfeus (version 0.7.2), https://github.com/digital-chemistry-laboratory/morfeus.

[292] B. C. Haas, Hardy, M. A., SigmanGroup/Get_Properties: Get_Properties_v1.0.3 (v1.0.3), **2024**. https://doi.org/10.5281/zenodo.10651727 (accessed: 03.09.2024).

[293] RDKit: Open-source cheminformatics (version 2024.03.5), https://www.rdkit.org.

[294] Fabian Pedregosa, Gaël Varoquaux, Alexandre Gramfort, Vincent Michel, Bertrand Thirion, Olivier Grisel, Mathieu Blondel, Peter Prettenhofer, Ron Weiss, Vincent Dubourg, Jake Vanderplas, Alexandre Passos, David Cournapeau, Matthieu Brucher, Matthieu Perrot, É. Duchesnay, *J. Mach. Learn. Res.* **2011**, *12*, 2825–2830.

[295] Q. Gu, E. Vessally, *RSC Adv.* **2020**, *10*, 16756-16768.

[296] C. Pratley, S. Fenner, J. A. Murphy, *Chem. Rev.* **2022**, *122*, 8181-8260.

[297] H. Zhang, W. Pu, T. Xiong, Y. Li, X. Zhou, K. Sun, Q. Liu, Q. Zhang, *Angew. Chem. Int. Ed.* **2013**, *52*.

[298] J. Cai, M. Zhi, J. Hu, T. Pu, K. Guo, L. Zhao, *RSC Adv.* **2022**, *12*, 24208-24216.

[299] O. Planas, V. Peciukenas, M. Leutzsch, N. Nöthling, D. A. Pantazis, J. Cornella, *J. Am. Chem. Soc.* **2022**, *144*, 14489-14504.

[300] F. Zhao, X.-F. Wu, *J. Catal.* **2021**, *397*, 201-204.

[301] D. H. R. Barton, N. Y. Bhatnagar, J.-C. Blazejewski, B. Charpiot, J.-P. Finet, D. J. Lester, W. B. Motherwell, M. T. B. Papoula, S. P. Stanforth, *J. Chem. Soc., Perkin Trans. 1* **1985**, 2657-2665.

[302] E. E. Kwan, Y. Zeng, H. A. Besser, E. N. Jacobsen, *Nat. Chem.* **2018**, *10*, 917-923.

[303] S. K. R, P. Ilayaperumal, *ICBC* **2021**, *1*, 1-3.

[304] G. S. Tâmega, M. O. Costa, A. de Araujo Pereira, M. A. Barbosa Ferreira, *Chem. Rec.* **2024**, *24*, e202400148.

[305] J. J. Stewart, *J. Mol. Model.* **2007**, *13*, 1173-1213.

[306] J. Rezac, J. Fanfrlik, D. Salahub, P. Hobza, *J. Chem. Theory Comput.* **2009**, *5*, 1749-1760.

[307] J. Rezac, P. Hobza, *J. Chem. Theory Comput.* **2012**, *8*, 141-151.

[308] A. S. Christensen, T. Kubar, Q. Cui, M. Elstner, *Chem. Rev.* **2016**, *116*, 5301-5337.

[309] D. Porezag, T. Frauenheim, T. Köhler, G. Seifert, R. Kaschner, *Phys. Rev. B* **1995**, *51*, 12947.

[310] M. Elstner, D. Porezag, G. Jungnickel, J. Elsner, M. Haugk, T. Frauenheim, S. Suhai, G. Seifert, *Phys. Rev. B* **1998**, *58*, 7260.

[311] M. Gaus, Q. Cui, M. Elstner, *J. Chem. Theory Comput.* **2011**, *7*, 931-948.

[312] M. Elstner, G. Seifert, *Philos. Trans. R. Soc. A* **2014**, *372*, 20120483.

[313] B. Hourahine, M. Berdakin, J. Bich, F. Bonafé, C. Camacho, Q. Cui, M. Deshaye, G. Díaz Mirón, S. Ehlert, M. Elstner, *J. Phys. Chem. A* **2025**.

[314] S. Grimme, C. Bannwarth, P. Shushkov, *J. Chem. Theory Comput.* **2017**, *13*, 1989-2009.

[315] A general-purpose semiempirical quantum mechanical method gxtb. https://github.com/grimme-lab/g-xtb. Accessed: 2025-6-25.

[316] T. Froitzheim, M. Müller, A. Hansen, S. Grimme, *ChemRxiv preprint* **2025**, DOI: 10.26434/chemrxiv-22025-bjxvt.

[317] D. M. Anstine, R. Zubatyuk, O. Isayev, *Chem. Sci.* **2025**, *16*, 10228-10244.

[318] D. P. Kovács, J. H. Moore, N. J. Browning, I. Batatia, J. T. Horton, Y. Pu, V. Kapil, W. C. Witt, I. B. Magdău, D. J. Cole, G. Csányi, *J. Am. Chem. Soc.* **2025**, *147*, 17598-17611.

[319] R. Remme, T. Kaczun, T. Ebert, C. A. Gehrig, D. Geng, G. Gerhartz, M. K. Ickler, M. V. Klockow, P. Lippmann, J. S. Schmidt, S. Wagner, A. Dreuw, F. A. Hamprecht, *J. Am. Chem. Soc.* **2025**, *147*, 28851-28859.

[320] D. Weininger, *J. Chem. Inf. Comput. Sci.* **1988**, *28*, 31-36.

[321] M. Krenn, F. Häse, A. Nigam, P. Friederich, A. Aspuru-Guzik, *Mach. Learn.: Sci. Technol.* **2020**, *1*, 045024.

[322] R. Chen, Y. Liu, Z. Chen, Y. Li, F. Yang, J. Lin, Z. Ke, *Commun. Chem.* **2025**, *8*, 255.

[323] O. Schilter, A. Vaucher, P. Schwaller, T. Laino, *Digit. Discov.* **2023**, *2*, 728-735.

[324] J. R. Ludwig, P. M. Zimmerman, J. B. Gianino, C. S. Schindler, *Nature* **2016**, *533*, 374-379.

[325] I. M. Pendleton, M. H. Pérez-Temprano, M. S. Sanford, P. M. Zimmerman, *J. Am. Chem. Soc.* **2016**, *138*, 6049-6060.

[326] A. L. Dewyer, P. M. Zimmerman, *Org. Biomol. Chem.* **2017**, *15*, 501-504.

[327] M. Steiner, M. Reiher, *Nat. Commun.* **2024**, *15*, 3680.

[328] J. P. Reid, M. S. Sigman, *Nature* **2019**, *571*, 343-348.

[329] M. E. Akana, S. Tcyrulnikov, B. D. Akana-Schneider, G. P. Reyes, S. Monfette, M. S. Sigman, E. C. Hansen, D. J. Weix, *J. Am. Chem. Soc.* **2024**, *146*, 3043-3051.

[330] D. T. Ahneman, J. G. Estrada, S. Lin, S. D. Dreher, A. G. Doyle, *Science* **2018**, *360*, 186-190.

[331] M. Saebi, B. Nan, J. E. Herr, J. Wahlers, Z. Guo, A. M. Zurański, T. Kogej, P.-O. Norrby, A. G. Doyle, N. V. Chawla, O. Wiest, *Chem. Sci.* **2023**, *14*, 4997-5005.

[332] N. Sanosa, D. Dalmau, D. Sampedro, J. V. Alegre-Requena, I. Funes-Ardoiz, *Artif. Intell. Chem.* **2024**, *2*, 100068.

[333] S. Singh, R. B. Sunoj, *Acc. Chem. Res.* **2023**, *56*, 402-412.

[334] G. E. Moore, *Electronics* **1965**, *38*, 114-117.

[335] R. Stocks, G. M. J. Barca, *J. Chem. Theory Comput.* **2025**.

[336] M. S. Gordon, G. Barca, S. S. Leang, D. Poole, A. P. Rendell, J. L. Galvez Vallejo, B. Westheimer, *J. Phys. Chem. A* **2020**, *124*, 4557-4582.

[337] X. Wu, Q. Sun, Z. Pu, T. Zheng, W. Ma, W. Yan, Y. Xia, Z. Wu, M. Huo, X. Li, W. Ren, S. Gong, Y. Zhang, W. Gao, *Wiley Interdiscip. Rev. Comput. Mol. Sci.* **2025**, *15*, e70008.

[338] D. B. Williams-Young, W. A. de Jong, H. J. J. van Dam, C. Yang, *Front. Chem.* **2020**, *8*.

[339] D. B. Williams-Young, A. Bagusetty, W. A. de Jong, D. Doerfler, H. J. J. van Dam, Á. Vázquez-Mayagoitia, T. L. Windus, C. Yang, *Parallel Comput.* **2021**, *108*, 102829.

[340] R. P. Feynman, *Int. J. Theor. Phys.* **1982**, *21*, 467-488.

[341] A. Lappala, *Curr. Opin. Struct. Biol.* **2024**, *89*, 102919.

[342] S. Boixo, T. F. Rønnow, S. V. Isakov, Z. Wang, D. Wecker, D. A. Lidar, J. M. Martinis, M. Troyer, *Nat. Phys.* **2014**, *10*, 218-224.

[343] J. D. Weidman, M. Sajjan, C. Mikolas, Z. J. Stewart, J. Pollanen, S. Kais, A. K. Wilson, *Cell Rep. Phys. Sci.* **2024**, *5*, 102105.

9
Appendix

XYZ files are uploaded to https://figshare.com. An implemented function allows viewing the structures. Each chapter is assigned an individual DOI:

Chapter 3: dx.doi.org/10.6084/m9.figshare.30540023

Chapter 4: dx.doi.org/10.6084/m9.figshare.30565955

Chapter 5: dx.doi.org/10.6084/m9.figshare.30571979

Chapter 6 (mechanistic studies): dx.doi.org/10.6084/m9.figshare.30565976

Chapter 6 (statistical modeling): dx.doi.org/10.6084/m9.figshare.30546209

(Until the manuscript including the results of Chapter 5 is submitted, only a temporary link is available: https://figshare.com/s/b68698e5102fb83ec55d)

Table 9.1: SCF energies at the level of theory of the geometry optimization (COSMO(∞)-M06-L-D3ZERO/def2-SVP, E(Opt)), SCF energies at the level of theory of the single point calculation (M06-2X-D4/def2-QZVPP, E(SP)), thermochemical corrections (ΔG(therm)), solvation correction obtained from COSMO-RS(MeCN), as well as final Gibbs free energy in solution (G(solution, SP)) for all calculations for Chapter 3.

Name	E(opt) (Hartree) COSMO(∞)-M06-L-D3ZERO/ def2-SVP	E(SP) (Hartree) M06-2X-D3ZERO/ def2-QZVPP	ΔG(therm) (kJ·mol^{-1})	ΔG(solv) (kJ·mol^{-1})	G(solution, SP) (kJ·mol^{-1})
1-S1	-1510.46523	-1511.79489	1252.4	-117.4	-3968082.5
1-S1_anion	-1071.48194	-1072.37957	700.6	-204.4	-2815036.3
1-S2	-1356.75884	-1357.94164	1091.6	-121.4	-3564305.6
1-S3	-1125.89335	-1126.88078	901.8	-106.0	-2957829.8
1b-S2	-1356.75819	-1357.94061	1098.2	-121.8	-3564296.7
2-S1	-1510.47779	-1511.80006	1252.2	-107.3	-3968086.2
2-S1_anion	-1071.48596	-1072.37955	699.2	-244.7	-2815078.0
2-S2	-1356.76691	-1357.94267	1088.6	-117.6	-3564307.5
2-S3	-1125.89758	-1126.87686	892.4	-109.5	-2957832.3
3-S1	-1071.48596	-1072.37955	699.2	-244.7	-2815078.0
3-S2	-918.28744	-919.10031	573.6	-63.0	-2412587.3
3-S3	-687.42488	-688.04020	381.7	-53.4	-1806121.2
3-S3-*p*CF_3-PhOH	-1024.17690	-1025.15472	375.4	-55.0	-2691223.4
3-S3-*p*Me-PhOH	-726.70929	-727.35469	447.0	-55.3	-1909278.1

4-S1	-1510.47452	-1511.79737	1249.5	-104.2	-3968078.7
4-S1 anion	-1071.48304	-1072.36857	699.4	-260.0	-2815064.3
4-S2	-1356.77816	-1357.94944	1093.4	-119.2	-3564322.1
4-S3	-1125.90470	-1126.88645	894.2	-94.1	-2957840.3
5-S1	-1510.45899	-1511.78340	1251.5	-124.0	-3968059.8
5-S2	-1356.77022	-1357.94639	1091.9	-120.7	-3564317.0
5-S3	-1125.89318	-1126.87882	897.4	-105.7	-2957828.7
6-S1	-1203.19764	-1204.24483	974.1	-108.4	-3160879.0
6-S2	-1049.51520	-1050.41908	834.3	-101.0	-2757142.0
MeCN	-132.64872	-132.75773	62.0	-22.8	-348516.2
P1	-764.74735	-765.43482	477.1	-54.6	-2009226.7
P2	-611.05933	-611.60061	329.0	-46.2	-1605474.6
P3	-380.18560	-380.53437	135.0	-32.5	-998990.5
P5	-419.47764	-419.85561	203.1	-35.1	-1102162.9
PhOH	-307.21828	-307.48441	206.0	-36.8	-807131.2
S1	-764.73958	-765.42760	469.9	-59.6	-2009219.8
S2	-611.04082	-611.58825	326.4	-47.0	-1605445.6
S3	-380.17740	-380.52819	135.1	-33.9	-998975.5
S5	-419.46425	-419.84681	203.2	-34.8	-1102139.4
TBD	-438.46586	-438.83627	457.3	-42.6	-1151750.0
TBDH$^+$	-438.95178	-439.25132	491.5	-208.5	-1152971.3
TBDH$^+$ PhO$^-$	-745.71163	-746.33070	702.9	-99.8	-1958888.2
TBD PhOH	-745.70541	-746.34490	700.6	-62.8	-1958890.7
TBD *p*CF$_3$-PhOH	-1082.46172	-1083.46388	696.1	-65.1	-2844003.4
TBD *p*Me-PhOH	-784.98857	-785.65773	767.3	-65.5	-2062042.5
TBDH$^+$ *p*CF$_3$-PhO$^-$	-1082.47141	-1083.45663	700.5	-93.7	-2844008.6
TBDH$^+$ *p*Me-PhO$^-$	-784.99362	-785.64358	766.2	-99.3	-2062040.3
TS1-S1	-1510.46042	-1511.78510	1249.3	-113.7	-3968056.2
TS1-S2	-1356.75339	-1357.93676	1089.0	-110.2	-3564284.1
TS1-S3	-1125.88698	-1126.87379	898.3	-99.3	-2957808.1
TS1b-S2	-1356.75360	-1357.93413	1096.1	-113.4	-3564273.4
TS2-S1	-1510.46485	-1511.79042	1255.6	-112.1	-3968062.2
TS2-S2	-1356.75529	-1357.93530	1090.8	-121.0	-3564289.3
TS2-S3	-1125.88923	-1126.87434	897.1	-105.4	-2957816.8
TS2b-S2	-1356.75216	-1357.93408	1090.8	-121.6	-3564286.7
TS3-S1	-1510.45412	-1511.78238	1237.9	-88.8	-3968035.6
TS3-S2	-1356.74860	-1357.92660	1072.6	-100.3	-3564264.0
TS3-S3	-1125.88909	-1126.87173	890.8	-83.3	-2957794.2
TS3-S3-*p*CF$_3$-PhOH	-1462.64518	-1463.99009	890.9	-78.8	-3842893.8
TS3-S3-*p*Me-PhOH	-1165.17460	-1166.18704	958.1	-85.1	-3060951.1
TS4-S1	-1510.45824	-1511.77652	1237.5	-103.4	-3968035.2

TS4-S2	-1356.75061	-1357.92394	1072.0	-103.8	-3564261.2
TS4-S3	-1125.88471	-1126.86760	884.0	-85.4	-2957792.3
TS4-S3-*p*CF$_3$-PhOH	-1462.64001	-1463.98236	884.3	-90.5	-3842891.9
TS4-S3-*p*Me-PhOH	-1165.16798	-1166.17723	944.4	-96.7	-3060950.6
TS5-S1	-1510.45679	-1511.77845	1249.6	-114.4	-3968039.1
TS5-S2	-1356.76482	-1357.93470	1090.9	-125.3	-3564292.0
TS5-S3	-1125.88652	-1126.86839	894.9	-105.4	-2957803.4
TS6-S1	-1510.45503	-1511.78255	1247.0	-109.0	-3968047.1
TS6-S2	-1356.76593	-1357.94375	1090.4	-108.0	-3564298.9
TS6-S3	-1125.89015	-1126.87430	894.0	-101.7	-2957816.2
TS7-S1	-1203.19112	-1204.24631	964.8	-95.0	-3160878.9
TS7-S2	-1049.49620	-1050.40838	813.5	-87.0	-2757120.7
TS8-S1	-1203.19263	-1204.24876	967.1	-84.2	-3160872.3
TS8-S2	-1049.50708	-1050.41503	819.2	-86.9	-2757132.4
***p*CF$_3$-PhOH**	-643.97305	-644.60098	200.0	-41.1	-1692241.0
***p*Me-PhOH**	-346.50170	-346.79823	270.9	-37.9	-910285.7

Table 9.2: SCF energies at the level of theory of the geometry optimization (COSMO(∞)-TPSS-D3ZERO/def2-SVP, E(Opt)), SCF energies at the level of theory of the single point calculation (ωB97x-D/def2-QZVPP, E(SP)), thermochemical corrections (ΔG(therm)), solvation correction obtained from COSMO-RS(water), as well as final Gibbs free energy in solution (G(solution, SP)) for all calculations for Chapter 4.

Name	E(opt) (Hartree) COSMO(∞)-TPSS-D3ZERO/ def2-SVP	E(SP) (Hartree) ωB97x-D/ def2-QZVPP	ΔG(therm) (kJ·mol^{-1})	ΔG(solv) (kJ·mol^{-1})	G(solution, SP) (kJ·mol^{-1})
1a	-2553.48456	-2554.07345	598.9	-620.4	-6705741.4
1b	-2610.03850	-2610.67472	675.3	-613.0	-6854264.1
1c	-2610.03745	-2610.67681	674.4	-606.3	-6854263.8
1d	-2666.57822	-2667.26378	754.2	-608.8	-7002755.7
1e	-2629.87796	-2630.54177	639.9	-622.8	-6906470.3
1f	-2706.26436	-2707.00274	681.5	-629.4	-7107183.6
1g	-3240.70936	-3241.71363	948.3	-463.5	-8510634.4
1h	-3297.26683	-3298.30960	1020.3	-483.0	-8659174.6
2a	-2496.44198	-2497.16480	472.8	-140.4	-6555973.7
2b	-2552.99282	-2553.75163	556.5	-173.9	-6704492.3
2c	-2609.53353	-2610.33713	630.1	-177.6	-6852987.6
2d	-3296.76429	-3297.93728	979.4	-146.1	-8657901.1
3	-3188.03381	-3188.98512	652.1	-148.4	-8372176.8
4	-3188.14903	-3189.12175	674.4	-174.9	-8372539.7
5	-2957.20607	-2958.06432	502.7	-188.8	-7766083.9

5-PhF	-2596.87029	-2597.68686	506.7	-193.3	-6819913.5
Aniline	-287.47090	-287.62872	186.3	-15.7	-754998.6
Cl^-	-460.22640	-460.29218	-50.3	-310.9	-1208858.3
Cu-4NH_3	-1866.26070	-1866.41542	254.1	-832.5	-4900852.0
F^-	-99.84100	-99.86234	-46.8	-408.5	-262643.9
H_2O	-76.37137	-76.44620	-11.9	-22.6	-200744.0
NH_3	-56.52086	-56.57046	18.8	-17.0	-148524.0
OH^-	-75.81942	-75.80030	-36.1	-402.7	-199452.5
OH^- 2H_2O	-228.64078	-228.77505	40.1	-309.1	-600917.9
OH H_2O	-152.23324	-152.29400	-15.1	-351.9	-400214.8
OMe-Phenanthroline	-800.27718	-800.71940	429.8	-52.3	-2101911.2
PhCl	-691.61751	-691.88451	117.5	0.2	-1816425.1
PhF	-331.30732	-331.52036	125.6	1.6	-870279.6
TS1	-3301.61274	-3302.51735	862.7	-574.8	-8670471.4
TS2a	-3188.04297	-3189.01671	651.5	-136.0	-8372247.9
TS2a-PhF	-2827.73611	-2828.65696	665.5	-133.8	-7426107.2
TS2b	-3244.59662	-3245.60036	731.1	-157.1	-8520749.7
TS2c	-3301.13780	-3302.18608	817.2	-177.2	-8669249.6

Table 9.3: SCF energies at the level of theory of the geometry optimization (COSMO(∞)-TPSS-D3ZERO/def2-SVP, E(Opt)), SCF energies at the level of theory of the single point calculation (ωB97x-D/def2-QZVPP, E(SP)), thermochemical corrections (ΔG(therm)), solvation correction obtained from COSMO-RS(chloroform), as well as final Gibbs free energy in solution (G(solution, SP)) for all calculations for Chapter 5.

Name	E(opt) (Hartree) COSMO(∞)-TPSS-D3ZERO/ def2-SVP	E(SP) (Hartree) ωB97x-D/ def2-QZVPP	ΔG(therm) ($kJ \cdot mol^{-1}$)	ΔG(solv) ($kJ \cdot mol^{-1}$)	G(solution, SP) ($kJ \cdot mol^{-1}$)
1a	-2519.40708	-2520.11439	556.7	-103.5	-6616107.1
1a-AC	-2288.44523	-2289.04181	370.6	-89.2	-6009597.9
1a-PA	-2402.91165	-2403.59401	438.7	-98.5	-6310295.9
1b	-2633.85396	-2634.63787	607.6	-103.0	-6916737.2
1c	-5038.86574	-5040.27734	1175.1	-142.8	-13232215.8
1c-AC	-4576.92442	-4578.10947	792.8	-125.2	-12019158.8
1d	-2519.39218	-2520.09593	561.8	-100.7	-6616050.8
1d-AC	-2288.43279	-2289.02210	373.2	-91.2	-6009545.6
1d-PA	-2402.90279	-2403.57963	449.0	-92.5	-6310241.9
2	-2633.86341	-2634.65972	632.0	-86.6	-6916753.7
2-BYD	-2517.37007	-2518.13994	512.9	-84.3	-6610947.8
2-PA	-2402.89944	-2403.58336	438.3	-77.2	-6310247.0
3	-2633.85301	-2634.63286	634.8	-117.2	-6916711.0

3-BYD	-2517.36455	-2518.11687	521.9	-115.7	-6610909.6
3-PA	-2402.89318	-2403.56017	442.4	-107.8	-6310212.7
3-S2	-3201.64016	-3202.83754	820.0	-126.3	-8408356.2
3-S3	-2904.10866	-2905.02890	890.5	-125.9	-7626388.7
3-S4	-2673.15506	-2673.95835	703.0	-116.7	-7019891.3
4	-2942.15017	-2943.08830	888.6	-102.1	-7726291.9
5	-2942.16178	-2943.10102	889.2	-108.1	-7726330.6
6	-5153.31456	-5154.80799	1260.3	-142.7	-13532830.9
7	-5461.59109	-5463.23333	1512.9	-139.9	-14342346.1
8	-5461.59385	-5463.23910	1513.0	-139.9	-14342361.1
9	-2402.91165	-2403.59401	438.7	-98.5	-6310295.9
AC	-77.29179	-77.33255	43.8	-6.8	-202999.6
BYD	-306.22533	-306.43659	151.0	-39.3	-804437.5
PA	-191.75826	-191.88445	83.6	-23.9	-503732.8
PPA	-422.71729	-422.95648	266.3	-38.6	-1110244.6
PPA-S2	-990.48220	-991.13715	445.4	-54.2	-2601839.4
PPA-S3	-692.96447	-693.34394	517.8	-50.9	-1819907.6
PPA-S4	-462.01677	-462.28031	333.4	-39.2	-1213422.8
PhAC	-308.25018	-308.40455	197.8	-22.2	-809540.6
S2	-682.21626	-682.71123	192.5	-24.6	-1792290.4
S3	-384.70829	-384.92562	264.5	-30.3	-1010388.0
S4	-153.74860	-153.85185	75.2	-15.3	-403878.1
TS1	-2633.83174	-2634.60975	612.8	-90.7	-6916645.8
TS2	-2519.38693	-2520.09309	557.7	-98.1	-6616044.8
TS3	-2633.84041	-2634.62407	624.0	-100.8	-6916682.4
TS3-PA	-2517.35125	-2518.10908	511.0	-92.1	-6610876.5
TS3-AC	-2402.88085	-2403.55185	435.1	-89.0	-6310179.3
TS3-S2	-3201.62027	-3202.82060	812.7	-104.1	-8408296.9
TS3-S3	-2904.09966	-2905.01931	884.3	-115.9	-7626359.8
TS3-S4	-2673.14403	-2673.95127	692.9	-102.5	-7019868.6
TS4	-2633.84992	-2634.63339	636.7	-100.2	-6916693.4
TS5	-2942.12236	-2943.06208	871.2	-96.1	-7726234.4
TS5-BYD	-2594.66378	-2595.46365	568.7	-83.3	-6813904.3
TS5-PA	-2480.18918	-2480.90008	487.8	-89.8	-6513205.2
TS6	-5153.30343	-5154.78294	1249.3	-147.1	-13532780.4
TS7	-5461.58854	-5463.22928	1503.5	-140.3	-14342345.3
TS8	-2594.66340	-2595.46288	565.2	-83.4	-6813906.0
Acetonitrile	-132.68973	-132.76398	51.7	-21.6	-348541.7
CH_2O	-114.43823	-114.51831	11.3	-10.3	-300666.9

Table 9.4: SCF energies at the level of theory of the geometry optimization (COSMO(∞)-BP86-D4/def2-TZVP, E(Opt)), SCF energies at the level of theory of the single point calculation (B3LYP-D4/def2-TZVP, E(SP)), thermochemical corrections (ΔG(therm)), solvation correction obtained from COSMO-RS(chloroform), as well as final Gibbs free energy in solution (G(solution, SP)) for all calculations for Chapter 6.

Name	E(opt) (Hartree) COSMO(∞)-BP86-D4/ def2-TZVP	E(SP) (Hartree) B3LYP-D4/ def2-TZVP	ΔG(therm) (kJ·mol^{-1})	ΔG(solv) (kJ·mol^{-1})	G(solution, SP) (kJ·mol^{-1})
1	-1752.44008	-1752.42176	322.4	-64.5	-4600725.5
1-L2-Cl	-2000.90878	-2000.89101	807.6	-80.5	-5252612.2
1-L2-OTFA	-2067.10173	-2067.08393	842.2	-79.8	-5426366.4
2	-2004.97286	-2004.94712	850.7	-96.2	-5263234.1
3	-2004.93835	-2004.91338	838.9	-96.9	-5263158.0
4^{+}	-1852.07077	-1851.99117	320.4	-174.4	-4862256.8
6	-4033.98779	-4033.94728	1307.1	-144.5	-10589966.0
8	-2141.45838	-2141.43078	800.2	-97.1	-5621623.4
9^{+}	-2141.27463	-2141.20803	788.1	-177.2	-5621130.8
Chloroform	-1419.52337	-1419.51901	-37.6	-15.7	-3727000.5
FB(OH)$_2$	-276.66762	-276.65372	14.3	-12.4	-726352.4
N-5	-3468.17588	-3468.14056	769.5	-117.9	-9104951.5
N-7	-3757.36733	-3757.32793	1237.3	-139.6	-9863766.8
N-7-L2-Cl	-4005.83240	-4005.79669	1715.4	-148.3	-10515652.1
N-7-L2-OTFA	-4072.03189	-4071.99403	1754.3	-152.4	-10689418.4
N-TS5a	-3757.33325	-3757.29623	1225.2	-140.4	-9863696.4
N-TS5a-L2-Cl	-4005.80401	-4005.76187	1703.8	-165.3	-10515589.3
N-TS5a-L2-OTFA	-4071.99804	-4071.95635	1743.4	-162.7	-10689340.7
N-TS5b	-3757.32810	-3757.29135	1227.4	-136.7	-9863677.7
N-TS5b-L2-Cl	-4005.80324	-4005.76789	1713.5	-154.4	-10515584.5
N-TS5b-L2-OTFA	-4071.99804	-4071.95635	1743.4	-162.7	-10689340.7
N-TS5c	-3757.33001	-3757.28592	1235.8	-149.6	-9863668.0
N-TS5c-L2-Cl	-4005.80978	-4005.77302	1713.3	-154.2	-10515597.9
NFSI	-1715.68157	-1715.65856	367.9	-75.2	-4504168.8
NSI^{-}	-1616.05069	-1615.94680	380.9	-277.3	-4242564.7
NSI radical	-1615.81240	-1615.78647	378.6	-75.0	-4241943.8
O-5	-3468.15815	-3468.10876	764.2	-142.5	-9104897.9
O-7	-3757.34928	-3757.30494	1227.7	-156.9	-9863733.3
O-7-L2-Cl	-4005.82238	-4005.78633	1711.2	-155.2	-10515635.9
O-7-L2-OTFA	-4072.02185	-4071.98113	1755.8	-158.7	-10689389.3
O-TS5a	-3757.33465	-3757.29466	1226.4	-143.0	-9863693.7
O-TS5a-L2-Cl	-4005.80471	-4005.76672	1707.9	-156.8	-10515589.4
O-TS5a-L2-OTFA	-4071.99842	-4071.96060	1751.6	-152.8	-10689333.8

O-TS5b	-3757.32424	-3757.28403	1219.5	-143.9	-9863673.5
O-TS5b-L2-Cl	-4005.79689	-4005.75078	1710.8	-173.3	-10515561.2
O-TS5b-L2-OTFA	-4071.99079	-4071.94869	1750.0	-165.8	-10689317.0
O-TS5c	-3757.31649	-3757.27035	1219.8	-160.6	-9863654.0
O-TS5c-L2-Cl	-4005.79728	-4005.76257	1699.7	-151.4	-10515581.4
TS1	-3468.11438	-3468.07225	755.0	-130.1	-9104798.8
TS2	-4033.97850	-4033.93242	1312.7	-148.6	-10589925.4
TS3	-4033.98712	-4033.94874	1311.5	-141.3	-10589962.2
TS4	-4033.99057	-4033.94671	1314.6	-143.6	-10589956.1
***p-t*Bu-Ph-B(OH)$_2$**	-565.80899	-565.79416	476.3	-39.3	-1485055.6

Eidesstattliche Versicherung gemäß § 8 der Promotionsordnung für die Naturwissenschaftlich-Mathematische Gesamtfakultät der Universität Heidelberg

1. Bei der eingereichten Dissertation zu dem Thema

   „*Quantum-Chemical Investigations in Homogeneous Catalysis*“

   handelt es sich um meine eigenständig erbrachte Leistung

2. Ich habe nur die angegebenen Quellen und Hilfsmittel (inkl. KI-basierter Hilfsmittel) benutzt und mich keiner unzulässigen Hilfe Dritter bedient. Insbesondere habe ich wörtlich oder sinngemäß aus anderen Werken übernommene Inhalte als solche kenntlich gemacht.

3. Die Arbeit oder Teile davon habe ich wie folgt/bislang nicht an einer Hochschule des Auslands als Bestandteil einer Prüfungs- oder Qualifikationsleistung vorgelegt.

4. Die Richtigkeit der vorstehenden Erklärungen bestätige ich.

5. Die Bedeutung der eidesstattlichen Versicherung und die strafrechtlichen Folgen einer unrichtigen oder unvollständigen eidesstattlichen Versicherung sind mir bekannt.

Ich versichere an Eides statt, dass ich nach bestem Wissen die reine Wahrheit erklärt und nichts verschwiegen habe.

…… ……

Ort und Datum Unterschrift